Registration of Prostate Surfaces for Image-Guided Robotic Surgery Via the *da Vinci* System

Ilias Sioutis

M.Phil. Thesis

Department of Computer Science

University College London

September 2015

I, Ilias Sioutis, confirm that the work presented in this thesis is my own. Where information has been derived from other sources, I confirm that this has been indicated in the thesis.

Abstract

Organ-confined prostate cancer represents a commonly diagnosed cancer among men rendering an early diagnosis and screening a necessity. The prostate laparoscopic surgery using the *da Vinci* system is a minimally invasive, computer assisted and image-guided surgery application that provides surgeons with (*i*) navigational assistance by displaying targeting lesions of the intraoperative prostate anatomy onto aligned preoperative high-field magnetic resonance imaging (MRI) scans of the pelvis; and (*ii*) an effective clinical management of intra-abdominal cancers in real time. Such an image guidance system can improve both functional and oncological outcomes as well as augment the learning curve of the process increasing simultaneously the eligibility of patients for surgical resection.

By segmenting MRI scans into $3D$ *models* of intraprostatic anatomy *preoperatively*, and overlaying them onto $3D$ *stereoendoscopic images* acquired *intraoperatively* using the *da Vinci* surgical system, a graphical representation of intraoperative anatomy can be provided for surgical navigation. The preoperative MRI surfaces are full $3D$ models and the stereoendoscopic images represent partial $3D$ views of the prostate due to occlusion. Hence achieving an accurate non-rigid image registration of full prostate surfaces onto occluded ones in real time becomes of critical importance, especially for use intraoperatively with the stereoendoscopic and MRI imaging modalities.

This work exploits the registration accuracy that can be achieved from the application of selected *state-of-the-art* non-rigid registration algorithms and in doing so identifies the most accurate technique(s) for registration of full prostate surfaces onto occluded ones; a series of rigorous computational registration experiments is performed on synthetic target prostate data, which are aligned manually onto the MRI prostate models before registration is initiated. This effort extends to using real target prostate data leading to visually acceptable non-rigid registration results. A great deal of emphasis is placed on examining the capacity of the selected non-rigid algorithms to recover the deformation of the intraoperative prostate surfaces; the deformation of prostate can become pronounced during the surgical intervention due to surgical-induced anatomical deformities and pathological or other factors.

The warping accuracy of the non-rigid registration algorithms is measured within the space of common overlap (established between the full MRI model and the target scene) and beyond.

From the results of the registrations to occluded and deformed prostate surfaces (in the space beyond common overlap) it is concluded that the *modified* versions of the Kernel Correlation/Thin-plane Spline (KC/TPS) and Gaussian Mixture Model/Thin-plane Spline (GMM/TPS) methodologies can provide the clinical accuracy required for image-guided prostate surgery procedures (performed by the *da Vinci* system) as long as the size of the target scene is greater than *ca.* 30% of the full MRI surface.

For the *modified* KC/TPS and GMM/TPS non-rigid registration techniques to be clinically acceptable when the measurement noise is also included in the simulations: (*i*) the size of the target model must be greater than *ca.* 38% of the full MRI surface; (*ii*) the standard deviation σ of the contributing Gaussian noise must be less than 0.345 for $\mu = 0$; and (*iii*) the observed deformation must not be characterized by excessively increased complexity. Otherwise the contribution of Gaussian noise must be explicitly parameterized in the objective cost functions of these non-rigid algorithms.

The Expectation Maximization/Thin-plane Spline (EM/TPS) non-rigid registration algorithm cannot recover the prostate surface deformation accurately in *full-model-to-occluded-model* registrations due to the way that the correspondences are estimated. However, EM/TPS is more accurate than $KC + TPS$ and $GMM + TPS$ in recovering the deformation of the prostate surface in *full-model-to-full-model* registrations.

Acknowledgements

I would like to acknowledge the encouragement, support and advice provided by my principal supervisor Prof. Simon Arridge. I would like to thank Yipeng Hu whose knowledge and experience of medical imaging and registration as well as friendship and support in difficult times have been critical for me to continue. Very many thanks go to all researchers in the lab that made my time enjoyable at UCL such as Holger Ruth, Tom Hampshire, Johannes Totz, Steve Thompson and Matt Clarkson.

I would also like to thank Laura Panagiotaki, Dominique Drai, Ron Gaston, Melanie Johnson and especially Marco Federighi for their support and help in extremely difficult and challenging times during the course of this research. I would not have been able to continue without the support from my family (Pavlos and Eleni) and friends (Vanda Glezakou, Alex Martin, Georgios Tserdanelis, Nigel Oram, Antonis Tsakotelis, Eleftherios Epameinondas, Manos Mavrakis, and Alexandros Piperakis).

This thesis is dedicated to all professional academics that act responsibly.

Contents

List of Figures

List of Tables

List of Algorithms

List of Abbreviations

A list of abbreviations used in this work follows:

AR − Augmented reality

CT − Computed tomography

EM − Expectation maximization

FEM − Finite element model

FLE − Fiducial localization error

FRE − Fiducial registration error

GMM − Gaussian mixture model

GRBF − Gaussian radial basis function

GUI − Graphical user interface

ICP − Iterative closest point

KC − Kernel Correlation

MRI − Magnetic resonance imaging

MS − Mean squares

ODE − Ordinary differential equation

RBF − Radial basis function

RKHS − Reproducing kernel Hilbert space

RMS − Root mean square

T − Tesla

TPS − Thin-plane spline

TRE − Target registration error

TRUS − Transrectal ultrasonography

TVE − Target visualization error

UCLH - University London College Hospital

US − Ultrasound

VTK − Visualization toolkit

2D − Two dimensional

3D − Three dimensional

Chapter 1

Introduction

1.1 Why is this work important from a clinical perspective?

Prostate cancer has become one of the most common cancers among men in the UK and the United States [1, 2] with an increasing incidence due to an aging population [1]. Radical prostatectomy, an already established technique for cancer treatment, contributes the most in increasing the survival rates [3].

Radical prostatectomy can be performed by open surgery (retropubic or perineal) and by minimally invasive approaches (laparoscopic and robot-assisted laparoscopic techniques) [4, 5]. The former ones result in increased blood loss and longer hospital stay. The laparoscopic methods are constrained by a $2D$ visualization of the surgery scene, reduced instrument motion and lack of haptic feedback [6]. The robotic-assisted laparoscopic techniques, especially those performed with the aid of the *da Vinci* Surgical System (see Figure 1.1), which has superior stereo-vision capabilities and can provide high-resolution digital video endoscopy, exhibit competitive advantages, *i.e.*, they provide: (*i*) motion-scaling and tremor loss, a wider range of motion for surgical instruments as well as advanced ergonomics; and (*ii*) $3D$ vision [6]. While all surgical modalities may cause nerve damage and other functional injuries [6], the potential of robotic-assisted technologies hasn’t yet been fully exploited [7].

Third party copyright image removed

Figure 1.1: The Intuitive Surgical's *da Vinci*® Surgical System (Intuitive Surgical, Sunnyvale, California). From left to right: main console where the surgeon operates from; four interactive robotic arms; a widescreen high-definition monitor view of the operating surgical field; a view of the main surgeon console from a different angle. Taken from Ref. 8.

Reduced depth perception and limited field of view are typical operative drawbacks of minimally invasive surgery. They can be addressed by computer-assisted technologies such as *Augmented Reality* (AR) systems [9, 10]: (i) segmented $3D$ medical image models [ultrasound (US), computed tomography (CT) or MRI] are first constructed to serve as virtual representations of anatomical structures and pathological features; and then (ii) they are projected onto corresponding $3D$ data views of patient structures with the aid of (manual or automatic) image *registration*. In doing so the hidden part of the anatomical structures below the exposed tissue surface (as displayed in the camera view, see Figure 1.2) is (virtually) revealed. Processes (i) and (ii) can effectively enhance the intraoperative navigation during surgery.

This work focuses on non-rigid image registration of prostate surfaces and on providing a reliable $3D$ AR environment for image guidance in robot-assisted (via the *da Vinci* System) minimally invasive prostate laparoscopic surgical interventions such as prostatectomy and prostate cancer management [11] (see Figure 1.2). The $3D$ MRI imaging has been chosen as the preoperative imaging modality. The mechanism of $3D$ measurement in the *da Vinci* System is based on $3D$ surface (stereo-vision) reconstruction of intraoperatively acquired (left and right) video images of prostate surface; this leads to a $3D$ intraoperative point-cloud representation of the prostate.

Soft prostate tissue movement and deformation due to patient position, tumour growth or other physiological aspects, breathing, heartbeat as well as surgical instrument mobilization of prostate make it a challenging task to achieve a clinically accurate real-time AR registration in the operating theatre. One of the main objectives of this thesis is to exploit extensively the impact of the deformation of the prostate surface on the non-rigid registration accuracy by simulating all possible clinical case scenarios.

Third party copyright image removed

Figure 1.2: Preoperatively constructed $3D$ MRI models overlaid onto $3D$ stereoendoscopic camera views in robot-assisted image-guided prostate surgical treatment procedures. Such MRI superimpositions enhance considerably the visualization and identification of relevant subsurface structures as well as intraprostatic and periprostatic anatomies, improving the precision of surgical interventions: (a) Dorsal-vein ligation; (b) Dissection of the lymph node; (c) Dissection of the bladder neck; (d) Dissection of the seminal vesicle; (e) Posterior dissection of Denonvilliers' fascia; (f) Nerve-sparing prostatectomy; and (g) Prostate mobilization. Taken from Ref. 11.

Preoperative MRI imaging is preferred over other imaging modalities for image-guided surgery. MR imaging of the prostate produces an optimal image representation and accurate definition of the gland, its margins, cancerous foci and adjacent structures as well as its substructure (central gland and peripheral zone) (see Refs. 1, 12-14 and Figure 1.3 for an example MRI scan). It is routinely performed by an MRI radiologist as part of surgical planning. MR imaging exceeds in quality CT imaging as the latter technique fails to provide adequate accuracy in defining prostate substructure as well as the inferior and superior borders of the prostate [15, 16].

Third party copyright image removed

Figure 1.3: A conventional $3T\ CUBE\ MRI$ scan. The anatomical boundaries of the prostate and adjacent anatomical structure can be identified. Taken from Ref. 1.

The principal objective of this work is to enhance the surgical accuracy and oncological cure of prostate cancer tumour performed by the *da Vinci* surgical system. As a robotic-assisted image guidance system, it can display the complicated environment of the pelvic anatomy in real time, and has the potential to perform an accurate macroscopic excision of the visible growth (reducing positive cancer margins). In doing so, injuries of the external sphincter and of the neurovascular bundle (see Figures 1.4 and 1.5) can be avoided, guidance for bladder neck dissection can be provided and a reduction of rectal injuries [1, 17] can be achieved.

Third party copyright image removed

Figure 1.4: The basic and postsurgical anatomies of prostate.

Third party copyright image removed

Figure 1.5: Intraprostatic and periprostatic anatomies.

1.2 Literature review on image registration

Section 1.2.1 defines and provides some general information about image registration so that its uses in various medical contexts throughout the literature review can be comprehended. This section also gives an example of rigid-body registration, presents the four categories that the non-rigid image registration methods can be classified into, and highlights their applications in computer-aided surgery.

As the available literature on the topic of non-rigid registration of prostate surfaces is sparse, the present review in Sections (1.2.2-1.2.5) has extended to include relevant work for other organs. While some of this material is not strictly linked to the stereo-vision endoscopic robotic surgery technique, which is the method of choice in the *da Vinci* System, it is still very useful as it provides further insight into the registration process itself, the clinical practices and the challenges encountered.

Section 1.2.2 describes three representative AR image-guidance technologies where the MRI (or CT) imaging modality is fused with intraoperative stereo viewing. The first two overlay systems are applied to radical prostatectomy and the last one to partial nephrectomy. The registrations are conducted without accounting for the non-linear deformation of the soft-tissue structures.

Section 1.2.3 outlines a non-rigid image surface matching registration scheme where a deformable model (constructed by preoperative MRI images of the prostate) is non-linearly registered onto intraoperative MRI volumetric images. Another image-guided technique (for hepatic tumour resection) that also uses the MRI (or CT) imaging modality preoperatively is presented in this section. It is combined with the laser range scanning technology which is used to produce surface representations of the liver intraoperatively. The preoperative image volume is registered onto the target using both rigid and non-rigid registration methodologies.

Section 1.2.4 describes an AR visualization system for radical prostatectomy which is used to superimpose a transrectal ultrasonography ($TRUS$) model of prostate anatomy onto stereoendoscopic video images. The process of registration is based upon a rigid spatial transformation scheme and is conducted with the aid of navigation aids. In another AR image-guidance application (for partial nephrectomy) a preoperative CT image of the kidney is rigidly aligned onto stereoendoscopic video images.

In Section 1.2.5 details about a $TRUS -$guided biopsy system (for prostate cancer management) are given. It involves the application of $TRUS - TRUS$ rigid surface- and image-based (or intensity-based) registration schemes to address prostate motion, and $TRUS - TRUS$ non-rigid surface- and image-based registration methods to treat both prostate motion and deformation effects. Section 1.2.6 provides a concluding summary of this review.

1.2.1 General information about image registration

Image registration can be defined as the process of geometric transformation or spatial mapping between two or more images ($3D$ feature point datasets in this work) taken at different times from different viewpoints, and with usually different image sensors, which brings them into a common global $3D$ coordinate system and causes all intersecting sections to overlap completely.

Image registration may be classified as: (*i*) *multi-temporal* where image data from the same patient (*i.e.*, *intrasubject*) are registered using a single imaging modality but at different times (*e.g.*, for monitoring tumour growth); and (*ii*) *multi-modal* where image data from the same patient are registered using various imaging modalities (*e.g.*, CT, MRI and US for structural analysis) as in the current study. Image data obtained from a single imaging modality but from different patients (*i.e.*, *intersubject*) can be registered to produce an atlas which in turn can be used for image registration and image-guided surgery.

Image registration was initially applied to $2D$ images and involved rigid (translation and/or rotation) or affine transformations (rigid plus shearing and/or scaling). Let's take as an example the rigid-body $3D$ *point-based* image-to-patient registration which is one type of $3D$-to-$3D$ volume registration. The spatial motion observed in the rigid-body transformation can be fully modelled by combinations of linear transformations. The registration takes place between *point-cloud* representations of preoperative surfaces (the *source* model) and intraoperatively acquired patient surfaces (the *target* model) [18, 19].

The patient surfaces may be obtained via laser range scanning or stereo-vision reconstruction methods. During the surgical planning step, intrinsic anatomical structures and features, extrinsic fiducial markers (*i.e.*, implanted fixed external landmarks) attached near anatomical regions of interest or security margins around tumours, surgical trajectories, *etc…*, are identified in preoperative $3D$ image (CT and/or MRI) segmentations of the relatively rigid structures.

The $3D$ point positions of the distinct intrinsic features or extrinsic fiducial markers of the preoperative images are matched against their correspondences in the intraoperative patient volumetric images. The geometric transformation parameters required to rigidly register the source model onto the target model can be computed directly as their $3D$ point correspondences are already known. Closed-form analytical solutions have been developed for *point-based* rigid registrations [20]. The intrinsic and extrinsic landmarks can be used as navigation aids [19, 20] as they can be easily tracked by external tracking devices intraoperatively and in real-time [21, 22].

While a rigid-body registration can accurately describe a shift of an "undeformable" organ, a non-rigid (elastic) body transformation would be more suitable for soft-tissue structures (*e.g.*, prostate, kidney, liver) as the imaged target anatomy involves non-linear organ deformations between image acquisitions. Patient position or routine tissue manipulation such as incision of organs and clamping of vessels can cause a change in the shape of an unconstrained organ or on the constellation of neighbouring organs [23]. Organ shifts may simultaneously take place due to cardiac motion, respiration or laparoscopic insufflation [24].

To describe the complex (periodic and non-periodic) motion of the organ, one approach could be to first apply a rigid-body registration and then include all residual errors (*i.e.*, corrections due to spatial distortion) arising from the non-linear organ deformation [25, 26]. A more rigorous approach would be to warp $3D$ preoperative images to match $3D$ intraoperatively acquired patient images in real time [27].

The available navigational systems and technologies are not always accurate in the registration of deformable organs (often obtaining clinically unacceptable values of registration accuracy) which in turn highlights the inherent difficulties of combining preoperative with intraoperative imaging modalities in a non-rigid registration scheme [28]. As it is computationally expensive to conduct rigorous and exact simulations of soft-tissue behaviour (despite the advantage of achieving an accurate registration), only simplified registration frameworks can be considered for surgical intervention and navigation [29]. However the use of such approximations leads to important registration errors [28, 30].

The non-rigid registration process between two medical images is formulated by: (i) the identification of correspondences between the images; (ii) the non-linear transformation function which maps the source model onto the target model so that anatomically homologous locations of the two feature datasets can be overlapped completely. Due to the high dimensionality introduced by (*i*) and (*ii*) in $3D$, the non-rigid registration becomes a difficult problem especially in the presence of outliers and noise.

During the non-rigid registration the deformation takes place with constraints (*i.e.*, the deformation is regularized) while a distance metric is simultaneously minimized. The non-linear transformation functions used can recover local deformations in contrast to rigid or affine transformations which can operate only globally.

The non-rigid medical image registration methods can be grouped in four categories: (*i*) *point-based*; (*ii*) *surface-based*; (*iii*) *intensity-based*; and (*iv*) *model-based*.

The non-rigid-body *point-based* registration methods (similar to rigid-body point-based registrations) involve the (manual or semi-automatic) identification of a set of homologous landmarks between the images that are registered. These must be identifiable by the imaging modality used and can be (*i*) intrinsic features of the patient's imaged organ anatomy which can be extracted directly from the imaging data; or (*ii*) extrinsic markers which can further be classified into internal fiducial markers (*i.e.*, surgically inserted coils prior to imaging) and external fiducial markers (*i.e.*, objects attached to a rigid structure). Hence the *point-based* methods can be categorised into intrinsic and extrinsic ones [31]. Their main advantage over the *surface-* and *intensity-based* registration approaches is in speed as the number of landmark pairs required is smaller in comparison to the number of pixels or voxels in the imaging data, which expedites the calculation of the transformation function.

The *surface-based* registration methods involve the segmentation of surfaces from raw imaging data followed by the extraction of equivalent surfaces from the segmented medical images [22]. Consequently, the accuracy of the surface segmentation has an impact on the accuracy of registration. *Surface-based* registration is usually combined with other techniques such as *point-based* registration [31]. Some comparative studies have highlighted the superiority of *intensity-based* registration techniques over *surface-based* methods [32, 33]. *Surface-based* registration is more suitable than *point-based* registration for some well-defined anatomical structures [34].

The *intensity-* or *voxel-based* registration methods operate directly on the grey values of the whole images bypassing any geometrical features of the anatomical structures. Of the most popular *intensity-based* non-rigid registration methods are those that incorporate mutual information as a measurement of image similarity [35-38]. In some studies the image similarity measure was combined with regularization of deformation and the optimization of the transformation function was conducted in such a way that the similarity metric could obtain a true global maximum [39].

The *model-based* registration methods depend upon models of deformation fields which in turn are based on the physical characteristics of the tissues or organs of interest. These techniques are more computationally expensive than other registration methods due to the non-parametric nature of the involved transformations (*i.e.*, the deformation of each voxel is computed directly). Simplified approximations of the physical system are usually used instead to expedite the process of registration, which however, reduces the registration accuracy.

The finite element model (FEM) technique is an example of a *model-based* registration approach. The area of interest is divided into an interconnected collection of elements each of which is characterised by a distinct set of physical properties. Deformations are described by displacement of nodes produced by exerting an external influence onto the system. They are modelled subject to a constraint imposed by an energy function which depends on the properties of each node. The FEM technique has been applied to image registration [40, 41] and to the validation of other medical image registration methods [42].

Non-rigid registration covers a wide range of applications such as (*i*) surgical planning and training where multi-modal medical images can be registered and visualized as part of operation planning or for educational purposes; and (*ii*) surgical navigation, image-guided surgery and treatment where image registration between preoperative and intraoperative images is critical for an accurate guidance of surgical instruments and tools.

1.2.2 Registration of preoperatively acquired MRI (or CT) image volumes of prostate (or other organ) surfaces onto stereoscopic video images

Cohen *et al.* [1] exploited the usefulness and applicability of an AR image guidance system for minimally-invasive laparoscopic prostatectomy using the $da\ Vinci$ system. Three-tesla MRI imaging of the pelvis was used as the preoperative imaging modality. The MRI scans were segmented into a $3D$ image of the pelvic anatomy, which was calibrated and scaled to adjust to the magnification observed intraoperatively. The segmented image was manually registered onto stereoendoscopic still images of a recorded robot-assisted surgery, in a post processing operative mode, for retrospective evaluation by the surgeon (see Figures 1.6-1.9).

Fusing the $3D$ MRI preoperative imaging modality with $3D$ intraoperative stereo viewing is a relatively new image-overlay technology which can provide visualization and identification of intraprostatic and periprostatic subsurface structures and anatomies (see also Figure 1.2).

Third party copyright image removed

Figure 1.6: $3D$ laparoscopic operative view of the surgeon. Taken from Ref. 1.

This work aimed more at determining the clinical efficacy of an image guidance system for robotic-assisted prostatectomy. The prostate tissue deformation due to pneumoperitoneum and surgical mobilisation of the prostate was not accounted for by the transformation function. Reconstruction, registration and tracking were done manually designating an early stage of development for the proposed image-guidance technology.

Third party copyright image removed

Figure 1.7: An overlay of the pelvic anatomy. The structure is colour coded based on the following scheme: prostate (green), seminal vesicles (pink), left-sided neurovascular bundle (yellow) and pelvic bony structure (white/gray). The anatomical structures that are important to identify at key stages of prostatectomy are: prostate, bladder, urethra, vas deferens, seminal vesicles, rectum, neurovascular bundles and ureters. Taken from Ref. 1.

Third party copyright image removed

Figure 1.8: Operative view of the dorsal vein complex before ligation. Taken from Ref. 1.

Third party copyright image removed

Figure 1.9: AR overlay including the dorsal vein complex. The overlaid pelvic anatomy is colour coded based on the following scheme: prostate (green), seminal vesicles (pink), left-sided neurovascular bundle (yellow) and pelvic bony structure (white/gray). (See also Figure 1.7.) Aside from the bony pelvis the structures are not accurately aligned due to pneumoperitoneum. The neurovascular bundle is clearly defined in the AR overlay but not on the video screenshot. Taken from Ref. 1.

The latest work on robot-assisted radical prostatectomy involved the design of AR image-guidance systems for abdominal laparoscopic surgery in real time [43]. Simple $T2-$ weighted MRI $2D$ slices of the prostate anatomy (such as those shown in Figure 1.10; see also Ref. 44) were used as preoperative images. The prostate, the tumour location, and the neurovascular bundles were identified on the MRI images by a radiologist. The preoperative images were then overlaid onto the stereoendoscopic intraoperative camera view.

Third party copyright image removed

Figure 1.10: On the left: operative view of the surgeon. On the right: preoperative $2D$ $T2-$ weighted MRI images overlaid onto the surgical view. Taken from Ref. 43.

The registration was conducted using two methods: (*i*) by manually (visually) aligning an ordered set of points selected from the inner surface of the pubic arch and identified in the $2D$ MRI image scan onto the surgical scene (see Figure 1.11); and (*ii*) by incorporating a $B-$mode US probe which could percutaneously image the pelvic bone throughout the surgery.

The selected wireframe data structure in (*i*) could only be observed in the surgical scene during the last stages of the surgery. Ultrasonography, in (*ii*), despite its accuracy, introduced significant computational complexity in the registration.

Both methods used: (*i*) the pelvic bone structure as a reference for minimizing registration errors as the prostate is near its centroid plus it is visible intraoperatively and in MRI images; and (*ii*) an optical tracking system to track the laparoscope camera lens which, however, reduced system accuracy in determining anatomical prostate points. Both methods involved large registration errors: the first one amounted to *ca.* 20 mm and the $US-$based technique to

7 mm due to the fact that neither of these methods accounted for the non-linear deformation of the prostate tissue.

Third party copyright image removed

Figure 1.11: On the left: a misaligned overlay of a wireframe of selected points over the surgical scene. On the right: a (manually) registered wireframe overlaid onto the surgical scene. The wireframe data structure was created by an ordered set of 42 points selected from the inner surface of the pubic arch and manually identified in the $2D$ MRI image scan. Taken from Ref. 43.

Pratt *et al.* [45] introduced a manual registration interface for image-guided intraoperative robotic (*da Vinci* Intuitive Surgical System robot) partial nephrectomy where live AR models could be overlaid onto $2D$ endoscope video in real time. The system architecture for image guidance was based on the $NVIDIA$ Quadro Digital Video Pipeline (see Figure 1.12).

CT and MRI scans of kidneys were segmented and the produced meshes were subsequently smoothed. A distinct feature (*i.e.*, a landmark on the target model surface) was located in the left stereo capture image, its stereo correspondence was tracked manually, and via relevant ray intersections the same feature was (manually) located on the surface of the $3D$ source mesh geometry. For the rigid registration of these two $3D$ correspondence points the source model was translated to the target image feature and the rotational degrees of freedom were manually adjusted.

Third party copyright image removed

Figure 1.12: System architecture for image guidance using the *NVIDIA* Quadro Digital Video Pipeline. The stereo video feed originating in the *da Vinci* stack is split via a distribution amplifier into two identical stereo video streams (blue and green in the figure). The primary inputs of a pair of auto-standby video switches receive a video stream directly from the distribution amplifier; this is further fed into the *da Vinci* console as raw stereo video signal. Their secondary inputs receive the augmented stereo feed produced by the digital video pipeline; this can also be displayed on the *da Vinci* console. Taken from Ref. 45.

Despite the successful implementation of live *AR* overlay systems for image guidance, visualization of tumour and adjacent anatomy as well as hilar vessel localisation, the proposed registration method is based upon a rigid spatial transformation scheme. Hence it cannot account for soft tissue deformation: the average registration error was as high as 4.76 mm, a level of accuracy that is not acceptable for clinical applications.

1.2.3 Registration of preoperatively acquired MRI (or CT) image volumes of prostate (or other organ) surfaces onto images recorded using other imaging modalities

Bharatha *et al.* [14] used rigid and non-rigid image registration techniques to match ($MRI -$guided brachytherapy) preoperative 1.5 tesla (T) $T2 -$weighted endorectal coil MR images of the prostate with $0.5\,T\ MR\ T2 -$weighted intraoperative image data. Their goal was to enhance the accuracy of intraprocedure navigation under real-time guidance. As Figure 1.13 depicts, the central gland and peripheral zone of the preoperative images and the total gland of the intraoperative images of the prostate were manually segmented.

Third party copyright image removed

Figure 1.13: Rigid and non-rigid registration processes between preoperative $1.5\,T\ MRI$ image data and intraoperative $0.5\,T\ MRI$ image data in prostate brachytherapy. Taken from Ref. 14.

A rigid registration step (involving translation only) that roughly aligned the pre- and intraoperatively segmented total gland $3D$ models was followed by a rigorous non-rigid image matching registration scheme (described extensively in Refs. 46 and 47).

This scheme involves the following steps: (i) a $3D$ mesh representation of an FEM is constructed using the $1.5\,T$ preoperatively segmented images of the peripheral zone and the central gland; (ii) as these structures can be distinguished in the tetrahedral mesh model distinct material properties can be assigned in each region (see Figure 1.14). The total gland surface of the preoperative image is considered an elastic membrane; (iii) an active image surface matching algorithm [48] is incorporated to non-linearly register (automatically) the deformable model of (ii) onto the prostate boundary surface of the segmented $0.5\,T$ intraoperative total gland model; (iv) a volumetric deformation field is computed from the surface deformation displacements of the preoperative total gland image surface in (iii). The deformation field serves as a boundary condition in these calculations; and (v) the computed volumetric deformation field from (iv) may be applied to the original segmented (or grayscale) preoperative MR image to produce deformed preoperative prostate label images of the total gland.

The FEM was constructed assuming a linearly elastic material and an isotropic framework [46]. To describe the deformation, a distinct pair of elastic properties (namely, Poisson's ratio and Young's elastic modulus) was attributed to the segmented images of the central gland and peripheral zone. By registering the preoperative total gland image onto the lower resolution intraoperative image the central gland, the peripheral zone and their boundary were revealed and their relative positions were defined.

Third party copyright image removed

Figure 1.14: $3D\ FEM$ of the central gland (in red) and peripheral zone (in dark blue) of the prostate. It was constructed using original $1.5\ T\ MR$ imaging data. Additional structure of pelvic anatomy is included: bladder and ureter (in blue); vas deferens and seminal vesicles (in yellow); endorectal coil (in black) and rectum (in brown). Taken from Ref. 14.

Whether the prostate tissue exhibits an isotropic behaviour or not is not certain. An elastic model would become more appropriate in the limit of diminishing prostate surface deformations. The best values for the elastic properties of each of the two model materials were chosen on the basis of an image match quality (*i.e.*, best anatomic resemblance) between the intraoperatively segmented structure and the registered preoperative image, after a number of experimental trial registrations. No *in vivo* studies were conducted to determine biomechanical prostate tissue properties. The experimental parameters cannot represent the microscopic properties of the prostate tissue. For a rigorous analysis further validation would be required incorporating higher resolution imaging and enhanced image contrast.

Figures 1.15 and 1.16 outline the non-rigid registration process. Figure 1.15 highlights the method's contribution, *i.e.*, the ability to accurately overlay the central gland/peripheral zone (and their boundary) segmentation interface onto the target prostate surface. Figure 1.16 displays original and deformed preoperative grayscale images and intraoperative ones demonstrating the good match of image surface contours after registration.

Non-negligible segmentation errors were incurred due to the variability in the segmentation of preoperative and intraoperative image data, which led to important registration errors. The rigid registration was restricted to translation and matching the centres of mass of the segmented total gland structures of the intraoperative and preoperative datasets. Any rotation that wasn't visually apparent was treated as deformation.

Third party copyright image removed

Figure 1.15: (a) Segmented preoperative 1.5 T image data before deformation. The central glad is depicted by gray and the peripheral zone by white; (b) segmented intraoperative 0.5 T image data. The data shown in (b) and the data shown in (a) are viewed across an axial slice plane; (c) deformed 1.5 T image data. Note the additional structure (central gland, peripheral zone and their boundary) inferred due to the interpolation of the computed volumetric deformation field; (d) same as (b). The (manually) segmented structure of the central gland, the peripheral zone and their boundary are overlaid onto the intraoperative image data of (b) (done independently by a human observer and can be considered as the ground truth. See also Figure 1.16). Taken from Ref. 14.

Third party copyright image removed

Figure 1.16: (a) Original preoperative $1.5\,T$ grayscale image. The segmentation of Figure 1.15(a) was derived from these image data; (b) deformed preoperative $1.5\,T$ grayscale image computed using the FEM volumetric deformation map. The deformed structure of Figure 1.15(c) was derived from these data; (c) original intraoperative $0.5\,T$ grayscale image. The segmentations of Figures 1.15(b) and (d) were derived from these data. (d) - (f) represent another series of preoperative and intraoperative images for a different patient. They are ranked in correspondence to (a) - (c). The anatomical boundary between the central gland and the peripheral zone cannot be delineated in the intraoperative image data of (f) due to poorer spatial resolution and soft tissue contrast. However, the total gland, central gland, peripheral zone contours and tumour foil can be identified by incorporating preoperative $1.5\,T\ T2-$weighted endorectal-coil MR imaging. Taken from Ref. 14.

Cash *et al.* [49] examined the feasibility of image-guided (open abdominal) hepatic tumour resection procedures. Preoperative CT (or MR imaging) volumes were manually segmented to produce $3D$ surface source models. These were further refined to provide smoother anatomical representations of the liver surface.

Intraoperative dense surface representations of liver were obtained using the laser range scanning technology. By capturing $3D$ surface points (using optical triangulation) and combining this input with the video image of the scene, a $3D$ texture-mapped point cloud can be produced. The preoperative tomographic image volume was then registered onto the so produced target feature dataset using the iterative closest point (ICP) surface matching algorithm.

When the range scanner captures (near) planar regions, multiple registrations may become equally valid which in turn can lead to false ICP registration matches. To overcome these problems, the ICP registration was performed with respect to anatomical landmarks and geometrically unique features that were identified by the surgeon.

The surface ICP registration error fell within the range between 2 and 6 mm. This variation was attributed to the intraoperative soft-tissue deformation, the liver motion due to respiration, the quality of intraoperative surface data, the size of the exposed surface region acquired by the range scanner, and surgery-induced deformities.

An FEM of the liver was also constructed: (i) the rigidly registered preoperative volumetric mesh served as a reference model; and (ii) the incurred intraoperative deformation was represented by a set of displacements from this reference structure, and was simulated by solving a system of partial differential equations subject to boundary conditions.

A better alignment between the preoperative image surface and intraoperative data was achieved when the FEM' s corrections were included as these captured much of the observed intraoperative deformation. The requirement for a large exposure of the organ's surface is, however, a major disadvantage of the laser range scanning technology.

1.2.4 Registration of preoperatively acquired image volumes (using other imaging modalities) of prostate (or other organ) surfaces onto stereoendoscopic images

Simpfendörfer *et al.* [50] implemented an AR visualization and navigation system that could superimpose a virtual model of prostate anatomy onto laparoscopic video images during radical prostatectomy and in real time (see Figure 1.17). Navigation needles were inserted into the prostate and a segmented $3D$ $TRUS$ model of the prostate was obtained. The navigation aids served as points of real-time registration between these two imaging modalities.

The (rigid) manual registration itself, referred to as "inside-out tracking" or "$2D$-$3D$ camera pose estimation", was calculated from the (dimensional) correspondence between the $2D$ projections of the $3D$ US image navigation aids and the $2D$ laparoscopic video image ones. The *target visualization error* (TVE), defined as the average offset between the back-projected registered $2D$ image points (redefined in the $3D$ domain) and the manually defined ones in the $TRUS$ $3D$ volume, was found as low as (0.55 ± 0.28) mm.

While this AR visualization approach overcomes the problem of tissue shift, it cannot compensate for organ deformation, especially when an extended change in the prostate morphology is involved. Aside from being invasive, this technique is heavily dependent upon the use of navigation aids. By inserting them in the target surgical area the *target registration error* (TRE) is reduced. However, the removal of cancer foci becomes problematic due to the introduced needle occlusion.

Third party copyright image removed

Figure 1.17: Endoscopic view of the prostate: [A] without AR visualization. Five needle-shaped navigation aids with coloured heads are shown; [B] with AR visualization. The $3D$ $TRUS$ image is superimposed. The neurovascular bundles are depicted by blue, the virtual navigation aids by yellow and the green colour designates the border of the prostate. The virtual navigation aids are superimposed onto the real ones. The tissue deformation was approximated by the changes in the spatial configuration of the navigation aids. Taken from Ref. 50.

Another study [51] on robot-assisted laparoscopic partial nephrectomy used AR overlays of preoperative $3D$ kidney models for surgical guidance. CT images were manually segmented leading to a $3D$ surface model of the kidney and tumour (or stone) (see Figure 1.18). After calibration of segments of the recorded stereoendoscopic video (done in a post processing mode), the preoperative $3D$ segmented kidney model was overlaid and manually aligned onto the stereoscopic view.

This manual registration was further refined using an automatic surface-based registration algorithm. Selected points (by the operating surgeon) of the kidney surface served as fixed reference points. By estimating their $3D$ positions via stereo triangulation and stereo reconstruction the orientation and position of the $3D$ mesh overlay could be determined. The automatic registration could by further augmented by means of a $3D$-to-$3D$ ICP registration. Due to occlusion of the kidney, only part of the $3D$ preoperative kidney model could participate in the ICP registration.

While an accurate $3D$-to-$3D$ registration presupposes an accurate segmentation of the preoperative CT image of the kidney and no major errors due to stereo reconstruction, it is largely affected by anatomical deformations during the surgery. These were not addressed in this work.

Third party copyright image removed

Figure 1.18: Process flow chart describing the registration process undergone to align a preoperative CT image onto stereoendoscopic video. Taken from Ref. 51.

1.2.5 Registration of preoperatively acquired image volumes (using other imaging modalities) of prostate (or other organ) surfaces onto images recorded from other intraoperative techniques

A $3D$ $TRUS$-guided biopsy system was developed [52] that can record and display the $3D$ locations of biopsy cores. The transducer probe can acquire a $3D$ image of the prostate in real time by reconstruction of 180 $2D$ $TRUS$ images. The segmented prebiopsy $3D$ image (see Figure 1.19) can then be used for needle guidance. By registering the prebiopsied image to real-time $3D$ images the correspondences for the segmented biopsy targets can be maintained throughout the biopsy procedure.

The prostate segmentation, as Figure 1.19 shows, was performed semiautomatically: an initial segmented contour of a prostate cross section ($2D$ transverse prostate image) was generated and used as a dynamically deformable model. This model would radially propagate slice by slice through 180 degrees to provide the initial platform for segmentation of adjacent slices matching the boundaries of the prostate throughout the process.

$3D$-$TRUS$-to-$3D$-$TRUS$ rigid surface- and image-based registration schemes were used to address prostate motion. $3D$-$TRUS$-to-$3D$-$TRUS$ non-rigid surface- and image-based registration methods were also applied to treat both prostate motion and deformation. The rigid surface-based registration was performed with the ICP algorithm while the non-rigid one incorporated the thin-plane spline (TPS) deformation model.

The prostate source and target $3D$ surfaces were represented by triangle meshes in the TPS registration. Their initial rigid alignment (using ICP) was followed by an equal ray angle parameterization of the target $3D$ prostate surface. The $3D$ intersection points between each ray and each one of the two prostate surfaces defined the correspondences between the source and target images. The $3D$ source image was registered to the target image by interpolation. See also Section 2.1 for more details about the TPS deformation model.

The rigid image-based (or intensity-based) registration algorithm is dependent upon the intensity information contained in the images. It is driven by a block matching approach where each source image block (rectangular region) is matched against each target image block according to a regularized vector field that is specifically constructed to perform this transformation. This process aims at the optimization of an image-to-image metric. It is iterated reducing the block size each time to obtain a finer image resolution registration between the source and target images according to a multi-resolution-image-pyramid approach.

The image-based non-rigid registration is also built upon an image-to-image metric concept. A $3D$ grid of $B-$spline control points was used to describe the observed prostate deformation of the moving image: an optimizer was used to estimate an optimal set of $B-$spline parameters that can yield the best match between the moving image and the fixed image. These parameters are used to describe the prostate deformation, which is encoded in the spatial configuration of the $B-$spline grid control points.

The registration errors were determined from anatomical-feature misalignments between the registered source and target images. The TRE was determined by computing the squared Euclidean distances between the $3D$ positions of prostate calcifications (see Figure 1.20) in the transformed source image and their correspondences in the target image and averaging the resulting values. The specific anatomical features were used only for registration evaluation purposes (as target points of reference) and not for the registration process per se due to the increased time required to accurately locate them in the image pairs.

The FLE and the impact of segmentation variability on registration accuracy were also estimated. The FLE is linked to the statistically defined variability (variance) in locating the $3D$ position of a fiducial marker. The variability of prostate segmentation caused variability of TRE values. Their standard deviation was used to measure the variability in registration due to variability in segmentation. This test was conducted for various volumes of $3D$ prostate $TRUS$ images.

Third party copyright image removed

Figure 1.19: (a) Initial outlined contour of a $2D$ transverse prostate image; (b) the initial contour of (a) is used as input contour for the adjacent prostate slice, and is dynamically deformed to match its boundaries. This process is repeated radially slice by slice through 180 degrees. This figure shows multiple contours that have been segmented in this way. Their projections appear onto the faces of a cube; (c) complete prostate segmentation. Taken from Ref. 52.

Third party copyright image removed

Figure 1.20: Three calcifications in a $2D$ cross section of a $3D$ $TRUS$ prostate image. Taken from Ref. 52.

The rigid image-based registration produced a smaller average TRE (by 0.39 mm) compared to the one generated by the rigid surface-based registration. The non-rigid image-based average TRE turned out to be smaller (by 0.59 mm) than the non-rigid surface-based average TRE. The average $TREs$ produced by the rigid and non-rigid surface- and image-based registrations were less than 3 mm, which can be considered as an acceptable upper bound value of accuracy for clinical applications.

An improvement of only 0.24 mm in registration accuracy (measured by average $TREs$) was achieved in going from rigid (1.74 ± 0.84 mm) to non-rigid image-based registration (1.50 ± 0.83 mm). An improvement by 0.04 mm was achieved in going from rigid (2.13 ± 0.80 mm) to non-rigid surface-based registration (2.09 ± 0.77 mm). The computed FLE was so small that had no critical impact on the overall TRE.

The impact of segmentation variability on the computed TRE in surface-based registration was found substantial leading to pronounced errors: poor image quality led to erroneous segmentations and large prostate sizes introduced shadowing effects. It was concluded that image-based registration could yield more accurate results within a shorter timeframe, and that performing rigid registration in near-real time may be sufficient for the $3D$ $TRUS$ $-$guided prostate biopsy procedures.

1.2.6 Summary

An extended range of image registration techniques and technologies for prostate and other organs, and in different operating theatre settings, has been used in much of the previous work. For an accurately performed image-guided prostatectomy or prostate cancer management, the preoperative $3D$ image must closely mimic the observed intraoperative prostate tissue deformations. This in turn necessitates the need of using accurate non-rigid registration frameworks and suitable deformation models that can achieve clinically acceptable registration accuracies for the prostate surfaces. Definitive progress along these lines has not yet taken place with regards to prostate cancer research.

1.3 Identifying *state-of-the-art* candidate algorithms for prostate surface non-rigid registration

The surface of the prostate is in general smooth and featureless containing no convoluted topologies. It may become subject to complex and pronounced deformations. Therefore the search for unambiguous correspondences becomes more difficult especially in the presence of noise and outliers or missing data. A reliable mechanism for prostate surface registration would also rely on a suitable regularization mechanism to control the deformation process.

In the following a number of non-rigid registration algorithms are reviewed with the express purpose of selecting the best candidates for registration of prostate surfaces. This review is also useful in terms of providing ideas for enhancing existing algorithms or possible algorithmic reformulations of promising registration frameworks.

Jian and Vemuri [53, 54] implemented a non-rigid point-set registration method for unstructured data addressing the presence of outliers and noise in the target point cloud. There are no explicitly defined prior point-to-point correspondences for such data. Source and target point sets are represented by Gaussian Mixture Models ($\mathcal{GMM}$) where each mixture component corresponds to each point of the point set (see Section 2.2). The idea of using $\mathcal{GMM}s$ has been extensively applied and widely studied in the literature [53-60]. Point-set registration is formulated as the process of aligning two $\mathcal{GMM}$ densities by minimizing the L_2 distance between them. The L_2 distance is minimized based on a robust parametric estimation algorithm, namely, the L_2E [61].

The TPS and Gaussian-radial-basis-function ($GRBF$) deformation models were considered in this study. The TPS transformation may be decoupled into a linear affine motion and a nonlinear part which is characterized by a set of TPS warping coefficients. The regularization term of the objective cost function is related to the bending energy of the TPS function.

In another study [62], which extended the work by Jian and Vemuri, the L_2E estimator was adapted by explicitly parameterizing the contribution of noise using a Gaussian normal distribution with zero mean and σ standard deviation. The transformation model was defined in the Reproducing Kernel Hilbert Space ($RKHS$). The transformation was expressed as an expansion of kernel representations over a set of control points with the size of their neighbourhoods determining the width of the range of interactions between the source points. As L_2E is differentiable with respect to the coefficients of expansion, the transformation can be estimated via numerical optimization techniques, and the overall computational complexity becomes linear in the number of correspondences.

Tsin and Kanade [55] formulated point-set registration as the process of maximizing the Kernel correlation ($\mathcal{KC}$) configuration of the two point sets that are registered for any choice of deformation model (see Section 2.3). While this straightforward methodology has often been utilized in the literature [53, 55, 63-65], its performance as a registration technique has not been sufficiently measured on clinical data. Due to its multiply-linked as well as "smoothing" (*i.e.,* when Gaussian kernels are used) mechanism, it may prove to be a robust technique in addressing noise and outliers especially for prostate surfaces.

Chui and Rangarajan in a pioneering work [57] formulated the registration problem as an expectation maximization ($\mathcal{EM}$) process using $\mathcal{GMM}s$. The proposed algorithm is capable of jointly solving for the correspondences and the geometric (rigid or non-rigid) transformation within a deterministic annealing scheme (see Section 2.4). Its performance has been tested on $2D$ and $3D$ data leading to satisfactory results even in the presence of noise and outliers, which makes this algorithm a good candidate for prostate surface registration.

Amberg *et al.* [66], following an approach similar to the one taken in [67], extended the ICP framework to nonrigid registration by incorporating a regularization term that involved both linear and nonlinear deformation. The registration was parameterized by assigning one affine transformation matrix per source template vertex.

The objective cost function was expressed as the weighted sum of: (*i*) a distance term which minimizes the distance between the deformed source template and the target (both models defined in $3D$ mesh representations); (*ii*) a local affine stiffness term which regularizes the local deformation isotropically by penalizing weighted differences between the affine transformation matrices assigned to neighbouring source vertices (in doing so the rotational and skew parts of the deformation are balanced against the translational part); and (*iii*) an optional landmark term which resembles the distance term of (*i*) and can be used to initialize the registration for a given set of landmarks.

As the cost function is expressed in a quadratic form it can be solved directly and exactly; however it involves $12m$ variables where m corresponds to the number of points in the source model. The optimization becomes more costly as the number of source point that participate in the registration approaches m.

The registration loops over a series of ICP cycles. In each cycle preliminary correspondences are first estimated from a nearest-point search and then an optimal deformation of the template is computed based upon the stiffness term.

The weight of the stiffness term is successively decreasing after each ICP cycle. As the stiffness weight determines the amount of acceptable deformation, it can incrementally recover the whole range of deformations in going from a strongly regularized one, where a global rigid alignment takes place, to lower stiffness weights, where more localized (nonlinear) deformations can be described, even when significant shape variations are involved.

Missing parts of the target surface can be recovered due to the stiffness term which incorporates the geometric information encoded in the source template mesh to propagate a regularized deformation into regions without correspondence.

The non-rigid registration algorithms proposed by (i) Jian and Vemuri; (ii) Tsin and Kanade; and (iii) Chui and Rangarajan are based on superior techniques for establishing point-to-point correspondences and can be combined with any RBF model for the description of deformation. Their C++ implementations are publicly available [68].

From some computational registration experiments that were conducted on $2D$ and $3D$ synthetic and real clinical data, one can deduce clear merits for these techniques in terms of registration accuracy and capacity to recover nonrigidly deformed surfaces. Such capabilities make them strong candidates for application to prostate which may undergo a large variation in shape in the presence of important amounts of noise and outliers.

These algorithms were, however, developed for registration between full $3D$ models. To make them applicable for full-model-to-partial-model registration, which is central to this thesis, some of the concepts used in the work by Amberg *et al.* will be implemented, after adjustments, having in mind that further modifications of these algorithms may also become necessary in the process, depending on the level of registration accuracy achieved, such as: (i) the need to explicitly parameterize the contribution of noise [62]; or (ii) modify the objective cost function by substituting constituent terms with more accurate mathematical expressions or by adding more relevant terms. The ultimate goal (set within a restricted timeframe) is to reformulate these *state-of-the-art* non-rigid algorithms to make them applicable and more accurate for non-rigid prostate surface registration as well as extend them to accurately recover deformation in occluded target scenes.

1.4 Estimating the accuracy of registration

Section 1.4.1 outlines the general methods that are conventionally used to measure the image registration accuracy in fiducial-based rigid-body registrations. Within this context, the *fiducial localization error*, the *fiducial registration error* and the *target registration error* are defined and their relationship is discussed using explicit analytical expressions from the literature. Methods for measuring the accuracy of non-rigid-body registrations are briefly summarized focusing on the mean-squares similarity metric as well as on the target registration error and its caveats as defined within the context of non-rigid registrations in the present study. Section 1.4.2 details the methodology used to evaluate the image registration accuracy achieved in the numerical simulations of Chapter 3.

1.4.1 General methods for measuring the image registration accuracy

The point-based rigid-body registration (as described in Section 1.2.1) is guided by the geometrical positions of fiducial markers which are commonly termed fiducial points and are established by some fiducial localization process. Point-based registration for rigid structures aims at identifying that rigid-body transformation that can bring the localized fiducial points in a clinically acceptable alignment. However, this process is subject to registration errors which determine the level of image registration accuracy that can be obtained in the registration system. The accuracy of point-based rigid registration methods can be measured [69] by the fiducial localization error, the fiducial registration error and the target registration error.

The fiducial registration error (FRE) is defined as the root-mean-square (RMS) distance between homologous fiducial points after rigid-body point-based registration. FRE can be expressed [70] by

$$FRE^2 = \frac{1}{N}\sum_{i=1}^{N} \|Rx_i + t - y_i\|^2$$

where t and R designate, in respect, the $3D$ translation and rotation required to rigidly align a set of N fiducial points $\{x_i, i = 1, \ldots, N\}$ (localized in the preoperatively prepared patient volumetric image) with their correspondences in the set $\{y_i, i = 1, \ldots, N\}$ (identified in the intraoperatively acquired patient image) such that the RMS of the displacements across all correspondence pairs is minimized. However the process of fiducial localization incurs an error.

The fiducial localization error (FLE) is defined in the literature [70] as the displacement of a localized fiducial point from its true fiducial position measured before registration. FLE can be rigorously determined via experimental measurements with phantoms for the given imaging modality.

The registration error in the *fiducial* point-based rigid-body alignment is determined by the number of fiducial points and by the $FLEs$ incurred in the localization of the exact positions of the fiducial points. This has been shown in a past study [71]:

$$\langle FRE^2 \rangle = \left(1 - \frac{2}{N}\right) \langle FLE^2 \rangle$$

where the expected squared FRE, represented by $\langle FRE^2 \rangle$, designates a measure of overall fiducial alignment and $\langle FLE^2 \rangle$ is the expected squared value of the FLE for a set of N fiducial points and in $3D$. The geometrical positions of the fiducials (termed fiducial configuration) have no effect on the value of the FRE. The FRE is also independent of the particular rigid object that is being registered. Due to the $FLEs$, the value of the FRE can never be zero.

The registration error of any target at a spatial position r $[TRE(r)]$ is defined as the geometrical distance between r and the position of its correspondence in the transforming image after rigid-body point-based registration (in others words, the TRE corresponds to the distance between homologous points other than the fiducials) [70]. The $TRE(r)$ here is measured with respect to a known fiducial configuration comprised of N fiducial markers, which already have accrued $FLEs$ in the process of their geometrical identification.

Errors in the registration of surgery targets such as tumours cannot be measured directly from the registration system in *fiducial*-based rigid-body registrations. They can only be statistically predicted incorporating the estimated $FLEs$, the fiducial configuration and (relative to it) the geometrical position of the target itself. An analytical approximate expression for the $TRE(r)$ statistic has been derived in the study by Fitzpatrick *et al.* [70]:

$$\langle TRE^2(r) \rangle \approx \langle FLE^2 \rangle \left(\frac{1}{N} + \mathcal{C}\right)$$

where $\langle TRE^2(r)\rangle$ corresponds to the expected value of the squared $TRE(r)$, $\langle FLE^2\rangle$ is the expected value of the squared FLE, N is the number of fiducial points, and the mathematical expression $\mathcal{C}$ represents the fiducial configuration and its spatial relationship with a particular target. For a given fiducial configuration the optimal position r for a target corresponds to the centroid of the configuration of fiducial points. (In rigid-body *fiducial*-based registration both statistics $\langle FRE^2\rangle$ and $\langle TRE^2(r)\rangle$ depend on the $\langle FLE^2\rangle$.).

The second most important expression that was derived in this study [70] is given by

$$\langle FRE_i^2\rangle = \langle FLE^2\rangle - \langle TRE_{r_i}^2\rangle$$

where $\langle FRE_i^2\rangle$ represents the expected squared FRE of an individual fiducial point i, $\langle FLE^2\rangle$ is the expected value of the squared FLE and $\langle TRE_{r_i}^2\rangle$ is the expected value of the squared $TRE(r_i)$. This relationship highlights the significance of using the TRE as a reliable measure of image registration accuracy in *fiducial*-based rigid-body transformations; this expression reveals counter-intuitive situations where small values of $FRE_i s$ arise from poor registrations (caused by poor fiducial configurations) which are characterized by large values of $TRE_{r_i}s$.

The accuracy of non-rigid registration methods can be assessed using a variety of image similarity metrics [22, 36, 72-74] such as those of mutual information, normalised mutual information, correlation coefficient, mean squares (MS), *etc…*

The MS metric, which is the metric of choice in this study, is defined as the mean squared difference between images A and B

$$MS(A,B) = \frac{1}{N}\sum_{i=1}^{N} \|\mathrm{A}_i - B_i\|^2$$

where A_i, B_i represent the position of the *i*-th point or intensity of the *i*-th voxel of A and B, respectively, and N is the number of points or voxels that are compared.

In the present study the image registration accuracy is measured by the TRE which evaluates the RMS distances between homologous *target points* after registration (see Section 1.4.2) *without*, however, the aid of fiducial configurations as described in the *fiducial*-based rigid-body registrations. For the non-rigid point-based registrations it is conjectured that the transformation function itself (emphasizing on its capacity to recover deformation accurately) will also have an impact on the value of the computed TRE aside from the number of targets and the FLE.

This working hypothesis can be exploited by addressing the following questions in the numerical simulations of Chapter 3: *(i)* does the TRE change significantly in going to higher numbers of (randomly chosen) target points of registration? Or does it show no major dependence on the number of targets? and ***(ii)*** in the computational experiments of Chapter 3 a (large) set of (random) configurations of (a fixed number of) target points is produced and a TRE value is estimated for each element of this set (see Section 1.4.2). Is the computed TRE dependent upon the target configuration? The $FLEs$ in localizing the target points of registration are by definition zero in the computational experiments of Chapter 3.

1.4.2 Methodology for evaluating the non-rigid registration accuracy in the present study

The evaluation protocol for assessing the accuracy of registration algorithms consists of the following three steps: (***i***) all necessary input parameters of the image registration technique being examined and associated experiment as well as relevant image data sets are specified; (***ii***) the registration output is compared with ground truth data. This comparison is based on defined evaluation metrics which measure the quality of registration in relation to the gold standard; and (***iii***) it is then determined whether the registration technique meets clinical requirements or not by ways of a statistical analysis process.

The evaluation of image registration accuracy in this study follows, after some modifications, the approach taken by Guo *et al*. [75]:

(i) The preoperative $3D$ MRI segmented prostate gland is the source model of registration. For the computational registration experiments of this work, the target model is represented by (a) synthetic prostate data in Chapter 3, which simulate the output from the surface reconstruction of stereo-endoscopically acquired images; and (b) real medical imaging data in Chapter 4. The intraoperative prostate images are collected in real time and reveal prostate shape deformations due to externally induced physical disturbances and/or intrinsic processes such as peristalsis. The target prostate surface usually involves more perturbations such as noise and outliers.

(*ii*) A number of points d will be randomly selected from the source. These source points and their true correspondences in the target will not participate in the registration process. [Their positions in the registered source model will be computed from the estimated transformation function and will be compared to their (non-included in the registration but known) actual correspondences in the target model, which represent the ground truth.] The selected points from the source will be quoted as "target markers or points of registration".

(*iii*) The source will be (non-rigidly) registered to the (synthetic or real) target models using a non-rigid registration algorithm. The new (transformed) positions of the target markers will be calculated from the transformation function.

(*iv*) The TRE will then be computed after registration using $TRE = \sqrt{MS}$. The RMS distances will be computed between the non-rigidly transformed target markers and their correspondences in the ground truth.

(*v*) Steps (*ii*) - (*iv*) will be repeated each time for a different spatial configuration of d target markers.

(*vi*) The mean and standard deviation of the $TREs$ will be calculated to determine the suitability of the examined registration algorithm for clinical applications.

(*vii*) Steps (*ii*) - (*vi*) will be repeated each time for a different algorithm. The corresponding mean $TREs$ and standard deviations will be compared and the most accurate registration algorithm will be identified and proposed for clinical applications.

1.5 Problem statement: thesis objectives and challenges

Objective of work: to exploit and propose medical image registration algorithms in $3D$ that can produce an accurate non-rigid registration (TRE < 3 mm) between a preoperatively constructed MRI prostate surface model (*the source*) and an intraoperatively acquired (via the *da Vinci* Robot System) prostate surface model (*the target*) for AR image guidance and navigation in prostate surgery.

- In particular *state-of-the-art* techniques will be tested to measure their sensitivity to prostate surface deformation and other effects and modified to account for occlusion and combined effects in the target model.

- Synthetic prostate data simulating a wide range of real medical imaging data will be designed and the algorithms' behaviour under different inputs will be examined.
- A series of validation mechanisms will be designed to determine registration accuracy.
- The solution space for the most accurate algorithms will be defined by examining the impact of deformation, noise, outliers, occlusion and combined effects on warping accuracy.
- The algorithm's suitability in terms of required clinical accuracy for the AR application in question will be determined.

Of particular importance is to obtain an accurate spatial alignment of the prostate gland, its substructure (central gland and peripheral zone) and margins as well as cancer foci, as robustly identified on the source surface, onto the target. An accurate macroscopic excision of the visible growth (or prostatectomy) will then become possible with AR guidance to avoid injuries of the pelvic anatomy. While past work on robot-assisted prostate laparoscopic surgery also incorporated AR image guidance, it did not address prostate tissue deformation resulting in large registration errors.

Challenges: (*i*) the target model corresponds to a deformed subset of the source and the region of overlap is not known *a priori*; (*ii*) the size and type of the deformation is not known *a priori*; (*iii*) no explicit point-to-point correspondences are provided before registration; and (*iv*) the target model may be subject to noise and/or may include outliers.

1.6 List of contributions

1. This thesis extended the *state-of-the-art* non-rigid registration algorithms introduced by (*i*) Jian and Vemuri; (*ii*) Tsin and Kanade; (*iii*) Chui and Rangarajan to address occlusion of $3D$ surfaces.

2. These registration techniques were applied to *synthetic prostate* feature datasets and the best algorithms for the application system at hand were identified on the basis of best performance in registration accuracy. The performance of the best algorithms was further exploited (by visual inspection) using *real* medical imaging data.

3. A comprehensive series of algorithms were developed with the express purpose of designing and constructing suitable *synthetic* prostate test datasets for simulation of an extensive range of real case scenarios. Structured tests were developed that could evaluate all candidate algorithms under a wide range of input datasets and parameters designating in parallel each algorithm's solution space.

4. The importance of using rigorous validation schemes for assessing the warping accuracy of non-rigid point-set warping methods was demonstrated via an extensive series of computational experiments.

5. Developed a software application that can be used for the manual initial alignment of the prostate surfaces before registration.

6. The output from this work can be used as a reference guide for implementation of AR support systems for image guidance and navigation in prostate surgery, and future development of more advanced non-rigid registration AR platforms.

1.7 Organization of material

This chapter has highlighted the importance of the work at hand from a clinical point of view. It gave some background information about rigid and non-rigid registration techniques, presented an overview of past work on registration of prostate and other organs' surfaces, identified suitable candidates for application to prostate surfaces, outlined the general methodologies used to measure the image registration accuracy, and presented this work's approach in evaluating the non-rigid prostate-surface registration accuracy. The remainder of this thesis is organized as follows:

Chapter 2 gives a brief overview of radial basis functions focusing on the thin-plate splines in the context of non-rigid registration in $2D$ and $3D$. The theoretical methodologies and the modifications of the selected non-rigid algorithms are also described.

Chapter 3 focuses on the design of synthetic test data and presents the computational results on registration accuracy of the non-rigid techniques described in Chapter 2 using these data.

Chapter 4 presents the output of registration on real prostate imaging data.

Chapter 5 discusses the computational results of Chapter 3 and identifies the best registration algorithms for the application system at hand.

Chapter 6 concludes this thesis with a summary of the work accomplished plus future work.

Chapter 2

Theory

2.1 Thin-plate splines: a class of radial-basis functions for non-rigid registration

2.1.1 Introduction

This section starts by providing a brief overview of the radial basis functions (RBF) and their methodology emphasizing their usefulness for application to various systems including non-rigid registration in $2D$ and $3D$. Section 2.1.1.2 applies the RBF formalism in $2D$ using a special class of $RBFs$ termed thin-plate splines. The deformation field of a $2D$ non-rigid registration is parametrically computed by using TPS functions. The optimization problem within the context of the $2D$ TPS interpolation scheme is outlined. Section 2.1.1.2 introduces the definition of the bending energy of a thin metal plate in $2D$ which is further detailed and generalized in Section 2.1.1.3. In Section 2.1.2 the TPS interpolation scheme is expanded to $3D$. The conditions for an accurate and reliable $3D$ non-rigid registration are derived. Section 2.1.3 presents a mathematical technique that will be extensively used in the present study to simplify the computational problem of Section 2.1.2. The notation used throughout Section 2.1 is given in Appendix $\boldsymbol{\mathcal{A}}$**.1**.

2.1.1.1 Radial basis functions

Approximations of mathematical functions (termed approximants) are usually used instead of their exact mathematical form (approximands). This takes place mainly for functions that (i) are represented by an infinite expansion; (ii) may be too computationally expensive (or demanding in terms of computer memory and time) to evaluate; and (iii) are unknown or not completely known.

Let's assume a set X of (L in number) discrete data x_i defined in a space of $N > 0$ dimensions, *i.e.*, $X = \{x_1, \ldots, x_L\} \subset \mathbb{R}^N$. No assumption on the "shape" of X is made which means that the data $x_i \in \mathbb{R}^N$ can be scattered. Assume also a set H comprised of the *corresponding known* "function values" of a multivariate real-valued function $h_x = h(x) \in \mathbb{R}$, *i.e.*, $H = \{h_{x_1}, \dots, h_{x_L}\} \subset \mathbb{R}$. The function h is assumed to be defined $\forall\, x \in \mathbb{R}^N$ and its mathematical form is unknown. Aside from the explicit function values than are contained in H no other values are known. The objective is to find a suitable approximant $\vartheta\colon \mathbb{R}^N \to \mathbb{R}$ to *approximate* the unknown approximand $h\colon \mathbb{R}^N \to \mathbb{R}$ (which is different from finding an approximant $\vartheta\colon X \to \mathbb{R}$ to $h\colon X \to \mathbb{R}$).

One class of methods that are used for such functional approximations are based on radial-basis-function (RBF) approaches [76]: a suitable approximant ϑ can be derived by using interpolation, *i.e.*, the function ϑ can be expressed as an interpolant over all elements of X where, according to the RBF methodology, it is explicitly required that *the interpolant ϑ is matching each h_{x_i}, $x_i \in X$ exactly*. Within the context of RBF approximations (or interpolations) the approximant ϑ can be expressed by a finite linear combination of $\phi(\|x - x_i\|)$ where ϕ represents a radially symmetric[1] basis function and $\|x - x_i\|$ is the Euclidean distance between $x_i \in X$ and any $x \in \mathbb{R}^N$:

$$\vartheta(x) = \mu(x) + \sum_{i=1}^{L} \alpha_i \, \phi(\|x - x_i\|) \qquad (2.1).$$

The term $\mu(x)$ in Equation (2.1) is polynomial and the α_i's are real-valued coefficients. Note that the data $x_i \in \mathbb{R}^N$ play a twofold role in Equation (2.1): (*i*) these are the points where the function values of the interpolant ϑ and approximand h must match exactly; and (*ii*) they form ***displacement vectors***. [It is also possible to approximate a vector-valued approximand $v\colon \mathbb{R}^N \to \mathbb{R}^K$, $K > 1$, by taking a component-wise approach. See Section 2.1.1.2 for $N = K = 2$ and Section 2.1.2 for $N = K = 3$.]

The RBF methodology can be applied to different occasions (such as $2D$ and $3D$ image mappings, neural network learning processes, measurements of temperature or potential on the earth's surface at scattered meteorological stations …) depending on $\phi(r)$, which can take various forms:

- The biharmonic spline: $\phi(r) = r$
- The triharmonic spline: $\phi(r) = r^3$

---

[1] The basis function ϕ is by definition radially symmetric when its function value depends only on the Euclidean distance of the function's argument from the origin (making it invariant to rotation).

- The thin-plate spline (in $2D$): $\phi(r) = r^2 \log r$
- The Gaussian: $\phi(r) = e^{-\beta r^2}$
- The multi-quadric: $\phi(r) = \sqrt{r^2 + c^2}$ ...

In the above equations, r represents Euclidean distance and β and c are positive parameters.

2.1.1.2 Thin-plate splines in $2D$

The theoretical foundation for the thin-plate splines was set by Duchon [77], Meinguet [78, 79] and Wahba [80]. Other applications can be found in Refs. 76, 81 and 82. As the smoothest interpolators [80, 82], the spline functions are usually invoked in the non-rigid registration of $2D$ medical imaging data.

Let's assume a source $2D$ surface and a deformed version of it which is termed the target. Assume a set Π of (n in number) discrete Cartesian $2D$ points $P_i = (x_i, y_i)$, *i.e.*, $\Pi = \{P_1, \dots, P_n\} \subset \mathbb{R}^2$. Let's also define the vector-valued multivariate function $g_P = g(x, y) \in \mathbb{R}^2$ whose mathematical form is unknown. The function g_P has known function values only for the Π set. These are contained in the set $\mathcal{G} = \{g_{P_1}, \dots, g_{P_n}\} \subset \mathbb{R}^2$. Let the unknown $g(x, y)$ be the function that models the deformation observed in the $2D$ target surface and the set $\mathcal{G}$ be a collection of *known* (not necessarily regularly spaced) $2D$ points of the deformed target surface.

The set Π can be selected to be any *valid* [76] reference grid of n discrete $2D$ points such that $\Pi \overset{g}{\Rightarrow} \mathcal{G}$. By letting the original source model act as reference $2D$ space and the set Π be comprised of the matching counterparts of the known $2D$ target (termed control) points onto the undeformed source dataset, the function g becomes a transformation function describing the transition from the undeformed source model to the deformed target surface in $2D$ [83]. In general the set $\mathcal{G}$ of target control points may consist of all points of the deformed surface or a subset of them (scattered or regularly spaced) as in the current case.

The TPS methodology can be used for encapsulating coordinate mappings and for modelling deformation of surfaces in $2D$ [83]. Let $D \subset \mathbb{R}^2$ be the domain of g. The vector-valued unknown approximand $g: D \to \mathbb{R}^2$ can be approximated by an approximant $f: D \to \mathbb{R}^2$ through a TPS interpolation scheme [83] which is expressed by

$$f(x,y) = [x' \quad y'] = [1 \quad x \quad y]\begin{bmatrix} t_x & t_y \\ r_{xx} & r_{xy} \\ r_{yx} & r_{yy} \end{bmatrix} +$$

$$[\phi(\|(x,y)-(x_1,y_1)\|) \quad \cdots \quad \phi(\|(x,y)-(x_n,y_n)\|)]\begin{bmatrix} \gamma_{x_1} & \gamma_{y_1} \\ \vdots & \vdots \\ \gamma_{x_n} & \gamma_{y_n} \end{bmatrix} \qquad (2.2)$$

where the set of scalars $\{t_x, t_y, r_{xx}, r_{xy}, r_{yx}, r_{yy}\}$ represents the affine transformation (**t**ranslation + **r**otation) coefficients, the set of real numbers $\{\gamma_{x_1}, \gamma_{y_1}, \gamma_{x_2}, \gamma_{y_2}, \dots, \gamma_{x_n}, \gamma_{y_n}\}$ corresponds to the TPS warping coefficients, $\|(x,y)-(x_i,y_i)\|$ refers to the Euclidean distance between the point $P_i = (x_i, y_i)$ from the set Π of the n source (control) $2D$ points and any Cartesian point $P \in D$. (Note that D represents the set of all $2D$ Cartesian points of the undeformed source surface.) The $2D$ TPS basis function represents a generalization of the $1D$ cubic spline $|x|^3$ [83]. The TPS basis function in $2D$, as was mentioned in Section 2.1.1.1 (see also Section 2.1.1.3 for more details), takes the following form:

$$\phi(r) = r^2 \log r.$$

Within the context of RBF interpolations it is explicitly required that $f_{P_i} = g_{P_i} \; \forall \, P_i \in \Pi$. Only when this requirement is satisfied[2] can the approximant f of Equation (2.2) (based on an optimized set of affine and TPS parameters) encapsulate accurately the TPS (smooth) multivariate *interpolation* of the whole[3] source surface (*i.e.,* $\forall \, P = (x,y) \in D$) over a fixed set of n source control points (defined by the set $\Pi = \{P_1, \dots, P_n\}$) onto the deformed target surface (which can only then be approximated accurately by a corresponding set of $f_P = (x' \quad y')$ values).

Equation (2.2) defines a general class of TPS interpolants f in $2D$. Let $\mathcal{X}$ be the space of such interpolants. Each of these forms of f is differentiable $\forall \, P = (x,y) \in D$ [80, 83] and is characterized by a distinct set of affine transformation and TPS warping coefficients.

---

[2] These constrains lead to an optimized set of affine and TPS parameters making the approximant f of Equation (2.2) an accurate $2D$ TPS interpolator for the source-to-target transformation [83].

[3] Specifically, while the source control points are required to match the target control points exactly all other $2D$ source Cartesian points are mapped to their correspondences in the target by smooth TPS interpolation.

Within the context of the TPS formulation [76, 80, 82, 83] *the bending energy of a thin metal plate* at a point (x, y) is proportional to the quantity $\left(\frac{\partial^2 f}{\partial x^2}\right)^2 + 2\left(\frac{\partial^2 f}{\partial x \partial y}\right)^2 + \left(\frac{\partial^2 f}{\partial y^2}\right)^2$ at that point in $2D$. The physical net bending energy of a thin metal plate $I(f)\ \forall\ P = (x, y) \in D$ is defined (see Section 2.1.1.3) by the space integral of the square of the second order partial derivatives of f

$$I(f) = \iint\limits_{\mathbb{R}^2} \left(\left(\frac{\partial^2 f}{\partial x^2}\right)^2 + 2\left(\frac{\partial^2 f}{\partial x \partial y}\right)^2 + \left(\frac{\partial^2 f}{\partial y^2}\right)^2\right) dxdy \qquad (2.3).$$

For a given source-to-target transition, only that form of $f \in \mathcal{X}$ that can minimize uniquely $I(f): D \to \mathbb{R}$ can be considered an *accurate* spatial mapping solution. This takes place only when the set of interpolation conditions $f_{P_i} = g_{P_i}\ \forall\ P_i \in \Pi$ are satisfied [83].

However, satisfying such “constraints” is not always a straightforward task, *i.e.*, when only the source control points are known and no prior point-to-point correspondences are assumed. The optimized form of f for a given source-to-target transformation in this case will arise from identifying the most probable correspondences of the source control points in the target. Only when the true target correspondences are determined will the (measurable) energy functional $I(f)\ \forall\ P = (x, y) \in D$ be uniquely minimized. This optimization process presupposes a good initial alignment between the undeformed source model and the deformed target model.

Summarizing, the optimization process within the context of the $2D$ TPS *interpolation scheme* can be outlined by the following:

(1) For a given system of $2D$ source and target models assume that the set of source $2D$ control points Π is known and the set of target $2D$ control points $\mathcal{G}$ is unknown. No prior point-to-point correspondences are assumed.
(2) Let the set $\mathcal{W}_f$ represent the affine transformation and TPS warping coefficients of the optimized form of f.
(3) The bending functional $I(f)$ can be approximated by Equation (2.3).
(4) The optimization takes places $\forall\ P = (x, y) \in D$ where D represents the domain of f.
(5) A good initial alignment between the source and the target is assumed.

The optimization problem is posed by: $\operatorname{argmin}_{f, \mathcal{W}_f} I(f) \quad s.t.\ \ f_{P_i} = g_{P_i}\ \forall\ P_i \in \Pi.$

2.1.1.3 Thin-plate bending functional

A few words of explanation with regards to the definition of the bending functional $I(f)$ in Equation (2.3) are in order. Let d designate the number of *imaging* dimensions and m denote the *total order* of the partial derivatives of f which obtain the form $\frac{\partial^m f}{\partial\rho_1^{\alpha_1}\ldots\partial\rho_d^{\alpha_d}}$ $(\alpha_1+\cdots+\alpha_d=m)$ with α_k being positive integers [they become $\frac{\partial^m f}{\partial x^{\alpha_1}\partial y^{\alpha_2}}$ $(\alpha_1+\alpha_2=m)$ for $d=2$]. The thin-plate penalty functional for $d=2$ and general m is given [80] by

$$I_m(f)=\sum_{v=0}^{m}\iint\limits_{\mathbb{R}^2}\binom{m}{v}\left(\frac{\partial^m f}{\partial x^v\partial y^{m-v}}\right)^2 dxdy \qquad (2.4)$$

which obtains the form of Equation (2.3) for $m=2$. The thin-plate penalty functional for general d,m is given [80, 82] by

$$I_m^d(f)=\sum_{\alpha_1+\cdots+\alpha_d=m}\frac{m!}{\alpha_1!\ldots\alpha_d!}\int_{-\infty}^{\infty}\cdots\int_{-\infty}^{\infty}\left(\frac{\partial^m f}{\partial\rho_1^{\alpha_1}\ldots\partial\rho_d^{\alpha_d}}\right)^2\prod_j d\rho_j \qquad (2.5).$$

When choosing m and d, the condition $2m-d>0$ must be satisfied [80, 82]. For $d=3, m=2$ (*i.e.,* $2m-d=1>0$) the thin-plate penalty functional becomes

$$I_2^3(f)=\iiint\limits_{\mathbb{R}^3}\left(\left(\frac{\partial^2 f}{\partial x^2}\right)^2+\left(\frac{\partial^2 f}{\partial y^2}\right)^2+\left(\frac{\partial^2 f}{\partial z^2}\right)^2+2\left(\frac{\partial^2 f}{\partial x\partial y}\right)^2+2\left(\frac{\partial^2 f}{\partial x\partial z}\right)^2 + 2\left(\frac{\partial^2 f}{\partial y\partial z}\right)^2\right)dxdydz \qquad (2.6).$$

The TPS basis functions, as was mentioned in Section 2.1.1.2, are a special class of $RBFs$. Their linear combinations are used to minimize the physical bending energy of a thin metal plate subject to interpolation conditions [76, 77, 82]. The TPS basis functions depend solely upon the total order m of the partial derivatives of f in $I_m^d(f)$ and the number of imaging dimensions d [See Ref. 80 pp. 31–32 and Ref. 82 pp. 193-195 for an explicit mathematical presentation.]. The (unique) solution of minimizing the functional in (2.5) is given in Appendix $\boldsymbol{\mathcal{A}}$**.2** based on the mathematical work in Wahba [80] and Rohr [82].

Table 2.1 lists the forms of the TPS basis functions for various (m,d) combinations. For $d=2, m=2$ and neglecting constants $\phi(r)=r^2\log r$, which is the same form of TPS basis function that was used in Section 2.1.1.2. Linear combinations of such $TPSs$ were used in that section to minimize the bending functional of Equation (2.3) (which was derived for $d = 2, m = 2$). Upon going to higher values of m and for $d = 2$ $(s.t. 2m - d > 0)$ the bending functional $I_m(f)$ of Equation (2.4) obtains more accurate energy expressions which in turn require different forms of $TPSs$ as shown in Table 2.1 (and could nominally lead to more accurate optimizations of the form described at the end of Section 2.1.1.2).

The following section extends the TPS formulation in $3D$ as this work involves transformations to deformed $3D$ prostate surfaces.

	$d = 1$	$d = 2$	$d = 3$	$d = 4$
$m = 1$	$(-{}^{1}/_{2})r$			
$m = 2$	$({}^{1}/_{12})r^3$	$({}^{1}/_{8\pi})r^2 \log r$	$(-{}^{1}/_{8\pi})r$	
$m = 3$	$(-{}^{1}/_{240})r^5$	$(-{}^{1}/_{128\pi})r^4 \log r$	$({}^{1}/_{96\pi})r^3$	$({}^{1}/_{64\pi^2})r^2 \log r$
$m = 4$	$({}^{1}/_{10080})r^7$	$({}^{1}/_{4608\pi})r^6 \log r$	$(-{}^{1}/_{2880\pi})r^5$	$(-{}^{1}/_{1536\pi^2})r^4 \log r$

Table 2.1: TPS basis functions $\phi(r)$ across an increasing total order m of the partial derivatives of f in $I_m^d(f)$ [see Equation (2.5)] and an increasing number of imaging dimensions d. Taken from Ref. 82.

2.1.2 Thin-plate splines in $3D$

Let's assume an undeformed $3D$ source model M_0 comprised of (m in number) $q = (x, y, z)$ points, which in matrix form can be expressed by $M_0 = (q_1, \dots, q_m)^T \in \mathbb{R}^{m\times 3}$. Suppose that the target model S represents a deformed version of M_0 such that $S = (t_1, \dots, t_m)^T \in \mathbb{R}^{m\times 3}$ where $t \in \mathbb{R}^3$ depicts a point of the deformed surface S. The set of (n in number) source control points is denoted by $\Omega = \{P_1, \dots, P_n\} \subseteq \{q_1, \dots, q_m\}$ where $P_i = (x_i^P, y_i^P, z_i^P): i \in \{1, \dots, n\}$ represents a source control point.

The vector-valued function $g(x, y, z) \in \mathbb{R}^3$ is the unknown transformation function that causes the $M_0 \rightarrow S$ transition. The domain[4] of g is defined by $D = \{q_1, \dots, q_m\} \subset \mathbb{R}^3$. The set of n target control points is denoted by $\mathcal{G} = \{g_{P_1}, \dots, g_{P_n}\} \subseteq S$ where $g_{P_i} = g(x_i^P, y_i^P, z_i^P)$, $\forall\, P_i \in \Omega$. The elements of $\mathcal{G}$ are the only known function values of g.

The vector-valued unknown approximand $g: D \rightarrow \mathbb{R}^3$ can be approximated by an approximant $f: D \rightarrow \mathbb{R}^3$ by way of TPS interpolation in $3D$. The $3D$ non-rigid TPS coordinate mapping is encapsulated by

$$f(x, y, z) = [x' \quad y' \quad z'] =$$

$$= [1 \quad x \quad y \quad z] \begin{bmatrix} \alpha_x & \alpha_y & \alpha_z \\ \beta_{xx} & \beta_{xy} & \beta_{xz} \\ \beta_{yx} & \beta_{yy} & \beta_{yz} \\ \beta_{zx} & \beta_{zy} & \beta_{zz} \end{bmatrix} + [V_1 \quad \dots \quad V_n] \begin{bmatrix} \theta_{x_1} & \theta_{y_1} & \theta_{z_1} \\ \theta_{x_2} & \theta_{y_2} & \theta_{z_2} \\ \theta_{x_3} & \theta_{y_3} & \theta_{z_3} \\ \vdots & \vdots & \vdots \\ \theta_{x_n} & \theta_{y_n} & \theta_{z_n} \end{bmatrix} \tag{2.7}$$

where $V_i = \phi(\|q - P_i\|) = \phi\left(\left\|(x, y, z) - (x_i^P, y_i^P, z_i^P)\right\|\right)$, $\forall\, P_i \in \Omega$ and for any $q \in D$. The TPS basis function in $3D$ and for $m = 2$ takes the form, neglecting the constant, $\phi(r) = r$ (see Table 2.1). The quantity $\left\|(x, y, z) - (x_i^P, y_i^P, z_i^P)\right\|$ is the Euclidean distance between the point $P_i = (x_i^P, y_i^P, z_i^P): i \in \{1, \dots, n\}$ from the set Ω of the n source (control) $3D$ points and any point $q \in D$. The global affine (linear) transformation component of f in Equation (2.7) is described by the set of real-valued coefficients $\{\alpha_x, \alpha_y, \alpha_z, \beta_{xx}, \beta_{xy}, \dots, \beta_{zx}, \beta_{zy}, \beta_{zz}\}$ and the local non-linear (non-rigid) deformation component is depicted by the set of scalars $\{\theta_{x_1}, \theta_{y_1}, \theta_{z_1}, \dots, \theta_{x_n}, \theta_{y_n}, \theta_{z_n}\}$ which correspond to the TPS warping coefficients. See also Figure 2.1.

Equation (2.7) can be rewritten $\forall\, q \in \{q_1, \dots, q_m\}$ by

$$f(M_0) = \begin{bmatrix} x_1' & y_1' & z_1' \\ x_2' & y_2' & z_2' \\ x_3' & y_3' & z_3' \\ \vdots & \vdots & \vdots \\ x_m' & y_m' & z_m' \end{bmatrix} = \begin{bmatrix} 1 & x_1 & y_1 & z_1 \\ 1 & x_2 & y_2 & z_2 \\ 1 & x_3 & y_3 & z_3 \\ \vdots & \vdots & \vdots & \vdots \\ 1 & x_m & y_m & z_m \end{bmatrix} \begin{bmatrix} \alpha_x & \alpha_y & \alpha_z \\ \beta_{xx} & \beta_{xy} & \beta_{xz} \\ \beta_{yx} & \beta_{yy} & \beta_{yz} \\ \beta_{zx} & \beta_{zy} & \beta_{zz} \end{bmatrix} +$$

---

[4] In general the function g may be defined $\forall\, (x, y, z) \in \mathbb{R}^3$. In this section the mathematical formulation is tailored specifically to non-rigid registration between full $3D$ prostate surfaces.

$$\begin{bmatrix} U_{11} & U_{12} & U_{13} & \cdots & U_{1n} \\ U_{21} & \cdots & \cdots & \cdots & U_{2n} \\ \vdots & \cdots & \cdots & \cdots & \vdots \\ U_{m1} & U_{m2} & U_{m3} & \cdots & U_{mn} \end{bmatrix} \begin{bmatrix} \theta_{x_1} & \theta_{y_1} & \theta_{z_1} \\ \theta_{x_2} & \theta_{y_2} & \theta_{z_2} \\ \theta_{x_3} & \theta_{y_3} & \theta_{z_3} \\ \vdots & \vdots & \vdots \\ \theta_{x_n} & \theta_{y_n} & \theta_{z_n} \end{bmatrix} \tag{2.8}$$

where $U_{ij} = \phi(\|q_i - P_j\|)$. A more compact form of Equation (2.8) can be given by

$$f(M_0) = M = [1|M_0]E^T + UQ \tag{2.9}$$

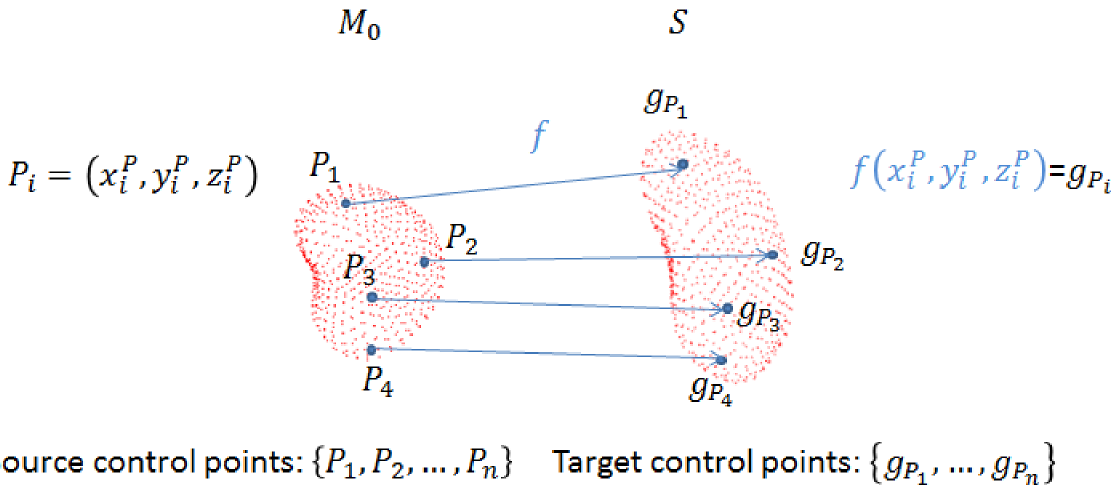

Figure 2.1: The source model M_0 and its deformed version, the target model S. The source control points are depicted by P_i and the target control points by g_{P_i}(only four pairs of control points are shown. The general number of pairs of control points that is assumed in the text is n). The approximant f encapsulates the *TPS interpolation* of the source surface M_0 over a fixed set of source control points onto the deformed target surface S. Within the context of *TPS* interpolations it is explicitly required that $f_{P_i} = g_{P_i}\ \forall\ P_i \in \{P_1, \dots, P_n\}$. See text for details.

where the $m \times 3$ matrix M defined by

$$M = \begin{bmatrix} x_1' & y_1' & z_1' \\ x_2' & y_2' & z_2' \\ x_3' & y_3' & z_3' \\ \vdots & \vdots & \vdots \\ x_m' & y_m' & z_m' \end{bmatrix} \qquad (2.10)$$

denotes an approximation of the target $3D$ model S (it represents the transformed source model in non-rigid point set registration), the $m \times 4$ matrix $[1|M_0]$ relates to

$$[1|M_0] = \begin{bmatrix} 1 & x_1 & y_1 & z_1 \\ 1 & x_2 & y_2 & z_2 \\ 1 & x_3 & y_3 & z_3 \\ \vdots & \vdots & \vdots & \vdots \\ 1 & x_m & y_m & z_m \end{bmatrix} \qquad (2.11),$$

the 3×4 matrix E which represents the affine transformation coefficients $\left[\text{translation } \{\alpha_i\} \text{ plus rotation } \{\beta_{ij}\}\right]$ is associated with

$$E = \begin{bmatrix} \alpha_x & \beta_{xx} & \beta_{yx} & \beta_{zx} \\ \alpha_y & \beta_{xy} & \beta_{yy} & \beta_{zy} \\ \alpha_z & \beta_{xz} & \beta_{yz} & \beta_{zz} \end{bmatrix} \qquad (2.12),$$

the $m \times n$ matrix U which is termed basis matrix corresponds to

$$U = \begin{bmatrix} U_{11} & U_{12} & U_{13} & \cdots & U_{1n} \\ U_{21} & \cdots & \cdots & \cdots & U_{2n} \\ \vdots & \cdots & \cdots & \cdots & \vdots \\ U_{m1} & U_{m2} & U_{m3} & \cdots & U_{mn} \end{bmatrix} \qquad (2.13)$$

and the $n \times 3$ matrix Q which contains the TPS parameters is given by

$$Q = \begin{bmatrix} \theta_{x_1} & \theta_{y_1} & \theta_{z_1} \\ \theta_{x_2} & \theta_{y_2} & \theta_{z_2} \\ \theta_{x_3} & \theta_{y_3} & \theta_{z_3} \\ \vdots & \vdots & \vdots \\ \theta_{x_n} & \theta_{y_n} & \theta_{z_n} \end{bmatrix} \qquad (2.14).$$

The $3D$ TPS interpolation scheme of Equation (2.8) is subject to the constraints $f_{P_i} = g_{P_i}$ $\forall\, P_i \in \Omega$. Suppose that the affine transformation component of the TPS energy function f of Equation (2.8) is zero. Equation (2.8) then $\forall\, P_i \in \Omega$ becomes

$$\begin{bmatrix} g_{P_1} \\ g_{P_2} \\ g_{P_3} \\ g_{P_4} \\ \vdots \\ g_{P_n} \end{bmatrix} = \begin{bmatrix} x_1^{P'} & y_1^{P'} & z_1^{P'} \\ x_2^{P'} & y_2^{P'} & z_2^{P'} \\ x_3^{P'} & y_3^{P'} & z_3^{P'} \\ \vdots & \vdots & \vdots \\ x_n^{P'} & y_n^{P'} & z_n^{P'} \end{bmatrix} =$$

$$= \begin{bmatrix} 0 & \phi(\|P_1 - P_2\|) & \phi(\|P_1 - P_3\|) & \cdots & \phi(\|P_1 - P_n\|) \\ \phi(\|P_2 - P_1\|) & \cdots & \cdots & \cdots & \phi(\|P_2 - P_n\|) \\ \vdots & \cdots & \cdots & \cdots & \vdots \\ \phi(\|P_n - P_1\|) & \phi(\|P_n - P_2\|) & \phi(\|P_n - P_3\|) & \cdots & 0 \end{bmatrix} \begin{bmatrix} \theta_{x_1} & \theta_{y_1} & \theta_{z_1} \\ \theta_{x_2} & \theta_{y_2} & \theta_{z_2} \\ \theta_{x_3} & \theta_{y_3} & \theta_{z_3} \\ \vdots & \vdots & \vdots \\ \theta_{x_n} & \theta_{y_n} & \theta_{z_n} \end{bmatrix} \qquad (2.15).$$

Equation (2.15) can be written in a more compact way by

$$T = \Phi Q \qquad (2.16)$$

where the $n \times 3$ matrix T includes the coordinates of the target control points[5] $\{g_{P_i}\}$ or $\{(x_i^{P'}, y_i^{P'}, z_i^{P'})\} \; \forall \; i \in \{1, \dots, n\}$ and is expressed by

$$T = \begin{bmatrix} x_1^{P'} & y_1^{P'} & z_1^{P'} \\ x_2^{P'} & y_2^{P'} & z_2^{P'} \\ x_3^{P'} & y_3^{P'} & z_3^{P'} \\ \vdots & \vdots & \vdots \\ x_n^{P'} & y_n^{P'} & z_n^{P'} \end{bmatrix} \qquad (2.17),$$

the matrix Q is given by Equation (2.14) and the matrix $\Phi \in \mathbb{R}^{n \times n}$ is defined by

$$\Phi = \begin{bmatrix} \phi(r_{11}) & \phi(r_{12}) & \phi(r_{13}) & \cdots & \phi(r_{1n}) \\ \phi(r_{21}) & \cdots & \cdots & \cdots & \phi(r_{2n}) \\ \vdots & \cdots & \cdots & \cdots & \vdots \\ \phi(r_{n1}) & \phi(r_{n2}) & \phi(r_{n3}) & \cdots & \phi(r_{nn}) \end{bmatrix} \qquad (2.18)$$

where $\Phi_{ij} = \Phi(P_i, P_j) = \phi(r_{ij})$ and $r_{ij} = \|P_i - P_j\| = \|(x_i^P, y_i^P, z_i^P) - (x_j^P, y_j^P, z_j^P)\|$. Note that $\phi(r_{11}) = \cdots = \phi(r_{nn}) = 0$ and $\phi(r_{ij}) = r_{ij}$. The matrix Φ of Equation (2.18) is a TPS kernel matrix in $3D$ (symmetric, conditionally positive definite and hence ***invertible***). Φ describes the internal structure of the source control point set.

If the affine transformation component of the TPS energy function f of Equation (2.8) is zero, then the $n \times 3$ matrix Q of the TPS parameters may be computed directly considering

---

[5] Note that $g(x_i^P, y_i^P, z_i^P) = f(x_i^P, y_i^P, z_i^P) = (x_i^{P'}, y_i^{P'}, z_i^{P'}) \; \forall \; P_i \in \Omega$.

that $\Phi Q = T \ \Rightarrow\ Q = \Phi^{-1}T$. If the affine part of f is nonzero, then the $n \times 4$ matrix A given by

$$A = \begin{bmatrix} 1 & x_1^P & y_1^P & z_1^P \\ 1 & x_2^P & y_2^P & z_2^P \\ 1 & x_3^P & y_3^P & z_3^P \\ \vdots & \vdots & \vdots & \vdots \\ 1 & x_n^P & y_n^P & z_n^P \end{bmatrix} = [1|P] \tag{2.19}$$

must be incorporated[6]. The $n \times 3$ matrix P in (2.19) represents n source control points. Specifically, let's define [83] the $(n+4) \times (n+4)$ matrix Ψ

$$\Psi = \begin{bmatrix} \Phi & A \\ A^T & 0 \end{bmatrix} \tag{2.20}$$

where 0 represents a 4×4 zero matrix. The last four rows of Ψ make sure that the function f of Equation (2.8) is regularized at infinity, *i.e.*, the affine subspace of the TPS warping space vanishes at infinity separating from the non-affine subspace (see Ref. 83 and Section 2.1.3). Let us also define the $(n+4) \times 3$ matrix Δ by

$$\Delta = \begin{bmatrix} \theta_{x_1} & \theta_{y_1} & \theta_{z_1} \\ \theta_{x_2} & \theta_{y_2} & \theta_{z_2} \\ \theta_{x_3} & \theta_{y_3} & \theta_{z_3} \\ \vdots & \vdots & \vdots \\ \theta_{x_n} & \theta_{y_n} & \theta_{z_n} \\ \alpha_x & \alpha_y & \alpha_z \\ \beta_{xx} & \beta_{xy} & \beta_{xz} \\ \beta_{yx} & \beta_{yy} & \beta_{yz} \\ \beta_{zx} & \beta_{zy} & \beta_{zz} \end{bmatrix} \tag{2.21}$$

where the first n rows of Δ correspond to the matrix Q of Equation (2.14) while the remaining four rows are the affine transformation coefficients (translation plus rotation) as defined in matrix E (specifically E^T for an exact correspondence) of Equation (2.12). Finally let the "augmented" form of T of Equation (2.17) be defined [83] by the $(n+4) \times 3$ matrix Υ

---

[6] Note that the set $\{P_i\} = \{(x_i^P, y_i^P, z_i^P)\}$: $\forall\, i \in \{1, \dots, n\}$ represents n source control points.

$$\Upsilon = \begin{bmatrix} T \\ 0 \end{bmatrix} = \begin{bmatrix} x_1^{P'} & y_1^{P'} & z_1^{P'} \\ x_2^{P'} & y_2^{P'} & z_2^{P'} \\ \vdots & \vdots & \vdots \\ x_n^{P'} & y_n^{P'} & z_n^{P'} \\ 0 & 0 & 0 \\ 0 & 0 & 0 \\ 0 & 0 & 0 \\ 0 & 0 & 0 \end{bmatrix} \qquad (2.22).$$

Thus the following system of linear equations holds

$$\Psi\Delta = \Upsilon \xRightarrow{Eqs.\text{: }(2.20),(2.21),(2.22)} \Delta = \Psi^{-1}\Upsilon \qquad (2.23).$$

The $(n+4) \times 3$ matrix Δ in (2.23), produced by solving the system of equations via standard routines, satisfies the set of constraints $f_{P_i} = g_{P_i}\ \forall\, P_i \in \Pi$ for the general case of a non-vanishing affine component of f of Equation (2.8). For these values of affine and TPS parameters the function f is guaranteed to uniquely minimize the bending functional of Equation (2.6) where $d = 3$ and $m = 2$.

2.1.3 TPS non-rigid transformation model in $3D$

Note that $I_2^3(f) \propto \mathrm{trace}(Q^T \Phi Q)$ [83]. Note also that Φ is a conditionally positive definite matrix [80], *i.e.*, $\theta^T \Phi \theta > 0\ \forall\ \theta \epsilon H^N$ where $H^N = \{\theta \epsilon \mathbb{R}^N : \sum_{i=1}^{N} \theta_i = 0\}$. By satisfying the boundary condition

$$A^T Q = Q^T A = Q^T[1|P] = 0 \qquad (2.24)$$

the affine subspace of the TPS warping vanishes at infinity and Φ is guaranteed to be conditionally positive definite (since, for the column vectors of Q, it holds that $\sum_{i=1}^{n} \theta_{x_i} = \sum_{i=1}^{n} \theta_{y_i} = \sum_{i=1}^{n} \theta_{z_i} = 0$). To simplify the computational part of the problem the null space of A^T, $\mathrm{Null}(A^T)$, (or equivalently the left null space of A) must be found. The following approach is proposed in the literature: (i) separation of the TPS warping space into its affine and non-affine subspaces:

$$Q = \mathcal{N}\psi \qquad (2.25)$$

where, for n being the number of source control points, $\psi \in \mathbb{R}^{(n-4)\times 3}$ relates to the non-affine part and $\mathcal{N} \in \mathbb{R}^{n\times(n-4)}$ represents the left null space of A $[\mathcal{N}^T A = 0]$ and is associated with the affine subspace of the TPS warping; followed by (ii) full rank $\boldsymbol{\mathcal{QR}}$ decomposition of the rectangular matrix A [84]:

$$A = \boldsymbol{\mathcal{QR}} = [\boldsymbol{\mathcal{Q}_1}|\boldsymbol{\mathcal{Q}_2}]\begin{bmatrix}\boldsymbol{\mathcal{R}_1}\\ \mathbf{0}\end{bmatrix}(= \boldsymbol{\mathcal{Q}_1\mathcal{R}_1}) \qquad (2.26)$$

where $\boldsymbol{\mathcal{Q}_1} \in \mathbb{R}^{n\times 4}$ contains the first four [= rank(A)] columns of the orthogonal $n \times n$ matrix $\boldsymbol{\mathcal{Q}}$, $\boldsymbol{\mathcal{Q}_2} \in \mathbb{R}^{n\times(n-4)}$ corresponds to the last $(n-4)$ columns of $\boldsymbol{\mathcal{Q}}$ and $\boldsymbol{\mathcal{R}} = \begin{bmatrix}\boldsymbol{\mathcal{R}_1}\\ \mathbf{0}\end{bmatrix} \in \mathbb{R}^{n\times 4}$ represents an upper triangular matrix with $\boldsymbol{\mathcal{R}_1} \in \mathbb{R}^{4\times 4}$. Also $\boldsymbol{\mathcal{Q}}_1^T\boldsymbol{\mathcal{Q}_1} = \boldsymbol{\mathcal{Q}_1}\boldsymbol{\mathcal{Q}}_1^T = I_4$ and $\boldsymbol{\mathcal{Q}}_2^T\boldsymbol{\mathcal{Q}_2} = \boldsymbol{\mathcal{Q}_2}\boldsymbol{\mathcal{Q}}_2^T = I_{n-4}$.

It follows, by theorem, that the $(n-4)$ columns of $\boldsymbol{\mathcal{Q}_2}$ correspond to the left null space of A, *i.e.*, $(i) \wedge (ii) \Rightarrow \mathcal{N} = \boldsymbol{\mathcal{Q}_2}$. The n columns of $\boldsymbol{\mathcal{Q}}$ make an orthonormal set of basis vectors for the column space of A, $C(A)$, and specifically those that are contained in $\boldsymbol{\mathcal{Q}_2}$ satisfy the boundary condition in (2.24). Hence,

$$\begin{aligned}\text{Equation (2.9)} \xrightarrow{(2.25)} f(M_0) &= M\\ &= [1|M_0]E^T + U\mathcal{N}\psi\\ &= [1|M_0|U\mathcal{N}]\begin{bmatrix}E^T\\ \psi\end{bmatrix} \qquad (2.27)\end{aligned}$$

where it becomes apparent that the total number of unknowns amounts to $n \times 3$.

2.2 Gaussian mixtures model incorporated in the non-rigid point set registration framework

2.2.1 Introduction

This section provides a brief overview of the $\mathcal{GMM}$ and highlights its merits as a means of representing source and target input point sets in non-rigid registration frameworks. The current work expands on that algorithmic variant [53] that formulates non-rigid registration as the process of aligning two Gaussian input models by minimizing the L_2 similarity (distance) measure between them. The work in [53] was motivated by the closed-form expression of L_2 and, due to this, the computational efficiency of the produced *multiply-linked* registration scheme. The modified version of the registration algorithm will be tested on synthetic prostate data and will be extensively validated through a series of computational experiments in Chapter 3.

2.2.2 Gaussian mixture model

Let $\{\boldsymbol{\mathcal{M}}_{\mathbf{0}}, \boldsymbol{\mathcal{M}}\} \in \mathbb{R}^{m\times 3}$ such that the source model point set $\boldsymbol{\mathcal{M}}_{\mathbf{0}} = (q_1, \dots, q_m)^T$ and the moving or transformed source model set $\boldsymbol{\mathcal{M}} = (v_1, \dots, v_m)^T$, and $\boldsymbol{\mathcal{S}} \in \mathbb{R}^{s\times 3}$ be the target set $\boldsymbol{\mathcal{S}} = (t_1, \dots, t_s)^T$ where in an asymmetric point matching case $m \neq s$. Each member of $\{\boldsymbol{\mathcal{M}}_{\mathbf{0}}, \boldsymbol{\mathcal{M}}, \boldsymbol{\mathcal{S}}\}$ is treated as a collection of unstructured Cartesian points bearing no prior information beyond their spatial coordinates.

The objective is to compute that non-rigid body transformation function $\mathcal{F}: \mathbb{R}^3 \to \mathbb{R}^3$ that yields the optimal alignment between $\boldsymbol{\mathcal{M}} = \mathcal{F}(\boldsymbol{\mathcal{M}}_{\mathbf{0}}; \theta)$ and $\boldsymbol{\mathcal{S}}$ following an iterating cycle of processes that augment accuracy of registration, until convergence. Registration does not depend upon the establishment of explicit prior point correspondences between $\boldsymbol{\mathcal{M}}$ and $\boldsymbol{\mathcal{S}}$. The parameterized spatial transformation $\mathcal{F}$ is modelled by TPS functions (see Section 2.1).

Let the training sets $\{v^{(i)}, i = 1, \dots, m\}$ and $\{t^{(i)}, i = 1, \dots, s\}$ be constructed from $\boldsymbol{\mathcal{M}}$ (or $\boldsymbol{\mathcal{M}}_{\mathbf{0}}$) and $\boldsymbol{\mathcal{S}}$, respectively, where $v^{(i)}$ and $t^{(i)}$ represent random variables. Let $t^{(i)} \sim \text{Multinomial Distribution}(\varphi) = \prod_{h=1}^{s} \varphi_h$ where $\varphi_h \in \{\varphi_1, \dots, \varphi_s\}$ represents the probability that the random variable $t^{(i)}$ will obtain each of the possible discrete values, *i.e.*, $\varphi_h = P(t^{(i)} = t^{(h)}; \varphi)$, $0 \leq \varphi_h \leq 1$, and $\sum_{h=1}^{s} \varphi_h = 1$. The bivariate joint probability distribution for the discrete variables $(v^{(i)}, t^{(i)})$ is given by

$$P(v^{(i)}, t^{(i)}) = P(v^{(i)} | t^{(i)}) P(t^{(i)}) \qquad (2.28).$$

We assume that the $v^{(i)\prime}$s are distributed IID (independently and identically distributed) according to the $3D$ multivariate normal distribution

$$v^{(i)} | t^{(i)} = t^{(h)};\ \mu_h, \Sigma_h \sim \boldsymbol{\mathcal{N}}_{v^{(i)}}(\mu_h, \Sigma_h) \qquad (2.29)$$

where $\boldsymbol{\mathcal{N}}_{v^{(i)}}$ denotes the density of the vector-valued random variable $v^{(i)}$ which is conditioned on the randomly chosen, from the set $\{t^{(1)}, \dots, t^{(s)}\}$, $t^{(i)} = t^{(h)}$ and is given by

$$P(v^{(i)} | t^{(i)} = t^{(h)};\ \mu_h, \Sigma_h\ ) = \frac{1}{\sqrt{det(2\pi\Sigma_h)}} exp\left[-\frac{1}{2}(v^{(i)} - \mu_h)^T \Sigma_h^{-1} (v^{(i)} - \mu_h)\right]$$

$$= \frac{1}{\sqrt{(2\pi)^3|\Sigma_h|}} exp\left[-\frac{1}{2}\left(v^{(i)} - \mu_h\right)^T \Sigma_h^{-1}\left(v^{(i)} - \mu_h\right)\right] \quad (2.30)$$

where for the mean vector $\mu_h \in \mathbb{R}^3$ it holds that $E\left(v^{(i)}\right) = \mu_h$. $\Sigma_h \in \mathbb{R}^{3\times 3}$ represents the covariance matrix and is symmetric and positive semi-definite. Hence each $v^{(i)}$ can be distributed as a mixture of Gaussian distributions by the probability density function

$$P\left(v^{(i)}; \varphi, \mu, \Sigma\right) = \sum_{h=1}^{s} \varphi_h \ P\left(v^{(i)} \middle| t^{(i)} = t^{(h)}; \mu_h, \Sigma_h\right)$$

$$= \sum_{h=1}^{s} \varphi_h \frac{1}{\sqrt{(2\pi)^3|\Sigma_h|}} exp\left[-\frac{1}{2}\left(v^{(i)} - \mu_h\right)^T \Sigma_h^{-1}\left(v^{(i)} - \mu_h\right)\right] \quad (2.31).$$

This model is called mixtures of Gaussians.

Due to the independence assumption on the $v^{(i)\prime}$s, the likelihood function becomes

$$L(\varphi, \mu, \Sigma) = P(\boldsymbol{\mathcal{M}}; \boldsymbol{\mathcal{S}}, \theta, \varphi, \mu, \Sigma)$$

$$= \prod_{i=1}^{m} P\left(\mathcal{F}\left(q^{(i)}; \theta\right); \varphi, \mu, \Sigma\right)$$

$$= \prod_{i=1}^{m} P\left(v^{(i)}; \varphi, \mu, \Sigma\right) \qquad (2.32).$$

The maximum likelihood principle requires a maximum value of $L(\varphi, \mu, \Sigma)$ or $\log L(\varphi, \mu, \Sigma)$:

$$l(\varphi, \mu, \Sigma) = \log L(\varphi, \mu, \Sigma)$$

$$= \log \prod_{i=1}^{m} P\left(v^{(i)}; \varphi, \mu, \Sigma\right)$$

$$= \sum_{i=1}^{m} \log P\left(v^{(i)}; \varphi, \mu, \Sigma\right)$$

$$= \sum_{i=1}^{m} \log\left(\sum_{t^{(j)}=t^{(1)}}^{t^{(s)}} P\left(v^{(i)} \middle| t^{(j)}; \mu, \Sigma\right) \ P\left(t^{(j)}; \varphi\right)\right) \qquad (2.33).$$

However, the maximum likelihood estimates of the (φ, μ, Σ) parameters cannot be obtained in closed form by setting to zero the derivatives of (2.33) with respect to (φ, μ, Σ) unless the association between $v^{(i)}$'s and $t^{(i)}$'s is known in advance, in which case:

$$\text{Eq. (2.33)} \rightarrow\ l(\varphi, \mu, \Sigma) = \sum_{i=1}^{m} \left(\log P\left(v^{(i)} \middle| t^{(i)}; \mu, \Sigma\right) + \log P\left(t^{(i)}; \varphi\right) \right) \qquad (2.34)$$

which in turn leads to the following solutions (derived in Appendix $\mathcal{B}.1$):

$$\varphi_h = \frac{1}{m} \sum_{i=1}^{m} 1\{t^{(i)} = t^{(h)}\}$$

$$\mu_h = \frac{\sum_{i=1}^{m} 1\{t^{(i)} = t^{(h)}\} v^{(i)}}{\sum_{i=1}^{m} 1\{t^{(i)} = t^{(h)}\}}$$

$$\Sigma_h = \frac{\sum_{i=1}^{m} 1\{t^{(i)} = t^{(h)}\} \left(v^{(i)} - \mu_h\right)\left(v^{(i)} - \mu_h\right)^T}{\sum_{i=1}^{m} 1\{t^{(i)} = t^{(h)}\}}$$

where, for the indicator functions, it holds that $1\{\text{True}\} = 1$ and $1\{\text{False}\} = 0$.

2.2.3 The minimization of the L_2 distance

Let $\boldsymbol{\mathcal{N}}_x(\mu_i, \Sigma_i)$ depict a d-dimensional Gaussian distribution of x [its $3D$ form is given by Equation (2.30)]. Then the product between the Gaussian densities $\boldsymbol{\mathcal{N}}_x(\mu_1, \Sigma_1)$ and $\boldsymbol{\mathcal{N}}_x(\mu_2, \Sigma_2)$ (which are not normalized) may be written [85] as

$$\boldsymbol{\mathcal{N}}_x(\mu_1, \Sigma_1) \boldsymbol{\mathcal{N}}_x(\mu_2, \Sigma_2) = \boldsymbol{\mathcal{C}} \boldsymbol{\mathcal{N}}_x\left(\mu_\psi, \Sigma_\psi\right)$$

$$= \frac{1}{\sqrt{det\left(2\pi(\Sigma_1 + \Sigma_2)\right)}} exp\left[-\frac{1}{2}(\mu_1 - \mu_2)^T (\Sigma_1 + \Sigma_2)^{-1} (\mu_1 - \mu_2)\right] \boldsymbol{\mathcal{N}}_x\left(\mu_\psi, \Sigma_\psi\right) \qquad (2.35)$$

where

$$\boldsymbol{\mathcal{N}}_x\left(\mu_\psi, \Sigma_\psi\right) = \boldsymbol{\mathcal{N}}_x\left(\left(\Sigma_{\mathbf{1}}^{-\mathbf{1}} + \Sigma_{\mathbf{2}}^{-\mathbf{1}}\right)^{-\mathbf{1}} \left(\Sigma_{\mathbf{1}}^{-\mathbf{1}} \mu_1 + \Sigma_{\mathbf{2}}^{-\mathbf{1}} \mu_2\right), \left(\Sigma_{\mathbf{1}}^{-\mathbf{1}} + \Sigma_{\mathbf{2}}^{-\mathbf{1}}\right)^{-\mathbf{1}}\right) \qquad (2.36).$$

Hence

$$\begin{aligned}\int \boldsymbol{\mathcal{N}}_x(\mu_1,\Sigma_1)\boldsymbol{\mathcal{N}}_x(\mu_2,\Sigma_2)\,\boldsymbol{dx} &= \int \boldsymbol{\mathcal{C}}\boldsymbol{\mathcal{N}}_x\left(\mu_\psi,\Sigma_\psi\right)\boldsymbol{dx}\\ &= \boldsymbol{\mathcal{C}}\int \boldsymbol{\mathcal{N}}_x\left(\mu_\psi,\Sigma_\psi\right)\boldsymbol{dx}\\ &= \boldsymbol{\mathcal{C}}\sqrt{det\left(2\pi\left(\Sigma_{\mathbf{1}}^{\mathbf{-1}}+\Sigma_{\mathbf{2}}^{\mathbf{-1}}\right)^{\mathbf{-1}}\right)}\\ &= \boldsymbol{\mathcal{C}}\sqrt{(2\pi)^d det\left(\left(\Sigma_{\mathbf{1}}^{\mathbf{-1}}+\Sigma_{\mathbf{2}}^{\mathbf{-1}}\right)^{\mathbf{-1}}\right)}\\ &= \boldsymbol{\mathcal{C}}\boldsymbol{\mathcal{U}}_{\{\Sigma_{\mathbf{1}}^{\mathbf{-1}},\Sigma_{\mathbf{2}}^{\mathbf{-1}}\}} \qquad (2.37).\end{aligned}$$

Jian and Vemuri [53] represented discrete point sets by *convex* combinations of Gaussian component densities where each component density corresponds to each point in the sets. This approach is derived from the description of Section 2.2.2 if we assume that for any discrete point set it holds that "$\boldsymbol{\mathcal{M}} \equiv \boldsymbol{\mathcal{S}}$" and that the "$v^{(i)}$'s" are associated with the "$t^{(i)}$'s" one-on-one. As a consequence the right part of Equation (2.31) is reduced to only one component, namely, the φ_h=1 term, and for each h point of the s points. The vector μ_h in the reduced form of Equation (2.31) corresponds to the location of the point h. Taking linear combinations of such Gaussian components is merely a mathematical convenience as will be shown below.

Assume two mixtures of Gaussians: one representing the moving source model set and the other the fixed target model set with density functions $\mathscr{gmm}(\boldsymbol{\mathcal{M}}) \equiv \mathcal{J}(x;\mathscr{a},\mu,\Sigma)$ and $\mathscr{gmm}(\boldsymbol{\mathcal{S}}) \equiv \mathcal{W}(x;\mathscr{b},v,\Gamma)$, respectively. They can be described by

$$\mathcal{J}(x;\mathscr{a},\mu,\Sigma) = \sum_{i=1}^{m} \mathscr{a}_i\ P(x;\mu_i,\Sigma_i) \qquad (2.38)$$

$$\mathcal{W}(x;\mathscr{b},v,\Gamma) = \sum_{j=1}^{s} \mathscr{b}_j\ P\left(x;v_j,\Gamma_j\right) \qquad (2.39)$$

where $P(x;\mu_i,\Sigma_i) = \frac{1}{\sqrt{det(2\pi\Sigma_i)}} exp\left[-\frac{1}{2}(x-\mu_i)^T\Sigma_i^{-1}(x-\mu_i)\right]$.

The L_2 distance measures the similarity between two $\mathcal{GMMs}$ and may be expressed by

$$L_2(\boldsymbol{\mathcal{M}}_{\mathbf{0}}, \boldsymbol{\mathcal{S}}; \theta) = \int \left(\mathscr{gmm}(\boldsymbol{\mathcal{M}}) - \mathscr{gmm}(\boldsymbol{\mathcal{S}})\right)^2 dx$$

$$= \int \left(\mathscr{gmm}\left(\mathcal{F}(\boldsymbol{\mathcal{M}}_{\mathbf{0}}; \theta)\right) - \mathscr{gmm}(\boldsymbol{\mathcal{S}})\right)^2 dx \qquad (2.40)$$

The non-rigid point set registration process becomes an optimization problem where the statistical dissimilarity between a non-rigidly deforming point set and a fixed deformed target set is minimized over a (usually regularized and) continuously optimizing transformation space. The L_2 distance function of Equation (2.40) represents a cost function which produces an optimized set of parameters θ at its minimal value. The L_2 distance between $\mathcal{J}(x; \mathscr{a}, \mu, \Sigma)$ and $\mathcal{W}(x; \mathscr{b}, \nu, \Gamma)$ can take a closed-form expression by incorporating Equation (2.37), namely:

$$L_2(\mathcal{J}, \mathcal{W}) = \int \left(\frac{\mathcal{J}}{m} - \frac{\mathcal{W}}{s}\right)^2 dx$$

$$= \int \left(\frac{\mathcal{J}}{m}\right)^2 dx + \int \left(\frac{\mathcal{W}}{s}\right)^2 dx - 2 \int \frac{\mathcal{J}\mathcal{W}}{ms} dx$$

$$= \frac{\sum_{i=1}^{m} \sum_{j=1}^{m} \mathscr{a}_i \mathscr{a}_j P\left(0; \mu_i - \mu_j, \Sigma_i + \Sigma_j\right) \boldsymbol{\mathcal{U}}_{\left\{\Sigma_i^{-1}, \Sigma_j^{-1}\right\}}}{m^2}$$

$$+ \frac{\sum_{i=1}^{s} \sum_{j=1}^{s} \mathscr{b}_i \mathscr{b}_j P\left(0; \nu_i - \nu_j, \Gamma_i + \Gamma_j\right) \boldsymbol{\mathcal{U}}_{\left\{\Gamma_i^{-1}, \Gamma_j^{-1}\right\}}}{s^2}$$

$$-2 \frac{\sum_{i=1}^{m} \sum_{j=1}^{s} \mathscr{a}_i \mathscr{b}_j P\left(0; \mu_i - \nu_j, \Sigma_i + \Gamma_j\right) \boldsymbol{\mathcal{U}}_{\left\{\Sigma_i^{-1}, \Gamma_j^{-1}\right\}}}{ms} \qquad (2.41).$$

Equation (2.41) can be simplified by assuming that the Gaussian components of $\mathcal{J}$ and $\mathcal{W}$ are weighted equally and that they all share *the same spherical* (*isotropic*) covariance matrix, *i.e.*, all of the components are spherical Gaussians with a uniform scale σ. (The latter assumption has been shown to be sufficient in most of the examined cases [86] as well as in the computational experiments of Chapter 3.) Hence,

$$\text{Equation (2.30)} \rightarrow \mathcal{J}(x; \mathscr{a}, \mu, \sigma) = \sum_{i=1}^{m} \mathscr{a} \frac{1}{\sqrt{(2\pi\sigma_i^2)^3}} exp\left[-\frac{1}{2} \frac{\|x - \mu_i\|^2}{\sigma_i^2}\right] \qquad (2.42).$$

The $P\left(0; (\mu/\nu)_i - (\mu/\nu)_j, (\Sigma/\Gamma)_i + (\Sigma/\Gamma)_j\right)$ terms of Equation (2.41) become

$$P(0;\mu_i-\mu_j,\Sigma_i+\Sigma_j)\cong P(\mu_{i/j};\mu_{j/i},\sigma_i^2+\sigma_j^2)$$

$$=(4\pi\sigma^2)^{-3/2}exp\left[-\frac{1}{4}\frac{\|\mu_i-\mu_j\|^2}{\sigma^2}\right] \quad (2.43)$$

and the $\boldsymbol{\mathcal{U}}$ terms of Equation (2.41) become in $3D$

$$\boldsymbol{\mathcal{U}}_{\{\Sigma_i^{-1},\Sigma_j^{-1}\}}=\boldsymbol{\mathcal{U}}_{\{\Gamma_i^{-1},\Gamma_j^{-1}\}}=\boldsymbol{\mathcal{U}}_{\{\Sigma_i^{-1},\Gamma_j^{-1}\}}\cong(\pi\sigma^2)^{3/2}$$

since $(\Sigma/\Gamma)_{i/j}\equiv\sigma^2 I$. Also, the L_2 integral term of the inner product of the fixed $\mathcal{GMM}$ with itself, *i.e.*, $\int\mathcal{W}^2dx$, is a constant and thus it can be left out from the optimization of the $L_2(\boldsymbol{\mathcal{M}_0},\boldsymbol{\mathcal{S}};\theta)$ cost function.

2.2.4 The minimization of the energy cost function

By choosing TPS as a deformation model (see Section 2.1.3) and letting $\boldsymbol{\mathcal{C}}=\{c_1,\dots,c_n\}$ represent a set of n source control points where

$$\boldsymbol{\mathcal{C}}\subset\{q_1,\dots,q_m\} \qquad (2.44)$$

the objective cost function $\mathcal{E}(\theta)$ may be expressed by the following regularized energy functional

$$\begin{aligned}\mathcal{E}(\theta)&=L_2(\boldsymbol{\mathcal{M}_0},\boldsymbol{\mathcal{S}};\theta)+\lambda I_{\mathcal{F}}(\theta)\\&=\int\left(\frac{\mathcal{J}_\theta}{m}-\frac{\mathcal{W}}{s}\right)^2dx+\lambda\text{trace}(Q^T\Phi Q)\\&\cong\int\left(\frac{\mathcal{J}_\theta}{m}\right)^2dx-2\int\frac{\mathcal{J}_\theta\mathcal{W}}{ms}dx+\lambda\text{trace}(\psi^T\mathcal{N}^T\Phi\mathcal{N}\psi) \qquad (2.45)\end{aligned}$$

where $I_{\mathcal{F}}$ corresponds to the bending energy of the TPS warping function $\mathcal{F}$, $\mathcal{J}_\theta$ represents the transformed source model point set warped by $\mathcal{F}$ and $\lambda>0$ controls the strength of the regularization. As the value of λ becomes smaller the transformation becomes a non-rigid topical one. A very large value of λ yields a nearly pure affine transformation as a larger extent of optimization is required for the trace$(\psi^T\mathcal{N}^T\Phi\mathcal{N}\psi)$ to become smaller. For a fixed λ, there exists a unique $\mathcal{F}(M_0)=[1|M_0]E^T+U\mathcal{N}\psi$ that minimizes Equation (2.45).

2.2.5 Derivatives of $\mathcal{E}$ with respect to the motion parameters

Equation (2.45) can be written

$$\mathcal{E}(\mathcal{F}) \cong L_2'(\mathcal{F}) + \lambda I(\mathcal{F}) \qquad (2.46)$$

$$\mathcal{F} = \mathcal{F}(\psi, E)$$

$$L_2'(\mathcal{F}) = \int \left(\frac{\mathcal{J}}{m}\right)^2 dx - 2\int \frac{\mathcal{J}\mathcal{W}}{ms} dx.$$

The derivatives of the cost function $\mathcal{E}$ with respect to the affine and TPS parameters can be written in analytical expressions:

$$\frac{\partial\mathcal{E}\big(\mathcal{F}(\psi, E)\big)}{\partial\psi} = \frac{\partial\mathcal{E}}{\partial\mathcal{F}}\frac{\partial\mathcal{F}}{\partial\psi}$$

$$= \left(\frac{\partial L_2'}{\partial\mathcal{F}} + \lambda\frac{\partial I}{\partial\mathcal{F}}\right)\frac{\partial\mathcal{F}}{\partial\psi} \qquad (2.47).$$

Based on the fact that $\Phi = (\Phi)^T$

$$\frac{\partial}{\partial\psi}\mathrm{Tr}[\psi^T\mathcal{N}^T\Phi\mathcal{N}\psi] = \mathcal{N}^T\Phi\mathcal{N}\psi + (\mathcal{N}^T\Phi\mathcal{N})^T\psi = 2\mathcal{N}^T\Phi\mathcal{N}\psi \qquad (2.48).$$

$$\text{Equation (2.47)} \xRightarrow{\text{Eq. (2.48)}} \quad \frac{\partial\mathcal{E}(\mathcal{F})}{\partial\psi} = (U\mathcal{N})^T\boldsymbol{\mathcal{H}} + 2\lambda\mathcal{N}^T\Phi\mathcal{N}\psi \qquad (2.49)$$

where

$$\boldsymbol{\mathcal{H}} = \left[\frac{\partial L_2'}{\partial\mathcal{F}}\right]^{\boldsymbol{T}} \qquad (2.50).$$

Similarly, the derivative of $\mathcal{E}$ with respect to the affine parameters can be described by

$$\frac{\partial\mathcal{E}\big(\mathcal{F}(\psi, E)\big)}{\partial E^T} = \left[\frac{\partial\mathcal{E}}{\partial\mathcal{F}}\frac{\partial\mathcal{F}}{\partial E}\right]^T = [1|M_0]^T\boldsymbol{\mathcal{H}} \qquad (2.51).$$

As $\mathcal{F}$ represents a spatial transformation in $3D$ and given the assumption that $L_2 \cong \int\left(\frac{\mathcal{J}}{m}\right)^2 dx - 2\int\frac{\mathcal{J}\mathcal{W}}{ms}dx$ then

$$\boldsymbol{\mathcal{H}} \cong \boldsymbol{2\mathcal{H}}_{\mathcal{J}^2} - \boldsymbol{2\mathcal{H}}_{\mathcal{J}\mathcal{W}} \qquad (2.52)$$

$$\boldsymbol{\mathcal{H}}_{(\mathcal{J}^2/\mathcal{JW})} = \begin{pmatrix} \boldsymbol{\mathcal{H}}_{\boldsymbol{1x}} & \boldsymbol{\mathcal{H}}_{\boldsymbol{1y}} & \boldsymbol{\mathcal{H}}_{\boldsymbol{1z}} \\ \vdots & \vdots & \vdots \\ \boldsymbol{\mathcal{H}}_{\boldsymbol{mx}} & \boldsymbol{\mathcal{H}}_{\boldsymbol{my}} & \boldsymbol{\mathcal{H}}_{\boldsymbol{mz}} \end{pmatrix} \in \mathbb{R}^{m\times 3} \quad (2.53).$$

Assume that ρ refers to each point of the transformed model set; then $\forall \rho \epsilon \{1, \dots, m\}$ it holds that

$$\boldsymbol{\mathcal{H}}_{\boldsymbol{\rho x}} \propto \sum_{j=1}^{\left(\frac{m}{s}\right)} -\frac{1}{2\sigma^2\left[m\left(\frac{m}{s}\right)\right]} exp\left[-\frac{\left\|\mu_\rho - \left(\frac{\mu}{\nu}\right)_j\right\|^2}{4\sigma^2}\right]\left(x_{\mu_\rho} - x_{\left(\frac{\mu}{\nu}\right)_j}\right) \quad (2.54)$$

$$\boldsymbol{\mathcal{H}}_{\boldsymbol{\rho y}} \propto \sum_{j=1}^{\left(\frac{m}{s}\right)} -\frac{1}{2\sigma^2\left[m\left(\frac{m}{s}\right)\right]} exp\left[-\frac{\left\|\mu_\rho - \left(\frac{\mu}{\nu}\right)_j\right\|^2}{4\sigma^2}\right]\left(y_{\mu_\rho} - y_{\left(\frac{\mu}{\nu}\right)_j}\right) \quad (2.55)$$

$$\boldsymbol{\mathcal{H}}_{\boldsymbol{\rho z}} \propto \sum_{j=1}^{\left(\frac{m}{s}\right)} -\frac{1}{2\sigma^2\left[m\left(\frac{m}{s}\right)\right]} exp\left[-\frac{\left\|\mu_\rho - \left(\frac{\mu}{\nu}\right)_j\right\|^2}{4\sigma^2}\right]\left(z_{\mu_\rho} - z_{\left(\frac{\mu}{\nu}\right)_j}\right) \quad (2.56).$$

An optimized set of affine and TPS parameters can be obtained as a minimum energy solution of Equation (2.46) with the aid of gradient-based numerical optimization techniques applied to Equations (2.49) and (2.51).

2.2.6 Modification of the algorithm

Based on the information of Section 2.2.3 and specifically the last term of the right side of Equation (2.41), it becomes obvious that the $\mathcal{GMM} + \mathcal{F}_{TPS}$ algorithm cannot be applied to the case where the registration pair point sets deviate significantly in number of points. The registration scheme is still appropriate for $m \neq s$ as long as $m \approx s$.

The algorithm was modified according to Figure 2.2 to account for registration between a full $3D$ source model $\boldsymbol{\mathcal{M}}$ and an occluded $3D$ target model $\boldsymbol{\mathcal{S}}$. The initial correspondences between these two point sets are identified on the basis of a one-to-one nearest neighbour correspondence criterion and by setting a maximum distance threshold as the upper limit of all possible correspondences. The initial approximation of considering every closest point pair to be a correspondence pair is a valid starting point so long as (i) the two point sets are already placed (with a good initial transformation) in approximate registration before the iterating non-rigid registration process of Figure 2.2 is initiated; and (*ii*) the majority of the extracted points from the source have true correspondences in the occluded target surface. This configuration is an ideal starting point as it maximizes the probability of finding the correct correspondences during the process of registration. However, obtaining a satisfactory initial transformation is a nontrivial problem.

Note that the $\mathcal{E}(\theta)$ multiply-linked objective cost function of Equation (2.45) is defined globally and not on nearest neighbouring points. Thus, it is the *same* cost function that is optimized as the source model point configuration dynamically evolves in each step of the minimization, which in turn alleviates the problem of correspondence error due to potential point mismatches. The overall correspondence error tends to further reduce when the target surface (and hence the identified overlap between the registration surfaces considered) is increased since then the number of true correspondence pairs, identified in the process of registration, is also increased (which helps in discriminating against outliers and overcoming the effect of noise). The TPS deformation can then be computed based on a larger internal structure of control points. The contribution of $E_l = \sum_i \sum_j l\left(\left(x_i - x_j\right)^2\right)$ terms in the distance cost function (where l is the Gaussian distance function) is increased. The probability of overall correct point assignments at convergence of the algorithm is also increased so long as the number of true correspondence pairs prevails. In effect the topology of the *available* target scene has a major effect on the correspondence error and by extension on the final output of the registration process depicted in Figure 2.2. Pauly *et al.* [87] combined point-to-point and point-to-plane metrics in order to avoid penalizing correspondences due to large featureless regions. While this formulation is very useful for registration of smooth surfaces, the current $\mathcal{GMM}$ methodology follows a more rigorous and superior approach.

The output produced from ‘establishing correspondences’ in Figure 2.2 consists of the extracted source model point set corr($\boldsymbol{\mathcal{M}}$) and the extracted target model point set corr($\boldsymbol{\mathcal{S}}$). These datasets take part in a $\mathcal{GMM} + \mathcal{F}_{TPS}$ registration process where for the set of control points $\boldsymbol{\mathcal{C}}$ it holds that $\boldsymbol{\mathcal{C}} = \mathrm{corr}(\boldsymbol{\mathcal{M}})$. The associated $\Phi, \mathcal{N}$, and U matrices are computed for the extracted source model (where $\Phi \equiv U$) and the energy cost function of Equation (2.45) is minimized producing a set of optimized parameters θ. Once the U matrix is computed for the full model $\boldsymbol{\mathcal{M}}$ taking corr($\boldsymbol{\mathcal{M}}$) to serve as $\boldsymbol{\mathcal{C}}$, the set of control points of $\boldsymbol{\mathcal{M}}$, (the matrix $\mathcal{N}$ hence remains the same) and given the estimated θ parameters [which populate the matrices

E^T and ψ; see Equation (2.27)], the non-rigid transformation $\mathcal{F}$ is applied to $\boldsymbol{\mathcal{M}}$. The output from this process overwrites the moving model, namely, $\boldsymbol{\mathcal{M}} \coloneqq \mathcal{F}(\boldsymbol{\mathcal{M}}; \boldsymbol{\theta})$, and the overall registration process repeats itself until a stopping criterion is satisfied. An increased number of correspondences is expected (which has been observed in the computational experiments of Chapter 3) in each iteration as a consequence of the gradual non-rigid deformation of the moving model.

Modified Algorithm.

Input: The original source model set $\boldsymbol{\mathcal{M}}_0$, the occluded target model set $\boldsymbol{\mathcal{S}}$ and the non-rigid parameterized TPS transformation model.

Output: The moving model $\boldsymbol{\mathcal{M}}$ registered onto the target scene $\boldsymbol{\mathcal{S}}$.

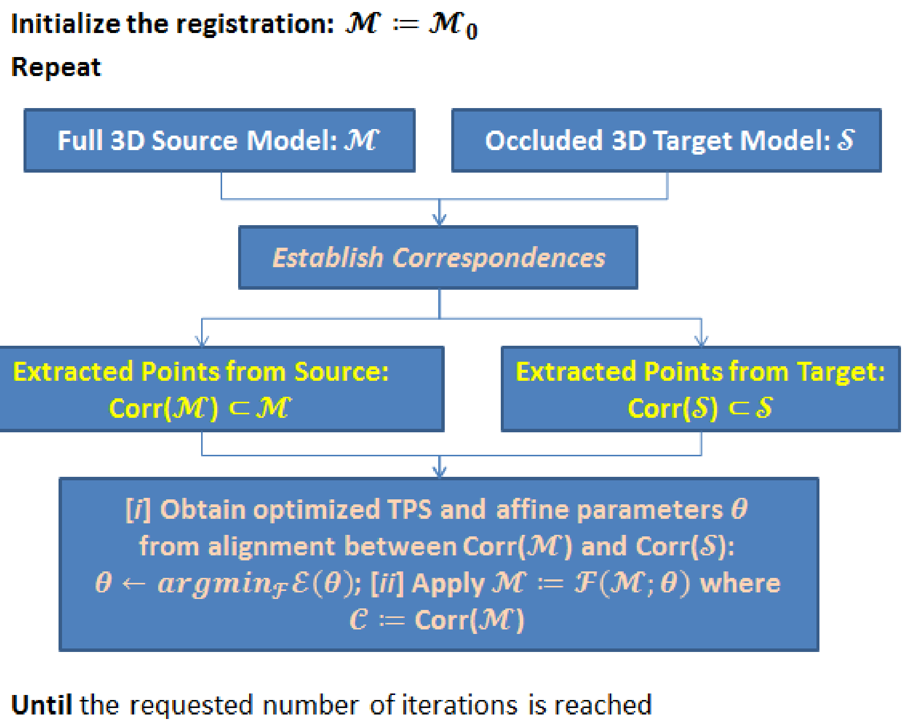

Figure 2.2: Modifications of the $\mathcal{GMM} + \mathcal{F}_{TPS}$ learning algorithm for full-model-to-occluded-surface non-rigid registration.

2.3 The kernel correlation technique applied to non-rigid point set registration

2.3.1 Introduction

In this Section the concept of Kernel Correlation ($\mathcal{KC}$) is defined and its usefulness with regards to point-set registration is outlined. Non-rigid registration is formulated as the process of aligning two point sets by maximizing the $\mathcal{KC}$ configuration dynamically between them [53, 55]. This is a similarity measure that can be described by a closed-form expression leading to a computationally efficient *multiply-linked* registration algorithm. This non-rigid algorithm is modified and further validated in the current work. The accuracy of the $\mathcal{KC}$ registration process is empirically studied in Chapter 3 by means of computational experiments.

2.3.2 Kernel correlation

Suppose two points s_i,$s_j \in \mathbb{R}^3$; their $\mathcal{KC}$ [88] is given by

$$\mathcal{KC}(s_i, s_j) = \int \mathcal{K}(s, s_i) \cdot \mathcal{K}(s, s_j)\, ds \qquad (2.57)$$

where $\mathcal{K}(s, s_{i/j})$ corresponds to a kernel function defined for the vectors s and $s_{i/j}$, and centred at $s_{i/j}$. The Gaussian Kernel function is used in this implementation which is a non-negative and symmetric function [89] in consistency with the requirements of the $\mathcal{KC}$ registration technique. Given the normalized form of this function in $3D$

$$\mathcal{K}_G(s, s_i) = (\pi\sigma^2)^{-3/2} exp\left[-\frac{\|s - s_i\|^2}{\sigma^2}\right] \quad (2.58),$$

Equation (2.57) → $\mathcal{KC}_G(s_i, s_j) = (2\pi\sigma^2)^{-3/2} exp\left[-\frac{1}{2}\frac{\|s_i - s_j\|^2}{\sigma^2}\right] \qquad (2.59)$

where σ corresponds to the Gaussian Kernel scale. Equation (2.59) can be taken as a measure of closeness between s_i and s_j; it is going to $(2\pi\sigma^2)^{-3/2}$ when s_i and s_j are coming closer while it is going to zero when s_i and s_j are moving further apart.

To obtain a proximity measure between a discrete point $s_l \in \mathrm{U} = \{s_1, \dots, s_m\}$ and the rest of the points of the set U, the following quantity is estimated

$$\mathcal{KC}_G(s_l, U) = (2\pi\sigma^2)^{-3/2} \sum_{s_l \neq s_k} exp\left[-\frac{1}{2}\frac{\|s_l - s_k\|^2}{\sigma^2}\right] \qquad (2.60)$$

and by extension $\forall\, s_l, s_k \in \mathrm{U}$

$$\mathcal{KC}_G(U) = \sum_{l=1}^{m} \mathcal{KC}_G(s_l, U) = 2\sum_{l \neq k} \mathcal{KC}_G(s_l, s_k) \qquad (2.61)$$

making $\mathcal{KC}_G(U)$ a compactness measure of the point set U. The larger the affinity between points across all pairs of points of U the larger $\mathcal{KC}_G(U)$ becomes.

2.3.3 The maximization of the correlation between kernel densities

Assume the moving model $\boldsymbol{\mathcal{M}} = \mathcal{F}(\boldsymbol{\mathcal{M}_0}; \theta) = (v_1, \dots, v_m)^T$ and the target model $\boldsymbol{\mathcal{S}} = (t_1, \dots, t_s)^T$ defined in Section 2.2.2 where $\boldsymbol{\mathcal{M}_0} = (q_1, \dots, q_m)^T$. Their kernel density estimates are defined by

$$P_{\mathcal{M}}(x; \theta) = \sum_{i=1}^{m} \frac{\mathcal{K}\big(x, \mathcal{F}(q_i; \theta)\big)}{m} \qquad (2.62)$$

$$P_{\mathcal{S}}(x) = \sum_{j=1}^{s} \frac{\mathcal{K}\big(x, t_j\big)}{s} \qquad (2.63).$$

The objective is to solve for the parameters θ of the non-rigid transformation $\mathcal{F}$ that can cause the largest minimization of the energy of the following normalized cost function

$$\int \left(\frac{P_{\mathcal{M}}}{I_{\mathcal{M}}} - \frac{P_{\mathcal{S}}}{I_{\mathcal{S}}}\right)^2 dx = \int \left(\frac{P_{\mathcal{M}}}{I_{\mathcal{M}}}\right)^2 dx + \int \left(\frac{P_{\mathcal{S}}}{I_{\mathcal{S}}}\right)^2 dx - 2\int \frac{P_{\mathcal{M}} P_{\mathcal{S}}}{I_{\mathcal{M}} I_{\mathcal{S}}} dx$$

$$= 2 - \frac{2}{I_{\mathcal{M}} I_{\mathcal{S}}} \int P_{\mathcal{M}} P_{\mathcal{S}}\, dx \qquad (2.64)$$

where the final output of Equation (2.64) arises due to the normalization terms

$$I_{\mathcal{M}} = \sqrt{\int P_{\mathcal{M}}^2\, dx} \qquad (2.65)$$

$$I_{\mathcal{S}} = \sqrt{\int P_{\mathcal{S}}^2 \, dx} \qquad (2.66).$$

$$\text{Equation (2.62)} \rightarrow m^2 \int P_{\mathcal{M}}^2 \, dx = \int \left(\sum_{i=1}^{m} \mathcal{K}\big(x, \mathcal{F}(q_i; \theta)\big) \right)^2 dx$$

$$= \left[\sum_{i=1}^{m} \int \mathcal{K}\big(x, \mathcal{F}(q_i; \theta)\big)^2 dx + 2 \sum_{i \neq j} \int \mathcal{K}\big(x, \mathcal{F}(q_i; \theta)\big) \cdot \mathcal{K}\left(x, \mathcal{F}\big(q_j; \theta\big)\right) dx \right]$$

$$= m(2\pi\sigma^2)^{-\frac{3}{2}} + \mathcal{KC}_G(\boldsymbol{\mathcal{M}}) \qquad (2.67).$$

Similarly, $$\text{Equation (2.63)} \rightarrow s^2 \int P_{\mathcal{S}}^2 \, dx = s(2\pi\sigma^2)^{-\frac{3}{2}} + \mathcal{KC}_G(\boldsymbol{\mathcal{S}}) \qquad (2.68).$$

While $\mathcal{KC}_G(\boldsymbol{\mathcal{M}})$ is not invariant under non-rigid registration, $\mathcal{KC}_G(\boldsymbol{\mathcal{S}})$ is a constant. The following relationships are produced:

$$\text{Equations (2.65)} \wedge \text{(2.67)} \rightarrow I_{\mathcal{M}}^2 \propto \mathcal{KC}_G(\boldsymbol{\mathcal{M}}) \qquad (2.69)$$

$$\text{Equations (2.66)} \wedge \text{(2.68)} \rightarrow I_{\mathcal{S}}^2 \propto \mathcal{KC}_G(\boldsymbol{\mathcal{S}}) \qquad (2.70).$$

To further exploit Equation (2.64)

$$\int P_{\mathcal{M}} P_{\mathcal{S}} \, dx = \int \left[\sum_{i=1}^{m} \frac{\mathcal{K}\big(x, \mathcal{F}(q_i; \theta)\big)}{m} \cdot \sum_{j=1}^{s} \frac{\mathcal{K}\big(x, t_j\big)}{s} \right] dx$$

$$= \frac{1}{ms} \sum_{i=1}^{m} \sum_{j=1}^{s} \mathcal{KC}_G\big(\mathcal{F}(q_i; \theta), t_j\big)$$

$$= -\frac{1}{ms} \Xi(\boldsymbol{\mathcal{M}_0}, \boldsymbol{\mathcal{S}}; \theta) \qquad (2.71)$$

The energy of the cost function of Equation (2.64) is minimized as the correlation between $P_{\mathcal{M}}$ and $P_{\mathcal{S}}$ is maximized or equivalently as the $\mathcal{KC}$ *multiply-linked* registration cost function Ξ, which represents the sum of all pairwise kernel correlations between the moving model and the fixed target model point sets, is minimized. Hence,

$$\text{Equation (2.64)} \xrightarrow{\text{Eq. (2.71)}} \int \left(\frac{P_{\mathcal{M}}}{I_{\mathcal{M}}} - \frac{P_{\mathcal{S}}}{I_{\mathcal{S}}}\right)^2 dx = 2 + \frac{2}{ms}\frac{\Xi(\boldsymbol{\mathcal{M}_0}, \boldsymbol{\mathcal{S}}; \theta)}{I_{\mathcal{M}} I_{\mathcal{S}}} \qquad (2.72).$$

2.3.4 The minimization of $\mathcal{E}$ and analytical expressions of $\mathcal{E}$

Following a similar process to the one described in Section 2.2.4

$$\mathcal{E}(\theta) = \int \left(\frac{P_{\mathcal{M}}(\theta)}{I_{\mathcal{M}}(\theta)} - \frac{P_{\mathcal{S}}}{I_{\mathcal{S}}}\right)^2 dx + \lambda \text{trace}(Q^T \Phi Q)$$

$$= 2 - \frac{2}{ms}\frac{\sum_{i=1}^{m}\sum_{j=1}^{s} \mathcal{K}\mathcal{C}_G\big(\mathcal{F}(q_i;\theta), t_j\big)}{I_{\mathcal{M}}(\theta) \cdot I_{\mathcal{S}}} + \lambda \text{trace}(\psi^T \mathcal{N}^T \Phi \mathcal{N} \psi) \qquad (2.73).$$

To simplify the computation of derivatives of $\mathcal{E}$, note that maximizing

$$\int \frac{P_{\mathcal{M}} P_{\mathcal{S}}}{I_{\mathcal{M}} I_{\mathcal{S}}} dx = \frac{1}{\sqrt{\int P_{\mathcal{M}}^2\, dx \int P_{\mathcal{S}}^2\, dx}} \int P_{\mathcal{M}} P_{\mathcal{S}}\, dx$$

is the same as minimizing

$$\int P_{\mathcal{S}}^2\, dx - \frac{(\int P_{\mathcal{M}} P_{\mathcal{S}}\, dx)^2}{\int {P_{\mathcal{M}}}^2\, dx}$$

or, for a fixed $P_{\mathcal{S}}$, equivalent to minimizing

$$-\frac{(\int P_{\mathcal{M}} P_{\mathcal{S}}\, dx)^2}{\int {P_{\mathcal{M}}}^2\, dx} = \Xi_{\mathcal{M}}$$

By following a similar pattern of work to the one described in Section 2.2.5

$$\frac{\partial \mathcal{E}(\mathcal{F})}{\partial \psi} \cong \frac{2}{msI_{\mathcal{S}}}(U\mathcal{N})^T \boldsymbol{\mathcal{R}} + 2\lambda \mathcal{N}^T \Phi \mathcal{N} \psi \qquad (2.74)$$

$$\boldsymbol{\mathcal{R}} = \left[\frac{\partial \Xi_{\mathcal{M}}}{\partial \mathcal{F}}\right]^{\boldsymbol{T}} \in \mathbb{R}^{m \times 3} \quad (2.75)$$

$$\frac{\partial \mathcal{E}(\mathcal{F})}{\partial E^T} = [1|M_0]^T \boldsymbol{\mathcal{R}} \qquad (2.76)$$

$$\boldsymbol{\mathcal{R}} = \frac{2\boldsymbol{\mathcal{H}}_{P_{\mathcal{M}}{}^{2}}\left(\int P_{\mathcal{M}}P_{\mathcal{S}}\,dx\right)^{\mathbf{2}} - 2\boldsymbol{\mathcal{H}}_{P_{\mathcal{M}}P_{\mathcal{S}}}\int P_{\mathcal{M}}P_{\mathcal{S}}\,dx\int {P_{\mathcal{M}}}^{2}dx}{\left(\int {P_{\mathcal{M}}}^{2}dx\right)^{\mathbf{2}}} \qquad (2.77).$$

$$\boldsymbol{\mathcal{H}}_{({P_{\mathcal{M}}}^{2}/P_{\mathcal{M}}P_{\mathcal{S}})} = \begin{pmatrix} \boldsymbol{\mathcal{H}}_{\mathbf{1}\boldsymbol{x}} & \boldsymbol{\mathcal{H}}_{\mathbf{1}\boldsymbol{y}} & \boldsymbol{\mathcal{H}}_{\mathbf{1}\boldsymbol{z}} \\ \vdots & \vdots & \vdots \\ \boldsymbol{\mathcal{H}}_{\boldsymbol{mx}} & \boldsymbol{\mathcal{H}}_{\boldsymbol{my}} & \boldsymbol{\mathcal{H}}_{\boldsymbol{mz}} \end{pmatrix} \in \mathbb{R}^{m\times 3} \quad (2.78).$$

Assume that ρ refers to each point of the transformed model set; then $\forall\rho\epsilon\{1,\dots,m\}$ it holds that

$$\boldsymbol{\mathcal{H}}_{\boldsymbol{\rho x}} \propto \sum_{j=1}^{\left(\frac{m}{s}\right)} -\frac{1}{\sigma^{2}\left[m\left(\frac{m}{s}\right)\right]}\,exp\left[-\frac{\left\|v_{\rho}-\left(\frac{v}{t}\right)_{j}\right\|^{2}}{2\sigma^{2}}\right]\left(x_{v_{\rho}}-x_{\left(\frac{v}{t}\right)_{j}}\right) \quad (2.79)$$

$$\boldsymbol{\mathcal{H}}_{\boldsymbol{\rho y}} \propto \sum_{j=1}^{\left(\frac{m}{s}\right)} -\frac{1}{\sigma^{2}\left[m\left(\frac{m}{s}\right)\right]}\,exp\left[-\frac{\left\|v_{\rho}-\left(\frac{v}{t}\right)_{j}\right\|^{2}}{2\sigma^{2}}\right]\left(y_{v_{\rho}}-y_{\left(\frac{v}{t}\right)_{j}}\right) \quad (2.80)$$

$$\boldsymbol{\mathcal{H}}_{\boldsymbol{\rho z}} \propto \sum_{j=1}^{\left(\frac{m}{s}\right)} -\frac{1}{\sigma^{2}\left[m\left(\frac{m}{s}\right)\right]}\,exp\left[-\frac{\left\|v_{\rho}-\left(\frac{v}{t}\right)_{j}\right\|^{2}}{2\sigma^{2}}\right]\left(z_{v_{\rho}}-z_{\left(\frac{v}{t}\right)_{j}}\right) \quad (2.81).$$

2.3.5 Modifications

The $\mathcal{GMM}+\mathcal{F}_{TPS}$ and $\mathcal{KC}+\mathcal{F}_{TPS}$ algorithms are both based on multiply-linked non-rigid registration methods. The $\int\frac{\mathcal{JW}}{ms}dx$ term of the L_2 distance (see Section 2.2.3) and the $\int P_{\mathcal{M}}P_{\mathcal{S}}\,dx$ term of Equation (2.64) are similar. The same series of modifications were performed on the $\mathcal{KC}+\mathcal{F}_{TPS}$ registration algorithm for recovering deformation in an occluded target surface as specifically presented in Section 2.2.6 and graphically outlined in Figure 2.2.

2.4 Gaussian mixtures model and $\mathcal{EM}$ incorporated in the non-rigid point set registration framework

2.4.1 Introduction

The $\mathcal{GMM}/\mathcal{EM}$ formalism [57] is combined with the TPS deformation model and is applied to non-rigid point registration. In the following, the fundamental principles of this technique are reviewed followed by relevant modifications of the algorithm.

2.4.2 The expectation maximization formalism applied to Gaussian mixture models

This Section has been prepared as an extension of Section 2.2.2; it follows the exact definition of $\mathcal{GMM}$ including the $\boldsymbol{\mathcal{EM}}$ formalism and its implications and caveats on optimization. For example, Equation (2.31) represents the probabilistic distribution of the transformed source model points across the set of fixed target points. If the association between the $v^{(i)\prime}$s and the $t^{(i)\prime}$s is known in advance then it is a straightforward task to evaluate the solutions of Equation (2.33), which, however, is not possible in point-set registration.

This is a mixture density estimation problem. The $\boldsymbol{\mathcal{EM}}$ iterative algorithm implements an efficient technique for the maximum likelihood estimation. It consists of two steps: (*i*) the $\boldsymbol{\mathcal{E}}$-step where the most probable assignments of the $v^{(i)\prime}$s to the $t^{(i)\prime}$s are made (producing optimized $f^{(i)}_{t^{(h)}}{}'$s, see Equation (2.82) below); and (*ii*) the $\boldsymbol{\mathcal{M}}$-step where the maximum likelihood estimates of the $(\varphi_h, \mu_h, \Sigma_h)$ parameters are updated using the best guesses of (*i*). The $\boldsymbol{\mathcal{E}}$- and $\boldsymbol{\mathcal{M}}$-steps iterate until (guaranteed) convergence to a local maximum of Equation (2.33). It is because of the $\boldsymbol{\mathcal{E}}$-step that the $(\varphi_h, \mu_h, \Sigma_h)$ parameters of the $\mathcal{GMM}$ of Equation (2.31) can be obtained in closed form in the $\boldsymbol{\mathcal{M}}$-step.

$\{\boldsymbol{\mathcal{E}} - \text{step}\}$:

$$f^{(i)}_{t^{(h)}} \coloneqq P\left(t^{(i)} = t^{(h)} \middle| v^{(i)};\ \varphi, \mu, \Sigma\ \right) \tag{2.82}$$

$$\mathcal{T} = \begin{pmatrix} \mathscr{t}_{t^{(1)}}^{(1)} & \mathscr{t}_{t^{(1)}}^{(2)} & \cdots & \mathscr{t}_{t^{(1)}}^{(m)} \\ \mathscr{t}_{t^{(2)}}^{(1)} & \mathscr{t}_{t^{(2)}}^{(2)} & \cdots & \mathscr{t}_{t^{(2)}}^{(m)} \\ \vdots & \vdots & \cdots & \vdots \\ \mathscr{t}_{t^{(s)}}^{(1)} & \mathscr{t}_{t^{(s)}}^{(2)} & \cdots & \mathscr{t}_{t^{(s)}}^{(m)} \end{pmatrix} \qquad s.t.$$

$$\forall\ (i,h){:}\ \ \mathscr{t}_{t^{(h)}}^{(i)} \in [0,1]$$

$$\sum_{h=1}^{s} \mathscr{t}_{t^{(h)}}^{(i)} = 1$$

$$0 < \sum_{i=1}^{m} \mathscr{t}_{t^{(h)}}^{(i)} < m$$

$\{\boldsymbol{\mathcal{M}} -$ step$\}$:

$$\varphi_h \coloneqq \frac{1}{m}\sum_{i=1}^{m} \mathscr{t}_{t^{(h)}}^{(i)} \qquad (2.83)$$

$$\mu_h \coloneqq \frac{\sum_{i=1}^{m} \mathscr{t}_{t^{(h)}}^{(i)} v^{(i)}}{\sum_{i=1}^{m} \mathscr{t}_{t^{(h)}}^{(i)}} \qquad (2.84)$$

$$\Sigma_h \coloneqq \frac{\sum_{i=1}^{m} \mathscr{t}_{t^{(h)}}^{(i)} \left(v^{(i)} - \mu_h\right)\left(v^{(i)} - \mu_h\right)^T}{\sum_{i=1}^{m} \mathscr{t}_{t^{(h)}}^{(i)}} \qquad (2.85).$$

By applying Bayes' rule to the $\boldsymbol{\mathcal{E}} -$ step the class posterior probability distribution of the $t^{(i)}$'s given the $v^{(i)}$'s can be written

$$P\left(t^{(i)} = t^{(h)} \middle| v^{(i)};\ \varphi,\mu,\Sigma\ \right) = \frac{P\left(v^{(i)} \middle| t^{(i)} = t^{(h)};\ \mu,\Sigma\ \right)P\left(t^{(i)} = t^{(h)};\ \varphi\right)}{P(v^{(i)};\varphi,\mu,\Sigma)}$$

$$= \frac{P\left(v^{(i)} \middle| t^{(i)} = t^{(h)};\ \mu,\Sigma\ \right)P\left(t^{(i)} = t^{(h)};\ \varphi\right)}{\sum_{g=1}^{s} P(v^{(i)}|t^{(i)} = t^{(g)};\ \mu,\Sigma\ )P(t^{(i)} = t^{(g)};\ \varphi)} \qquad (2.86)$$

where the class priors $P\left(t^{(i)} = t^{(h)};\ \varphi\right) = \varphi_h$ and

$$P\left(v^{(i)} \middle| t^{(i)} = t^{(h)};\ \mu,\Sigma\ \right) = \frac{1}{\sqrt{(2\pi)^3|\Sigma_h|}} exp\left[-\frac{1}{2}\left(v^{(i)} - \mu_h\right)^T \Sigma_h^{-1}\left(v^{(i)} - \mu_h\right)\right] \qquad (2.87).$$

Hence,

$$\mathscr{f}_{t^{(h)}}^{(i)} := \frac{\varphi_h \frac{1}{\sqrt{(2\pi)^3|\Sigma_h|}} exp\left[-\frac{1}{2}\left(v^{(i)} - \mu_h\right)^T \Sigma_h^{-1}\left(v^{(i)} - \mu_h\right)\right]}{\sum_{g=1}^{s} \varphi_g \frac{1}{\sqrt{(2\pi)^3\left|\Sigma_g\right|}} exp\left[-\frac{1}{2}\left(v^{(i)} - \mu_g\right)^T \Sigma_g^{-1}\left(v^{(i)} - \mu_g\right)\right]} \qquad (2.88).$$

The numerator and denominator of the output of Equations (2.86) and (2.88) contain similar terms.

According to the literature: (*i*) $\mathscr{f}_{t^{(h)}}^{(i)} \in [0,1]$ which implies ‘soft’ guesses. The softassign technique [90-92] is based on this choice; or (*ii*) $\mathscr{f}_{t^{(h)}}^{(i)} \in \{0,1\}$ which indicates single best guesses (*i.e.*, see solutions of Equation 2.34 in Section 2.22). Appendix $\boldsymbol{\mathcal{B}}$.1 presents the mathematical derivation of the maximum likelihood estimates of the $(\varphi_h, \mu_h, \Sigma_h)$ parameters. Appendix $\boldsymbol{\mathcal{B}}$.2 and appendix $\boldsymbol{\mathcal{B}}$.3 give details about the convergence property of the $\mathcal{EM}$ algorithm and the combined $\mathcal{GMM}$ and $\mathcal{EM}$ formalism that led to Equations $(2.82) - (2.85)$, respectively.

2.4.3 The minimization of the log-posterior cost function via the $\mathcal{EM}$ algorithm

It is mathematically convenient to assume that the target model points are the ones that undergo the non-linear transformation $\mathcal{F}$. Equation (2.32) of Section 2.2.2 can then be written

$$P(\boldsymbol{\mathcal{M}}; \boldsymbol{\mathcal{S}}, \theta, \varphi, \mu, \Sigma) = \prod_{i=1}^{m} P\left(q^{(i)}; \varphi, \mu, \Sigma\right) =$$

$$= \prod_{i=1}^{m} \sum_{h=1}^{s} P\left(\mathcal{F}\left(t^{(h)}; \theta\right); \varphi\right)\ P\left(q^{(i)} \middle| \mathcal{F}\left(t^{(h)}; \theta\right); \mu, \Sigma\right)$$

$$= \prod_{i=1}^{m} \sum_{h=1}^{s} \varphi_h \frac{1}{\sqrt{(2\pi)^3|\Sigma_h|}} exp\left[-\frac{1}{2}\left(q^{(i)} - \mathcal{F}\left(t^{(h)}; \theta\right)\right)^T \Sigma_h^{-1} \left(q^{(i)} - \mathcal{F}\left(t^{(h)}; \theta\right)\right)\right] \qquad (2.89)$$

since the *transformed* target set points in Equation (2.89) serve as centres of Gaussian clusters and hence $\mu_h \equiv \mathcal{F}\left(t^{(h)}; \theta\right)$.

To address outliers in the fixed source model point set, a fictitious Gaussian cluster centre, $h = (s+1)$, can be introduced. Equation (2.89) then becomes

$$P(\boldsymbol{\mathcal{M}};\boldsymbol{\mathcal{S}},\theta,\varphi,\mu,\Sigma) =$$

$$= \prod_{i=1}^{m}\sum_{h=1}^{s+1}\varphi_h \frac{1}{\sqrt{(2\pi)^3|\Sigma_h|}} exp\left[-\frac{1}{2}\left(q^{(i)}-\mathcal{F}\left(t^{(h)};\theta\right)\right)^T \Sigma_h^{-1}\left(q^{(i)}-\mathcal{F}\left(t^{(h)};\theta\right)\right)\right] \quad (2.90).$$

Consider the posterior probability distribution of θ given $\boldsymbol{\mathcal{M}}$

$$P(\theta|\boldsymbol{\mathcal{M}},\boldsymbol{\mathcal{S}},\varphi,\mu,\Sigma\,) = \frac{P(\boldsymbol{\mathcal{M}}|\boldsymbol{\mathcal{S}},\theta,\varphi,\mu,\Sigma\,)P(\theta)}{P(\boldsymbol{\mathcal{M}})} \quad (2.91)$$

where the class prior density $P(\theta)$ is expressed by

$$P(\theta) = \frac{e^{-\lambda I(\theta)}}{\sum_{\theta_f} e^{-\lambda I(\theta_f)}} = \frac{e^{-\lambda I(\theta)}}{\mathcal{Z}(\lambda)} \quad (2.92).$$

The value of $e^{-\lambda I(\theta)}$ in Equation (2.92) represents the likelihood of having θ while $I(\theta)$ and λ have their usual meaning (see also Equation (2.46) of Section 2.2.5); $\mathcal{Z}(\lambda)$ is a partition normalization function. $P(\theta)$ corresponds to a normalized probability, *i.e.*, $0 \ll P(\theta) \ll 1$ and $\sum_{\theta_f} P\left(\theta_f\right) = 1$.

It can be proved (see Appendix $\boldsymbol{\mathcal{B}}$.4) that

$$\begin{aligned}
&\underset{\theta}{\operatorname{argmax}} P(\theta|\boldsymbol{\mathcal{M}},\boldsymbol{\mathcal{S}},\varphi,\mu,\Sigma\,) \\
&\cong \underset{\theta}{\operatorname{argmin}}\left[\sum_{i=1}^{m}\sum_{h=1}^{s+1}\mathscr{f}_{t^{(h)}}^{(i)}\frac{\left(q^{(i)}-\mathcal{F}\left(t^{(h)};\theta\right)\right)^T\Sigma_h^{-1}\left(q^{(i)}-\mathcal{F}\left(t^{(h)};\theta\right)\right)}{2} - \sum_{i=1}^{m}\sum_{h=1}^{s+1}\mathscr{f}_{t^{(h)}}^{(i)}\log\varphi_h\right. \\
&+\sum_{i=1}^{m}\sum_{h=1}^{s+1}\frac{3\mathscr{f}_{t^{(h)}}^{(i)}}{2}\log(2\pi)+\sum_{i=1}^{m}\sum_{h=1}^{s+1}\frac{\mathscr{f}_{t^{(h)}}^{(i)}}{2}\log|\Sigma_h|+\sum_{i=1}^{m}\sum_{h=1}^{s+1}\mathscr{f}_{t^{(h)}}^{(i)}\log\mathscr{f}_{t^{(h)}}^{(i)} \\
&\left.+\lambda I(\theta)\right] \qquad (2.93)
\end{aligned}$$

where $\forall\ (i,h)$: $\mathscr{f}_{t^{(h)}}^{(i)} \in [0,1]$, $\sum_{h=1}^{s+1}\mathscr{f}_{t^{(h)}}^{(i)} = 1$ for $1 \le i \le m$, and $0 < \sum_{i=1}^{m}\mathscr{f}_{t^{(h)}}^{(i)} < m$.

The term $\mathfrak{D}_M\left(q^{(i)}\right) = \sqrt{\left(q^{(i)} - \mathcal{F}(t^{(h)};\theta)\right)^T \Sigma_h^{-1}\left(q^{(i)} - \mathcal{F}(t^{(h)};\theta)\right)}$ of Equation (2.93) is the *Mahalanobis* distance, *i.e.*, the distance of $q^{(i)}$ from μ_h given Σ_h. The term $\mathfrak{B}(\mathcal{T}) = \sum_{i=1}^{m}\sum_{h=1}^{s+1} \mathscr{t}_{t^{(h)}}^{(i)} \log \mathscr{t}_{t^{(h)}}^{(i)}$ represents a measure of statistical uncertainty which makes sure that the $\mathscr{t}_{t^{(h)}}^{(i)}$ values of the matrix of posterior probabilities $\mathcal{T}$ are away from zero or one [93] (at the beginning and during the alternating $\boldsymbol{\mathcal{E}}-$ and $\boldsymbol{\mathcal{M}}-$step optimization). Note that now $\mathcal{T} \in \mathbb{R}^{(s+1)\times m}$. Only when the transformation starts to converge to an optimal solution (towards the end of the optimization) will the $\mathscr{t}_{t^{(h)}}^{(i)}$'s start acquiring binary values.

The update rule of the $\boldsymbol{\mathcal{E}}-$step which optimizes the $\mathscr{t}_{t^{(h)}}^{(i)}$'s is summarized now by

$$\mathscr{t}_{t^{(h)}}^{(i)} := \frac{\varphi_h \frac{1}{\sqrt{(2\pi)^3|\Sigma_h|}} exp\left[-\frac{1}{2}\left(q^{(i)} - \mathcal{F}\left(t^{(h)};\theta\right)\right)^T \Sigma_h^{-1}\left(q^{(i)} - \mathcal{F}\left(t^{(h)};\theta\right)\right)\right]}{\sum_{g=1}^{s+1}\varphi_g \frac{1}{\sqrt{(2\pi)^3\left|\Sigma_g\right|}} exp\left[-\frac{1}{2}\left(q^{(i)} - \mathcal{F}(t^{(g)};\theta)\right)^T \Sigma_g^{-1}\left(q^{(i)} - \mathcal{F}(t^{(g)};\theta)\right)\right]} \tag{2.94}$$

and is applied $\forall\, \mathscr{t}_{t^{(h)}}^{(i)} \in \mathcal{T}$. The (continuous-valued) matrix $\mathcal{T}$ corresponds initially to a *fuzzy* approximation of the (discrete-valued) correspondence matrix $\mathfrak{J}$ or $\left\{\mathfrak{j}_{(h)}^{(i)}\right\}$ which has a binary classification character. The energy function of Equation (2.93) is well behaved as $\mathcal{T} \to \mathfrak{J}$ owing to the continuous character of $\mathcal{T}$.

In the $\boldsymbol{\mathcal{M}}-$step Equation (2.93) is minimized *w.r.t* θ and (φ_h, Σ_h) using the computed from the $\boldsymbol{\mathcal{E}}-$step matrix $\mathcal{T}$, which is kept fixed in this step. As the μ_h's are not considered free parameters they are not optimized in the $\boldsymbol{\mathcal{M}}-$step. However, treating the (φ_h, Σ_h) 's as free parameters of the optimization can increase the number of local minima of Equation (2.93), *i.e.*, various non-rigid point-set transformations may become valid solutions given the ‘flexibility’ provided in the optimization by these additional parameters, especially in the presence of symmetry-breaking random noise.

Consider the following approximation

$$\frac{\mathfrak{D}_M^2\left(q^{(i)}\right)}{2} \approx \frac{1}{2}\frac{\left\|q^{(i)} - \mathcal{F}\left(t^{(h)};\theta\right)\right\|^2}{\sigma^2} = \frac{1}{2}\frac{\left\|q^{(i)} - \mathcal{F}\left(t^{(h)};\theta\right)\right\|^2}{T} \tag{2.95}$$

and that T, the temperature parameter, as defined in Equation (2.95) is subject to linear deterministic annealing [91, 92, 94-96]. As the magnitude of T becomes larger, the elements of $\left\{\mathscr{t}_{t^{(h)}}^{(i)}: 1 \leq i \leq m, 1 \leq h \leq s+1\right\}$ tend to take the $\frac{1}{s+1}$ value, which implies a global point matching process. As the magnitude of $T \rightarrow 0$, the set $\left\{\mathscr{t}_{t^{(h)}}^{(i)}: 1 \leq i \leq m, 1 \leq h \leq s\right\}$ acquires a binary character, *i.e.*, the $q^{(i)}$'s are assigned to the closest Gaussian clusters centred at $\mathcal{F}\left(t^{(h)}; \theta\right)$ which implies a local point matching process. The case for $h = s+1$ is reserved for the class of outliers in the source model; it is reasonable to choose a large constant value for the temperature parameter, *i.e.*, $T = T_0$, and let the fictitious μ_{s+1} be the centre of mass of $\left\{\mathcal{F}\left(t^{(1)}; \theta\right), \ldots, \mathcal{F}\left(t^{(s)}; \theta\right)\right\}$.

The other free parameter, φ_h, can be chosen specifically for non-rigid point set registration to be

$$\varphi_h = \frac{1}{m+1} \qquad (2.96)$$

$$1 \leq h \leq s.$$

Equation (2.96) summarizes the following two choices: (*i*) another fictitious Gaussian cluster centre, $i = (m+1)$, is introduced to address outliers in the moving target point set. Thus the matrix $\mathcal{T}$ becomes

$$\mathcal{T} = \begin{pmatrix} \mathscr{t}_{t^{(1)}}^{(1)} & \mathscr{t}_{t^{(1)}}^{(2)} & \cdots & \mathscr{t}_{t^{(1)}}^{(m)} & \mathscr{t}_{t^{(1)}}^{(m+1)} \\ \mathscr{t}_{t^{(2)}}^{(1)} & \mathscr{t}_{t^{(2)}}^{(2)} & \cdots & \mathscr{t}_{t^{(2)}}^{(m)} & \mathscr{t}_{t^{(2)}}^{(m+1)} \\ \vdots & \vdots & \cdots & \vdots & \vdots \\ \mathscr{t}_{t^{(s)}}^{(1)} & \mathscr{t}_{t^{(s)}}^{(2)} & \cdots & \mathscr{t}_{t^{(s)}}^{(m)} & \mathscr{t}_{t^{(s)}}^{(m+1)} \\ \mathscr{t}_{t^{(s+1)}}^{(1)} & \mathscr{t}_{t^{(s+1)}}^{(2)} & \cdots & \mathscr{t}_{t^{(s+1)}}^{(m)} & \mathscr{t}_{t^{(s+1)}}^{(m+1)} \end{pmatrix} \qquad s.t.$$

$$\mathscr{t}_{t^{(h)}}^{(i)} \in [0,1] \text{ for } 1 \leq i \leq m+1 \text{ and } 1 \leq h \leq s+1 \text{, except } \mathscr{t}_{t^{(s+1)}}^{(m+1)} \equiv 0$$

$$\sum_{h=1}^{s+1} \mathscr{t}_{t^{(h)}}^{(i)} = 1 \quad \forall\, i \in \{1,2,\ldots,m\}.$$

The cluster of target model outliers is centred at the fictitious q_{m+1} which corresponds to the centre of mass of $\{q_1, \ldots, q_m\}$, and for $T = T_0$; and (*ii*) from Equation (2.83) of the $\boldsymbol{\mathcal{M}}-$step

$$\sum_{i=1}^{m+1} \mathscr{t}_{t^{(h)}}^{(i)} = 1 \Leftrightarrow \varphi_h = \frac{1}{m+1} \quad \forall\, h \in \{1,2,\dots,s\}.$$

The row normalization of the affinity matrix $\mathcal{T}$ in (*ii*) is particularly useful for non-rigid point matching that involves outliers in the target model or points of the target model for which no reliable and most probable correspondences can be established with points of the source from the onset of registration.

An example is those points of the target that have true correspondences in the source but cannot immediately, right from the onset of registration, be assigned to them with a large probability in the $\boldsymbol{\mathcal{E}}-$ step (*i.e.*, in the registration between the original full source and an occluded, extensively deformed and noisy target surface). Due to the continuous classification character of $\mathcal{T}$ and the row summation constraint, they may initially be considered more as outliers (by some probability value) in the $\boldsymbol{\mathcal{E}}-$ step of the algorithm and gradually converge to their true correspondences in the source as the registration progresses and the deformation is recovered.

In the absence of row normalization, as specifically defined in this section, such points (or in general any outliers of the target) will be forced by the column normalization of $\mathcal{T}$ to erroneous correspondences with the source (including potential outliers of the source in the absence of column normalization) during the optimization. This leads to the calculation of an erroneous transformation function (derived exclusively from the established correspondence pairs, see Equation (2.100) later on in the text) that not only reinforces the mismatched correspondences but also causes the creation of new erroneous correspondences (which in turn are further reinforced in the next cycle of iterations of the $\boldsymbol{\mathcal{E}}-$ and $\boldsymbol{\mathcal{M}}-$ step$s$).

Similar arguments can be raised for the column normalization of the affinity matrix $\mathcal{T}$ which has been extended to explicitly treat outliers in the source; it does not favour the assignment of outliers of the source to target points (including potential outliers of the target in the absence of row normalization). The case where the source points have true correspondences in the target but these cannot be readily determined in the $\boldsymbol{\mathcal{E}}-$ step at the beginning of registration (due to extreme deformation of the target surface) is addressed by the column summation constraint and the continuous classification character of $\mathcal{T}$.

The common overlap between the original full source and an occluded and deformed target surface or an occluded, deformed and noisy target surface cannot always be determined precisely, *i.e.*, the extracted surface from the original full source may contain points that have no true correspondences in the extracted target surface (which can either be identical to the original occluded target model or be a subset of it) and cannot be rejected as outliers. This depends upon the distance threshold that was imposed in the extraction of the common overlap combined with the extent of deformation in the occluded target and the character of the registering surface itself (which is quite smooth for prostate). Only when the extracted source surface consists of points with true correspondences in the target and points that can be qualified as outliers can the $\mathcal{EM} + \mathcal{F}_{TPS}$ methodology be used for full-model-to-occluded model non-rigid registration.

The row normalization of $\mathcal{T}$ is another constraint of the algorithm that must be satisfied $\forall\, h \in \{1,2,\dots,s\}$. Consider the example of Figure 2.3. It shows the converged form of $\mathcal{T}$ which is the binary (from linear-assignment) correspondence matrix $\mathfrak{J}$.

$\boldsymbol{\mathfrak{i}}_{(h)}^{(i)} \in \{\mathbf{0},\mathbf{1}\}$	$\boldsymbol{q_1}$	$\boldsymbol{q_2}$	$\boldsymbol{q_3}$	$\cdots$	$\boldsymbol{q_m}$	**Centre of target outliers: $\boldsymbol{q_{m+1}}$**
$\boldsymbol{t_1}$	**1**	**0**	**0**	**0**	**0**	**0**
$\boldsymbol{t_2}$	**0**	**0**	**0**	**0**	**0**	**1**
$\boldsymbol{t_3}$	**0**	**0**	**1**	**0**	**0**	**0**
$\vdots$	$\vdots$	$\vdots$	$\vdots$	$\vdots$	$\vdots$	$\vdots$
$\boldsymbol{t_s}$	**0**	**0**	**0**	**0**	**0**	**1**
Centre of source outliers: $\boldsymbol{\mu_{s+1}}$	**0**	**1**	**0**	$\cdots$	**1**	**0**

Figure 2.3: The binary correspondence matrix $\mathfrak{J}$. Taken from Ref. [57] and modified accordingly for the purposes of this presentation.

The ‘fuzzy correspondence’ matrix is defined by

$$\text{Ƒ} = \begin{pmatrix} \text{ƒ}_{t^{(1)}}^{(1)} & \cdots & \text{ƒ}_{t^{(1)}}^{(m)} \\ \vdots & \cdots & \vdots \\ \text{ƒ}_{t^{(s)}}^{(1)} & \cdots & \text{ƒ}_{t^{(s)}}^{(m)} \end{pmatrix}.$$

The row and column summation constraints guarantee (*i*) a one-to-one correspondence between transformed target points and fixed source points; and (*ii*) the identification of outliers in the source and target models upon convergence of F (shown in blue in Figure 2.3), following a graduated assignment scheme.

The row normalization of $\mathcal{T}$ plays a major role in the $\boldsymbol{\mathcal{E}}-$ step as it quantifies the presence of outliers in the set of target points as well as augments the overall process of correct point matching. It has however a minor impact on the optimization of Equation (2.93) of the $\boldsymbol{\mathcal{M}}-$ step. In general the values of $\varphi_h \; \forall \, h \in \{1,2,\dots,s\}$ are optimized in the $\boldsymbol{\mathcal{M}}-$ step based on Equation (2.83) where the value of $\sum_{i=1}^{m+1} \mathscr{t}_{t^{(h)}}^{(i)}$ arising from each of the s rows of T is indirectly dictated (within the context of non-rigid point set registration) by the normalization of the $\mathscr{t}_{t^{(h)}}^{(i)}$'s of each of the m columns of T in the $\boldsymbol{\mathcal{E}}-$ step.

The energy cost function is given by (see Appendix $\boldsymbol{\mathcal{B}}$.5)

$$\begin{aligned}
\mathcal{E}_2(\mathcal{T},\theta) = {} & \sum_{i=1}^{m}\sum_{h=1}^{s} \mathscr{t}_{t^{(h)}}^{(i)} \frac{\left\| q^{(i)} - \mathcal{F}\left(t^{(h)};\theta\right)\right\|^2}{2} + \sum_{h=1}^{s} \mathscr{t}_{t^{(h)}}^{(m+1)} \frac{\left\| q_{m+1} - \mathcal{F}\left(t^{(h)};\theta\right)\right\|^2}{2} \\
& + \sum_{i=1}^{m} \mathscr{t}_{t^{(s+1)}}^{(i)} \frac{\left\| q^{(i)} - \mu_{s+1}\right\|^2}{2} + T\sum_{i=1}^{m}\sum_{h=1}^{s} \frac{3}{2}\mathscr{t}_{t^{(h)}}^{(i)} \log T + T\sum_{h=1}^{s}\frac{3}{2}\mathscr{t}_{t^{(h)}}^{(m+1)} \log T_0 \\
& + T\sum_{i=1}^{m}\frac{3}{2}\mathscr{t}_{t^{(s+1)}}^{(i)} \log T_0 \\
& + T\left(\sum_{i=1}^{m}\sum_{h=1}^{s} \mathscr{t}_{t^{(h)}}^{(i)} \log \mathscr{t}_{t^{(h)}}^{(i)} + \sum_{h=1}^{s} \mathscr{t}_{t^{(h)}}^{(m+1)} \log \mathscr{t}_{t^{(h)}}^{(m+1)} + \sum_{i=1}^{m} \mathscr{t}_{t^{(s+1)}}^{(i)} \log \mathscr{t}_{t^{(s+1)}}^{(i)}\right) \\
& + \lambda T I(\theta) \qquad\qquad (2.97).
\end{aligned}$$

The term of Equation (2.97)

$$\begin{aligned}
T\mathfrak{B}(\mathcal{T}) = T\sum_{i=1}^{m+1}\sum_{h=1}^{s+1} \mathscr{t}_{t^{(h)}}^{(i)} \log \mathscr{t}_{t^{(h)}}^{(i)} = \\
= T\left(\sum_{i=1}^{m}\sum_{h=1}^{s} \mathscr{t}_{t^{(h)}}^{(i)} \log \mathscr{t}_{t^{(h)}}^{(i)} + \sum_{h=1}^{s} \mathscr{t}_{t^{(h)}}^{(m+1)} \log \mathscr{t}_{t^{(h)}}^{(m+1)} + \sum_{i=1}^{m} \mathscr{t}_{t^{(s+1)}}^{(i)} \log \mathscr{t}_{t^{(s+1)}}^{(i)}\right)
\end{aligned}$$

represents now the fuzziness of $\mathcal{T}$.

Let's assume $T = T_1$. The benefit matrix $\mathcal{T}$ is evaluated in the $\boldsymbol{\mathcal{E}}-$ step and is used as input in the $\boldsymbol{\mathcal{M}}-$ step where $\underset{\theta}{\operatorname{argmin}} \mathcal{E}_2(\mathcal{T},\theta)$. The computed transformation is then applied to the set of target points leading to an updated target model. The $\boldsymbol{\mathcal{E}}-$ and $\boldsymbol{\mathcal{M}}-$ steps will be repeated until pre-specified stopping criteria are satisfied. The target model is transformed during the optimization of $(\mathcal{T},\theta)$ for a given temperature T. Hence this algorithm produces a distinct set of $(\mathcal{T},\theta)$ parameters upon convergence for $T=T_1$ as a result of a sequential alternating optimization process. The converged θ parameters at T_1 can be applied to the original target model to produce the registered target surface in one step (as the θ parameters produced by the $\mathcal{GMM}+\mathcal{F}_{TPS}$ and $\mathcal{KC}+\mathcal{F}_{TPS}$ algorithms at convergence were applied onto the original source model to generate the registered source surface at a given λ). The next round of optimizations in the $\boldsymbol{\mathcal{E}}-$ and $\boldsymbol{\mathcal{M}}-$ steps take place for $T_2(<T_1)$, according to a deterministic *linear* annealing schedule, and so forth. As the non-rigid transformation $\mathcal{F}$ is regularized by λT in Equation (2.97), λ can now be considered a constant.

Summarizing, the $\boldsymbol{\mathcal{EM}}$ algorithm, embedded within a deterministic annealing mechanism, optimizes the following two steps:

$\{\boldsymbol{\mathcal{E}}-$ step$\}$:

The optimization of $\mathcal{T}$ is initiated by (*i*) the column normalization of $\mathcal{T}$ $\left(\sum_{h=1}^{s+1}\mathscr{m}_{t^{(h)}}^{(i)}=1\right)$

$$\mathscr{m}_{t^{(h)}}^{(i)}:=\frac{\frac{1}{\sqrt{(2\pi T)^3}}exp\left[-\frac{1}{2T}\left(q^{(i)}-\mathcal{F}\left(t^{(h)};\theta\right)\right)^T\left(q^{(i)}-\mathcal{F}\left(t^{(h)};\theta\right)\right)\right]}{\sum_{g=1}^{s+1}\frac{1}{\sqrt{(2\pi T)^3}}exp\left[-\frac{1}{2T}\left(q^{(i)}-\mathcal{F}(t^{(g)};\theta)\right)^T\left(q^{(i)}-\mathcal{F}(t^{(g)};\theta)\right)\right]} \tag{2.98}$$

$$\left\{\mathscr{m}_{t^{(h)}}^{(i)}:1\le i\le m,1\le h\le s+1\right\}$$

where $T=T_0$ and $\mu_h=\mu_{s+1}$ for $h=s+1$; (*ii*) followed by the row normalization of $\mathcal{T}$ $\left(\sum_{i=1}^{m+1}\mathscr{m}_{t^{(h)}}^{(i)}=1\right)$

$$\mathscr{m}_{t^{(h)}}^{(i)}:=\frac{\frac{1}{\sqrt{(2\pi T)^3}}exp\left[-\frac{1}{2T}\left(q^{(i)}-\mathcal{F}\left(t^{(h)};\theta\right)\right)^T\left(q^{(i)}-\mathcal{F}\left(t^{(h)};\theta\right)\right)\right]}{\sum_{g=1}^{m+1}\frac{1}{\sqrt{(2\pi T)^3}}exp\left[-\frac{1}{2T}\left(q^{(g)}-\mathcal{F}(t^{(h)};\theta)\right)^T\left(q^{(g)}-\mathcal{F}(t^{(h)};\theta)\right)\right]} \tag{2.99}$$

$$\left\{\mathscr{m}_{t^{(h)}}^{(i)}:1\le i\le m+1,1\le h\le s\right\}$$

where $T = T_0$ and $q^{(i)} \equiv q_{m+1}$ for $i = m + 1$. Equations (2.98) and (2.99) were derived assuming that φ_g is constant $\forall\, g \in \{1, \dots, s + 1\}$ and $\forall\, g \in \{1, \dots, m + 1\}$, respectively. The benefit matrix $\mathcal{T}$ will be affected by the output from the optimization of the non-rigid transformation function of the $\boldsymbol{\mathcal{M}} -$ step.

$\{\boldsymbol{\mathcal{M}} -$ step$\}$:

The process of $\min_\theta \mathcal{E}_2(\mathcal{T}, \theta)$ comes into play and the following least-squares problem is solved for the *correspondence pairs* established in the $\boldsymbol{\mathcal{E}} -$ step

$$\min_\theta \mathcal{E}_2(\mathcal{T}, \theta) = \min_\theta \mathcal{E}_3(\theta) =$$

$$= \min_\theta \left(\sum_{i=1}^{m} \sum_{h=1}^{s} \mathcal{t}_{t^{(h)}}^{(i)} \frac{\left\| q^{(i)} - \mathcal{F}\left(t^{(h)}; \theta\right) \right\|^2}{2} + \lambda TI(\theta) \right) \tag{2.100}$$

$$\approx \min_\theta \left(\sum_{h=1}^{s} \frac{\left\| \mathcal{w}_h - \mathcal{F}\left(t^{(h)}; \theta\right) \right\|^2}{2} + \lambda TI(\theta) \right) \tag{2.101}$$

where $\forall\, h \in \{1, \dots, s\}$: $\mathcal{w}_h = \sum_{i=1}^{m} \mathcal{t}_{t^{(h)}}^{(i)}\, q^{(i)}$. The sole purpose of $\mathcal{w}_h$ is to simplify the mathematical problem.

There are two types of non-rigid registration that are being considered in this study: (*i*) registration between full source and full target models where $s \cong m$ [the maximum number of *correspondence pairs* is equal to $min(s, m)$]; and (*ii*) registration between full source and occluded target models (the total number of points in the common overlap will define the maximum number of *correspondence pairs*).

As discussed earlier the effective number of *correspondence pairs* may not always be the maximum possible. It can be reduced by spurious points in the target or in the source model. These points will have no impact on the calculation of $\mathcal{F}$ during $\min_\theta \mathcal{E}_3(\theta)$ in the present implementation. Only the linear motion of such target points will be affected (determined by the computed $\mathcal{F}$) which won't disqualify them from continuing to be spurious points of the moving target model.

2.4.4 Integration of the TPS deformation model in the $\mathcal{GMM}/\mathcal{EM}$ algorithm

The objective of the $\boldsymbol{\mathcal{M}}-$ step is to minimize $\mathcal{E}_3$ *w.r.t* θ

$$\mathcal{E}_3(\theta)=\sum_{h=1}^{s}\frac{\left\|w_h-\mathcal{F}\left(t^{(h)};\theta\right)\right\|^2}{2}+\lambda T\mathrm{trace}(\psi^T\mathcal{N}^T\Phi\mathcal{N}\psi) \qquad (2.102)$$

for any given temperature T during the linear annealing schedule [$\mathcal{N}$ here is specifically defined as the left null space of $[1|\boldsymbol{\mathcal{S}}_0]$ where $\boldsymbol{\mathcal{S}}_0$ refers to the original target model; it is assumed that $\boldsymbol{\mathcal{S}}_0\equiv$ control points, see also Equation (2.105) below and text for details] or to minimize $\mathcal{E}_4$ *w.r.t* θ

$$\mathcal{E}_4(\theta)=\sum_{h=1}^{s}\frac{\left\|w_h-\mathcal{F}\left(t^{(h)};\theta\right)\right\|^2}{2}+\lambda\mathrm{trace}(\psi^T\mathcal{N}^T\Phi\mathcal{N}\psi) \qquad (2.103)$$

as the reduction of temperature T, which controls the transition from rigid to non-rigid registration, has an impact on the benefit matrix $\mathcal{T}$ and hence must be associated with the $\boldsymbol{\mathcal{E}}-$ step.

Based on Equation (2.27) of Section 2.1.3

$$\mathcal{F}(\boldsymbol{\mathcal{S}}_0)=\boldsymbol{\mathcal{S}}=[1|\boldsymbol{\mathcal{S}}_0]E^T+U\mathcal{N}\psi \qquad (2.104)$$

$$=[1|\boldsymbol{\mathcal{S}}_0]E^T+\Phi\mathcal{N}\psi \qquad (2.105)$$

where $\boldsymbol{\mathcal{S}}$ is the transformed target model, Φ is the TPS kernel matrix, U is the basis matrix, ψ relates to the non-affine subspace of the TPS warping, and E^T represents the affine transformation. Equation (2.105) was produced by selecting $\boldsymbol{\mathcal{S}}_0$ to be the set of control points which means that $U\equiv\Phi\in\mathbb{R}^{s\times s}$ and $\mathcal{N}$ is the left null space of $[1|\boldsymbol{\mathcal{S}}_0]$ (see also Appendix $\boldsymbol{\mathcal{B}}$.6). This choice is applicable to non-rigid point set registration between a full source model and a full target model where $s\cong m$.

Let the set of w_h' s $\forall\ h\in\{1,\dots,s\}$ be represented by $\mathbb{W}\in\mathbb{R}^{s\times 3}$

$$\mathbb{W}=\begin{pmatrix}w_1\\ \vdots\\ w_s\end{pmatrix}=\begin{pmatrix}w_x^{(1)} & w_y^{(1)} & w_z^{(1)}\\ \vdots & \vdots & \vdots\\ w_x^{(s)} & w_y^{(s)} & w_z^{(s)}\end{pmatrix}$$

$$= \begin{pmatrix} \mathscr{f}_{t^{(1)}}^{(1)} & \cdots & \mathscr{f}_{t^{(1)}}^{(m)} \\ \vdots & \cdots & \vdots \\ \mathscr{f}_{t^{(s)}}^{(1)} & \cdots & \mathscr{f}_{t^{(s)}}^{(m)} \end{pmatrix} \begin{pmatrix} q_x^{(1)} & q_y^{(1)} & q_z^{(1)} \\ \vdots & \vdots & \vdots \\ q_x^{(m)} & q_y^{(m)} & q_z^{(m)} \end{pmatrix}$$

$$= \text{Ꞙ}\boldsymbol{\mathcal{M}_0} \qquad (2.106)$$

where $\mathscr{w}_{(x/y/z)}^{(h)} = \sum_{i=1}^{m} \mathscr{f}_{t^{(h)}}^{(i)} q_{(x/y/z)}^{(i)}$, Ꞙ is the correspondence matrix and $\boldsymbol{\mathcal{M}_0}$ refers to the original source model.

The objective cost function of Equation (2.103) can be rewritten into (see Appendix $\boldsymbol{\mathcal{B}}$.6)

$$\mathcal{E}_5(E^T, \psi) = 2\mathcal{E}_4(E^T, \psi) =$$

$$= \|\text{Ꞙ}\boldsymbol{\mathcal{M}_0} - \boldsymbol{\mathcal{Q}_1}\boldsymbol{\mathcal{R}_1}E^T - \Phi\mathcal{N}\psi\|_F^2 + 2\lambda\text{trace}(\psi^T\mathcal{N}^T\Phi\mathcal{N}\psi)$$

$$= \|\Phi\mathcal{N}\psi - \text{Ꞙ}\boldsymbol{\mathcal{M}_0}\|_F^2 + \|\boldsymbol{\mathcal{Q}_1}\boldsymbol{\mathcal{R}_1}E^T\|_F^2 + 2\text{trace}[(\Phi\mathcal{N}\psi - \text{Ꞙ}\boldsymbol{\mathcal{M}_0})(\boldsymbol{\mathcal{Q}_1}\boldsymbol{\mathcal{R}_1}E^T)^{\boldsymbol{T}}]$$
$$+ 2\lambda\text{trace}(\psi^T\mathcal{N}^T\Phi\mathcal{N}\psi) \qquad (2.107).$$

Also,

$$\min_{\psi} \mathcal{E}_5(E^T, \psi) \Rightarrow \psi = \mathcal{N}^T(\Phi - 2\lambda I)^{-1}\text{Ꞙ}\boldsymbol{\mathcal{M}_0} \qquad (2.108)$$

$$\min_{E^T} \mathcal{E}_5(E^T, \psi) \Rightarrow E^T = \boldsymbol{\mathcal{R}}_1^{-1}\boldsymbol{\mathcal{Q}}_1^T(\text{Ꞙ}\boldsymbol{\mathcal{M}_0} - \Phi\mathcal{N}\psi) \qquad (2.109)$$

where $\boldsymbol{\mathcal{Q}_1}$ and $\boldsymbol{\mathcal{R}_1}$ arise from the full rank $\boldsymbol{\mathcal{QR}}$ decomposition of $[1|\boldsymbol{\mathcal{S}}_0]$ according to

$$[1|\boldsymbol{\mathcal{S}}_0] = \boldsymbol{\mathcal{QR}} = [\boldsymbol{\mathcal{Q}_1}|\mathcal{N}]\begin{bmatrix}\boldsymbol{\mathcal{R}_1}\\ \mathbf{0}\end{bmatrix} = \boldsymbol{\mathcal{Q}_1}\boldsymbol{\mathcal{R}_1} \qquad (2.110).$$

Once the correspondences are established in the $\boldsymbol{\mathcal{E}} -$ step, the least-squares cost function of Equation (2.107) is minimized *w.r.t.* ψ based on Equation (2.108) and then *w.r.t.* E^T based on Equation (2.109) for a given temperature. The transforming target model is then updated and this alternating process is repeated until convergence. The same joint optimization over the correspondence matrix Ꞙ and transformation parameters (E^T, ψ) takes place again for a lower temperature, starting from the last updated target model, following a predefined linear deterministic annealing mechanism, and so forth.

To account for the possibility of choosing a set of control points from $\boldsymbol{\mathcal{S}}_0$, the objective cost function of Equation (2.103) can be rewritten for $U \neq \Phi'$ into (see Appendix $\boldsymbol{\mathcal{B}}$.7)

$$\mathcal{E}_6(E'^T, \psi') = \|\text{Ғ}\boldsymbol{\mathcal{M}}_{\mathbf{0}} - \boldsymbol{\mathcal{Q}}_{\mathbf{1}}\boldsymbol{\mathcal{R}}_{\mathbf{1}}E'^T - U\mathcal{N}'\psi'\|_F^2 + 2\lambda\mathrm{trace}(\psi'^T\mathcal{N}'^T\Phi'\mathcal{N}'\psi') =$$

$$= \|U\mathcal{N}'\psi' - \text{Ғ}\boldsymbol{\mathcal{M}}_{\mathbf{0}}\|_F^2 + \|\boldsymbol{\mathcal{Q}}_{\mathbf{1}}\boldsymbol{\mathcal{R}}_{\mathbf{1}}E'^T\|_F^2 + 2\mathrm{trace}[(U\mathcal{N}'\psi' - \text{Ғ}\boldsymbol{\mathcal{M}}_{\mathbf{0}})(\boldsymbol{\mathcal{Q}}_{\mathbf{1}}\boldsymbol{\mathcal{R}}_{\mathbf{1}}E'^T)^{\boldsymbol{T}}]$$
$$+ 2\lambda\mathrm{trace}(\psi'^T\mathcal{N}'^T\Phi'\mathcal{N}'\psi') \qquad (2.111)$$

where $E'^T \in \mathbb{R}^{4\times3}$ represents the affine transformation, $U \in \mathbb{R}^{s\times n}$ is the basis matrix, $\Phi' \in \mathbb{R}^{n\times n}$ is the TPS kernel matrix, $\boldsymbol{\mathcal{Q}}_{\mathbf{1}}$ and $\boldsymbol{\mathcal{R}}_{\mathbf{1}}$ arise from the full rank $\boldsymbol{\mathcal{QR}}$ decomposition of $[1|\boldsymbol{\mathcal{S}}_0]$ according to Equation (2.110), $\psi' \in \mathbb{R}^{(n-4)\times3}$ relates to the non-affine subspace of the TPS warping, $\mathcal{N}' \in \mathbb{R}^{n\times(n-4)}$ represents the left null space of $[1|\boldsymbol{\mathcal{P}}_0] \in \mathbb{R}^{n\times4}$ and $\boldsymbol{\mathcal{P}}_0 = \{P_1, \dots, P_n\}$ corresponds to the set of the original target control points.

Also,

$$\min_{\psi'} \mathcal{E}_6(E'^T, \psi') \Rightarrow \psi' = \boldsymbol{\mathcal{U}}^{\mathbf{-1}}\mathcal{N}'^T U^T \text{Ғ}\boldsymbol{\mathcal{M}}_{\mathbf{0}} \qquad (2.112)$$

where $\boldsymbol{\mathcal{U}} = [\mathcal{N}'^T U^T U\mathcal{N}' - 2\lambda\mathcal{N}'^T\Phi'\mathcal{N}']$ and

$\min_{E'^T} \mathcal{E}_6(E'^T, \psi') \Rightarrow E'^T = \boldsymbol{\mathcal{R}}_1^{-1}\boldsymbol{\mathcal{Q}}_1^T(\text{Ғ}\boldsymbol{\mathcal{M}}_{\mathbf{0}} - U\mathcal{N}'\psi')$ (2.113).

2.4.5 Modifications

The available C++ algorithm [68] was rewritten using the output from the mathematical derivations of Sections 2.4.3 and 2.4.4. As the perturbation from spurious points in the target or in the source model was not accounted for in the codes, Equations (2.98) and (2.99) of Section 2.4.3 were implemented for an extended affinity matrix $\mathcal{T}$ (see Figure 2.3). This modification is necessary for the non-rigid point set registration between a full source model and an occluded and extensively deformed target surface, and other cases, as described in Section 2.4.3.

The energy cost function of Equation (2.107) was derived by selecting the original target model to be the set of control points (*i.e.*, $U \equiv \Phi$) which affords higher accuracy of registration. Equation (2.111) is produced by selecting the set of control points to be a subset of the original target model (*i.e.*, $U \neq \Phi'$). While the $\mathcal{GMM}/\mathcal{EM}$ formalism as presented in this study is consistent with relevant machine-learning concepts and specifically the work published in Ref. [57], there is discrepancy between Equations (15), (16) and (17) of Ref. [57] and the results of this work.

One way to perform non-rigid point set registration between a full source model $\boldsymbol{\mathcal{M}}_{\mathbf{0}}$ and an occluded target model $\boldsymbol{\mathcal{S}}_0$ using the modified algorithm may be by transforming $\boldsymbol{\mathcal{S}}_0$ onto $\boldsymbol{\mathcal{M}}_{\mathbf{0}}$ where $\boldsymbol{\mathcal{S}}_0 \equiv \text{control points}$. The reliability of registration depends upon the quality of the correspondence matrix Ғ which is constructed at the $\boldsymbol{\mathcal{E}}-$ step. The matrix Ғ is of good quality when the true correspondences are only identified and the remainder from $\boldsymbol{\mathcal{M}}_{\mathbf{0}}$ is treated as outliers of the source. Considering the morphology of the prostate surface, this option must be rejected.

A second approach is to register $\boldsymbol{\mathcal{M}}_{\mathbf{0}}$ onto $\boldsymbol{\mathcal{S}}_0$. By imposing tight non-rigid registration conditions, all points of the source with valid correspondences in the target can - theoretically - be discriminated against the remainder (which is treated as outliers of the source) at the end of the annealing process. By using this set of source points as control points of the registration and applying the computed $\mathcal{F}$ onto $\boldsymbol{\mathcal{M}}_{\mathbf{0}}$ the remainder of the full source can be transformed accordingly. Determining this set of source control points is however not possible in our calculations. This way is also not promising considering the smooth topology of the prostate surfaces.

Another approach is to first obtain the one-on-one nearest-neighbour correspondences between $\boldsymbol{\mathcal{M}}_{\mathbf{0}}$ and $\boldsymbol{\mathcal{S}}_0$ by setting a maximum distance threshold as the upper limit of all correspondences, as Figure 2.4 shows. The two point sets must be in approximate registration before the non-rigid registration process of Figure 2.4 is initiated and the initial correspondences must be produced from the closest point pairs (by imposing a low value for the maximum distance threshold).

The output from ‘establishing nearest neighbour correspondences’ in Figure 2.4 consists of the extracted source model point set $\text{corr}(\boldsymbol{\mathcal{M}})$ and the extracted target model point set $\text{corr}(\boldsymbol{\mathcal{S}})$. The $\text{corr}(\boldsymbol{\mathcal{M}})$ dataset is aligned onto $\text{corr}(\boldsymbol{\mathcal{S}})$ based on the modified $\mathcal{GMM}/\mathcal{EM} + \mathcal{F}_{TPS}$ registration algorithm where for the set of control points $\boldsymbol{\mathcal{C}}$ it holds that $\boldsymbol{\mathcal{C}} = \text{corr}(\boldsymbol{\mathcal{M}})$. The initial value for temperature, T_0, of the deterministic annealing mechanism must be so large as the largest squared distance that can be computed from all point-pair combinations between $\text{corr}(\boldsymbol{\mathcal{M}})$ and $\text{corr}(\boldsymbol{\mathcal{S}})$. In doing so all possible correspondences between the two datasets become equally probable in the $\boldsymbol{\mathcal{E}}-$step. The correspondence matrix Ғ is then characterized by a high degree of fuzziness.

In the $\boldsymbol{\mathcal{M}} -$ step, the energy cost function of Equation (2.107) is minimized *w.r.t* θ given the estimated F in the $\boldsymbol{\mathcal{E}} -$ step according to Equations (2.108) and (2.109). The $\Phi(= U)$ and $\mathcal{N}$ matrices, which are also required in the calculations, are estimated. The dataset $\mathrm{corr}(\boldsymbol{\mathcal{M}})$ is updated using the optimized TPS and affine parameters θ. The final set of optimized parameters θ at T_0 is obtained after a series of alternating $\boldsymbol{\mathcal{E}} -$ and $\boldsymbol{\mathcal{M}} -$ step optimizations.

The temperature is then reduced (by a fixed annealing rate) and the same process is repeated for the already transformed dataset $\mathrm{corr}(\boldsymbol{\mathcal{M}})$. As the temperature is gradually reduced the correspondences are further fine-tuned recovering the local structures, as is expected from Equations (2.98) and (2.99).

The optimized TPS and affine parameters θ obtained at the end of the annealing schedule will then be used to calculate the non-rigid transformation $\mathcal{F}$ that will be applied to $\boldsymbol{\mathcal{M}}$. The U matrix for the full model $\boldsymbol{\mathcal{M}}$ is computed taking $\mathrm{corr}(\boldsymbol{\mathcal{M}})$ to be the set of control points of $\boldsymbol{\mathcal{M}}$. The output from this process overwrites the moving model, namely, $\boldsymbol{\mathcal{M}} \coloneqq \mathcal{F}(\boldsymbol{\mathcal{M}}; \boldsymbol{\theta})$, and the overall process is repeated until a stopping criterion is satisfied. An increased number of correspondences is expected due to the gradual non-rigid deformation of the moving model. This approach can lead to reliable non-rigid registration results between full models and occluded surfaces only if the extracted source surface consists of points with true correspondences in the extracted target model (plus possible outliers), hence it is worthwhile further exploiting it.

Modified Algorithm.

Input: The original full source model set $\mathcal{M}_0$, the original occluded (and deformed and noisy) target model set $\mathcal{S}_0$ and the non-rigid parameterized TPS transformation model.

Output: The moving model $\mathcal{M}$ registered onto the target scene $\mathcal{S}_0$.

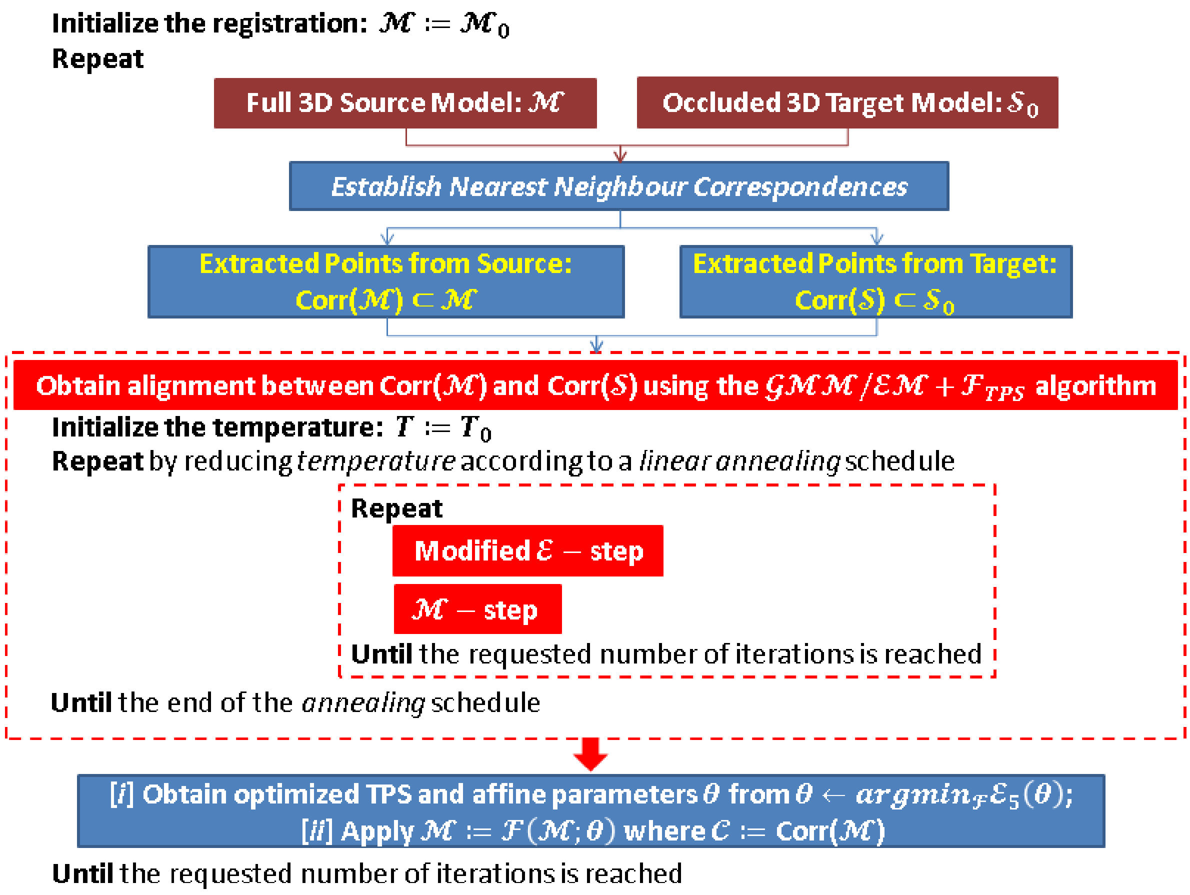

Figure 2.4: Modifications of the $\mathcal{GMM}/\mathcal{EM} + \mathcal{F}_{TPS}$ learning algorithm for full-model-to-occluded-surface non-rigid registration.

2.5 Summary

The *state-of-the-art* registration algorithms proposed by (*i*) Jian and Vemuri [53, 54]; (*ii*) Tsin and Kanade [55]; and (*iii*) Chui and Rangarajan [57] were formulated exclusively for non-rigid registration between “complete” general surfaces ($2D$ or $3D$). These techniques are subject to the condition that the registration pair datasets must not deviate significantly in number of points. In this work the algorithms are modified to account for non-rigid registration between $3D$ full *prostate* surfaces and occluded ones. A mechanism for producing valid initial correspondences between them is designed and invoked as the initial stage before the registration process is initiated using all three types of algorithms.

For (i) and (ii) the emphasis is placed on designing and implementing a suitable process for achieving reliable final correspondences between the transformed full source and the occluded target. It is designed having in mind the multiply-linked character of the associated (globally defined) objective cost functions. The approach of performing non-rigid registration between the extracted datasets from the full source and occluded target is tested. It is because of the multiply-linked nature of the relevant energy functions that the overall correspondence error can be considerably reduced during the non-rigid registration of the extracted source and target point datasets (which in turn is based on the original algorithmic formulation of the non-rigid registration models of (i) and (ii)). The prostate surfaces can undergo a large variation in shape in the presence of important amounts of noise and outliers. To provide an accurate non-rigid registration scheme specifically for the smooth and (often extensively) perturbed prostate surfaces: (a) the complete set of extracted source points is chosen to serve as the set of control points in the non-rigid registration with the extracted target point dataset; and (b) the complete set of extracted source points (which is gradually increasing in size as the deformation is incrementally being recovered) is chosen to serve as control points for the calculation of the TPS deformation of the remainder of the registering full source model. As a consequence higher levels of registration accuracy between the full prostate source and the partial deformed view of it (which also bears the effects of additional perturbations) are achieved.

For (iii), aside from the proposed general methodology that is applied to (i) and (ii), which has been suitably adjusted, a series of algorithmic reformulations are performed. These are based on (a) the exact mathematical expressions that are derived in this work; and (b) implementations of relevant terms which were not part of the available algorithm [68] in their optimal form such as the mathematical expressions for the column and row normalization of an extended affinity matrix $\mathcal{T}$ as specifically derived in Section 2.4.3.

Chapter 3

Design of synthetic test prostate data and assessment of registration accuracy of selected non-rigid algorithms via computational experiments

3.1 Introduction

The sensitivity of the selected non-rigid algorithms, defined by registration accuracy, with respect to a series of perturbation effects must be measured. And for that purpose suitable synthetic prostate data were carefully designed to simulate a wide variety of available real medical imaging data.

The preparation of prostate synthetic data was guided by a large volume of real prostate data that were collected intraoperatively via the aid of the *da Vinci* Surgical System. Clinical cases of deformed prostate surfaces characterized by geometric features with high-frequency details (*i.e.*, a sharp creases) were observed. A number of other synthetic prostate surfaces were also constructed spanning unobserved but possible clinical scenarios. The familiar geometric structure of the prostate surface was maintained in all simulations.

A number of validation schemes for assessing the registration accuracy of the non-rigid algorithms were also developed and tested via an extensive series of computational experiments. The registration accuracy was determined by computing the $TREs$ using the approach of Section 1.4.2.

Sections 3.3-3.6 refer to registration between *full* $3D$ models while 3.7 and 3.8 to *full*-model-to-*partial*-model registration. The computational registration experiments were conducted after an optimal initial manual alignment between the source and the target model (see Section 3.2). As was mentioned in Chapter 2, no prior point-to-point correspondences are assumed between them. Also, the identification of the final correspondences between the registering source and the target arises from an optimization process (as implemented in the registration algorithms), which is initiated by an approximate manual alignment between the datasets. The more "unrealistic" the initial alignment is the more deteriorated the non-rigid registration accuracy will be computed (*i.e.*, the estimated final correspondences would further deviate from the true ones). Even for an ideal initial alignment between the source and the target, it is not guaranteed that the examined algorithms will identify the exact final correspondences (which is a particularly challenging task considering the smoothness of the prostate surfaces and that no intrinsic features or extrinsic markers are used to guide the non-rigid registration (see Section 1.2.1). If the true correspondences could be identified by the examined algorithms that would imply $TRE = 0$.) By performing an optimal initial alignment before registration, we set the condition for establishing "the best warping accuracies that can be computed" using the given algorithms (or measuring their capacity to identify the true final correspondences). This output can be used as a benchmark against which the improvement of accuracy should be aimed at starting from less-optimal cases of initial alignment considering that the computational experiments of this work were conducted based on an extensive series of representative simulations of real medical imaging data.

The $3D$ prostate surface mesh of Figure 3.1 was used in these experiments[7]. The C++ computer algorithms that are presented in this Chapter were developed with the aid of the Visualization Toolkit (VTK, version 5.8.0. See Ref. [97]). The computational registration experiments were conducted at the Computer Science cluster of UCL (Sun N1 Grid Engine 6.1. See Ref. [98]) by submitting batch jobs.

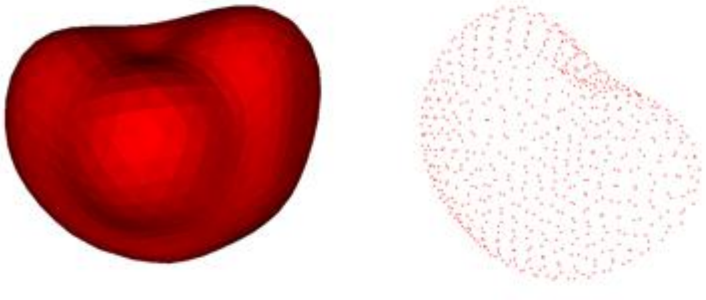

Figure 3.1: In the left panel: the $3D$ prostate segmented image volume. In the right panel: the $3D$ point-cloud representation of the prostate surface mesh.

---

[7] The MRI prostate segmentation was provided by Yipeng Hu and was prepared by a radiologist at University London College Hospital (UCLH). The MRI scans were acquired at UCLH with local ethical approval for the research purpose.

3.2 Initial alignment of the source model onto the target surface

A software application was implemented for the manual alignment of the source model onto the target scene before the non-rigid registration is initiated (see Figure 3.2). The graphical user interface (GUI) was developed using the Qt library [99] and the visualization utility is managed by VTK and PCL [100]. The main features of the software are:

- The ability to scale and superimpose the source model onto the target scene or the target onto the source and save the new orientation(s) and size(s) of the manually registered (colour-coded) model(s) into a designated directory.
- The option of downsampling feature datasets using VTK or PCL.
- The option of producing a surface-reconstructed point cloud using VTK.
- Crop a full model to produce a partial view of it.
- Load three (or two or one) $3D$ images and view them in the same geometrical coordinate system.
- Produce synthetic test data.
- Calculate the $TREs$.

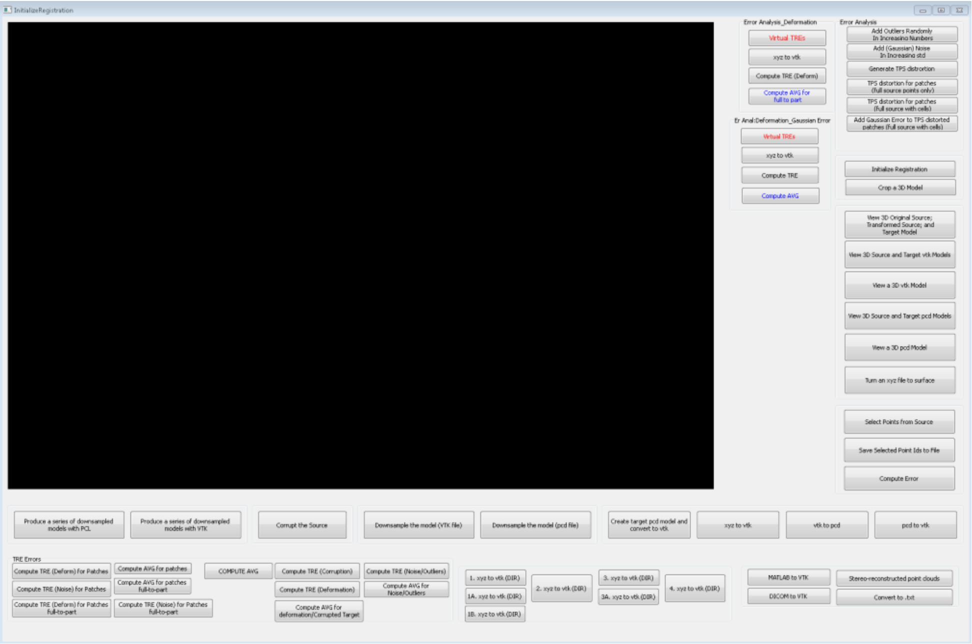

Figure 3.2: Screenshot of the GUI developed for the initial manual alignment of the source model onto the target scene.

3.3 Deformation effects and their impact on TRE

The capabilities of the nonrigid algorithms to recover deformation are tested by systematically increasing the size and the extent of the non-linear transformation applied onto the source. This is a very critical examination considering the smoothness of prostate surface and that it is lacking distinctive features. Algorithm 1 shows the pseudocode for a routine which implements a way of producing warped prostate surfaces for registration.

***Algorithm* 1:** Generation of *full* target models of registration by application of a TPS warp onto the source.

Input: The original *full* source model set $\boldsymbol{\mathcal{M}}_{\mathbf{0}}$; number of elements $\boldsymbol{\mathcal{N}}_{\mathbf{1}}$ of a subset of $\boldsymbol{\mathcal{M}}_{\mathbf{0}}$, call it $\boldsymbol{\mathcal{M}}$, which serves as the source model of registration; minimum $\boldsymbol{\mathcal{N}}_{\mathbf{2}}$ and maximum $\boldsymbol{\mathcal{N}}_{\mathbf{3}}$ number of points selected randomly from $\boldsymbol{\mathcal{M}}_{\mathbf{0}}$ to serve as source control points for the (random) TPS transformation applied onto $\boldsymbol{\mathcal{M}}_{\mathbf{0}}$ to produce $\mathcal{F}_1^{(i)}(\boldsymbol{\mathcal{M}}_{\mathbf{0}};\theta)$; and $\boldsymbol{\mathcal{N}}_{\mathbf{4}}$, $\boldsymbol{\mathcal{N}}_{\mathbf{5}}$, and $\boldsymbol{\mathcal{N}}_{\mathbf{6}}$ which represent, respectively, the upper limits of three uniform distributions with lower limits zero.

Output: The $\boldsymbol{\mathcal{M}}$ model set and the difference $\boldsymbol{\mathcal{M}}_{\mathbf{0}}-\boldsymbol{\mathcal{M}}$ which provides the set of “target markers” for the TRE calculations (see ***Algorithm* 2**); $\left\{\mathcal{F}_1^{(i)}(\boldsymbol{\mathcal{M}}_{\mathbf{0}};\theta)\right\}$, $\left\{\mathcal{F}_1^{(i)}(\boldsymbol{\mathcal{M}};\theta)\right\}$, and $\left\{\mathcal{F}_1^{(i)}(\boldsymbol{\mathcal{M}}_{\mathbf{0}}-\boldsymbol{\mathcal{M}};\theta)\right\}$.

```
Randomly select $\boldsymbol{\mathcal{N}}_{\mathbf{1}}$ points from $\boldsymbol{\mathcal{M}}_{\mathbf{0}}$ to produce $\boldsymbol{\mathcal{M}}$.
Identify the labels of those points of $\boldsymbol{\mathcal{M}}_{\mathbf{0}}$ that form $\boldsymbol{\mathcal{M}}$ and exclude them from the list
    of point labels of $\boldsymbol{\mathcal{M}}_{\mathbf{0}}$ to generate $\boldsymbol{\mathcal{M}}_{\mathbf{0}}-\boldsymbol{\mathcal{M}}$.
$for$   $\boldsymbol{i}=\boldsymbol{\mathcal{N}}_{\mathbf{2}}$   $to$   $\boldsymbol{\mathcal{N}}_{\mathbf{3}}$      {by adding $\boldsymbol{\mathcal{N}}_{\mathbf{2}}$, $i.e.$, $\boldsymbol{i}:=\boldsymbol{i}+\boldsymbol{\mathcal{N}}_{\mathbf{2}}$}
Randomly select $i$ points from $\boldsymbol{\mathcal{M}}_{\mathbf{0}}$ to form the set of source control points required
    for the calculation of the affine and $TPS$ transformation parameters of $\mathcal{F}_1^{(i)}$. The
    complexity of deformation across $\boldsymbol{\mathcal{M}}_{\mathbf{0}}$ is governed by the variable $i$.
        $for$   $\boldsymbol{j}=1$   $to$   $\boldsymbol{i}$      {$\boldsymbol{j}:=\boldsymbol{j}+1$}
        $x_j' := x_j + X_j$; $y_j' := y_j + Y_j$; and $z_j' := z_j + Z_j$
```

```
        where $(x_j, y_j, z_j)$ represents the $3D$ $jth$ control point which, by application of the $TPS$ transformation $\mathcal{F}_1^{(i)}$ onto $(x_j, y_j, z_j)$ or $\boldsymbol{\mathcal{M}_0}$, will be mapped exactly to its correspondence, i.e., the $jth$ target point $(x'_j, y'_j, z'_j)$. $\{X_j, Y_j, Z_j\}$ represents a set of random numbers each of which arises from a distinct uniform distribution (one for each dimension). Each of the three distributions is lying between zero and an upper value which is: $\boldsymbol{\mathcal{N}_4}$ (for the $x$ dimension); $\boldsymbol{\mathcal{N}_5}$ (for the $y$ dimension); and $\boldsymbol{\mathcal{N}_6}$ (for the $z$ dimension). Hence $X_j \in [0, \boldsymbol{\mathcal{N}_4}]$; $Y_j \in [0, \boldsymbol{\mathcal{N}_5}]$; and $Z_j \in [0, \boldsymbol{\mathcal{N}_6}]$. This step determines $\{(x'_j, y'_j, z'_j)\}$, i.e., the set of all ("randomly" produced) target points of the $TPS$ deformation, which are also required for the calculation of the affine and $TPS$ transformation parameters of $\mathcal{F}_1^{(i)}$. The size of deformation across $\boldsymbol{\mathcal{M}_0}$ is governed by $(\boldsymbol{\mathcal{N}_4}, \boldsymbol{\mathcal{N}_5}, \boldsymbol{\mathcal{N}_6})$.
        $end\ for$
    Calculate the $TPS$ transformation $\mathcal{F}_1^{(i)}$ and apply it onto $\boldsymbol{\mathcal{M}_0}$ to produce $\mathcal{F}_1^{(i)}(\boldsymbol{\mathcal{M}_0}; \theta)$.
    Identify the correspondences of $\boldsymbol{\mathcal{M}}$ and those of $\boldsymbol{\mathcal{M}_0} - \boldsymbol{\mathcal{M}}$ in $\mathcal{F}_1^{(i)}(\boldsymbol{\mathcal{M}_0}; \theta)$ to produce the target model of registration $\mathcal{F}_1^{(i)}(\boldsymbol{\mathcal{M}}; \theta)$ and the set of "deformed" target markers $\mathcal{F}_1^{(i)}(\boldsymbol{\mathcal{M}_0} - \boldsymbol{\mathcal{M}}; \theta)$, respectively.
$end\ for$
```

Ten different sets of computational registration experiments, $Exp\ A - Exp\ J$, were conducted for each registration algorithm and for fixed $\boldsymbol{\mathcal{M}_0}$, $\boldsymbol{\mathcal{N}_1} = 330$ points, $\boldsymbol{\mathcal{N}_2} = 2$ and $\boldsymbol{\mathcal{N}_3} = 200$ while $\boldsymbol{\mathcal{N}_4}$, $\boldsymbol{\mathcal{N}_5}$, and $\boldsymbol{\mathcal{N}_6}$ were varied. The tests in $Exp\ E$ and $Exp\ H - Exp\ J$ simulate as close as possible the available clinical data. Various other combinations of input parameters that could lead to possible instances of prostate deformation were also tested. See Table 3.1 and Figures 3.3 and 3.4.

	$\mathcal{N}_4$	$\mathcal{N}_5$	$\mathcal{N}_6$
Exp A	**10**	**10**	**10**
Exp B	**9**	**9**	**9**
Exp C	**8**	**8**	**8**
Exp D	**7**	**7**	**7**
Exp E	**6**	**6**	**6**
Exp F	**5**	**5**	**5**
Exp G	**4**	**4**	**4**
Exp H	**4**	**4**	**8**
Exp I	**4**	**8**	**4**
Exp J	**8**	**4**	**4**

Table 3.1: Ten different sets of deformed target models of registration are produced from *Algorithm* 1 by varying $\mathcal{N}_4$, $\mathcal{N}_5$, and $\mathcal{N}_6$. See also Figures 3.3 and 3.4, and text for details.

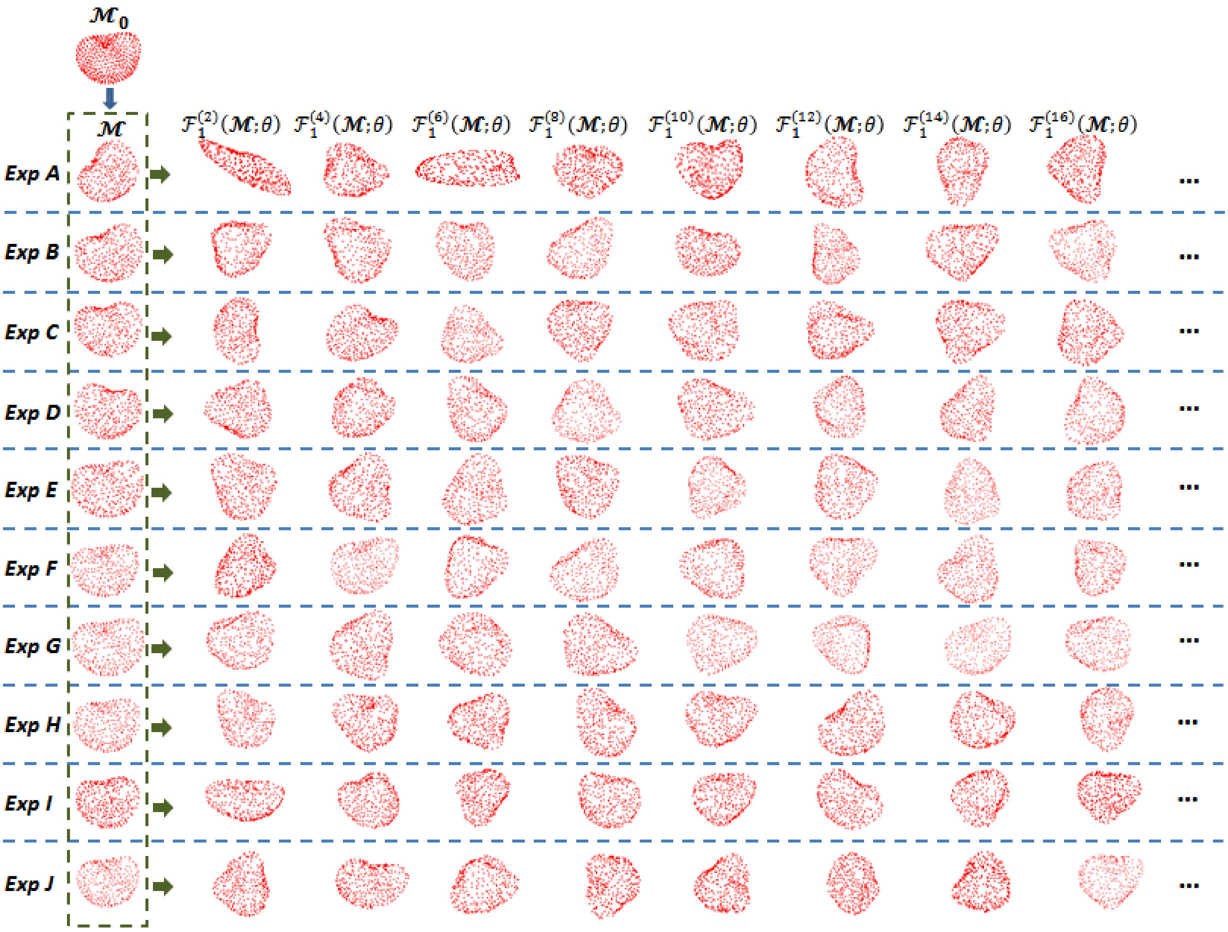

Figure 3.3: Examples of synthetic prostate datasets which represent nonlinearly deformed target models of registration and were produced from *Algorithm* 1. The 3*D* point-cloud representations are not in scale. See Table 3.1 and text for details.

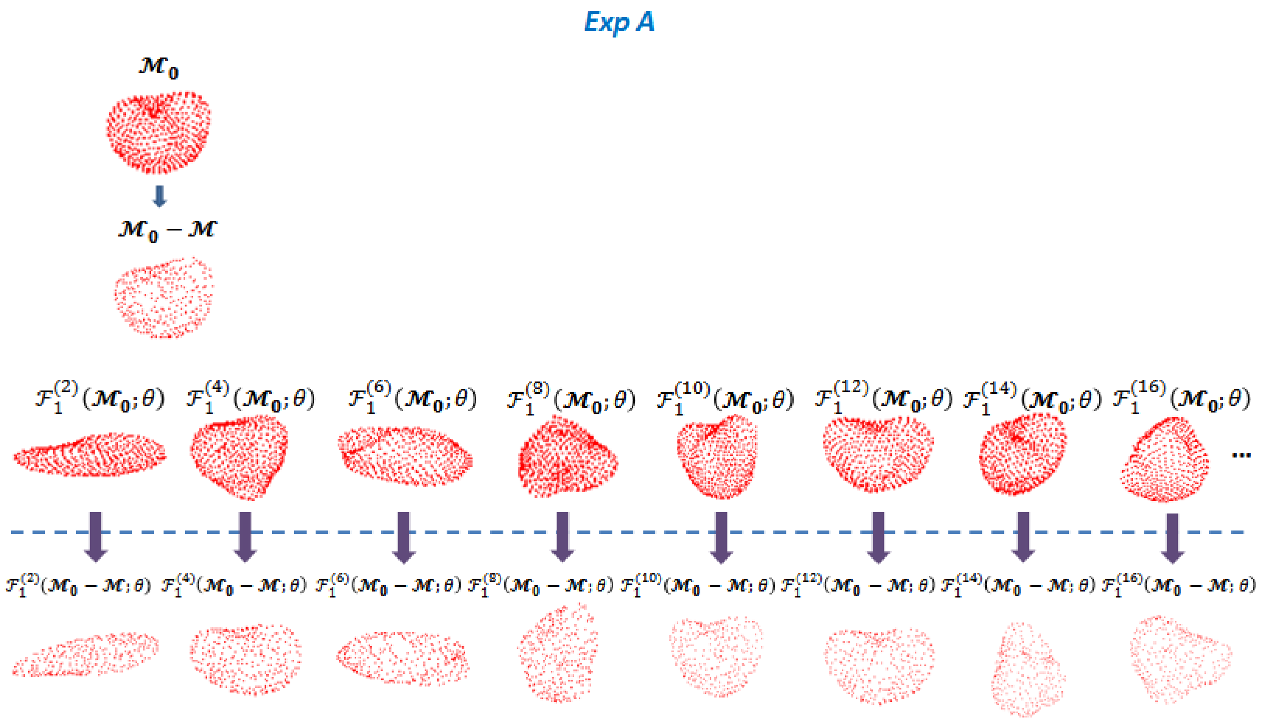

Figure 3.4: Examples of sets of original and "deformed" target markers from *Exp A*. These sets were produced from *Algorithm* 1 and are used in the *TRE* calculations. The *3D* datasets are not in scale. See Table 3.1 and text for details.

The registration takes place between $\mathcal{M}$ and each element of $\left\{\mathcal{F}_1^{(i)}(\mathcal{M};\theta)\right\}$ of each experiment producing as output a set of affine and *TPS* transformation parameters $\left\{\left(E^{(i)},\psi^{(i)}\right)\right\}$ as well as $\left\{\mathcal{F}_2^{(i)}(\mathcal{M};\theta)\right\}$. Since $\mathcal{M}$ serves as the set of control points in the $\mathcal{F}_2^{(i)}$ *TPS* transformation it holds that $U \equiv \Phi$. The $\mathcal{F}_2^{(i)}$ *TPS* transformation, constructed based upon $\left(E^{(i)},\psi^{(i)}\right)$, is then applied onto $\mathcal{M}_0 - \mathcal{M}$ according to Equation (2.27) of Section 2.1.3 where $\mathcal{M}$ is also used as control points in this transformation. This leads to the set $\left\{\mathcal{F}_2^{(i)}(\mathcal{M}_0 - \mathcal{M};\theta)\right\}$. See also Figure 3.5 for a graphical representation of an example registration experiment.

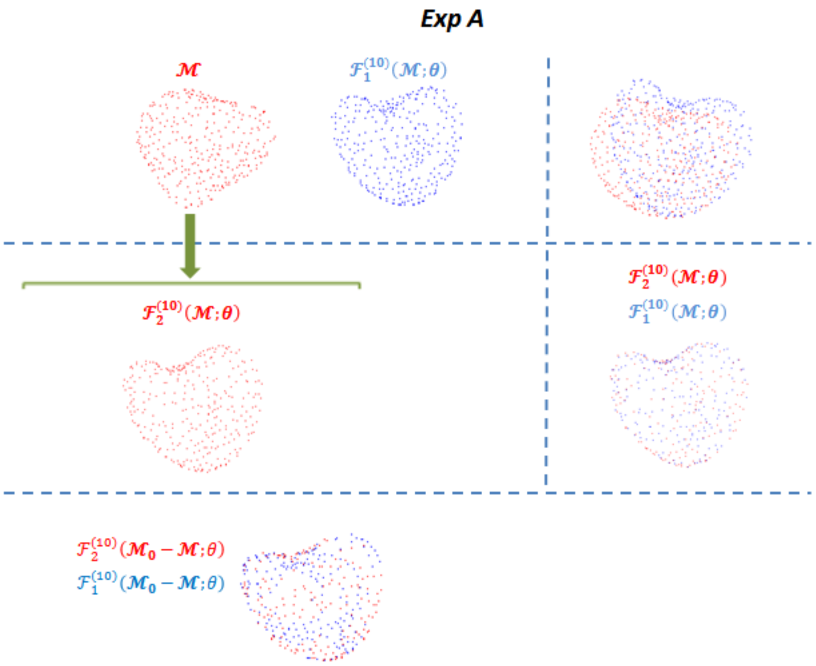

Figure 3.5: Registration between $\boldsymbol{\mathcal{M}}$ and $\mathcal{F}_1^{(10)}(\boldsymbol{\mathcal{M}};\theta)$ of $Exp\ A$. The average TRE computed with the $EM+TPS$ method and for $\boldsymbol{d}=15$ is (0.2812 ± 0.2103) mm. See text for details.

The TRE calculations are conducted by randomly pooling a number of points from $\mathcal{F}_1^{(i)}(\boldsymbol{\mathcal{M}}_{\mathbf{0}}-\boldsymbol{\mathcal{M}};\theta)$ and comparing them to their correspondencies in $\mathcal{F}_2^{(i)}(\boldsymbol{\mathcal{M}}_{\mathbf{0}}-\boldsymbol{\mathcal{M}};\theta)$. This process takes place between each element of $\left\{\mathcal{F}_1^{(i)}(\boldsymbol{\mathcal{M}}_{\mathbf{0}}-\boldsymbol{\mathcal{M}};\theta)\right\}$ and its counterpart in $\left\{\mathcal{F}_2^{(i)}(\boldsymbol{\mathcal{M}}_{\mathbf{0}}-\boldsymbol{\mathcal{M}};\theta)\right\}$ and for different numbers of randomly selected target markers (and for each experiment and non-rigid registration method), as ***Algorithm* 2** demonstrates below:

***Algorithm* 2:** Calculation of $TREs$.

Input: The $\boldsymbol{\mathcal{M}}_{\mathbf{0}}-\boldsymbol{\mathcal{M}}$ model set; $\left\{\mathcal{F}_1^{(i)}(\boldsymbol{\mathcal{M}}_{\mathbf{0}}-\boldsymbol{\mathcal{M}};\theta)\right\}$ and $\left\{\mathcal{F}_2^{(i)}(\boldsymbol{\mathcal{M}}_{\mathbf{0}}-\boldsymbol{\mathcal{M}};\theta)\right\}$ where $\boldsymbol{\mathcal{K}}_{\mathbf{1}}$ is the number of elements in each set; $\boldsymbol{\mathcal{K}}_{\mathbf{2}}$ is the number of times that a fixed number of target markers $\boldsymbol{d} \epsilon \{3,5,10,15\}$ is randomly selected from $\boldsymbol{\mathcal{M}}_{\mathbf{0}}-\boldsymbol{\mathcal{M}}$.

Output: Consider a list of $TREs$ each arising from a random configuration of $\boldsymbol{d}$ target markers drawn from $\boldsymbol{\mathcal{M}}_{\mathbf{0}}-\boldsymbol{\mathcal{M}}$; they are computed by first identifying their correspondences in $\mathcal{F}_1^{(i)}(\boldsymbol{\mathcal{M}}_{\mathbf{0}}-\boldsymbol{\mathcal{M}};\theta)$ and $\mathcal{F}_2^{(i)}(\boldsymbol{\mathcal{M}}_{\mathbf{0}}-\boldsymbol{\mathcal{M}};\theta)$ and then using the relationship

$$TRE^2 = \frac{1}{d}\sum_{j=1}^{d}\left\|\left(\mathcal{F}_1^{(i)}(\boldsymbol{\mathcal{M}}_{\mathbf{0}} - \boldsymbol{\mathcal{M}};\theta)\right)_j - \left(\mathcal{F}_2^{(i)}(\boldsymbol{\mathcal{M}}_{\mathbf{0}} - \boldsymbol{\mathcal{M}};\theta)\right)_j\right\|^2 \qquad (3.1)$$

where $\left(\mathcal{F}_{1/2}^{(i)}(\boldsymbol{\mathcal{M}}_{\mathbf{0}} - \boldsymbol{\mathcal{M}};\theta)\right)_j$ represent the $3D$ Cartesian target marker coordinates of the jth pair of spatial correspondences. A distinct list of $TREs$ can be produced for each element of $\left\{\mathcal{F}_1^{(i)}(\boldsymbol{\mathcal{M}}_{\mathbf{0}} - \boldsymbol{\mathcal{M}};\theta)\right\}$ and its counterpart in $\left\{\mathcal{F}_2^{(i)}(\boldsymbol{\mathcal{M}}_{\mathbf{0}} - \boldsymbol{\mathcal{M}};\theta)\right\}$ for a fixed $\boldsymbol{d}$. The same process can be repeated $\forall\ \boldsymbol{d} \in \{3,5,10,15\}$.

```
1:   $for \quad \boldsymbol{d} = 3,5,10,15$ {number of target markers}
2:       $for \quad \boldsymbol{i} = 1 \quad to \quad \boldsymbol{\mathcal{K}_1} \qquad \{\boldsymbol{i} \coloneqq \boldsymbol{i} + 1\}$
3:           $for \quad \boldsymbol{m} = 1 \quad to \quad \boldsymbol{\mathcal{K}_2} \qquad \{\boldsymbol{m} \coloneqq \boldsymbol{m} + 1\}$
4:               Randomly select $\boldsymbol{d}$ points from $\boldsymbol{\mathcal{M}}_{\mathbf{0}} - \boldsymbol{\mathcal{M}}$ and identify their point labels.
5:               $for \quad \boldsymbol{n} = 1 \quad to \quad \boldsymbol{d} \qquad \{\boldsymbol{n} \coloneqq \boldsymbol{n} + 1\}$
6:                   Find the correspondences of the target marker in $\mathcal{F}_1^{(i)}(\boldsymbol{\mathcal{M}}_{\mathbf{0}} - \boldsymbol{\mathcal{M}};\theta)$ and $\mathcal{F}_2^{(i)}(\boldsymbol{\mathcal{M}}_{\mathbf{0}} - \boldsymbol{\mathcal{M}};\theta)$ based on its already identified point label.
7:                   Calculate the squared distance between the two correspondences and add the result to a running total.
8:               $end\ for$
9:               Divide the sum of the computed squared distances in $(5 - 8)$ by $\boldsymbol{d}$, take the square root of the output to compute the $TRE$, and append the result onto a list specifically linked to $\boldsymbol{i}$.
10:          $end\ for$
11:      $end\ for$
12:  $end\ for$
```

Consider the average value and the standard deviation of all $TREs$[8] originating in $\boldsymbol{\mathcal{K}_2}$ random configurations of $\boldsymbol{d}$ target markers drawn from $\mathcal{F}_1^{(i)}(\boldsymbol{\mathcal{M}_0} - \boldsymbol{\mathcal{M}}; \theta)$ as described in the output section of ***Algorithm* 2**. A list of average values and standard deviations of $TREs$ can be produced by iteratively examining each element of $\left\{\mathcal{F}_1^{(i)}(\boldsymbol{\mathcal{M}_0} - \boldsymbol{\mathcal{M}}; \theta)\right\}$ and its counterpart in $\left\{\mathcal{F}_2^{(i)}(\boldsymbol{\mathcal{M}_0} - \boldsymbol{\mathcal{M}}; \theta)\right\}$ for a fixed $\boldsymbol{d}$ and for all experiments and registration methods.

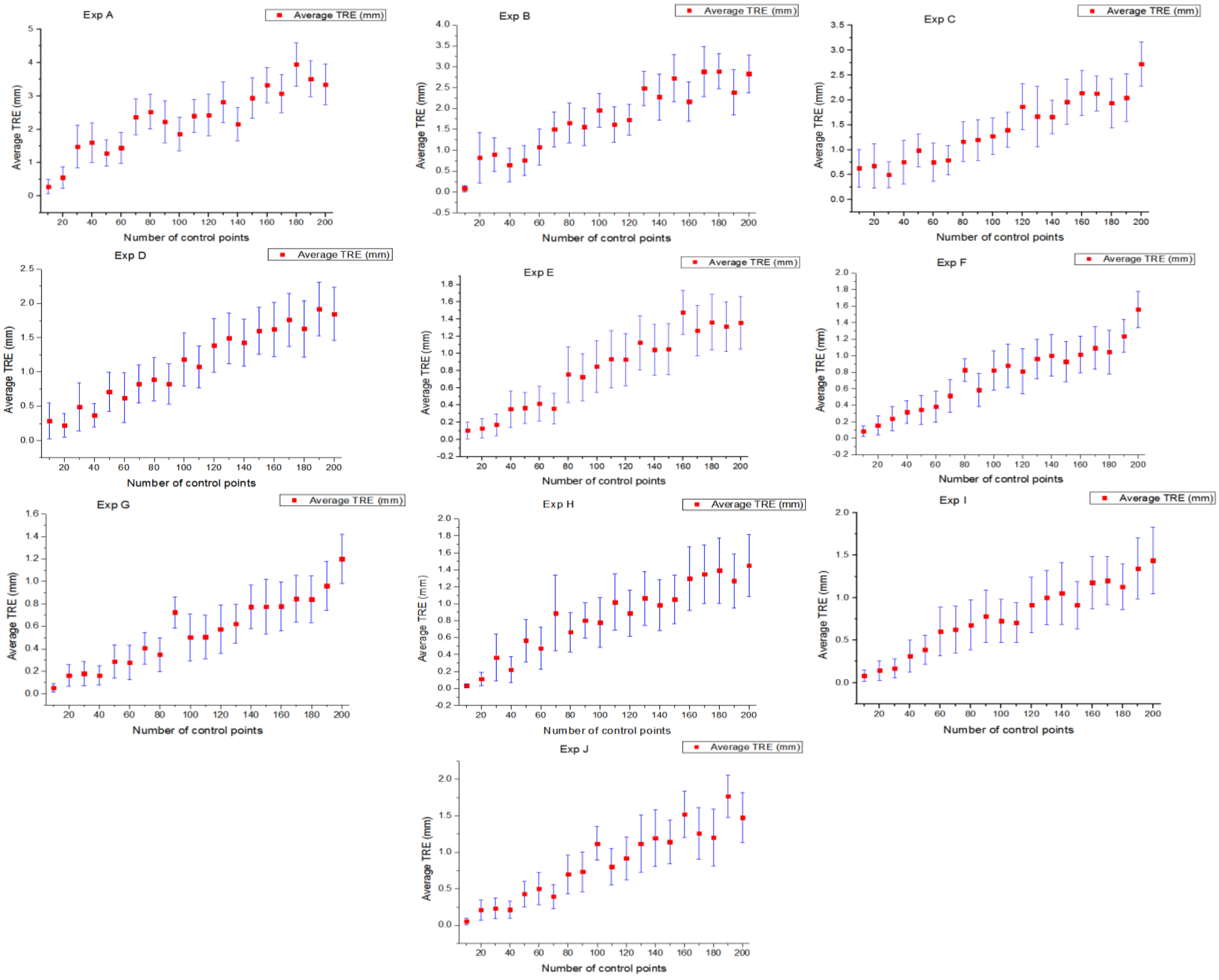

Figures 3.6: Average $TREs$ computed with the $EM + TPS$ method to determine sensitivity to deformation. $\boldsymbol{\mathcal{K}_1} = 100$, $\boldsymbol{\mathcal{K}_2} = 100$, and $\boldsymbol{d} = 15$. Only a subset of the available data is graphically presented.

---

[8] The $TREs$ showed no significant dependence on the (random) configuration of target markers as can be seen in Figures 3.6-3.8.

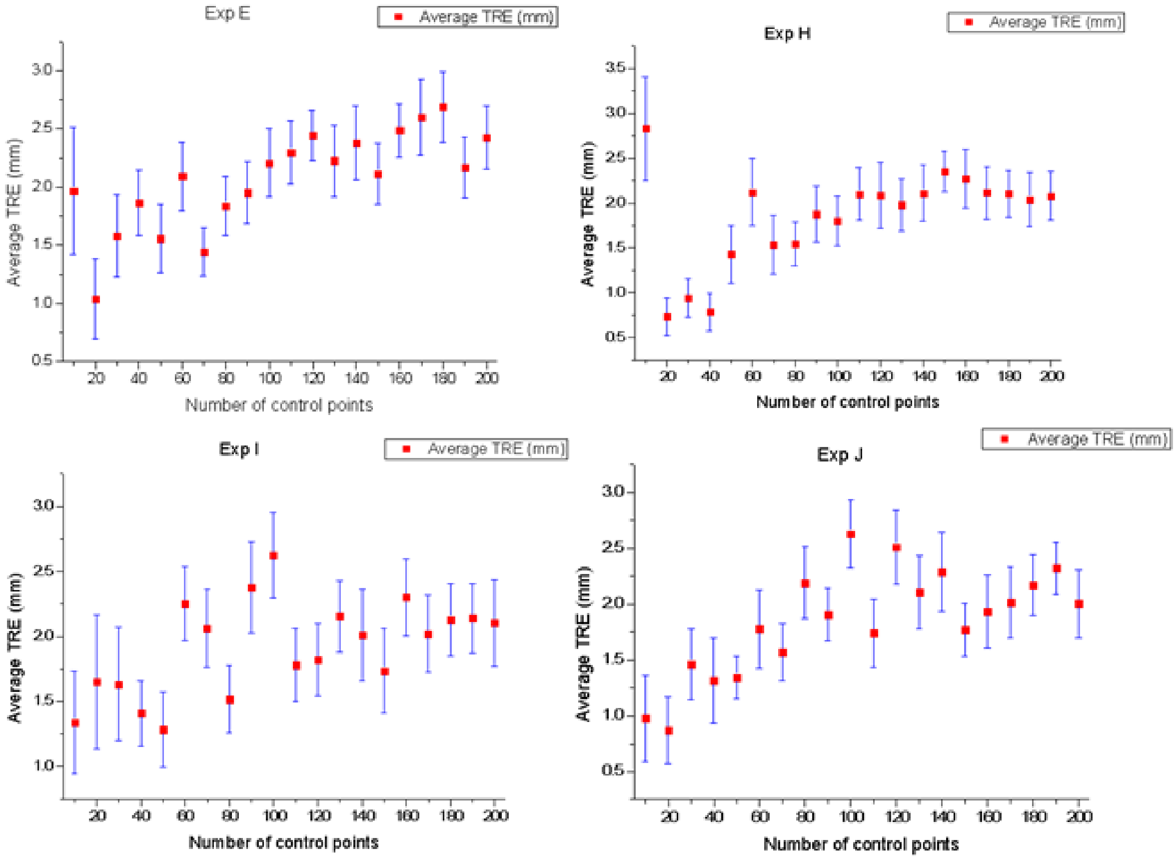

Figure 3.7: Average $TREs$ computed with the $KC + TPS$ method to determine sensitivity to deformation. $\boldsymbol{\mathcal{K}_1} = 100$, $\boldsymbol{\mathcal{K}_2} = 100$, and $\boldsymbol{d} = 15$. Only a subset of the available data is graphically presented. Only results from Experiments E, H, I and J are shown, as most representative of the clinical data.

Hence the impact that the varying size of deformation (as implemented in the various experiments) has on the TRE in going from $\boldsymbol{\mathcal{N}_2}$ to $\boldsymbol{\mathcal{N}_3}$ source control points can be determined $\forall\, \boldsymbol{d} \in \{3,5,10,15\}$. As the $TREs$ showed no significant dependence on $\boldsymbol{d}$ across all experiments and for all registration methods (using the same input files), we report here the results only for $\boldsymbol{d} = 15$. See also Figures 3.6-3.8.

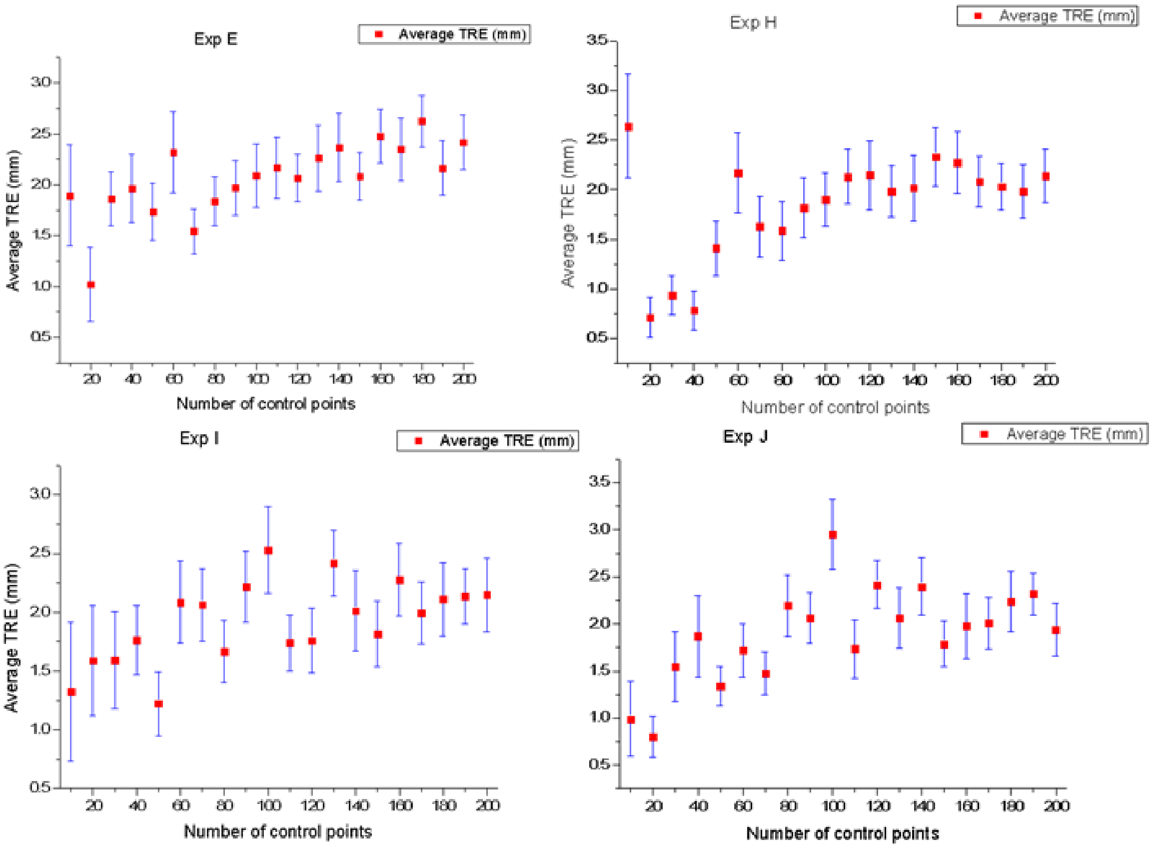

Figure 3.8: Average $TREs$ computed with the $GMM + TPS$ method to determine sensitivity to deformation. $\mathcal{K}_1 = 100$, $\mathcal{K}_2 = 100$, and $\boldsymbol{d} = 15$. Only a subset of the available data is graphically presented. Only results from Experiments E, H, I and J are shown, as most representative of the clinical data.

3.4 The effect of Gaussian noise and its impact on TRE

The intraoperatively acquired clinical data are perturbed by noise, which, in this work, is assumed to be of Gaussian type. The target model of registration is produced by injecting Gaussian noise in the source. Its impact on TRE is determined as a function of increasing size of Gaussian noise.

The perturbation from Gaussian noise can be explicitly modelled in the objective cost function (its contribution can be parameterized using a Gaussian normal distribution with zero mean and σ standard deviation, see Ref. [62]). The available “noisy” clinical data were qualitatively compared to simulated analogues, *i.e.*, “noisy” synthetic target models of registration, a range of standard deviations of the Gaussian normal distribution were deduced on the basis of similarity assuming zero mean, and the relevant impact on TRE was determined for this range. Additional calculations were also conducted by extending this identified range of standard deviations.

The best learning algorithm for prostate surface registration must be able to quantify the underlined noise level in the real clinical data, and decide whether to account for noise explicitly in its energy cost function (which could increase the accuracy of registration to clinically acceptable levels) or not; the present analysis gives more insight into this question assuming that all points of the synthetic target model are subject to Gaussian noise.

***Algorithm* 3:** Generation of *full* target models of registration by adding noise to the *full* source model. The injected noise is generated from a Gaussian normal distribution with fixed mean and varying standard deviation. (See also Figure 3.9 for a diagrammatic presentation.)

Input: $\boldsymbol{\mathcal{M}_0}$ and $\boldsymbol{\mathcal{N}_1}$ as defined in ***Algorithm* 1** ($\boldsymbol{\mathcal{M}}$ and $\boldsymbol{\mathcal{M}_0 - \mathcal{M}}$ maintain the same definitions); the mean μ of the Gaussian normal distribution; σ_3 and σ_2 which represent, in respect, the maximum standard deviation of the Gaussian distribution and an increment parameter that is iteratively added to the running standard deviation σ until σ_3 is reached.

Output: $\boldsymbol{\mathcal{M}}$ and $\boldsymbol{\mathcal{M}_0 - \mathcal{M}}$; $\{\boldsymbol{\mathcal{J}}_\sigma\}$ where $\boldsymbol{\mathcal{J}}_\sigma$ corresponds to updated $\boldsymbol{\mathcal{M}}$ according to (μ, σ).

```
Randomly select $\boldsymbol{\mathcal{N}_1}$ points from $\boldsymbol{\mathcal{M}_0}$ to produce $\boldsymbol{\mathcal{M}}$ and $\boldsymbol{\mathcal{M}_0 - \mathcal{M}}$.
$for \quad \sigma = \sigma_2 \quad to \quad \sigma_3 \qquad \{\sigma := \sigma + \sigma_2\}$
    $for \quad \boldsymbol{i} = 1 \quad to \quad \boldsymbol{\mathcal{N}_1} \qquad \{\boldsymbol{i} := \boldsymbol{i} + 1\}$
        $x_i' := x_i + X_i; y_i' := y_i + Y_i; z_i' := z_i + Z_i$
        where $(x_i, y_i, z_i)$ and $(x_i', y_i', z_i')$ represent the original $3D\ ith$ point of $\boldsymbol{\mathcal{M}}$ and its updated version, respectively. $\{X_i, Y_i, Z_i\}$ corresponds to a set of random numbers that are generated from a Gaussian normal distribution with fixed mean $\mu$ and (increasing) standard deviation $\sigma$. A new copy of the original $\boldsymbol{\mathcal{M}}$ is updated for each new value of $\sigma$.
    $end\ for$
$end\ for$
```

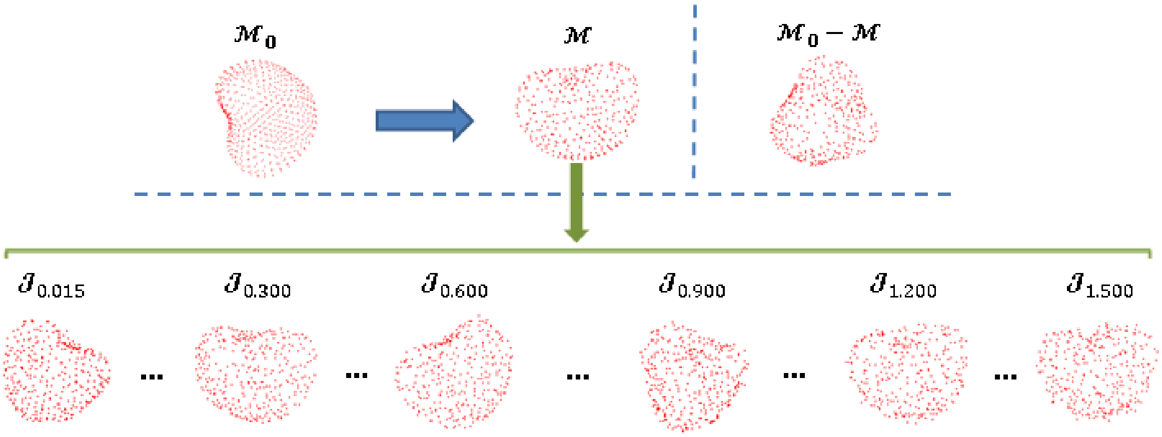

Figure 3.9: A diagrammatic representation of ***Algorithm* 3**.

Four different sets of computational registration experiments, $Exp\ A - ExpD$, were conducted for each registration algorithm and for fixed $\boldsymbol{\mathcal{M}_0}$, $\mu = 0$, $\sigma_2 = 0.015$ and $\sigma_3 = 1.500$ while $\boldsymbol{\mathcal{N}_1}$ was varied, as shown in Table 3.2. The objective of this exercise is to quantify the relationship between registration accuracy and number of perturbed target points as the level of noise is increased. The number of target points won't be a constant throughout the process of a real clinical operation. Thus it is critical to define the minimum threshold for achieving acceptable registration accuracy.

	$Exp\ A$	$Exp\ B$	$Exp\ C$	$Exp\ D$
$\boldsymbol{\mathcal{N}_1}$	**52**	**131**	**244**	**329**

Table 3.2: Four different sets of noisy target models of registration are produced from *Algorithm* 3 by varying $\mathcal{N}_1$ and σ. See also Figure 3.9 and text for details.

This relationship cannot be predicted by mathematical derivations. As the number of target points is reduced the possibility of establishing a valid registration between source and "noisy" target (using any of the non-rigid registration algorithms, even under an ideal initial alignment between them) may be decreased (mainly due to the increased possibility of establishing erroneous correspondences) for the same increase of level of noise. This becomes a determining factor for the validity of registrations to “noisy” and occluded target surfaces (probably less so to full “noisy” target models) above a certain noise threshold.

$\boldsymbol{\mathcal{M}}$ ($\equiv$ control points) is registered against each element of $\{\boldsymbol{\mathcal{J}_\sigma}\}$ leading to $\left\{\left(E^{(\sigma)}, \psi^{(\sigma)}\right)\right\}$ and $\left\{\mathcal{F}^{(\sigma)}(\boldsymbol{\mathcal{M}}; \theta)\right\}$, and by extension to $\left\{\mathcal{F}^{(\sigma)}(\boldsymbol{\mathcal{M}_0} - \boldsymbol{\mathcal{M}}; \theta)\right\}$ following a similar approach to the one taken in Section 3.2. The registration accuracy is determined by averaging out all $TREs$ produced by randomly selecting (100 times) d Cartesian points (where $\boldsymbol{d} \in \{3,5,10,15\}$) from $\boldsymbol{\mathcal{M}_0} - \boldsymbol{\mathcal{M}}$ and calculating the distances between them and their correspondences in $\mathcal{F}^{(\sigma)}(\boldsymbol{\mathcal{M}_0} - \boldsymbol{\mathcal{M}}; \theta)$, according to Equation (3.1).

The $TREs$ showed no dependence on $\boldsymbol{d}$ and the random configurations of target markers. The average $TREs$ were computed for all registration methods using the same input files and for $d = 15$. The results are shown in Figures 3.10 – 3.12.

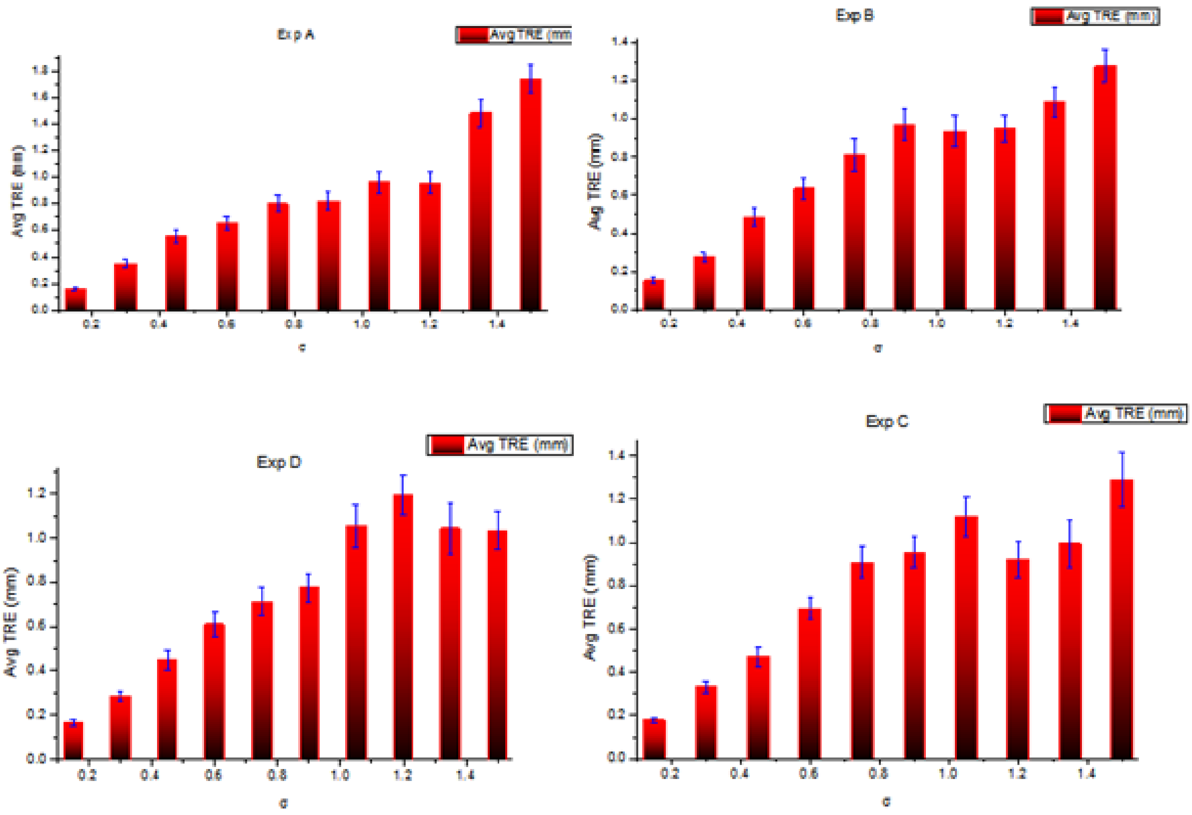

Figure 3.10: Average $TREs$ computed with the $KC + TPS$ method to determine sensitivity to noisy. Only a subset of the available data is presented in the graphs.

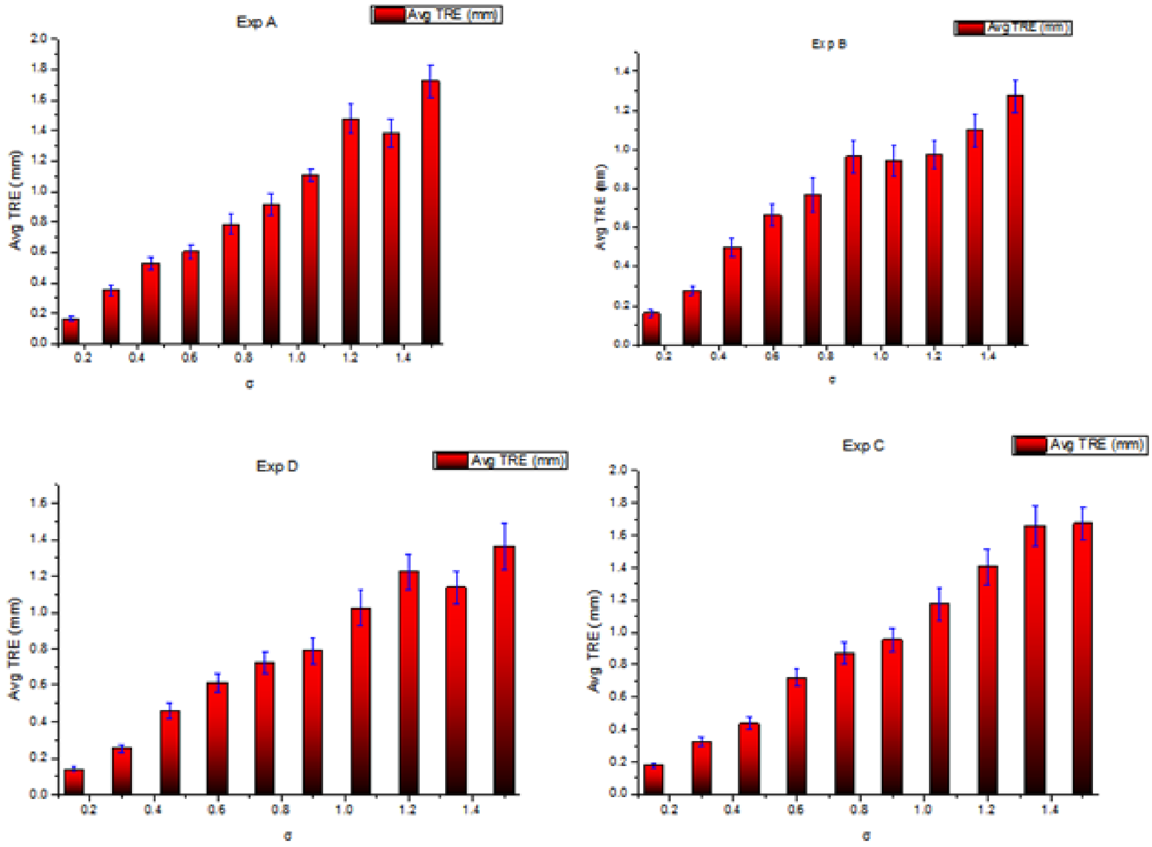

Figure 3.11: Average $TREs$ computed with the $GMM + TPS$ method to determine sensitivity to noise. Only a subset of the available data is presented in the graphs.

The learning algorithms would behave ideally if $\mathcal{F}^{(\sigma)}(\boldsymbol{\mathcal{M}};\theta) \equiv \boldsymbol{\mathcal{M}}$ and hence $\mathcal{F}^{(\sigma)}(\boldsymbol{\mathcal{M}}_\mathbf{0} - \boldsymbol{\mathcal{M}};\theta) \equiv \boldsymbol{\mathcal{M}}_\mathbf{0} - \boldsymbol{\mathcal{M}}$. The computed $TREs$ would then be strictly attributed to the injected Gaussian noise.

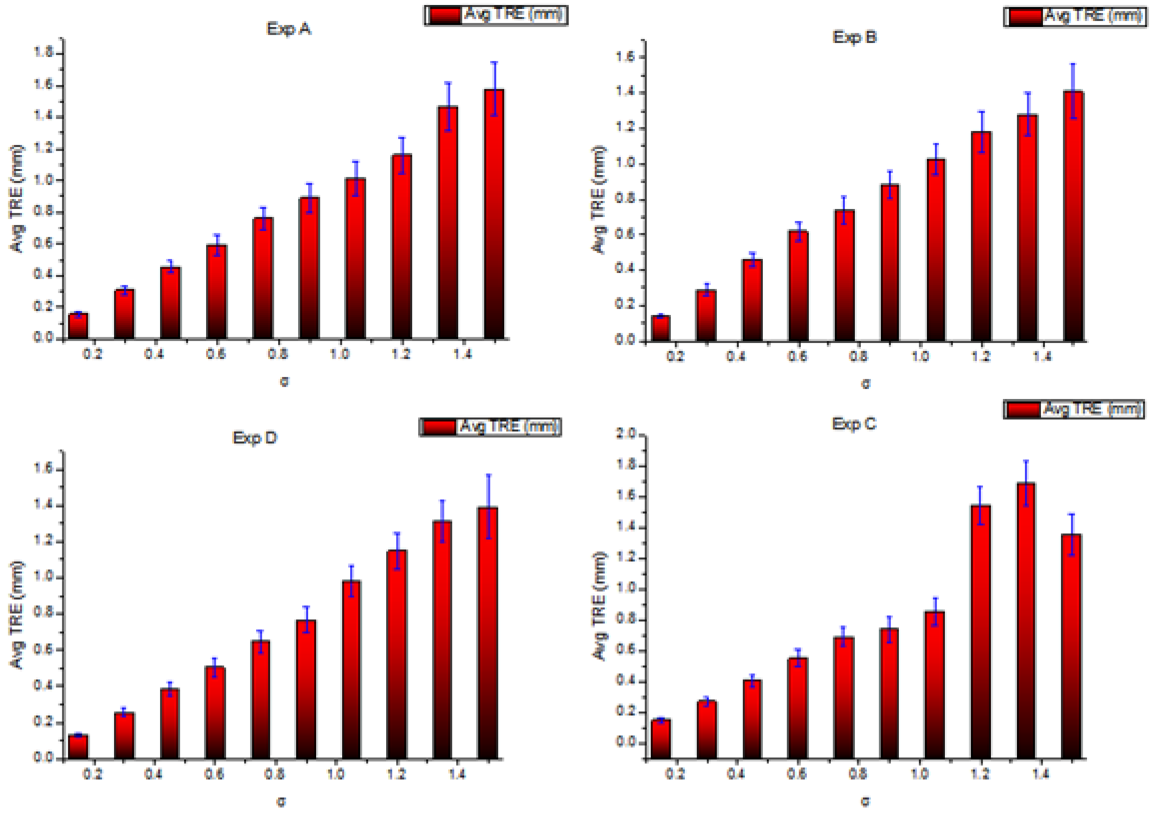

Figure 3.12: Average $TREs$ computed with the $EM + TPS$ method to determine sensitivity to noise. Only a subset of the available data is presented in the graphs.

3.5 The presence of outliers and their impact on TRE

As mentioned in Section 1.1, the $3D$ target model arises from stereo-based reconstruction of endoscopically acquired intraoperative (left and right) stereo image planes. However, stereo correspondence cannot always be achieved for all features leading to a reconstructed point-cloud surface with "holes". It can also be erroneous for some $2D$ points leading to outliers.

Another source of outliers for the prostate target surface, probably the most important, may be the surrounding environment itself. This section focuses on this possibility while the other possibility is examined in Section 3.6 where the target model of registration is also subject to deformation, as this combination simulates some clinical data.

The target model of registration is produced by adding outliers randomly to the source as Algorithm 4 below demonstrates. The number of outliers is systematically increased and its impact on TRE is examined.

***Algorithm* 4:** Generation of *full* target models of registration by adding outliers to the *full* source model. (See also Figure 3.13.)

Input: $\boldsymbol{\mathcal{M}_0}$ and $\boldsymbol{\mathcal{N}_1}$ as defined in ***Algorithm* 1** ($\boldsymbol{\mathcal{M}}$ and $\boldsymbol{\mathcal{M}_0 - \mathcal{M}}$ maintain the same definitions); the integer number $\boldsymbol{\mathcal{N}_3}$ which corresponds to the maximum number of outliers added; $\boldsymbol{\mathcal{N}_2}$ represents the number of outliers that are recursively added to a running total $\boldsymbol{n}$ until $\boldsymbol{\mathcal{N}_3}$ is reached; and $\boldsymbol{\mathcal{N}_4}$, $\boldsymbol{\mathcal{N}_5}$, and $\boldsymbol{\mathcal{N}_6}$ which represent, respectively, the upper limits of three uniform distributions with lower limits zero (as in ***Algorithm* 1**).

Output: $\boldsymbol{\mathcal{M}}$ and $\boldsymbol{\mathcal{M}_0 - \mathcal{M}}$; $\{\boldsymbol{\mathcal{L}_h}\}$ where $\boldsymbol{\mathcal{L}_h}$ corresponds to $\boldsymbol{\mathcal{M}}$ plus $\boldsymbol{n}$ outliers.

```
Randomly select $\boldsymbol{\mathcal{N}_1}$ points from $\boldsymbol{\mathcal{M}_0}$ to produce $\boldsymbol{\mathcal{M}}$ and $\boldsymbol{\mathcal{M}_0 - \mathcal{M}}$.
    $for \quad n = \boldsymbol{\mathcal{N}_2} \quad to \quad \boldsymbol{\mathcal{N}_3} \qquad \{n := n + \boldsymbol{\mathcal{N}_2}\}$
    Randomly select $n$ points from $\boldsymbol{\mathcal{M}_0}$.
        $for \quad \boldsymbol{i} = 1 \quad to \quad n \qquad \{\boldsymbol{i} := \boldsymbol{i} + 1\}$
        $x_i' := x_i + X_i; y_i' := y_i + Y_i; z_i' := z_i + Z_i$
        where $(x_i, y_i, z_i)$ and $(x_i', y_i', z_i')$ represent the original $3D\ ith$ point of
        $\boldsymbol{\mathcal{M}_0}$ and its updated version, respectively. The set $\{X_i, Y_i, Z_i\}$ is defined
        in Algorithm 1. This step creates $n$ random outliers.
        $end\,for$
Append $n$ outliers onto $\boldsymbol{\mathcal{M}}$ to generate the target model of registration $\boldsymbol{\mathcal{L}_h}$.
    $end\,for$
```

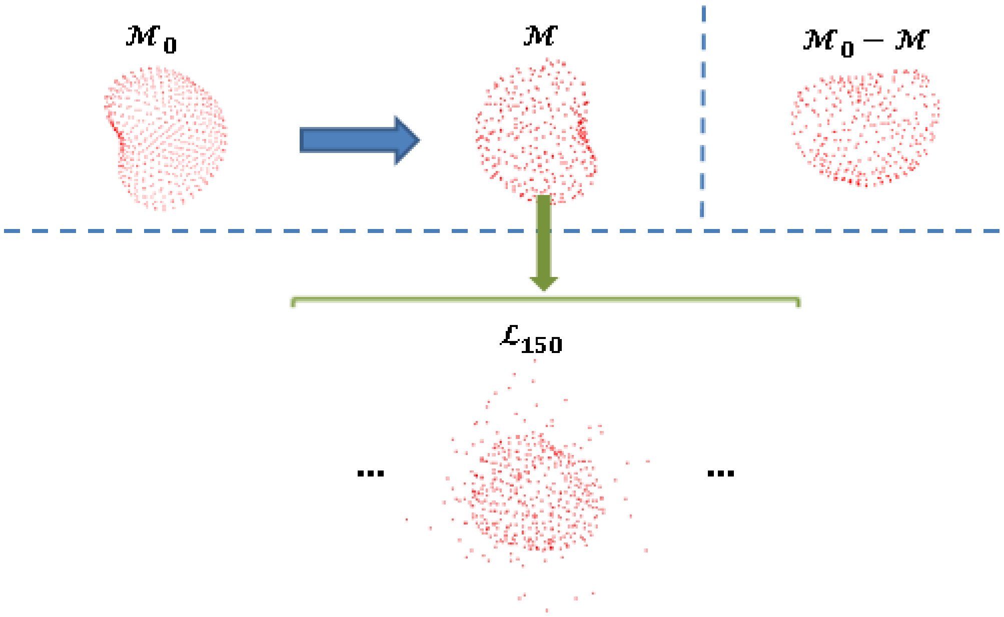

Figure 3.13: A diagrammatic representation of ***Algorithm* 4**.

One set of computational registration experiments for each registration algorithm was performed using as input $\mathcal{N}_1 = 321$ points, $\mathcal{N}_3 = 303$, $\mathcal{N}_2 = 3$, and $\mathcal{N}_4 = \mathcal{N}_5 = \mathcal{N}_6 = 50$. $\mathcal{M}$ ($\equiv$ control points) is registered against each element of $\{\mathcal{L}_h\}$ leading to $\{(E^{(h)}, \psi^{(h)})\}$ and $\{\mathcal{F}^{(h)}(\mathcal{M};\theta)\}$, and by extension to $\{\mathcal{F}^{(h)}(\mathcal{M}_0 - \mathcal{M};\theta)\}$. The registration accuracy is determined by averaging out $4 \times 100 \times 100$ distinct $TREs$ computed via a similar process to the one followed in Section 3.3. The same input files were used for all registration methods. See Table 3.3 for results. The computed $TREs$ would take zero values if $\mathcal{F}^{(h)}(\mathcal{M};\theta) \equiv \mathcal{M}$ and hence $\mathcal{F}^{(h)}(\mathcal{M}_0 - \mathcal{M};\theta) \equiv \mathcal{M}_0 - \mathcal{M}$, which is equivalent to saying that the non-rigid registration algorithms can fully discriminate against outliers.

	Average $TREs$ (mm)
$KC + TPS$	**0.0071 ± 0.0040**
$GMM + TPS$	**0.0093 ± 0.0056**
$EM + TPS$	**0.0000 ± 0.0000**

Table 3.3: The average $TREs$ computed with all registration methods to determine the sensitivity to outliers.

3.6 The effect of non-Gaussian noise onto a deformed target model and its impact on TRE

This Section examines the effect of random (non-Gaussian) noise and/or artefacts from erroneous stereo correspondence onto a deformed target model as a function of number of points in the target dataset, and their impact on registration accuracy (see ***Algorithm* 5**).

***Algorithm* 5:** Generation of *full* target models of registration by application of a TPS warp onto the *full* source model followed by the injection of random non-Gaussian noise. See also Figure 3.14 for a diagrammatic representation.

Input: The original *full* source model set $\boldsymbol{\mathcal{M}_0}$; the number of points $\boldsymbol{\mathcal{N}_1}$ selected randomly from $\boldsymbol{\mathcal{M}_0}$ to serve as source control points for the (random) TPS transformation applied onto $\boldsymbol{\mathcal{M}_0}$ to produce $\mathcal{F}_1(\boldsymbol{\mathcal{M}_0};\theta)$; $\boldsymbol{\mathcal{N}_2}$, $\boldsymbol{\mathcal{N}_3}$, and $\boldsymbol{\mathcal{N}_4}$ which represent, respectively, the upper limits of three uniform distributions with lower limits zero (defined as $\boldsymbol{\mathcal{N}_4}$, $\boldsymbol{\mathcal{N}_5}$, and $\boldsymbol{\mathcal{N}_6}$ in ***Algorithm* 1**, respectively); $\boldsymbol{\mathcal{M}_3}$ and $\boldsymbol{\mathcal{M}_2}$ which correspond, in respect, to the maximum number of points selected randomly from $\mathcal{F}_1(\boldsymbol{\mathcal{M}_0};\theta)$ and an increment parameter that is iteratively added to the running total of selected points μ until $\boldsymbol{\mathcal{M}_3}$ is reached; $\boldsymbol{\mathcal{K}_1}$, $\boldsymbol{\mathcal{K}_2}$, and $\boldsymbol{\mathcal{K}_3}$ which relate, respectively, to the lower limits of another three uniform distributions with corresponding upper limits $\boldsymbol{\mathcal{L}_1}$, $\boldsymbol{\mathcal{L}_2}$, and $\boldsymbol{\mathcal{L}_3}$.

Output: $\mathcal{F}_1(\boldsymbol{\mathcal{M}_0};\theta)$; $\{\boldsymbol{\mathcal{W}_\mu}\}$ where $\boldsymbol{\mathcal{W}_\mu}$ corresponds to a random subset of $\mathcal{F}_1(\boldsymbol{\mathcal{M}_0};\theta)$ perturbed by random noise (defined as the target of registration); $\{\boldsymbol{\mathcal{S}_\mu}\}$ where $\boldsymbol{\mathcal{S}_\mu}$ refers to the correspondences of $\boldsymbol{\mathcal{W}_\mu}$ in $\boldsymbol{\mathcal{M}_0}$ (defined as the source of registration); $\{\boldsymbol{\mathcal{M}_0}-\boldsymbol{\mathcal{S}_\mu}\}$ where $\boldsymbol{\mathcal{M}_0}-\boldsymbol{\mathcal{S}_\mu}$ provides the set of (source) target marker points for the TRE calculations; and $\{\mathcal{F}_1(\boldsymbol{\mathcal{M}_0};\theta)-\boldsymbol{\mathcal{W}_\mu}\}$ where $\mathcal{F}_1(\boldsymbol{\mathcal{M}_0};\theta)-\boldsymbol{\mathcal{W}_\mu}$ represents the set of deformed target marker points (without noise).

```
1:  Randomly select $\boldsymbol{\mathcal{N}_1}$ points from $\boldsymbol{\mathcal{M}_0}$ and produce the target points of the $TPS$ deformation according to Step 5 of Algorithm 1.
2:  Calculate the $TPS$ transformation $\mathcal{F}_1$ and apply it onto $\boldsymbol{\mathcal{M}_0}$ to produce $\mathcal{F}_1(\boldsymbol{\mathcal{M}_0};\theta)$.
3:      $for \quad \mu=\boldsymbol{\mathcal{M}_2} \quad to \quad \boldsymbol{\mathcal{M}_3} \quad \{\mu := \mu+\boldsymbol{\mathcal{M}_2}\}$
4:          Randomly select $\mu$ points from $\mathcal{F}_1(\boldsymbol{\mathcal{M}_0};\theta)$ and identify their point labels.
```

```
        $for \quad j = 1 \quad to \quad \boldsymbol{\mu} \quad \{j \coloneqq j + 1\}$
            $x_j' \coloneqq x_j + X_j; y_j' \coloneqq y_j + Y_j; z_j' \coloneqq z_j + Z_j$
            where $(x_j, y_j, z_j)$ and $(x_j', y_j', z_j')$ represent the original $3D\ jth$ point of $\mathcal{F}_1(\boldsymbol{\mathcal{M}_0}; \theta)$ from the selection of $\mu$ points and its updated version (which belongs to $\boldsymbol{\mathcal{W}_\mu}$), respectively. $\{X_j, Y_j, Z_j\}$ represents a set of random numbers each of which arises from a distinct uniform distribution (one for each dimension) s.t.
            $X_j \in [\boldsymbol{\mathcal{K}_1}, \boldsymbol{\mathcal{L}_1}]; Y_j \in [\boldsymbol{\mathcal{K}_2}, \boldsymbol{\mathcal{L}_2}]; Z_j \in [\boldsymbol{\mathcal{K}_3}, \boldsymbol{\mathcal{L}_3}]$.
        $end\ for$
    Identify the correspondences of $\boldsymbol{\mathcal{W}_\mu}$ in $\boldsymbol{\mathcal{M}_0}$ to produce $\boldsymbol{\mathcal{S}_\mu}$ and $\boldsymbol{\mathcal{M}_0} - \boldsymbol{\mathcal{S}_\mu}$.
    Select and generate $\mathcal{F}_1(\boldsymbol{\mathcal{M}_0}; \theta) - \boldsymbol{\mathcal{W}_\mu}$.
    $end\ for$
```

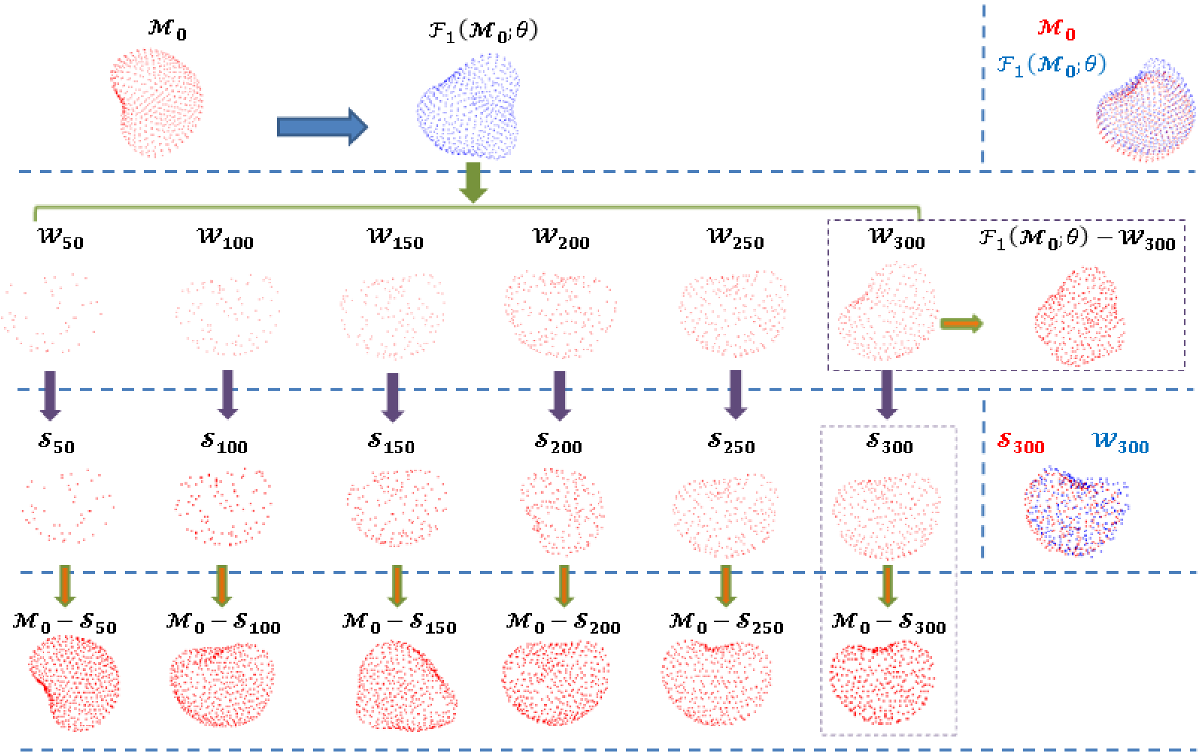

Figure 3.14: A diagrammatic representation of ***Algorithm* 5**. The input $3D$ meshes originate in $Test$ 2 of $Exp\ B$. See text for details.

Two experiments, $Exp\ A$ and $Exp\ B$, consisting of four sets of tests each, $Test\ 1 - Test\ 4$, were conducted for all registration methods where in each set of tests all input parameters were kept fixed save $\boldsymbol{\mathcal{N}_2}$, $\boldsymbol{\mathcal{N}_3}$, and $\boldsymbol{\mathcal{N}_4}$ (see Table 3.4). The difference between $Exp\ A$ and $Exp\ B$ lies in the values chosen for $(\boldsymbol{\mathcal{K}_1}, \boldsymbol{\mathcal{K}_2}, \boldsymbol{\mathcal{K}_3})$ and $(\boldsymbol{\mathcal{L}_1}, \boldsymbol{\mathcal{L}_2}, \boldsymbol{\mathcal{L}_3})$: for the set of tests of $Exp\ A$, $\boldsymbol{\mathcal{K}_1} = \boldsymbol{\mathcal{K}_2} = \boldsymbol{\mathcal{K}_3} = -1$ and $\boldsymbol{\mathcal{L}_1} = \boldsymbol{\mathcal{L}_2} = \boldsymbol{\mathcal{L}_3} = 1$; for the set of tests of $Exp\ B$, $\boldsymbol{\mathcal{K}_1} = \boldsymbol{\mathcal{K}_2} = \boldsymbol{\mathcal{K}_3} = -2$ and $\boldsymbol{\mathcal{L}_1} = \boldsymbol{\mathcal{L}_2} = \boldsymbol{\mathcal{L}_3} = 2$.

	$Exp\ A$ and $Exp\ B$		
	$\mathcal{N}_2$	$\mathcal{N}_3$	$\mathcal{N}_4$
$Test\ 1$	**4**	**4**	**4**
$Test\ 2$	**4**	**4**	**8**
$Test\ 3$	**4**	**8**	**4**
$Test\ 4$	**8**	**4**	**4**

Table 3.4 : Experimental parameters of $\boldsymbol{\mathcal{N}_2}$, $\boldsymbol{\mathcal{N}_3}$ and $\boldsymbol{\mathcal{N}_4}$ for the sets of tests of $Exps\ \ A$ and B. The fixed input parameters are: $\boldsymbol{\mathcal{N}_1} = 20$ points, $\boldsymbol{\mathcal{M}_3} = 300$ and $\boldsymbol{\mathcal{M}_2} = 50$. See also text for details.

Each element of $\{\boldsymbol{\mathcal{S}_\mu}\}$ where $\boldsymbol{\mathcal{S}_\mu} \equiv$ control points is registered against each corresponding element of $\{\boldsymbol{\mathcal{W}_\mu}\}$ leading to $\{(E^{(\mu)}, \psi^{\mu)})\}$ and $\{\mathcal{F}_2(\boldsymbol{\mathcal{S}_\mu}; \theta)\}$, and by extension to $\{\mathcal{F}_2(\boldsymbol{\mathcal{M}_0} - \boldsymbol{\mathcal{S}_\mu}; \theta)\}$ using $\boldsymbol{\mathcal{S}_\mu}$ as control points. The registration accuracy is calculated by averaging out all $TREs$ arising from random selections (100 times in number) of $\boldsymbol{d}$ Cartesian points from $\mathcal{F}_1(\boldsymbol{\mathcal{M}_0}; \theta) - \boldsymbol{\mathcal{W}_l}$ and determining the distances between them and their correspondences in $\mathcal{F}_2(\boldsymbol{\mathcal{M}_0} - \boldsymbol{\mathcal{S}_l}; \theta)$ according to Equation (3.1), and $\forall\ \boldsymbol{d} \in \{3,5,10,15\}$ and for each set of tests in $Exps\ \ A$ and B. This process is repeated between each element of $\{\mathcal{F}_1(\boldsymbol{\mathcal{M}_0}; \theta) - \boldsymbol{\mathcal{W}_\mu}\}$ and its counterpart in $\{\mathcal{F}_2(\boldsymbol{\mathcal{M}_0} - \boldsymbol{\mathcal{S}_\mu}; \theta)\}$. The same input files were used for all registration methods. The computed $TREs$ showed no dependence on $\boldsymbol{d}$ and the random configuration of target markers. The average $TREs$ for each set of tests of $Exp\ A$ and $Exp\ B$ are tabulated in Tables 3.5 and 3.6, respectively.

		Average $TREs$ for $Exp\ A$ (mm)					
		$s_{50} \rightarrow w_{50}$	$s_{100} \rightarrow w_{100}$	$s_{150} \rightarrow w_{150}$	$s_{200} \rightarrow w_{200}$	$s_{250} \rightarrow w_{250}$	$s_{300} \rightarrow w_{300}$
$KC + TPS$	$Test\ 1$	▨	**1.5520±0.1918**	**1.2533±0.1567**	**1.2365±0.1900**	**1.4987±0.2943**	**1.1437±0.1695**
	$Test\ 2$	▨	**2.0206±0.3313**	**2.1647±0.3804**	**2.0431±0.3867**	**1.9324±0.3545**	▨
	$Test\ 3$	▨	**2.0074±0.2409**	▨	**1.2250±0.2114**	**1.5649±0.2595**	**1.650±0.2114**
	$Test\ 4$	**2.1498±0.2596**	**1.4365±0.1860**	**1.7726±0.2058**	▨	▨	▨
$GMM + TPS$	$Test\ 1$	▨	▨	▨	▨	▨	▨
	$Test\ 2$	**2.2475±0.3047**	**2.0114±0.3295**	**2.2435±0.3809**	**2.0866±0.4189**	**1.9576±0.3632**	**1.9354±0.3393**
	$Test\ 3$	**1.7484±0.1977**	**2.0677±0.2725**	**1.4203±0.1508**	**1.3041±0.2276**	**1.5930±0.3021**	**1.6465±0.1669**
	$Test\ 4$	**2.1511±0.2796**	**1.4467±0.1813**	**1.7103±0.1941**	**1.7267±0.1997**	**1.4554±0.2134**	**1.3450±0.2337**
$EM + TPS$	$Test\ 1$	**0.8029±0.1000**	**0.6936±0.0991**	**0.5911±0.0774**	▨	**0.5823±0.0693**	**0.5475±0.0767**
	$Test\ 2$	▨	**0.6351±0.0878**	**0.5997±0.0825**	**0.5492±0.0674**	▨	**0.5624±0.0612**
	$Test\ 3$	**0.8678±0.1200**	**0.6767±0.1046**	**0.5897±0.0919**	**0.5679±0.0788**	**0.5877±0.0713**	**0.5620±0.0744**
	$Test\ 4$	**0.7223±0.1298**	**0.7120±0.1537**	**0.6424±0.1002**	**0.5901±0.0680**	**0.6160±0.1021**	**0.8822±0.3037**

Table 3.5: Average $TREs$ for each set of tests of $Exp\ A$, $\boldsymbol{d} = 15$, and for all registration methods. Empty spaces represent failed registrations.

		Average $TREs$ for $Exp\ B$ (mm)					
		$s_{50} \rightarrow w_{50}$	$s_{100} \rightarrow w_{100}$	$s_{150} \rightarrow w_{150}$	$s_{200} \rightarrow w_{200}$	$s_{250} \rightarrow w_{250}$	$s_{300} \rightarrow w_{300}$
$KC + TPS$	$Test\ 1$	**2.1903±0.1782**	▨	**1.7820±0.1261**	**1.8724±0.1787**	**1.7356±0.1338**	**1.8936±0.1624**
	$Test\ 2$	**2.4687±0.2397**	**2.8344±0.3788**	**2.2143±0.2117**	**2.2359±0.1873**	**2.5476±0.2358**	**2.2117±0.2290**
	$Test\ 3$	**3.0463±0.3208**	**2.0409±0.1983**	**2.5483±0.1865**	**2.5077±0.2063**	**2.4344±0.2293**	**2.3744±0.2066**
	$Test\ 4$	**2.5737±0.2327**	**2.1146±0.1833**	▨	▨	**2.2232±0.2516**	**2.1490±0.1746**
$GMM + TPS$	$Test\ 1$	▨	**2.3020±0.2411**	**1.7840±0.1154**	**1.9119±0.1455**	**1.7140±0.1465**	**2.0292±0.1623**
	$Test\ 2$	**2.4666±0.2246**	▨	**2.2364±0.2183**	**2.2595±0.1557**	**2.4297±0.1649**	**2.3578±0.1991**
	$Test\ 3$	▨	**2.1625±0.1815**	**2.5500±0.2115**	**2.6899±0.2261**	**2.3701±0.2387**	▨
	$Test\ 4$	▨	▨	▨	▨	▨	▨
$EM + TPS$	$Test\ 1$	▨	**1.3170±0.1017**	**1.1466±0.1105**	**1.0911±0.0882**	**1.4985±0.2095**	**1.0171±0.1074**
	$Test\ 2$	**1.6750±0.1345**	**1.4960±0.2571**	**1.1166±0.0918**	**1.0526±0.1071**	**1.1806±0.2677**	**0.9735±0.0924**
	$Test\ 3$	▨	**1.1785±0.1315**	▨	**1.1180±0.1114**	**1.1201±0.1252**	**1.0702±0.1017**
	$Test\ 4$	**1.3659±0.1089**	**1.1613±0.1027**	**1.1344±0.1010**	**1.1451±0.1395**	**1.1805±0.1570**	**1.2799±0.2195**

Table 3.6: Average $TREs$ for each set of tests of $Exp\ B$, $\boldsymbol{d} = 15$, and for all registration methods. Empty spaces represent failed registrations.

3.7 Measuring the accuracy of registration within the space of common overlap

3.7.1 Occlusion, deformation and their combined impact on TRE

The capabilities of the non-rigid algorithms to handle incomplete (due to occlusion) and deformed target surfaces are examined. The target model is produced by randomly selecting surface patches from the source followed by the application of a random TPS transformation. The size for the area of the target surface (hence the common overlap) is fixed in these experiments (it is varied in the experiments of Section 3.8).

Incomplete surfaces in the target will be ‘statistically’ recovered using the algorithms’ surface-hole- and partial-view- filling capabilities. Large parts of missing surface in the target (more than half missing) can be recovered by incorporating the geometric information encoded in the *corresponding* source template point cloud to propagate a regularized deformation along the missing surface. The accuracy of registration is determined by TRE calculations.

***Algorithm* 6:** Generation of *occluded* and deformed target models of registration by random selection of source surface patches and application of a TPS warp onto them. (See also Figure 3.15.)

Input: The original *full* source model set $\boldsymbol{\mathcal{M}_0}$; $\boldsymbol{\mathcal{N}_1}$ which corresponds to the number of elements of $\{\boldsymbol{\mathcal{P}_i}\}$ where $\boldsymbol{\mathcal{P}_i}$ represents a surface patch randomly selected from $\boldsymbol{\mathcal{M}_0}$; $\boldsymbol{\mathcal{N}_2}$ which is the number of *cells* (geometric arrangements of $3D$ Cartesian points) per surface patch; $\boldsymbol{\mathcal{M}_3}$ which is the maximum number of points selected randomly from $\boldsymbol{\mathcal{P}_i}$ to serve as source control points for the (random) TPS transformation applied onto $\boldsymbol{\mathcal{P}_i}$ to produce $\mathcal{F}_1^{(l)}(\boldsymbol{\mathcal{P}_i};\theta)$; the increment parameter $\boldsymbol{\mathcal{M}_2}$ which is iteratively added to the running total of selected source control points k until $\boldsymbol{\mathcal{M}_3}$ is reached; $\boldsymbol{\mathcal{N}_3}$, $\boldsymbol{\mathcal{N}_4}$, and $\boldsymbol{\mathcal{N}_5}$ which relate, respectively, to the upper limits of three uniform distributions with lower limits zero (defined as $\boldsymbol{\mathcal{N}_4}$, $\boldsymbol{\mathcal{N}_5}$ and $\boldsymbol{\mathcal{N}_6}$ in ***Algorithm* 1**, respectively); the number of elements $\boldsymbol{\mathcal{N}_6}$ of a random subset of $\boldsymbol{\mathcal{P}_i}$, call it $\boldsymbol{\mathcal{V}_i}$, which serves as the source model of registration.

Output: $\{\boldsymbol{\mathcal{P}}_i\}$; $\{\boldsymbol{\mathcal{V}}_i\}$; $\{\boldsymbol{\mathcal{P}}_i - \boldsymbol{\mathcal{V}}_i\}$ which provides the set of source target marker points for the TRE calculations; $\left\{\mathcal{F}_1^{(l)}(\boldsymbol{\mathcal{P}}_i;\theta)\right\}$, $\left\{\mathcal{F}_1^{(l)}(\boldsymbol{\mathcal{V}}_i;\theta)\right\}$ and $\left\{\mathcal{F}_1^{(l)}(\boldsymbol{\mathcal{P}}_i - \boldsymbol{\mathcal{V}}_i;\theta)\right\}$ $\forall\ i \in \{1,\dots,\boldsymbol{\mathcal{N}}_1\}$. The number of elements of the latter sets are $\frac{\boldsymbol{\mathcal{M}}_3-\boldsymbol{\mathcal{M}}_2}{\boldsymbol{\mathcal{M}}_2}$ for a given i, *i.e.*, $l \in \left\{1,\dots,\frac{\boldsymbol{\mathcal{M}}_3-\boldsymbol{\mathcal{M}}_2}{\boldsymbol{\mathcal{M}}_2}\right\}$.

```
Compute the total number of cells for $\boldsymbol{\mathcal{M}}_0$, call it $\boldsymbol{\tau}$.
$for \quad i = 1 \quad to \quad \boldsymbol{\mathcal{N}}_1 \qquad \{i \coloneqq i+1\}$
    Randomly select a cell from $\boldsymbol{\mathcal{M}}_0$, call it $\delta$.
    $if\ (\delta + \boldsymbol{\mathcal{N}}_2 \le \boldsymbol{\tau})$
        $for \quad f = \delta \quad to \quad \delta + \boldsymbol{\mathcal{N}}_2 \qquad \{f \coloneqq f+1\}$
            Select corresponding cell labels from $\boldsymbol{\mathcal{M}}_0$ to produce a continuous surface patch $\boldsymbol{\mathcal{P}}_i$.
        $end\ for$
    $else$
        $for \quad f = \delta \quad to \quad \boldsymbol{\tau} \qquad \{f \coloneqq f+1\}$
            Select corresponding cell labels from $\boldsymbol{\mathcal{M}}_0$ to produce part of a continuous surface patch $\boldsymbol{\mathcal{P}}_i$.
        $end\ for$
        Randomly select a new cell from $\boldsymbol{\mathcal{M}}_0$, call it $\boldsymbol{\gamma}$.
            $if\ (\boldsymbol{\gamma} + \delta + \boldsymbol{\mathcal{N}}_2 - \boldsymbol{\tau} \le \boldsymbol{\tau})$
                $for \quad f = \boldsymbol{\gamma} \quad to \quad \boldsymbol{\gamma} + \delta + \boldsymbol{\mathcal{N}}_2 - \boldsymbol{\tau} \qquad \{f \coloneqq f+1\}$
                    Select corresponding cell labels from $\boldsymbol{\mathcal{M}}_0$ to produce another random continuous surface patch s.t. the total number of cells of $\boldsymbol{\mathcal{P}}_i$ becomes $\boldsymbol{\mathcal{N}}_2$.
                $end\ for$
            $else$
```

```
18:             $for \quad f = 0 \quad to \quad \delta + \boldsymbol{\mathcal{N}_2} - \boldsymbol{\tau} \qquad \{f \coloneqq f + 1\}$
19:                 Select corresponding *cell* labels from $\boldsymbol{\mathcal{M}_0}$ counting from the first *cell* label to produce another continuous surface patch *s.t.* the total number of *cells* of $\boldsymbol{\mathcal{P}_i}$ becomes $\boldsymbol{\mathcal{N}_2}$.
20:             $end\ for$
21:         $end\ if$
22:     $end\ if$
23:     Randomly select $\boldsymbol{\mathcal{N}_6}$ points from $\boldsymbol{\mathcal{P}_i}$ to produce $\boldsymbol{\mathcal{V}_i}$ and $\boldsymbol{\mathcal{P}_i} - \boldsymbol{\mathcal{V}_i}$.
24:         $for \quad k = \boldsymbol{\mathcal{M}_2} \quad to \quad \boldsymbol{\mathcal{M}_3} \qquad \{k \coloneqq k + \boldsymbol{\mathcal{M}_2}\}$
25:             Randomly select $k$ points from $\boldsymbol{\mathcal{P}_i}$ to form the set of source control points required for the calculation of the affine and $TPS$ transformation parameters of $\mathcal{F}_1^{(l)}$.
26:             Produce the random target points of $\mathcal{F}_1^{(l)}$ according to Step 5 of ***Algorithm*** **1**, compute the transformation and apply it onto $\boldsymbol{\mathcal{P}_i}$ to generate $\mathcal{F}_1^{(l)}(\boldsymbol{\mathcal{P}_i}; \theta)$.
27:             Identify the correspondences of $\boldsymbol{\mathcal{V}_i}$ and $\boldsymbol{\mathcal{P}_i} - \boldsymbol{\mathcal{V}_i}$ in $\mathcal{F}_1^{(l)}(\boldsymbol{\mathcal{P}_i}; \theta)$ to produce the target model of registration $\mathcal{F}_1^{(l)}(\boldsymbol{\mathcal{V}_i}; \theta)$ and the set of "deformed" target markers $\mathcal{F}_1^{(l)}(\boldsymbol{\mathcal{P}_i} - \boldsymbol{\mathcal{V}_i}; \theta)$, respectively.
28:         $end\ for$
29:     $end\ for$
```

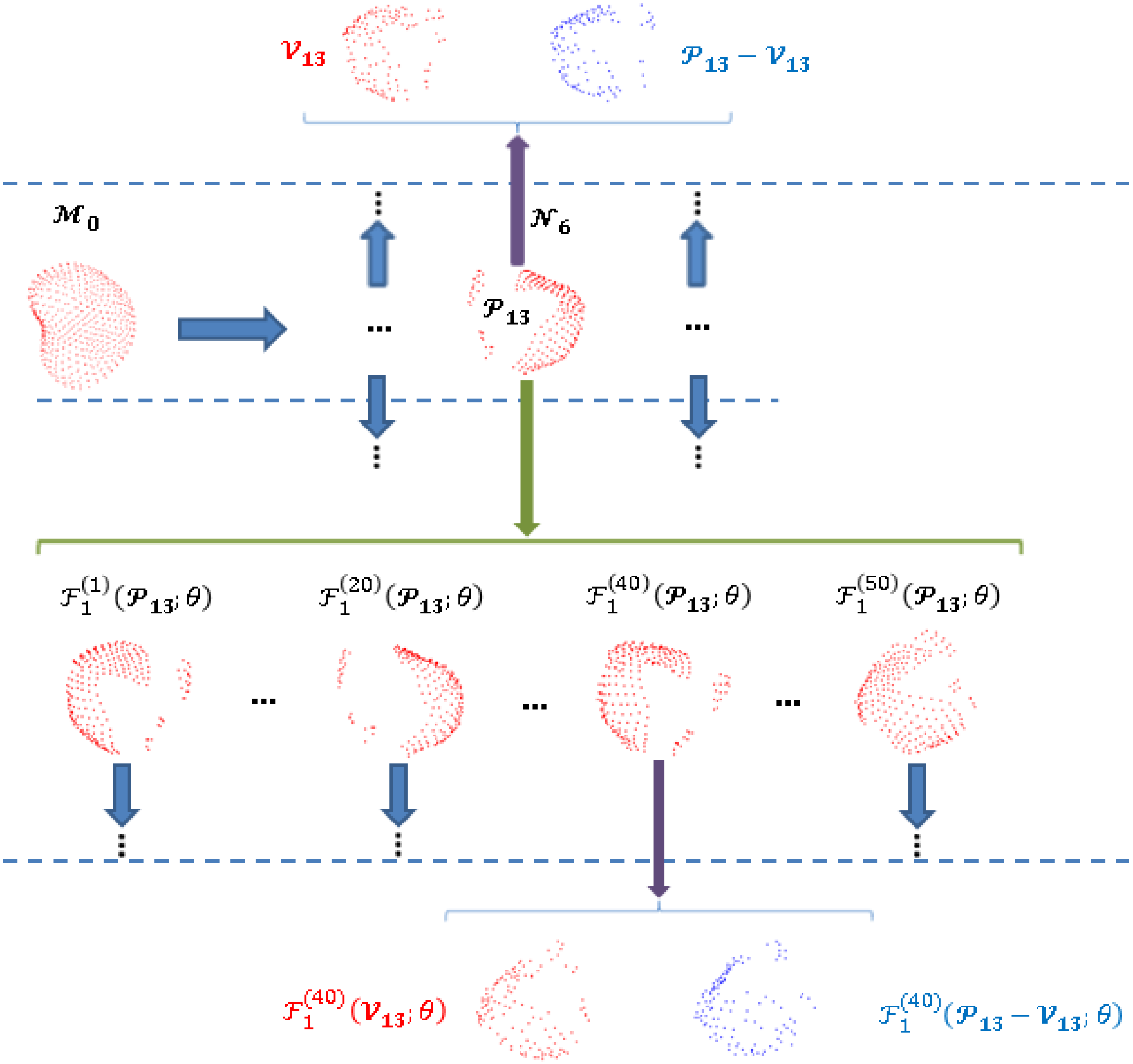

Figure 3.15: A diagrammatic representation of ***Algorithm* 6**.

One experiment for each registration method was conducted where $\mathcal{N}_1 = 100$, $\mathcal{N}'_2 = 300$ points (converted from $\mathcal{N}_2$; it corresponds to 46% of total source surface), $\mathcal{M}_3 = 51$, $\mathcal{M}_2 = 1$, $\mathcal{N}_3 = \mathcal{N}_4 = \mathcal{N}_5 = 3$, and $\mathcal{N}_6 = 150$.

In order to exploit the "correctness" of the established correspondences in *full*-to-*partial* model registration, the registration process takes place twice: (*i*) between $\mathcal{V}_i$ ($\equiv$ control points) and each element of $\left\{\mathcal{F}_1^{(l)}(\mathcal{V}_i;\theta)\right\}$, *i.e.*, $\forall\ l \in \left\{1,\dots,\frac{\mathcal{M}_3-\mathcal{M}_2}{\mathcal{M}_2}\right\}$ for a given i, producing as output $\left\{\left(E_i{}^{(l)},\psi_i{}^{(l)}\right)\right\}$ and $\left\{\mathcal{F}_2^{(l)}(\mathcal{V}_i;\theta)\right\}$ as well as $\left\{\mathcal{F}_2^{(l)}(\mathcal{P}_i-\mathcal{V}_i;\theta)\right\}$ using $\mathcal{V}_i$

as control points. The same process is repeated $\forall\ i\ \epsilon\{1,\dots,\boldsymbol{\mathcal{N}}_{\mathbf{1}}\}$; and (*ii*) between $\boldsymbol{\mathcal{M}}_{\mathbf{0}}$ (using as control points the set of extracted points from the *full* source; both the set of control points and the *full* source are updated during the process of registration) and each element of $\left\{\mathcal{F}_1^{(l)}(\boldsymbol{\mathcal{V}}_{\boldsymbol{i}};\theta)\right\}$, *i.e.*, $\forall\ l \in \left\{1,\dots,\frac{\boldsymbol{\mathcal{M}}_3-\boldsymbol{\mathcal{M}}_2}{\boldsymbol{\mathcal{M}}_2}\right\}$ and $\forall\ i\ \epsilon\{1,\dots,\boldsymbol{\mathcal{N}}_{\mathbf{1}}\}$, producing as final output $\left\{\mathcal{F}_i^{(l)}(\boldsymbol{\mathcal{M}}_{\mathbf{0}};\theta)\right\}$ as well as $\left\{\mathcal{F}_2'^{(l)}(\boldsymbol{\mathcal{P}}_{\boldsymbol{i}}-\boldsymbol{\mathcal{V}}_{\boldsymbol{i}};\theta)\right\}$.

Each element of the latter set corresponds to the final positions of the transformed target markers which are updated iteratively during the process of registration based upon the affine and TPS parameters produced from the registration between the (updated) extracted source model (which also serves as control points for the transformation applied to the set of target markers) and the fixed target model.

The intersection between the (updated) extracted source model and the set of (transformed) target markers should be the null set. Otherwise the computed accuracy of registration between the *full* source model and the occluded target model may be misleading. As it is impossible to impose this requirement in these experiments, the computational results of this section should be viewed with this in mind. Random visual inspections of these sets have indicated some overlap.

The TRE calculations for (*i*) [and (*ii*)] are conducted by randomly selecting $\boldsymbol{d}$ points (where $\boldsymbol{d} \in \{3,5,10,15\}$) from $\mathcal{F}_1^{(l)}(\boldsymbol{\mathcal{P}}_{\boldsymbol{i}}-\boldsymbol{\mathcal{V}}_{\boldsymbol{i}};\theta)$ and determining the distances between them and their correspondences in $\mathcal{F}_2^{(l)}(\boldsymbol{\mathcal{P}}_{\boldsymbol{i}}-\boldsymbol{\mathcal{V}}_{\boldsymbol{i}};\theta)$ $\left[\mathcal{F}_2'^{(l)}(\boldsymbol{\mathcal{P}}_{\boldsymbol{i}}-\boldsymbol{\mathcal{V}}_{\boldsymbol{i}};\theta)\right]$ for a given (l,i). This process takes place 100 times and is repeated between each element of $\left\{\mathcal{F}_1^{(l)}(\boldsymbol{\mathcal{P}}_{\boldsymbol{i}}-\boldsymbol{\mathcal{V}}_{\boldsymbol{i}};\theta)\right\}$ and its counterpart in $\left\{\mathcal{F}_2^{(l)}(\boldsymbol{\mathcal{P}}_{\boldsymbol{i}}-\boldsymbol{\mathcal{V}}_{\boldsymbol{i}};\theta)\right\}$ $\left[\left\{\mathcal{F}_2'^{(l)}(\boldsymbol{\mathcal{P}}_{\boldsymbol{i}}-\boldsymbol{\mathcal{V}}_{\boldsymbol{i}};\theta)\right\}\right]$ $\forall\ i\ \epsilon\{1,\dots,\boldsymbol{\mathcal{N}}_{\mathbf{1}}\}$,$\forall\ l \in \left\{1,\dots,\frac{\boldsymbol{\mathcal{M}}_3-\boldsymbol{\mathcal{M}}_2}{\boldsymbol{\mathcal{M}}_2}\right\}$ and $\forall\ \boldsymbol{d} \in \{3,5,10,15\}$ using a similar approach to the one taken in ***Algorithm* 2**. The input files were the same for all registration methods. The computed $TREs$ showed no significant dependence on the value of $\boldsymbol{d}$ and the random configuration of target markers. The average TRE is computed by the relationship $Average\ TRE = \frac{\sum_{l,i,d,z} TRE_z^{(l;i;d)}}{Total\ Number\ of TREs}$ where $z \in \{1,\dots,100\}$ designates the zth random selection of $\boldsymbol{d}$ markers and $Total\ Number\ of TREs = 100 \times 50 \times 100 \times 4 = 2000000$. The computed registration accuracies for (*i*) and (*ii*) and all registration methods are shown in Table 3.7.

	$Average\ TRE\ (mm)$	
	(*i*)	**(*ii*)**
$KC + TPS$	**0.7621 ± 0.6544**	**1.2197 ± 1.2198**
$GMM + TPS$	**0.7503 ± 0.7953**	**1.2911 ± 1.2520**
$EM + TPS$	**0.2527 ± 0.3258**	**3.2141 ± 0.6542**

Table 3.7: Average $TREs$ for (*i*) and (*ii*) and all registration methods.

The large discrepancy between the $EM + TPS$ results and the $GMM + TPS$ and $KC + TPS$ ones in (*ii*) of Table 3.7 is attributed to the fact that the extracted source model contains (aside from points with true correspondences in the target) points that have no correspondences in the target. The latter ones are treated in the $EM + TPS$ algorithm as equally strong candidates for assignment to target points due to the smoothness of the prostate surface, which reduces the accuracy of the computed affine and TPS parameters. The $GMM + TPS$ and $KC + TPS$ algorithms treat the surface of the extracted source model as a whole in determining correspondences based upon a smoother process of optimization. (See Chapter 5 for more details).

3.7.2 Occlusion, deformation, Gaussian noise and their combined impact on TRE

The output from ***Algorithm* 6** of Section 3.7.1, specifically, $\left\{\mathcal{F}_1^{(l)}(\boldsymbol{\mathcal{V}}_i;\theta)\right\}$ $\forall\ i \in \{1,\dots,\boldsymbol{\mathcal{N}_1}\}$ and $\forall\ l \in \left\{1,\dots,\frac{\boldsymbol{\mathcal{M}_3}-\boldsymbol{\mathcal{M}_2}}{\boldsymbol{\mathcal{M}_2}}\right\}$, becomes input for ***Algorithm* 7** and is updated to include the contribution of Gaussian noise. (See also Figure 3.16.)

***Algorithm* 7:** Generation of *occluded*, deformed and noisy target models of registration.

Input: The mean μ of the Gaussian normal distribution and its standard deviation σ; $\boldsymbol{\mathcal{N}_1}$, $\boldsymbol{\mathcal{M}_3}$, $\boldsymbol{\mathcal{M}_2}$, and $\left\{\mathcal{F}_1^{(l)}(\boldsymbol{\mathcal{V}}_i;\theta)\right\}$ $\forall\ i \in \{1,\dots,\boldsymbol{\mathcal{N}_1}\}$ and $\forall\ l \in \left\{1,\dots,\frac{\boldsymbol{\mathcal{M}_3}-\boldsymbol{\mathcal{M}_2}}{\boldsymbol{\mathcal{M}_2}}\right\}$ (as defined in ***Algorithm* 6**).

Output: $\left\{\mathcal{G}_1^{(l)}(\boldsymbol{\mathcal{V}}_i;\theta)\right\}$ $\forall\ i \in \{1,\dots,\boldsymbol{\mathcal{N}_1}\}$ and $\forall\ l \in \left\{1,\dots,\frac{\boldsymbol{\mathcal{M}_3}-\boldsymbol{\mathcal{M}_2}}{\boldsymbol{\mathcal{M}_2}}\right\}$ where $\mathcal{G}_1^{(l)}(\boldsymbol{\mathcal{V}}_i;\theta)$ represents $\mathcal{F}_1^{(l)}(\boldsymbol{\mathcal{V}}_i;\theta)$ perturbed by Gaussian noise.

```
for $i = 1$ to $\boldsymbol{\mathcal{N}_1}$ $\{i \coloneqq i+1\}$
    for $l = 1$ to $\boldsymbol{\mathcal{M}_3} - \boldsymbol{\mathcal{M}_2}$ $\{l \coloneqq l+1\}$
        $\mathcal{F}_1^{(l)}(\boldsymbol{\mathcal{V}_i};\theta)$ is updated to include the effect of Gaussian noise for fixed $(\mu,\sigma)$
        generating $\mathcal{G}_1^{(l)}(\boldsymbol{\mathcal{V}_i};\theta)$ (following a similar approach to the one taken in
        Section 3.4).
    end for
end for
```

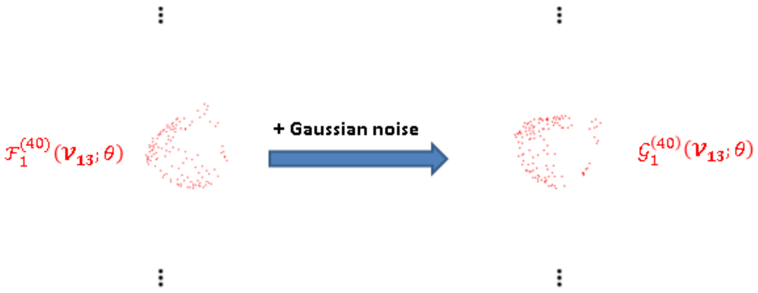

Figure 3.16: The injection of Gaussian noise with $(\mu,\sigma) = (0, 0.450)$ in an occluded and deformed target surface.

The registration occurs twice: (*i*) between $\boldsymbol{\mathcal{V}_i}$ ($\equiv$ control points) and each element of $\left\{\mathcal{G}_1^{(l)}(\boldsymbol{\mathcal{V}_i};\theta)\right\}$ $\forall\ i \in \{1,\ldots,\boldsymbol{\mathcal{N}_1}\}$ and $\forall\ l \in \left\{1,\ldots,\frac{\boldsymbol{\mathcal{M}_3}-\boldsymbol{\mathcal{M}_2}}{\boldsymbol{\mathcal{M}_2}}\right\}$ producing as output $\left\{\left({E_i}^{(l)},{\psi_i}^{(l)}\right)\right\}$ and $\left\{\mathcal{G}_2^{(l)}(\boldsymbol{\mathcal{V}_i};\theta)\right\}$ as well as $\left\{\mathcal{G}_2^{(l)}(\boldsymbol{\mathcal{P}_i}-\boldsymbol{\mathcal{V}_i};\theta)\right\}$ using $\boldsymbol{\mathcal{V}_i}$ as control points; and (*ii*) between $\boldsymbol{\mathcal{M}_0}$ and each element of $\left\{\mathcal{G}_1^{(l)}(\boldsymbol{\mathcal{V}_i};\theta)\right\}$ $\forall\ i \in \{1,\ldots,\boldsymbol{\mathcal{N}_1}\}$ and $\forall\ l \in \left\{1,\ldots,\frac{\boldsymbol{\mathcal{M}_3}-\boldsymbol{\mathcal{M}_2}}{\boldsymbol{\mathcal{M}_2}}\right\}$ producing as final output $\left\{\mathcal{G}_i^{(l)}(\boldsymbol{\mathcal{M}_0};\theta)\right\}$ as well as $\left\{\mathcal{G}_2'^{(l)}(\boldsymbol{\mathcal{P}_i}-\boldsymbol{\mathcal{V}_i};\theta)\right\}$. The computed average *TREs* are given in Table 3.8.

	$\boldsymbol{Average\,TRE}$ $\boldsymbol{(mm)}$	
	(*i*)	**(*ii*)**
$\boldsymbol{KC+TPS}$	**1.0306 ± 0.5587**	**2.0246 ± 1.2965**
$\boldsymbol{GMM+TPS}$	**1.0160 ± 0.5435**	**2.1313 ± 1.3521**
$\boldsymbol{EM+TPS}$	**[†]0.6893 ± 0.4751**	**3.2350 ± 0.6538**

Table 3.8: Average $TREs$ for (*i*) and (*ii*) computed by adding Gaussian noise $(\mu,\sigma)=(0, 0.450)$ on occluded and deformed surfaces and for all registration methods. [†]The corresponding value in the absence of row and column normalization of $\mathcal{T}$ is (2.8872 ± 0.5332) mm.

3.8 Measuring the accuracy of registration in the space beyond common overlap

3.8.1 Occlusion, deformation and their combined impact on TRE

***Algorithm* 8:** Generation of *occluded* and deformed target models of registration for measuring the accuracy of registration beyond common overlap. (See also Figure 3.17.)

Input: The original *full* source model set $\boldsymbol{\mathcal{M}_0}$; $\boldsymbol{\mathcal{M}_2}$ which corresponds to the maximum number of points selected randomly from $\boldsymbol{\mathcal{M}_0}$ to serve as source control points for the (random) TPS transformation applied onto $\boldsymbol{\mathcal{M}_0}$ to produce $\mathcal{F}_1^{(l)}(\boldsymbol{\mathcal{M}_0};\theta)$; the increment parameter $\boldsymbol{\mathcal{M}_1}$ which is iteratively added to the running total of selected source control points k until $\boldsymbol{\mathcal{M}_2}$ is reached; $\boldsymbol{\mathcal{N}_1}$, $\boldsymbol{\mathcal{N}_2}$, and $\boldsymbol{\mathcal{N}_3}$ which relate, respectively, to the upper limits of three uniform distributions with lower limits zero (defined as $\boldsymbol{\mathcal{N}_4}$, $\boldsymbol{\mathcal{N}_5}$ and $\boldsymbol{\mathcal{N}_6}$ in ***Algorithm* 1**, respectively); $\boldsymbol{\mathcal{N}_4}$ which corresponds to the number of elements of $\left\{\boldsymbol{\mathcal{P}_i^{(l)}}\right\}$ where $\boldsymbol{\mathcal{P}_i^{(l)}}$ represents a surface patch randomly selected from $\mathcal{F}_1^{(l)}(\boldsymbol{\mathcal{M}_0};\theta)$. $\boldsymbol{\mathcal{P}_i^{(l)}}$ is the target of registration; $\boldsymbol{\mathcal{N}_5}$ which relates to the number of *cells* per surface patch $\left(\boldsymbol{\mathcal{P}_i^{(l)}}\right)$; the number of elements $\boldsymbol{\mathcal{N}_6}$ of a random subset of $\boldsymbol{\mathcal{M}_0}-\boldsymbol{\mathcal{O}_i^{(l)}}$, call it $\boldsymbol{\mathcal{V}_i^{(l)}}$, where $\boldsymbol{\mathcal{O}_i^{(l)}}$ represents the correspondence of $\boldsymbol{\mathcal{P}_i^{(l)}}$ in $\boldsymbol{\mathcal{M}_0}$. $\boldsymbol{\mathcal{V}_i^{(l)}}$ is appended to $\boldsymbol{\mathcal{O}_i^{(l)}}$ to produce the *full* source model of registration. $\boldsymbol{\mathcal{M}_0}-\boldsymbol{\mathcal{O}_i^{(l)}}-\boldsymbol{\mathcal{V}_i^{(l)}}$ provides the set of source target marker points for the "virtual" TRE calculations (see below). Assume that the correspondences of $\boldsymbol{\mathcal{M}}_{\mathbf{0}} - \boldsymbol{\mathcal{O}}_{\boldsymbol{i}}^{(l)} - \boldsymbol{\mathcal{V}}_{\boldsymbol{i}}^{(l)}$ in $\mathcal{F}_1^{(l)}(\boldsymbol{\mathcal{M}}_{\mathbf{0}};\theta) - \boldsymbol{\mathcal{P}}_{\boldsymbol{i}}^{(l)}$ are represented by $\boldsymbol{\mathcal{D}}_{\boldsymbol{i}}^{(l)}$.

Output: $\left\{\mathcal{F}_1^{(l)}(\boldsymbol{\mathcal{M}}_{\mathbf{0}};\theta)\right\}\ \forall\, l \in \left\{1,\dots,\frac{\boldsymbol{\mathcal{M}}_2-\boldsymbol{\mathcal{M}}_1}{\boldsymbol{\mathcal{M}}_1}\right\}$; $\left\{\boldsymbol{\mathcal{P}}_{\boldsymbol{i}}^{(l)}\right\}$, $\left\{\boldsymbol{\mathcal{O}}_{\boldsymbol{i}}^{(l)}\right\}$, $\left\{\mathcal{F}_1^{(l)}(\boldsymbol{\mathcal{M}}_{\mathbf{0}};\theta) - \boldsymbol{\mathcal{P}}_{\boldsymbol{i}}^{(l)}\right\}$, $\left\{\boldsymbol{\mathcal{V}}_{\boldsymbol{i}}^{(l)}\right\}$, $\left\{\boldsymbol{\mathcal{M}}_{\mathbf{0}} - \boldsymbol{\mathcal{O}}_{\boldsymbol{i}}^{(l)}\right\}$, $\left\{\boldsymbol{\mathcal{M}}_{\mathbf{0}} - \boldsymbol{\mathcal{O}}_{\boldsymbol{i}}^{(l)} - \boldsymbol{\mathcal{V}}_{\boldsymbol{i}}^{(l)}\right\}$, $\left\{\boldsymbol{\mathcal{V}}_{\boldsymbol{i}}^{(l)} + \boldsymbol{\mathcal{O}}_{\boldsymbol{i}}^{(l)}\right\}$ and $\left\{\boldsymbol{\mathcal{D}}_{\boldsymbol{i}}^{(l)}\right\}$ $\forall\, i \in \{1,\dots,\boldsymbol{\mathcal{N}}_{\mathbf{4}}\}$ and $\forall\, l \in \left\{1,\dots,\frac{\boldsymbol{\mathcal{M}}_2-\boldsymbol{\mathcal{M}}_1}{\boldsymbol{\mathcal{M}}_1}\right\}$.

```
$for \quad k = \boldsymbol{\mathcal{M}}_{\mathbf{1}} \quad to \quad \boldsymbol{\mathcal{M}}_{\mathbf{2}} \qquad \{k \coloneqq k + \boldsymbol{\mathcal{M}}_{\mathbf{1}}\}$
    Randomly select $k$ points from $\boldsymbol{\mathcal{M}}_{\mathbf{0}}$ to form the set of source control points required for the calculation of the affine and $TPS$ transformation parameters of $\mathcal{F}_1^{(l)}$.
    Produce the random target points of $\mathcal{F}_1^{(l)}$ according to Step 5 of Algorithm 1, compute the transformation and apply it onto $\boldsymbol{\mathcal{M}}_{\mathbf{0}}$ to generate $\mathcal{F}_1^{(l)}(\boldsymbol{\mathcal{M}}_{\mathbf{0}};\theta)$.
    $for \quad i = 1 \quad to \quad \boldsymbol{\mathcal{N}}_{\mathbf{4}} \qquad \{i \coloneqq i + 1\}$
        Apply steps 3-22 of Algorithm 6 to produce $\boldsymbol{\mathcal{P}}_{\boldsymbol{i}}^{(l)}$ from $\mathcal{F}_1^{(l)}(\boldsymbol{\mathcal{M}}_{\mathbf{0}};\theta)$.
        Identify the correspondences of $\boldsymbol{\mathcal{P}}_{\boldsymbol{i}}^{(l)}$ and those of $\mathcal{F}_1^{(l)}(\boldsymbol{\mathcal{M}}_{\mathbf{0}};\theta) - \boldsymbol{\mathcal{P}}_{\boldsymbol{i}}^{(l)}$ in $\boldsymbol{\mathcal{M}}_{\mathbf{0}}$ to produce $\boldsymbol{\mathcal{O}}_{\boldsymbol{i}}^{(l)}$ and $\boldsymbol{\mathcal{M}}_{\mathbf{0}} - \boldsymbol{\mathcal{O}}_{\boldsymbol{i}}^{(l)}$, respectively.
        Randomly select $\boldsymbol{\mathcal{N}}_{\mathbf{6}}$ Cartesian $3D$ points from $\boldsymbol{\mathcal{M}}_{\mathbf{0}} - \boldsymbol{\mathcal{O}}_{\boldsymbol{i}}^{(l)}$ to generate $\boldsymbol{\mathcal{V}}_{\boldsymbol{i}}^{(l)}$.
        Append $\boldsymbol{\mathcal{V}}_{\boldsymbol{i}}^{(l)}$ onto $\boldsymbol{\mathcal{O}}_{\boldsymbol{i}}^{(l)}$ to produce the full source model of registration.
        Identify the correspondences of $\boldsymbol{\mathcal{M}}_{\mathbf{0}} - \boldsymbol{\mathcal{O}}_{\boldsymbol{i}}^{(l)} - \boldsymbol{\mathcal{V}}_{\boldsymbol{i}}^{(l)}$ in $\mathcal{F}_1^{(l)}(\boldsymbol{\mathcal{M}}_{\mathbf{0}};\theta) - \boldsymbol{\mathcal{P}}_{\boldsymbol{i}}^{(l)}$ to produce $\boldsymbol{\mathcal{D}}_{\boldsymbol{i}}^{(l)}$.
    $end\ for$
$end\ for$
```

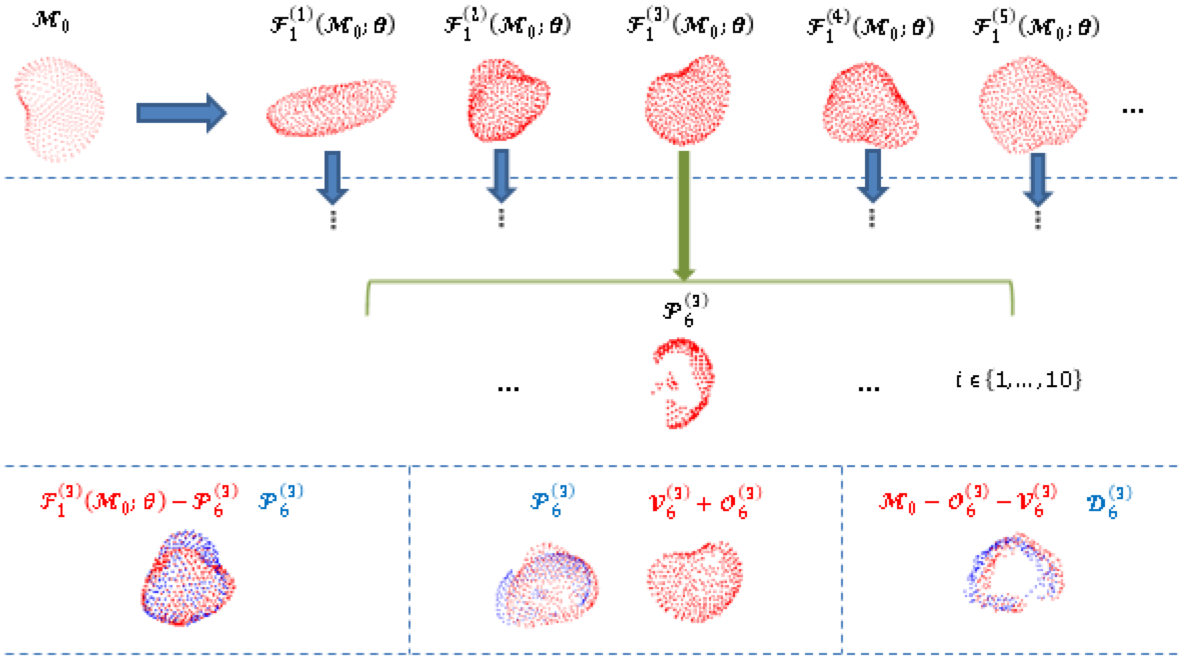

Figure 3.17: A diagrammatic representation of ***Algorithm* 8**.

Five different sets of experiments, $Exp\ A - Exp\ E$, were performed for all registration methods where all input parameters were kept fixed except $\mathcal{N}_5$ and $\mathcal{N}_6$ (See Table 3.9). As a result the accuracy of registration (measured in the space beyond common overlap) can be determined as a function of the size of the target surface (hence the area of common overlap) which is subject to deformation.

	$\boldsymbol{\mathcal{N}'_5}$	$\%\ \boldsymbol{of\ Total\ Surface}$	$\boldsymbol{\mathcal{N}_6}$
$Exp\ A$	50	7.6	320
$Exp\ B$	100	15	280
$Exp\ C$	150	23	250
$Exp\ D$	200	31	230
$Exp\ E$	250	38	210

Table 3.9: Experimental parameters of $\boldsymbol{\mathcal{N}'_5}$ and $\boldsymbol{\mathcal{N}_6}$ for the sets of experiments $A-E$. $\boldsymbol{\mathcal{N}'_5}$ is derived from $\boldsymbol{\mathcal{N}_5}$, and represents the number of $3D$ points per surface patch. The values of $\boldsymbol{\mathcal{N}_6}$ were specifically chosen to make the density of points across $\boldsymbol{\mathcal{V}_i^{(l)}}+\boldsymbol{\mathcal{O}_i^{(l)}}$ approximately constant. The fixed input parameters are: $\boldsymbol{\mathcal{N}_1}=\boldsymbol{\mathcal{N}_2}=\boldsymbol{\mathcal{N}_3}=6$, $\boldsymbol{\mathcal{M}_2}=105$, $\boldsymbol{\mathcal{M}_1}=5$ and $\boldsymbol{\mathcal{N}_4}=10$. See also text for details.

The registration takes place between $\boldsymbol{\mathcal{V}_i^{(l)}}+\boldsymbol{\mathcal{O}_i^{(l)}}$ (using as control points the set of extracted points from the *full* source model) and $\boldsymbol{\mathcal{P}_i^{(l)}}$ $\forall\, i \in \{1,\dots,\boldsymbol{\mathcal{N}_4}\}$ and $\forall\, l \in \left\{1,\dots,\frac{\boldsymbol{\mathcal{M}_2}-\boldsymbol{\mathcal{M}_1}}{\boldsymbol{\mathcal{M}_1}}\right\}$ producing as final output $\left\{\boldsymbol{\mathcal{B}}\left(\boldsymbol{\mathcal{V}_i^{(l)}}+\boldsymbol{\mathcal{O}_i^{(l)}};\theta\right)\right\}$ as well as $\left\{\boldsymbol{\mathcal{B}}\left(\boldsymbol{\mathcal{M}_0}-\boldsymbol{\mathcal{O}_i^{(l)}}-\boldsymbol{\mathcal{V}_i^{(l)}};\theta\right)\right\}$. See also Figure 3.18.

The TRE calculations were conducted by randomly selecting $\boldsymbol{d}$ target marker points (where $\boldsymbol{d} \in \{3,5,10,15\}$) from $\boldsymbol{\mathcal{B}}\left(\boldsymbol{\mathcal{M}_0}-\boldsymbol{\mathcal{O}_i^{(l)}}-\boldsymbol{\mathcal{V}_i^{(l)}};\theta\right)$ and determining the distances between them and their correspondences in $\boldsymbol{\mathcal{D}_i^{(l)}}$. The selection of $\boldsymbol{d}$ points is repeated 100 times. This process takes place $\forall\, i \in \{1,\dots,\boldsymbol{\mathcal{N}_4}\}$, $\forall\, l \in \left\{1,\dots,\frac{\boldsymbol{\mathcal{M}_2}-\boldsymbol{\mathcal{M}_1}}{\boldsymbol{\mathcal{M}_1}}\right\}$ and $\forall\, \boldsymbol{d} \in \{3,5,10,15\}$. The input files were the same for all registration methods. The computed $TREs$ showed no dependence on the value of $\boldsymbol{d}$ and the random configuration of the target markers.

The average TRE is computed by the relationship $Average\ TRE = \frac{\sum_{l,i,d,z} TRE_z^{(l;i;d)}}{Total\ Number\ of\ TREs}$ where $z \in \{1,\dots,100\}$ designates the zth random selection of $\boldsymbol{d}$ markers and $Total\ Number\ of\ TREs = 200000$. The computed registration accuracies for the sets of experiments $A-E$ and all registration methods are shown in Table 3.10.

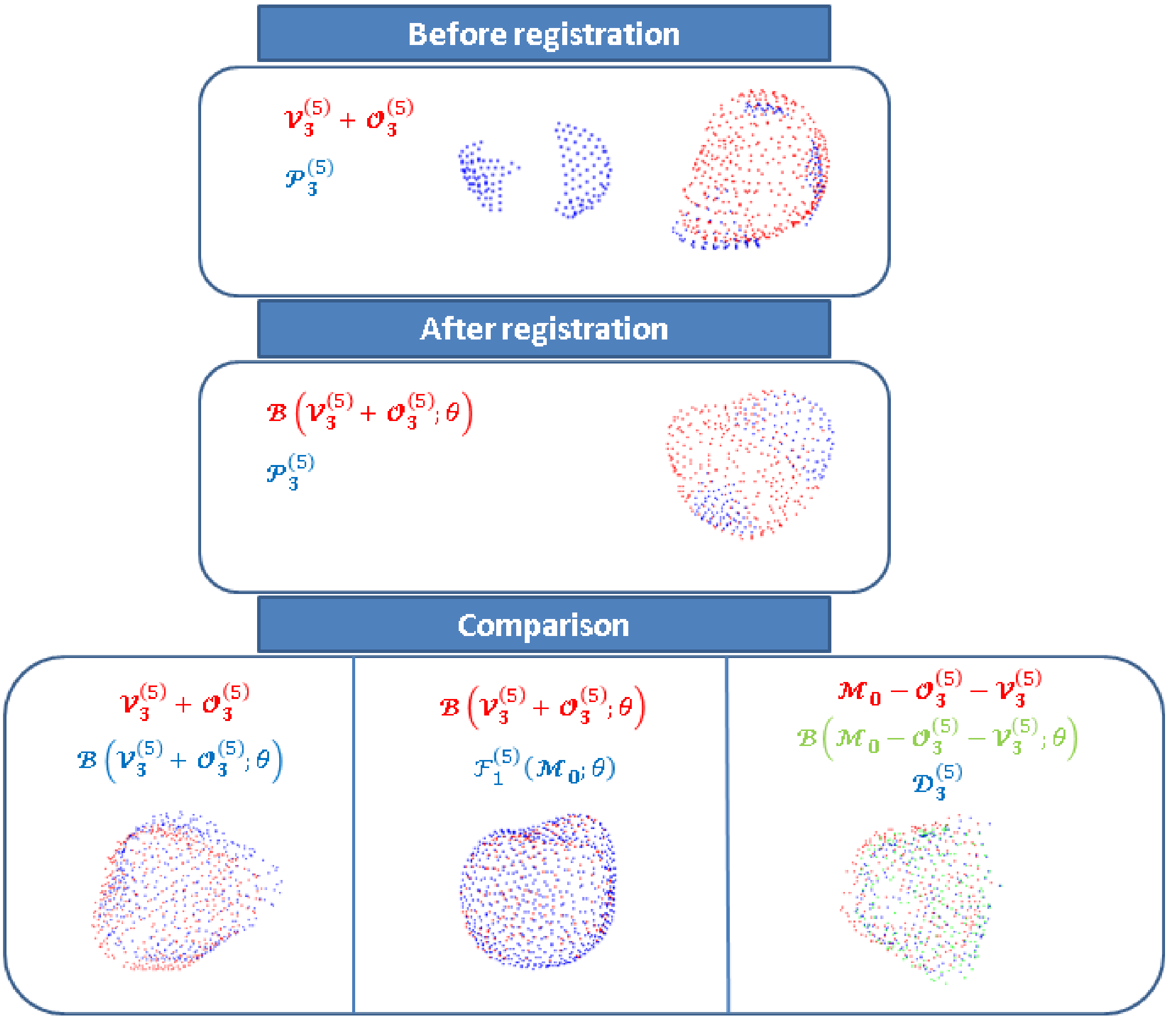

Figure 3.18: An example registration from the set of experiments C. $\boldsymbol{d} = 15$ markers are selected randomly from $\mathcal{B}\left(\mathcal{M}_0 - \mathcal{O}_3^{(5)} - \mathcal{V}_3^{(5)}; \theta\right)$ and the distances between them and their correspondences in $\mathcal{D}_3^{(5)}$ are determined. This process is repeated 100 times. By averaging out the so produced $TREs$ using the $KC + TPS$ method, it is calculated that Average $TRE = (2.0619 \pm 0.2643)\ mm$. The intersection between the (updated) extracted source model and the set of (transformed) target markers is by definition the null set.

	$\boldsymbol{Avg\ TRE\ (mm)}$				
	$\boldsymbol{Exp\ A}$	$\boldsymbol{Exp\ B}$	$\boldsymbol{Exp\ C}$	$\boldsymbol{Exp\ D}$	$\boldsymbol{Exp\ E}$
$\boldsymbol{KC+TPS}$	**3.4801±1.3737**	**2.7107±1.0604**	**2.4739±0.9746**	**2.2145±0.9751**	**2.1650±1.0154**
$\boldsymbol{GM+TPS}$	**3.5581±1.4063**	**2.7202±1.0547**	**2.4648±0.9620**	**2.2605±1.0233**	**2.1677±0.9716**
$\boldsymbol{EM+TPS}$					†**4.8100±0.8724**

Table 3.10: Average $TREs$ for the sets of experiments $A-E$. †The extracted source model is comprised of points with true correspondences in the target and points with no matching counterparts in the target. The latter originate in $\boldsymbol{\mathcal{V}}_{\boldsymbol{i}}^{(l)}$despite the fact that the maximum distance imposed in the extraction of the common overlap obtained quite low values. The empty spaces denote failed registrations.

3.8.2 Occlusion, deformation, Gaussian noise and their combined impact on $\boldsymbol{TRE}$

***Algorithm* 9:** Generation of *occluded*, deformed and noisy target models of registration for measuring the accuracy of registration beyond common overlap. (See also Figure 3.19.)

Input: $\boldsymbol{\mathcal{M}}_{\mathbf{0}}$, $\boldsymbol{\mathcal{M}}_{\mathbf{2}}$, $\boldsymbol{\mathcal{M}}_{\mathbf{1}}$, $\boldsymbol{\mathcal{N}}_{\mathbf{1}}$, $\boldsymbol{\mathcal{N}}_{\mathbf{2}}$, $\boldsymbol{\mathcal{N}}_{\mathbf{3}}$ and $\boldsymbol{\mathcal{N}}_{\mathbf{5}}$ as defined in ***Algorithm* 8** ($\mathcal{F}_1^{(l)}(\boldsymbol{\mathcal{M}}_{\mathbf{0}};\theta)$ maintains the same definition); the mean μ of the Gaussian normal distribution; σ_3 and σ_2 which represent, in respect, the maximum standard deviation of the Gaussian distribution and an increment parameter that is iteratively added to the running standard deviation σ until σ_3 is reached; $\boldsymbol{\mathcal{N}}_{\mathbf{4}}$ which corresponds to the number of elements of $\left\{\boldsymbol{\mathcal{P}}(i)_\sigma^{(l)}\right\}$ where $\boldsymbol{\mathcal{P}}(i)_\sigma^{(l)}$ represents the ith surface patch randomly selected from $\mathcal{G}_\sigma^{(l)}(\boldsymbol{\mathcal{M}}_{\mathbf{0}};\theta)$, which in turn relates to the updated $\mathcal{F}_1^{(l)}(\boldsymbol{\mathcal{M}}_{\mathbf{0}};\theta)$ with Gaussian noise (μ,σ). $\boldsymbol{\mathcal{P}}(i)_\sigma^{(l)}$ is the target of registration; the number of elements $\boldsymbol{\mathcal{N}}_{\mathbf{6}}$ of a random subset of $\boldsymbol{\mathcal{M}}_{\mathbf{0}}-\boldsymbol{\mathcal{O}}(i)_\sigma^{(l)}$, call it $\boldsymbol{\mathcal{V}}(i)_\sigma^{(l)}$, where $\boldsymbol{\mathcal{O}}(i)_\sigma^{(l)}$ represents the correspondence of $\boldsymbol{\mathcal{P}}(i)_\sigma^{(l)}$ in $\boldsymbol{\mathcal{M}}_{\mathbf{0}}$. $\boldsymbol{\mathcal{V}}(i)_\sigma^{(l)}$ is appended to $\boldsymbol{\mathcal{O}}(i)_\sigma^{(l)}$ to produce the *full* source model of registration. $\boldsymbol{\mathcal{M}}_{\mathbf{0}}-\boldsymbol{\mathcal{O}}(i)_\sigma^{(l)}-\boldsymbol{\mathcal{V}}(i)_\sigma^{(l)}$ provides the set of source target marker points for the "virtual" TRE calculations. Assume that the correspondences of $\boldsymbol{\mathcal{M}}_{\mathbf{0}}-\boldsymbol{\mathcal{O}}(i)_\sigma^{(l)}-\boldsymbol{\mathcal{V}}(i)_\sigma^{(l)}$ in $\mathcal{G}_\sigma^{(l)}(\boldsymbol{\mathcal{M}}_{\mathbf{0}};\theta)-\boldsymbol{\mathcal{P}}(i)_\sigma^{(l)}$ are represented by $\boldsymbol{\mathcal{D}}(i)_\sigma^{(l)}$.

Output: $\left\{\mathcal{F}_1^{(l)}(\boldsymbol{\mathcal{M}}_{\mathbf{0}};\theta)\right\}$ $\forall\, l \in \left\{1,\dots,\frac{\boldsymbol{\mathcal{M}}_{\mathbf{2}}-\boldsymbol{\mathcal{M}}_{\mathbf{1}}}{\boldsymbol{\mathcal{M}}_{\mathbf{1}}}\right\}$; $\left\{\mathcal{G}_\sigma^{(l)}(\boldsymbol{\mathcal{M}}_{\mathbf{0}};\theta)\right\}$ $\forall\, l \in \left\{1,\dots,\frac{\boldsymbol{\mathcal{M}}_{\mathbf{2}}-\boldsymbol{\mathcal{M}}_{\mathbf{1}}}{\boldsymbol{\mathcal{M}}_{\mathbf{1}}}\right\}$ and $\forall\, \sigma \in \{0.015,\dots,\sigma_3\}$; $\left\{\boldsymbol{\mathcal{P}}(i)_\sigma^{(l)}\right\}$, $\left\{\boldsymbol{\mathcal{O}}(i)_\sigma^{(l)}\right\}$, $\left\{\mathcal{G}_\sigma^{(l)}(\boldsymbol{\mathcal{M}}_{\mathbf{0}};\theta)-\boldsymbol{\mathcal{P}}(i)_\sigma^{(l)}\right\}$, $\left\{\boldsymbol{\mathcal{V}}(i)_\sigma^{(l)}\right\}$, $\left\{\boldsymbol{\mathcal{M}}_{\mathbf{0}}-\boldsymbol{\mathcal{O}}(i)_\sigma^{(l)}\right\}$, $\left\{\boldsymbol{\mathcal{M}}_{\mathbf{0}}-\boldsymbol{\mathcal{O}}(i)_\sigma^{(l)}-\boldsymbol{\mathcal{V}}(i)_\sigma^{(l)}\right\}$, $\left\{\boldsymbol{\mathcal{V}}(i)_\sigma^{(l)}+\boldsymbol{\mathcal{O}}(i)_\sigma^{(l)}\right\}$ and $\left\{\boldsymbol{\mathcal{D}}(i)_\sigma^{(l)}\right\}$ $\forall\, i \in \{1,\dots,\boldsymbol{\mathcal{N}}_{\mathbf{4}}\}$ and $\forall\, l \in \left\{1,\dots,\frac{\boldsymbol{\mathcal{M}}_{\mathbf{2}}-\boldsymbol{\mathcal{M}}_{\mathbf{1}}}{\boldsymbol{\mathcal{M}}_{\mathbf{1}}}\right\}$ and $\forall\, \sigma \in \{0.015,\dots,\sigma_3\}$.

```
for $k = \boldsymbol{\mathcal{M}}_{\mathbf{1}}$ to $\boldsymbol{\mathcal{M}}_{\mathbf{2}}$   $\{k \coloneqq k + \boldsymbol{\mathcal{M}}_{\mathbf{1}}\}$
Same as steps 2 and 3 of **Algorithm 8**.
    for $\sigma = 0.015$ to $\sigma_3$   $\{\sigma \coloneqq \sigma + \sigma_2\}$
    Same as step 3 of **Algorithm 3**. $\mathcal{F}_1^{(l)}(\boldsymbol{\mathcal{M}}_{\mathbf{0}};\theta)$ is updated to $\mathcal{G}_\sigma^{(l)}(\boldsymbol{\mathcal{M}}_{\mathbf{0}};\theta)$.
        for $i = 1$ to $\boldsymbol{\mathcal{N}}_{\mathbf{4}}$   $\{i \coloneqq i + 1\}$
        Apply steps 3-22 of **Algorithm 6** to produce $\boldsymbol{\mathcal{P}}(i)_\sigma^{(l)}$ from $\mathcal{G}_\sigma^{(l)}(\boldsymbol{\mathcal{M}}_{\mathbf{0}};\theta)$.
        Identify the correspondences of $\boldsymbol{\mathcal{P}}(i)_\sigma^{(l)}$ and those of
        $\mathcal{G}_\sigma^{(l)}(\boldsymbol{\mathcal{M}}_{\mathbf{0}};\theta)-\boldsymbol{\mathcal{P}}(i)_\sigma^{(l)}$ in $\boldsymbol{\mathcal{M}}_{\mathbf{0}}$ to produce $\boldsymbol{\mathcal{O}}(i)_\sigma^{(l)}$ and $\boldsymbol{\mathcal{M}}_{\mathbf{0}}-\boldsymbol{\mathcal{O}}(i)_\sigma^{(l)}$, respectively.
        Randomly select $\boldsymbol{\mathcal{N}}_{\mathbf{6}}$ Cartesian $3D$ points from $\boldsymbol{\mathcal{M}}_{\mathbf{0}}-\boldsymbol{\mathcal{O}}(i)_\sigma^{(l)}$ to generate $\boldsymbol{\mathcal{V}}(i)_\sigma^{(l)}$.
        Append $\boldsymbol{\mathcal{V}}(i)_\sigma^{(l)}$ onto $\boldsymbol{\mathcal{O}}(i)_\sigma^{(l)}$ to produce the *full* source model of registration.
        Identify the correspondences of $\boldsymbol{\mathcal{M}}_{\mathbf{0}}-\boldsymbol{\mathcal{O}}(i)_\sigma^{(l)}-\boldsymbol{\mathcal{V}}(i)_\sigma^{(l)}$ in $\mathcal{G}_\sigma^{(l)}(\boldsymbol{\mathcal{M}}_{\mathbf{0}};\theta)-\boldsymbol{\mathcal{P}}(i)_\sigma^{(l)}$ to produce $\boldsymbol{\mathcal{D}}(i)_\sigma^{(l)}$.
        end for
    end for
end for
```

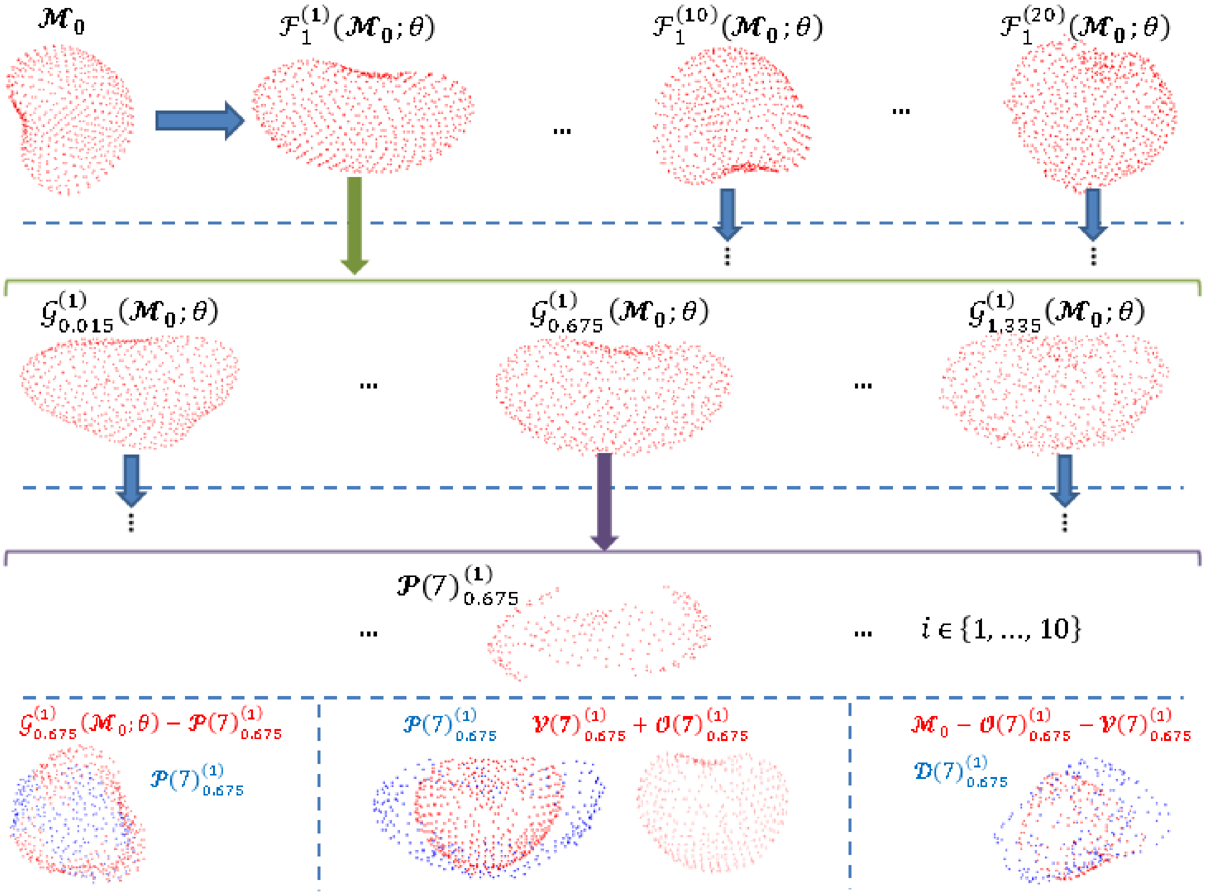

Figure 3.19: A diagrammatic representation of ***Algorithm* 9**.

Five different sets of experiments, $Exp\ A - Exp\ E$, were conducted for all registration methods where all input parameters were kept fixed except $\mathcal{N}_5$ and $\mathcal{N}_6$ (See Table 3.11). As a result the accuracy of registration (measured in the space beyond common overlap) can be determined as a function of the size of the target surface (hence the area of common overlap) which is subject to deformation plus noise. Such synthetic target models closely mimic some of the available clinical data [where $\sigma \approx (0.105 - 0.300)$].

	$\boldsymbol{\mathcal{N}}'_{\mathbf{5}}$	$\%\ \boldsymbol{of\ Total\ Surface}$	$\boldsymbol{\mathcal{N}}_{\mathbf{6}}$
Exp A	50	7.6	320
Exp B	100	15	280
Exp C	150	23	250
Exp D	200	31	230
Exp E	250	38	210

Table 3.11: Experimental parameters of $\boldsymbol{\mathcal{N}}'_{\mathbf{5}}$ and $\boldsymbol{\mathcal{N}}_{\mathbf{6}}$ for the sets of experiments $A - E$. $\boldsymbol{\mathcal{N}}'_{\mathbf{5}}$ is derived from $\boldsymbol{\mathcal{N}}_{\mathbf{5}}$, and represents the number of $3D$ points per surface patch. The values of $\boldsymbol{\mathcal{N}}_{\mathbf{6}}$ were specifically chosen to make the density of points across $\boldsymbol{\mathcal{V}}(i)_{\sigma}^{(l)} + \boldsymbol{\mathcal{O}}(i)_{\sigma}^{(l)}$ approximately constant. The fixed input parameters are: $\boldsymbol{\mathcal{N}}_{\mathbf{1}} = \boldsymbol{\mathcal{N}}_{\mathbf{2}} = \boldsymbol{\mathcal{N}}_{\mathbf{3}} = 6$, $\boldsymbol{\mathcal{M}}_{\mathbf{2}} = 105$, $\boldsymbol{\mathcal{M}}_{\mathbf{1}} = 5$, $\boldsymbol{\mathcal{N}}_{\mathbf{4}} = 10$, $\boldsymbol{\mu} = 0$, $\boldsymbol{\sigma}_{\mathbf{2}} = 0.165$, and $\boldsymbol{\sigma}_{\mathbf{3}} = 1.335$. See also text for details.

The registration takes place between $\boldsymbol{\mathcal{V}}(i)_{\sigma}^{(l)} + \boldsymbol{\mathcal{O}}(i)_{\sigma}^{(l)}$ (using as control points the set of extracted points from the *full* source model) and $\boldsymbol{\mathcal{P}}(i)_{\sigma}^{(l)}$ $\forall\, i \in \{1, \dots, \boldsymbol{\mathcal{N}}_{\mathbf{4}}\}$, $\forall\, l \in \left\{1, \dots, \frac{\boldsymbol{\mathcal{M}}_{\mathbf{2}} - \boldsymbol{\mathcal{M}}_{\mathbf{1}}}{\boldsymbol{\mathcal{M}}_{\mathbf{1}}}\right\}$ and $\forall\, \sigma \in \{0.015, \dots, \sigma_3\}$, producing as final output $\left\{\boldsymbol{\mathcal{B}}\left(\boldsymbol{\mathcal{V}}(i)_{\sigma}^{(l)} + \boldsymbol{\mathcal{O}}(i)_{\sigma}^{(l)}; \theta\right)\right\}$ as well as $\left\{\boldsymbol{\mathcal{B}}\left(\boldsymbol{\mathcal{M}}_{\mathbf{0}} - \boldsymbol{\mathcal{O}}(i)_{\sigma}^{(l)} - \boldsymbol{\mathcal{V}}(i)_{\sigma}^{(l)}; \theta\right)\right\}$. See Figure 3.20.

The TRE calculations were conducted by randomly selecting $\boldsymbol{d}$ target marker points (where $\boldsymbol{d} \in \{3,5,10,15\}$) from $\boldsymbol{\mathcal{B}}\left(\boldsymbol{\mathcal{M}}_{\mathbf{0}} - \boldsymbol{\mathcal{O}}(i)_{\sigma}^{(l)} - \boldsymbol{\mathcal{V}}(i)_{\sigma}^{(l)}; \theta\right)$ and determining the distances between them and their correspondences in $\boldsymbol{\mathcal{D}}(i)_{\sigma}^{(l)}$. The selection of $\boldsymbol{d}$ points is repeated 100 times. This process takes place $\forall\, i \in \{1, \dots, \boldsymbol{\mathcal{N}}_{\mathbf{4}}\}$, $\forall\, l \in \left\{1, \dots, \frac{\boldsymbol{\mathcal{M}}_{\mathbf{2}} - \boldsymbol{\mathcal{M}}_{\mathbf{1}}}{\boldsymbol{\mathcal{M}}_{\mathbf{1}}}\right\}$, $\forall\, \sigma \in \{0.015, \dots, \sigma_3\}$ and $\forall\, \boldsymbol{d} \in \{3,5,10,15\}$. The computed $TREs$ showed no dependence on the value of $\boldsymbol{d}$ and the random configuration of the target markers. Sections 3.8.2.1 and 3.8.2.2 present the computed TRE results for all methods and $\boldsymbol{d} = 15$. The input files were the same for all registration methods.

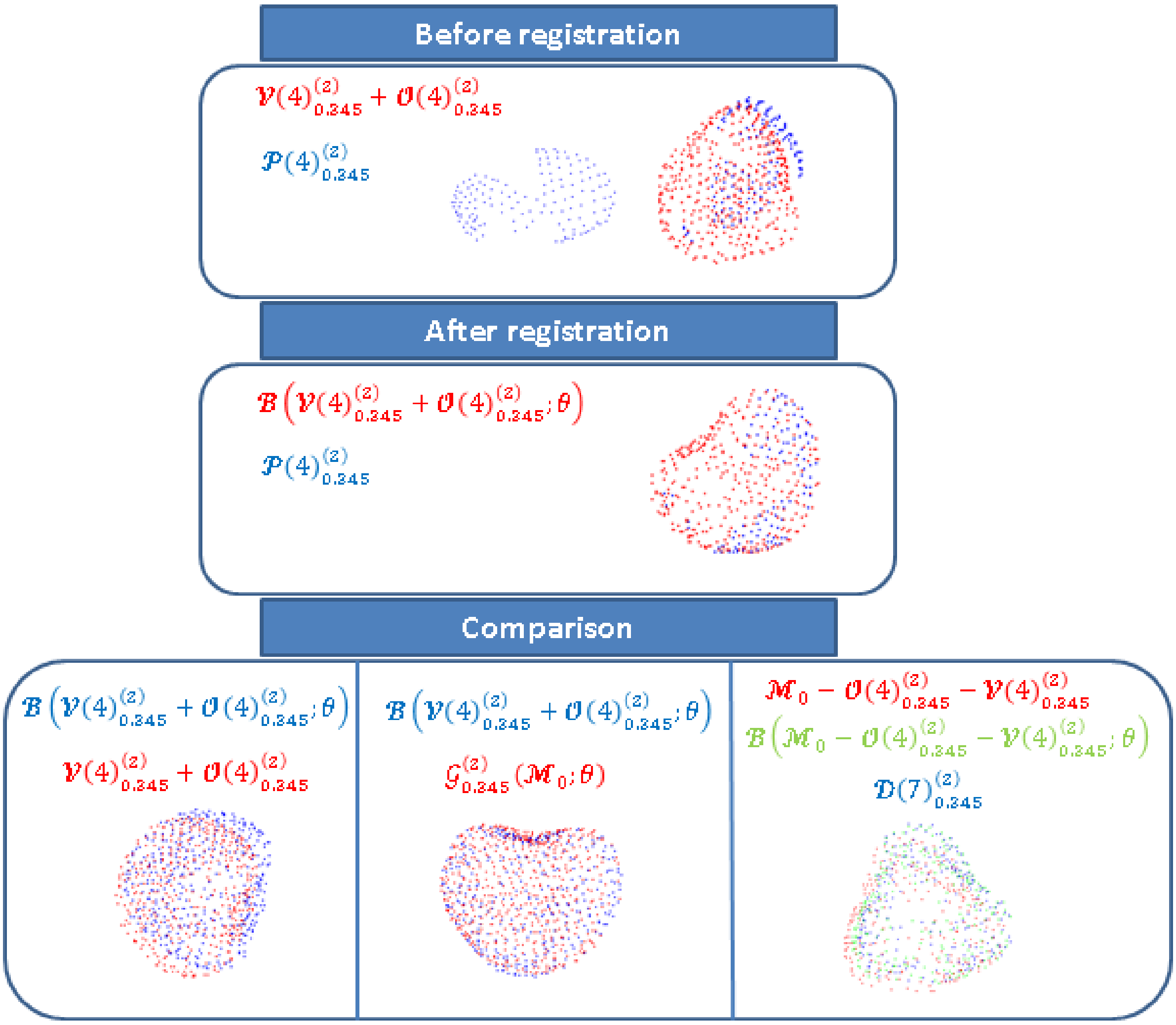

Figure 3.20: An example registration from the set of experiments C. $\boldsymbol{d} = 15$ markers are selected randomly from $\boldsymbol{\mathcal{B}}\left(\boldsymbol{\mathcal{M}}_{\mathbf{0}} - \boldsymbol{\mathcal{O}}(4)^{(2)}_{0.345} - \boldsymbol{\mathcal{V}}(4)^{(2)}_{0.345}; \theta\right)$ and the distances between them and their correspondences in $\boldsymbol{\mathcal{D}}(4)^{(2)}_{0.345}$ are determined. This process is repeated 100 times. By averaging out the so produced $TREs$ using the $KC + TPS$ method, it is calculated that Average $TRE = (3.0048 \pm 0.1907)\ mm$. The intersection between the (updated) extracted source model and the set of (transformed) target markers is by definition the null set.

3.8.2.1 $TREs$ computed using the $KC + TPS$ technique

Consider the set of experiments E and a given (l, σ). The average TRE value at (l, σ) is computed by averaging out $100 \times \boldsymbol{\mathcal{N}_4}$ $TREs$, *i.e.*, $\forall\, i \in \{1, \dots, \boldsymbol{\mathcal{N}_4}\}$. These values were calculated using the $KC + TPS$ method.

Figure 3.21 represents graphically the computed average $\forall\, l \in \{2, \dots, 20\}$, where l is even, and $\forall\, \sigma \in \{0.015, 0.18, 0.345.0.51\}$. As the average $TREs$ for the odd values of l were consistent with the registration accuracy pattern of Figure 3.21 they were omitted for better clarity. The simulations produced by injecting Gaussian noise with $\sigma > 0.345$ go beyond the solution space defined by the observed noise in the available clinical data.

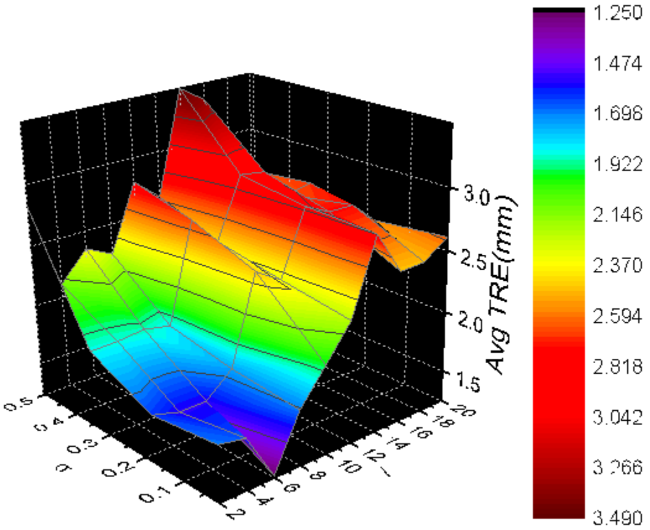

Figure 3.21: Average $TREs$ for the set of experiments E. They were computed $\forall\, l \in \{2, \dots, 20\}$, where l is even, and $\forall\, \sigma \in \{0.015, 0.18, 0.345.0.51\}$ using the $KC + TPS$ technique.

For $Exp\ E$ the maximum allowable σ from the set $\{0.015, 0.18, 0.345.0.51\}$ that can lead to clinically acceptable registration accuracies is 0.345. Figure 3.22 presents a slice of Figure 3.21 across $\sigma_{max} = 0.345$ (the $TREs$ are *ca.* $\leq 3\,mm$). See also Table $C.1$ of Appendix $\boldsymbol{C}$ which lists the corresponding average $TREs$ for σ_{max} and $\forall\, l \in \{1, \dots, 20\}$ for $Exp\ A -$

$Exp\ E$. Figure 3.23 represents graphically the average $TREs$ for the set of experiments $A - D$ computed $\forall\ l \in \{2, \dots ,20\}$, where l is even, and $\forall\ \sigma \in \{0.015,0.18,0.345.0.51\}$.

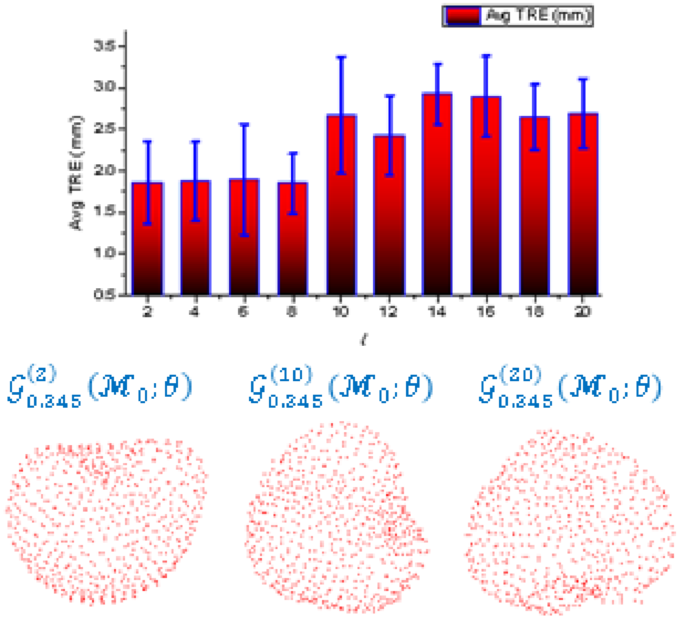

Figure 3.22: A slice of Figure 3.21 across $\sigma = 0.345$.

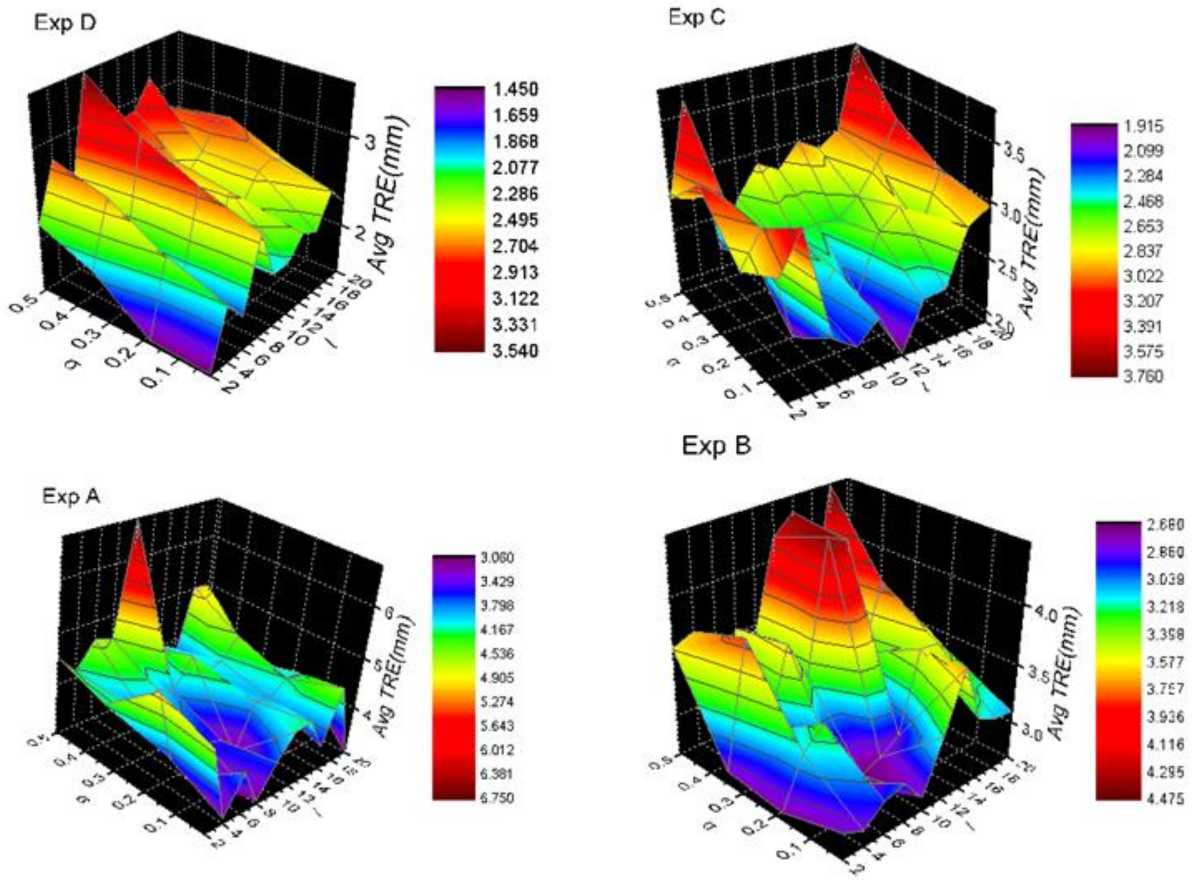

Figure 3.23: Average $TREs$ for the set of experiments $A - D$. They were computed $\forall\ l \in \{2, \ldots, 20\}$, where l is even, and $\forall\ \sigma \in \{0.015, 0.18, 0.345.0.51\}$ using the $KC + TPS$ technique. See text for details.

3.8.2.2 $\boldsymbol{TREs}$ computed using the $\boldsymbol{GMM + TPS}$ technique

This section follows a similar approach to the one taken in Section 3.8.2.1. The average $TREs$ were calculated using the $GMM + TPS$ method. The results for the set of experiments E are graphically presented in Figure 3.24. Figure 3.25 shows the slice of Figure 3.24 across $\sigma_{max} = 0.345$. The average $TREs$ for σ_{max} and $\forall\ l \in \{1, \ldots, 20\}$ for $Exp\ A - Exp\ E$ are listed in Table $C.2$ of Appendix $\boldsymbol{C}$. Figure 3.26 represents graphically the average $TREs$ for the set of experiments $A - D$ computed $\forall\ l \in \{2, \ldots, 20\}$, where l is even, and $\forall\ \sigma \in \{0.015, 0.18, 0.345.0.51\}$.

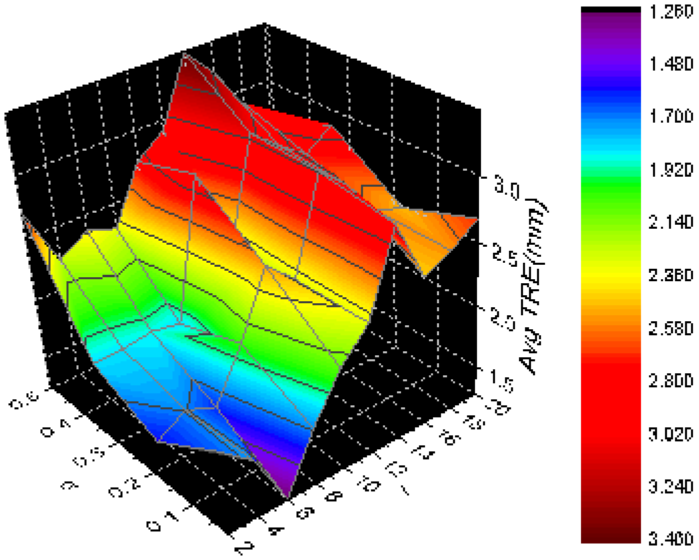

Figure 3.24: Average $TREs$ for the set of experiments E. They were computed $\forall\ l \in \{2, \ldots, 20\}$, where l is even, and $\forall\ \sigma \in \{0.015, 0.18, 0.345.0.51\}$ using the $GMM + TPS$ technique.

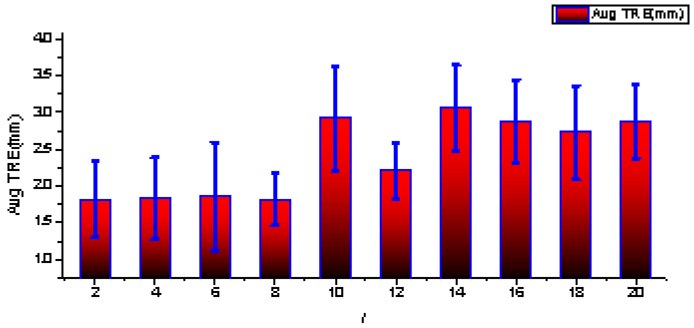

Figure 3.25: A slice of Figure 3.24 across $\sigma = 0.345$.

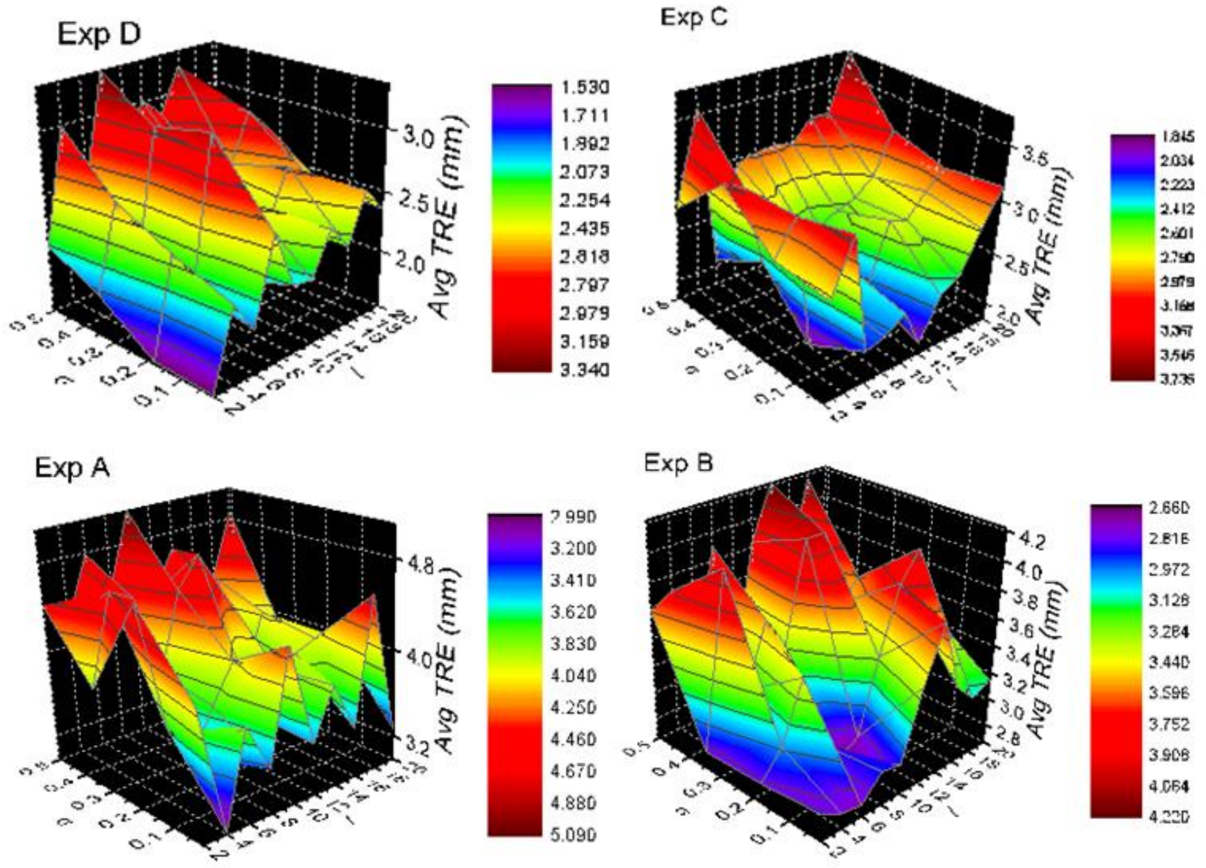

Figure 3.26: Average $TREs$ for the set of experiments $A-D$. They were computed $\forall\ l \in \{2,\ldots,20\}$, where l is even, and $\forall\ \sigma \in \{0.015,0.18,0.345.0.51\}$ using the $GMM+TPS$ technique. See text for details.

Chapter 4

Registration of medical imaging data

Trial computational registration experiments were conducted using real prostate imaging data[9] following the process described below:

(i) The $3D$ source mesh prepared from the MRI segmentation of the prostate surface[10] is transformed into a (downsampled) point-cloud representation (see Figure 4.1).

(ii) The $3D$ target (left and right) video images of the prostate surface are acquired endoscopically via the aid of the *da Vinci* Surgical System; they undergo surface (stereo-vision) reconstruction leading to a point-cloud representation of the prostate, which is also downsampled (see Figure 4.2).

(iii) The source and target models are manually aligned before the non-rigid registration is initiated by, *i.e.,* superimposing the (scaled) source onto the target scene; the orientation(s) and size(s) of the corresponding dataset(s) are saved in a designated directory (see Figure 4.3).

(iv) The $GMM + TPS$ and $KC + TPS$ non-rigid registration algorithms are executed using as input the aligned models of (iii) and their output is qualitatively examined (see Figure 4.4).

(v) Steps (ii)-(iv) are repeated for different $3D$ target images (see Figure 4.5 and Appendix $\boldsymbol{\mathcal{D}}$).

---

[9] The medical imaging prostate data were provided by Daniel Stoyanov.

[10] The MRI prostate segmentation was provided by Yipeng Hu and was prepared by a radiologist at University London College Hospital (UCLH). The MRI scans were acquired at UCLH with local ethical approval for the research purpose.

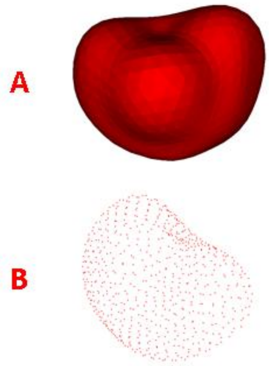

Figure 4.1: [A] $3D$ MRI prostate mesh; [B] Point-cloud representation (downsampled to 654 data points).

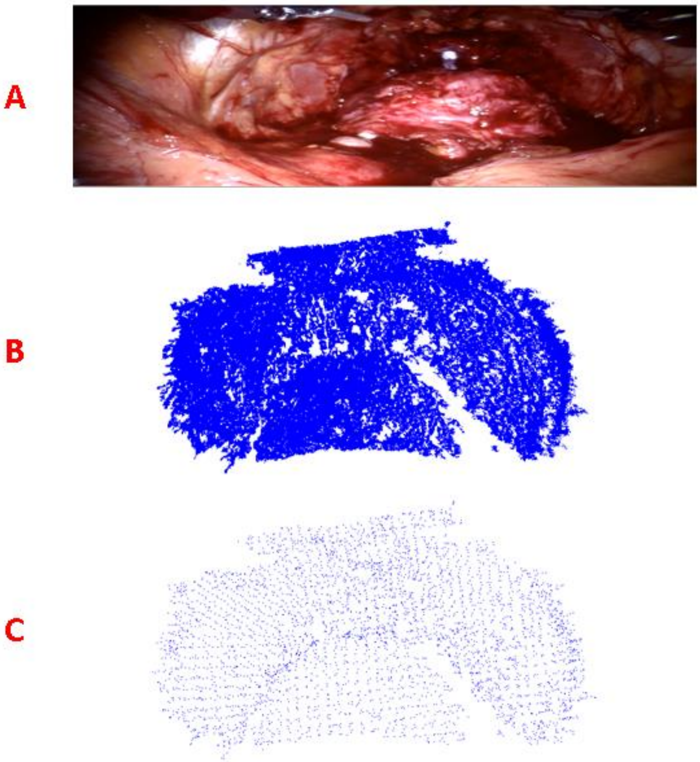

Figure 4.2: [A] $3D$ video prostate image; [B] $3D$ stereo-reconstructed surface (*ca*. 60K data points); [C] downsampled version of [B] (*ca*. 4K data points).

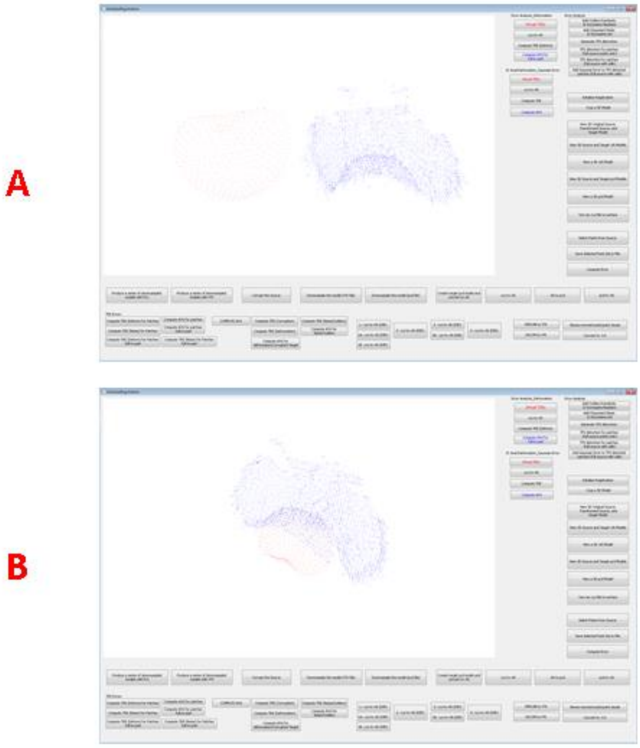

Figure 4.3: [A] Initial orientations of the downsampled source and target models; [B] The (scaled) source model is manually superimposed onto the target surface.

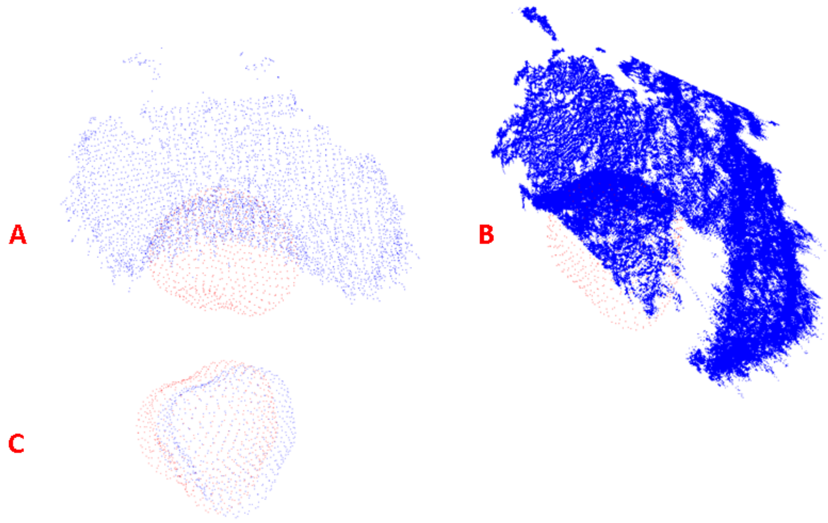

Figure 4.4: [A] The source model (*in red*) is registered onto the downsampled target scene (*in blue*); [B] The source model (*in red*) is registered onto the original target scene (*in blue*); [C] The original manually aligned source model (*in red*) and the registered source model (*in blue*). The registration was conducted using the $KC + TPS$ algorithm. The overlapping area between the datasets is about 50% of the surface of the full source model.

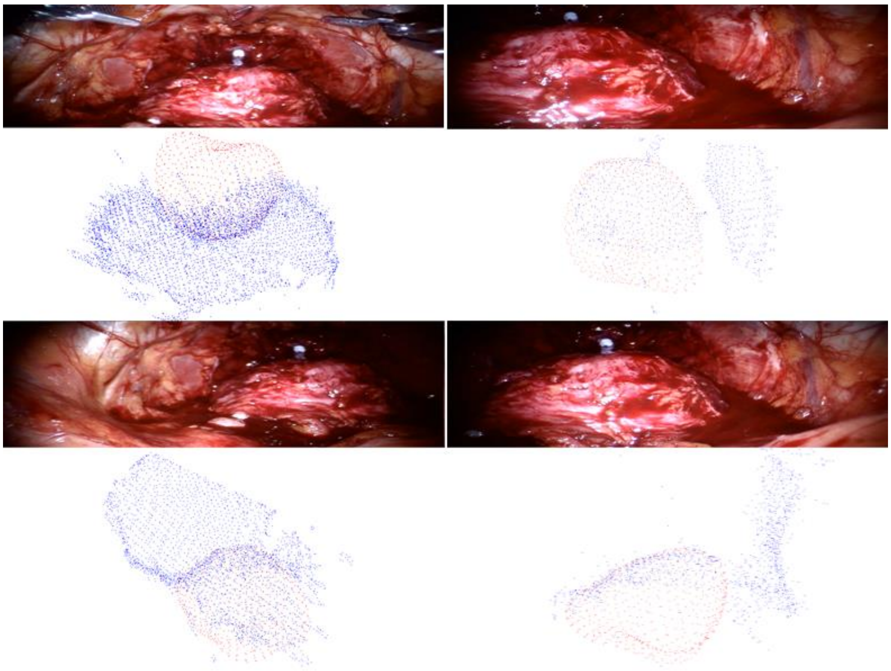

Figure 4.5: Selected video prostate images followed by the output of $KC + TPS$ non-rigid registration. The registered source is *in red* and the target prostate scene and its surrounding area are *in blue*. The registration output is not in scale to the video images.

Chapter 5

Discussion

The results from the computational *full-model-to-full-model* registration experiments of Chapter 3 are compared. The best *full-model-to-occluded-scene* non-rigid registration approaches are identified based on performance in registration accuracy, and their suitability for AR prostate surgery applications is examined. Their solution space is also determined.

The experiments $A - C$ of Section 3.3 allow for a relatively large size of deformation across $\boldsymbol{\mathcal{M}_0}$ (which can incrementally obtain a higher magnitude in going from $Exp\ C$ to $Exp\ A$; see Table 3.1 and Figure 3.3) leading to the possibility of exaggerated cases of prostate surface deformation (where the $TREs$ can be as high as 4 mm). As the number of source control points of $\mathcal{F}_1^{(i)}$ is increased, the *complexity* of deformation across $\boldsymbol{\mathcal{M}_0}$ is also increased. The synthetic datasets of Experiments E and $H - J$ are the ones that simulate the closest the available prostate imaging data. The best $TREs$ arise from the application of the $EM + TPS$ (shape-based) registration algorithm (< 2 mm) for these test datasets. This clearly demonstrates the superiority of the $EM + TPS$ technique over $KC + TPS$ and $GMM + TPS$ in establishing valid point-to-point correspondences during the *full-model-to-full-model* deformation process especially for large nonrigid variations in prostate surface.

Section 3.4 aims at determining the relationship between registration accuracy and number of perturbed (by Gaussian noise) points of a *full* target model as the Gaussian noise level is increased. The Gaussian standard deviations σ that can be deduced from the clinical data (and for $\mu = 0$) are in the range 0.105-0.300. All algorithms produce approximately the same $TREs$ in this range (and beyond), irrespective of the number of points of the *full* target model. The computed values of the $TREs$ can be attributed mainly to the magnitude of injected Gaussian noise. All algorithms can also discriminate effectively against outliers in the *full* target scene (which may be originating in the surrounding environment of the target model) as the TRE results of Section 3.5 clearly indicate.

Section 3.6 focuses on exploiting the relationship between TRE and number of perturbed (by non-Gaussian noise in *Exps* A and B) target points for a series of deformed *full* target models (*Test 1*-*Test 4*). The general conclusions stemming from Tables 3.5 and 3.6 are that (*i*) all three non-rigid registration algorithms can establish in most of the times valid correspondences and recover the deformation accurately, even when the deformed target scene is perturbed by non-Gaussian noise; (*ii*) combined with (*i*), the $EM + TPS$ technique outperforms the $KC + TPS$ and $GMM + TPS$ methods in the identification of true correspondences during the *full-model-to-full-model* registration process; (*iii*) the establishment of erroneous correspondences becomes more frequent when the number of points of the noisy and deformed *full* target datasets goes below a certain threshold (*i.e.*, when the number of target points becomes 50 in these computational experiments, see Tables 3.5 and 3.6); and (*iv*) while the TRE values arising from the $EM + TPS$ registrations are affected mainly by the non-Gaussian noise, the corresponding ones produced by the $KC + TPS$ and $GMM + TPS$ registration methods are also affected by the correspondence error.

In the *full-model-to-partial-model* non-rigid registration experiments of Section 3.7.1, the size of the synthetic target scene is fixed to *ca*. 46% of the total source surface and the incurred deformation is mild. From the average TRE results of column (*i*) of Table 3.7 it can be observed that the accuracy of the non-rigid registration between a *partial* source model and a *partial* target model is still affected by some correspondence error (which turns out to be the smallest when the $EM + TPS$ method is used), despite the fact that the source model is comprised of only points with true correspondences in the (mildly) deformed target. The correspondence error is further increased in going to *full-model-to-partial-model* non-rigid registrations as can be seen in column (*ii*) of Table 3.7.

The correspondence error is considerably higher for the registrations performed with $EM + TPS$ than that produced by $KC + TPS$ and $GMM + TPS$. This discrepancy can be attributed to the way that the correspondences are estimated in each technique. For example the $\mathcal{GMM}$ methodology of establishing correspondences (see Section 2.2) is completely different in comparison to that of the $\mathcal{GMM}/\mathcal{EM}$ technique (Section 2.4). The optimization of the $\mathcal{GMM}$ *multiply-linked* cost function takes place *w.r.t.* θ given a set of Euclidean distances that arises from all possible point-pair combinations that can be formed within the source and between the source and the target based on Equations 2.49, 2.51 and 2.52-2.56. In other words the optimal transformation of the moving model is computed by taking as input not only all possible correspondence pairs that can be formed between the moving model and the target (depicted by $\boldsymbol{\mathcal{H}}_{\mathcal{JW}}$ of Equation 2.53; the most probable ones are those with the smallest Euclidean distance) but also its (transforming) configuration of points as a whole

($\boldsymbol{\mathcal{H}}_{\mathcal{J}^2}$). Hence the latter term participates in (and governs) the establishment of correspondences during the non-rigid registration process according to the $\mathcal{GMM}$ methodology. The $\mathcal{KC}$ technique of Section 2.3, as a *multiply-linked* methodology, follows a similar approach of identifying correspondences as Equations 2.74, 2.76 and 2.77-2.81 indicate. In the $\mathcal{GMM}/\mathcal{EM}$ formulation the correspondences are identified in a one-on-one basis according to the row and column summation constraints imposed in the $\boldsymbol{\mathcal{E}}-$step without considering the effect that the so computed transformation will have on the moving model as a whole. Let's assume that the moving prostate model contains also points that have no matching counterparts in the target. While the $\mathcal{GMM}$ and $\mathcal{KC}$ optimizations of the corresponding energy functions won't be affected much by the presence of such points, the optimization of the $\mathcal{GMM}/\mathcal{EM}$ cost function can be largely affected by them leading to erroneous non-rigid transformations. Considering the smooth surface of the prostate the extracted source model is quite likely to include such points.

Any correspondence error in the $\boldsymbol{\mathcal{E}}-$step of the $\mathcal{GMM}/\mathcal{EM}$ technique will propagate into a larger error in the estimation of θ in the $\boldsymbol{\mathcal{M}}-$step (based on Equation 2.101) than it could have been had the optimization of the energy function $w.r.t\ \theta$ been ***smoother***. The latter is guaranteed in the $\mathcal{GMM}$ and $\mathcal{KC}$ techniques owing to Equations 2.54-2.56 and 2.79-2.81, respectively, where in the calculation of $\boldsymbol{\mathcal{H}}_{(\mathcal{J}^2/\mathcal{JW})}$ (Equation 2.53) and $\boldsymbol{\mathcal{H}}_{(P_{\boldsymbol{\mathcal{M}}}{}^2/P_{\boldsymbol{\mathcal{M}}}P_{\boldsymbol{\mathcal{S}}})}$ (Equation 2.78) the Euclidean distances are modulated by ***exponential*** functions. Reformulating the optimization of the $\mathcal{E}_3$ cost function $w.r.t\ \theta$ to become a smoother process may be one additional modification that can help in correcting possible point mismatches in the next iteration of the $\boldsymbol{\mathcal{E}}-$step for the registration of prostate surfaces. This must be combined with the imposition of a "tight" distance threshold in the extraction of the overlapping area.

The occluded and deformed synthetic prostate surfaces that were generated in Section 3.7.1 are further perturbed by the injection of a relatively increased ($\sigma = 0.450$) Gaussian noise (see Section 3.7.2). From the average $TREs$ that are computed from the *partial-model-to-partial-model* non-rigid registrations (see column (*i*) of Table 3.8) it can be observed that (*i*) the registrations are still valid despite the addition of one more perturbation; (*ii*) the establishment of correspondences doesn't seem to be largely deteriorated by the injected Gaussian noise (for the specific size of the synthetic target scene) across all three methods (compare with corresponding $Avg\ TREs$ under column (*i*) of Table 3.7); (*iii*) the overall correspondence error is consistently increased for all three non-rigid techniques; and (*iv*) the $Avg\,TRE$ computed by $\mathcal{EM}+TPS$ is considerably smaller when the row and column normalization of the affinity matrix $\mathcal{T}$ (see Section 2.4.3) is also included in the method's formulation. The establishment of correct correspondences in the $\mathcal{KC}+TPS$ and $\mathcal{GMM}+TPS$ *full-model-to-partial-model* registrations [see column (*ii*) of Table 3.8] is less affected by the additional points (those with no matching counterparts in the target) that arise from the extraction of common overlap than that in the $\mathcal{EM}+TPS$ registrations.

An extensive series of computational experiments were conducted for the assessment of the warping accuracy of the $\mathcal{KC}+TPS$ and $\mathcal{GMM}+TPS$ *full-model-to-partial-model* registrations in the region beyond common overlap (in Section 3.8). In these experiments the size of the deformed target scene is not constant ($Exp\ A-ExpE$). Such tests are critical for determining the algorithms' suitability for AR prostate laparoscopic surgery applications.

The deformation applied onto the occluded prostate target scenes of Section 3.8.1 resembles in size and complexity the one that was synthesized in $Exp\ E$ of Section 3.3 [see Figure 3.3; it can be observed in Figures 3.7 and 3.8, for the range of number of control points until and including 105, that the $TREs$ stemming from the $\mathcal{KC}+TPS$ and $\mathcal{GMM}+TPS$ *full-model-to-full-model* registrations, in respect, do not go higher than *ca.* 2.5 mm]. Such simulations represent the "upper bound of all possible prostate deformations" based on the available clinical data although some that go beyond this limit (approximately for the range of numbers of control points >20 in Figures 3.7 and 3.8) are also included. From inspection of Table 3.10 it can be concluded that, for the case of deformed and occluded target surfaces, both the $\mathcal{KC}+TPS$ and $\mathcal{GMM}+TPS$ methodologies can provide the clinical accuracy ($TRE \lesssim 3$ mm) that is required for AR prostate surgery applications as long as the size of the target scene is greater than *ca.* 30% of the total (scaled) source surface (*i.e.*, from $Exp\ D$ and above in Table 3.10).

The occluded target models of Section 3.8.2 were deformed in a similar way to the one used in Section 3.8.1. In the $\mathcal{KC}+TPS$ and $\mathcal{GMM}+TPS$ computational experiments only a subset of those models that could simulate the closest the clinically observed deformation (specifically those arising from the range of numbers of control points until and including 20; see Section 3.8.2 for details and also $Exp\ E$ of Figure 3.3) were perturbed by Gaussian noise. From the analysis of Section 3.8.2.1 and Table $\mathcal{C}.1$ of Appendix $\boldsymbol{\mathcal{C}}$ it can be concluded that the $\mathcal{KC}+TPS$ technique is a clinically acceptable non-rigid registration method for "noisy", occluded and deformed target surfaces as long as (*i*) the size of the target model is greater than *ca.* 38% of the total (scaled) source surface; (*ii*) the standard deviation σ of the Gaussian noise is less than 0.345 for $\mu = 0$; and (*iii*) the observed deformation is not characterized by overly increased complexity as defined in this work (*i.e.*, when it does not exceed the levels of deformation observed in the current medical imaging data). From the analysis of Section 3.8.2.2 and Table $\mathcal{C}.2$ of Appendix $\boldsymbol{\mathcal{C}}$ a similar set of conclusions can be drown for the $\mathcal{GMM} + TPS$ technique. The second condition and as a consequence the third one can be relaxed by parameterizing the contribution of noise explicitly in the objective cost function [62].

All three requirements lie within the solution space defined by the observed occlusion, deformation and noise in the available prostate imaging data which can be considered as representative samples. Hence both the $\mathcal{KC} + TPS$ and $\mathcal{GMM} + TPS$ techniques can produce a clinically accurate non-rigid registration between a preoperatively prepared MRI prostate surface and prostate target scenes which reinforces their suitability for use in AR image guidance and navigation in prostate surgery. Chapter 4 and Appendix $\boldsymbol{\mathcal{D}}$ investigate the performance (by visual inspection) of a number of $\mathcal{KC} + TPS$ and $\mathcal{GMM} + TPS$ non-rigid registrations to real medical imaging data; the observed deformations in all cases that were examined seem to be fully recovered by these medical imaging registration methodologies.

The work by Papazov and Burschka [101] involves an interesting concept that could potentially be used to reformulate the $\mathcal{EM} + TPS$ algorithm making it more suitable for *full-model-to-partial-model* prostate surface registration. The authors have developed a deformable $3D$ shape (dense) registration algorithm based on a system of ordinary differential equations (ODE). Each ODE consists of a correspondence term and a regularization term and yields a trajectory that maps the transition and motion of each source point from its initial undeformed position to its end position on the target.

All vectors connecting each source point to its closest point on the target surface are initially computed based on a closest-point search scheme leading to a preliminary correspondence vector field. This is further refined by the following smoothing procedure: only those (displacement) vectors that show no deviations from their corresponding average values are allowed to terminate on the target points. The latter are computed over all neighbouring points of each source point.

This local optimization procedure returns an effective smooth correspondence field improving significantly the correspondence estimation especially when consecutive acquisitions (at high video frame rates) of imaging data of smoothly deforming objects are involved (such as in the case of stereoendoscopic acquisition of smoothly deforming prostate surfaces) as the interframe displacements are relatively small. This formulation could considerably improve the closest-point search mechanism that is currently used in the extraction of the common overlap between the full source and the occluded target model and provide a more reliable extracted source model for the $\boldsymbol{\mathcal{E}}-$ step of the modified $\mathcal{E}\mathcal{M}+TPS$ algorithm.

Chapter 6

Conclusions and future work

Three robust *state-of-the-art* nonrigid registration schemes were examined for their suitability in supporting robot-assisted AR prostate surgical treatment procedures. The objective of this work is to enhance the surgical accuracy and oncological cure of prostate cancer tumour performed by the *da Vinci* surgical system.

Computational experiments were conducted first for *full-model-to-full-model* prostate surface registrations using synthetic prostate data. Their output was collected and analysed providing some initial insight to their capacity of recovering prostate deformation as well as treating noise, outliers and the combined effects of noise and deformation. The $EM + TPS$ technique outperforms the $KC + TPS$ and $GMM + TPS$ methods in these type of registrations. The warping accuracies computed by $EM + TPS$ are below 2 mm for all clinically relevant simulations.

The registration algorithms were reformulated to address occlusion based on modified concepts originating in the work of other workers. Their accuracy was exploited in the surface of common overlap and in the space beyond common overlap using synthetic prostate imaging data.

In the first case the size of the occluded target scene was kept fixed bearing the effect of a mild deformation. The computational experiments were performed in the absence and presence of Gaussian noise. The objective was to obtain some initial input about the capacity of the modified algorithms to provide valid registrations in the presence of occlusion, (not extreme) prostate deformation and measurement noise and, for those that they could, quantify the size of the inherent correspondence error. The $KC + TPS$ and $GMM + TPS$ techniques were the only ones that could provide valid point-to-point (and 'clinically' acceptable) correspondences during the *full-model-to-partial-model* deformation process.

The suitability of non-rigid point-set warping methods for AR prostate surgery applications can be assessed by measuring the registration accuracy in the space beyond common overlap which is the most reliable validation scheme. The synthetic prostate data that were used in these experiments resemble as close as possible the available prostate imaging data both in deformation and noise.

The $\mathcal{KC}+TPS$ and $\mathcal{GMM}+TPS$ techniques can produce clinically accurate non-rigid registrations as long as the size of the target scene is greater than *ca*. 30% of the total (scaled) source surface, in the absence of noise. The relationship between the (minimum) size of the target scene and the (maximum) magnitude of the standard deviation σ of the Gaussian noise that the occluded and deformed target models are subject to was determined for obtaining clinically accurate *full-model-to-partial-model* prostate surface registrations. The EM/TPS non-rigid registration algorithm cannot recover the prostate surface deformation accurately in *full-model-to-occluded-model* registrations due to the way that the correspondences are estimated.

The warping accuracy measured in the space beyond common overlap from the registration to occluded (~38 % of original total surface) and deformed synthetic target prostate surfaces is estimated (2.1650±1.0154) mm using the modified KC/TPS technique, and (2.1677±0.9716) mm based on the modified GMM/TPS method. The maximum allowable standard deviation σ of Gaussian noise with $\mu=0$ that may be added to these surfaces without overshooting the mean value of the registration error above 3 mm is 0.345 for both $KC+TPS$ and $GMM+TPS$.

The results from the $\mathcal{KC}+TPS$ and $\mathcal{GMM}+TPS$ registration schemes can be used as a point of reference in developing more advanced nonrigid registration platforms for *full-model-to-partial-model* prostate surface registrations applied to AR prostate surgery. The $\mathcal{KC}+TPS$ and $\mathcal{GMM}+TPS$ algorithms and any other more advanced ones must be quantitatively evaluated by a series of custom-built prostate tissue phantom studies. These can be conducted by the experimental protocol proposed in the following:

- MRI/CT scans of a prostate tissue phantom with implanted *target markers* will be taken; their segmentation will produce a $3D$ prostate surface, which will be the source.
- Mechanical pressure (in arbitrary directions) will be exerted onto the source leading to a set of deformed phantoms. Their MRI/CT scans will be taken and will be segmented to produce deformed prostate volumes ($3D$ target models). The target

models represent the ground truth and will be used to measure the performance of registration algorithms in warping accuracy.

- The source will be nonrigidly registered to each of the target models using a registration algorithm.
- The TRE will be computed.
- The first four steps will be repeated each time for a different configuration and number of randomly implanted *target markers*. The mean and standard deviation of the $TREs$ will be calculated for the applied registration algorithm.
- The first five steps will be repeated each time for a different algorithm. The corresponding mean $TREs$ and standard deviations of registrations algorithms can then be compared and the best one for clinical applications can be determined.

Appendix $\mathcal{A}$

Supporting material for the TPS interpolation scheme

$\mathcal{A}$.1 Notation

Symbols for Section 2.1.1.1

Symbol	Definition	Type
X	$X = \{x_1, \dots, x_L\} \subset \mathbb{R}^N$	Set of discrete data $x_i \in \mathbb{R}^N$
H	$H = \{h_{x_1}, \dots, h_{x_L}\} \subset \mathbb{R}$	Set of values of $h_x = h(x) \in \mathbb{R}$
ϑ	Approximant $\vartheta: \mathbb{R}^N \to \mathbb{R}$	Function
h	Approximand $h: \mathbb{R}^N \to \mathbb{R}$	Function
ϕ	Radially symmetric basis function	Function
$\|x - x_i\|$	Euclidean distance between x_i and x	Real number
α_i	Coefficients of the interpolant ϑ	Scalars

Symbols for Section 2.1.1.2

Symbol	Definition	Type
P_i	$P_i = (x_i, y_i)$: source control point	$2D$ point
n	Number of source and target control points	Integer value
Π	$\Pi = \{P_1, \dots, P_n\}$: source control points	Set of points $P_i \in \mathbb{R}^2$
$\mathcal{G}$	$\mathcal{G} = \{g_{P_1}, \dots, g_{P_n}\}$: target control points	Set of values of $g_P = g(x, y)$
g	Approximand $g: D \to \mathbb{R}^2$	Function
D	Domain of g and f	Set of $2D$ points
f	Approximant $f: D \to \mathbb{R}^2$	Function
t_x, t_y	Translation coefficients of the interpolant f	Scalars
$r_{xx}, \dots, r_{yy}$	Rotation coefficients of the interpolant f	Scalars

$\gamma_{x_1}, \dots, \gamma_{y_n}$	TPS warping coefficients of the interpolant f	Scalars
ϕ	$\phi(r) = r^2 \log r$: $2D$ TPS basis function	Function
$\mathcal{X}$	Space of TPS interpolants f	Set of functions
$I(f)$	Thin-plate bending functional of f in $2D$	Real nonnegative value
$\mathcal{W}_f$	Affine and TPS coefficients of optimized f	Set of real values

Symbols for Section 2.1.1.3

Symbol	**Definition**	**Type**
f	Approximant f	Function
d	Number of imaging dimensions	Integer value
m	Total order of the partial derivatives of f	Integer value
$I_m(f)$	Thin-plate functional for $d = 2$ and general m	Real nonnegative value
$I_m^d(f)$	Thin-plate penalty functional for general d, m	Real nonnegative value

Symbols for Section 2.1.2

Symbol	**Definition**	**Type**
q	$q = (x, y, z)$: $3D$ point of the source model M_0	$3D$ point
m	Number of $3D$ points of the source and target models	Integer value
M_0	$M_0 = (q_1, \dots, q_m)^T$: undeformed $3D$ source model	$m \times 3$ matrix
t	$t = (x, y, z)$: $3D$ point of the target model S	$3D$ point
S	$S = (t_1, \dots, t_m)^T$: $3D$ target model	$m \times 3$ matrix
n	Number of source and target control points	Integer value
P_i	$P_i = (x_i^P, y_i^P, z_i^P)$: $i \in \{1, \dots, n\}$: source control point	$3D$ point
Ω	$\Omega = \{P_1, \dots, P_n\} \subseteq \{q_1, \dots, q_m\}$: source control points	Set of $3D$ points
$\mathcal{G}$	$\mathcal{G} = \{g_{P_1}, \dots, g_{P_n}\}$: target control points	Set of $g_{P_i} = g(x_i^P, y_i^P, z_i^P)$ values
g	Approximand $g: D \to \mathbb{R}^3$	Function
D	$D = \{q_1, \dots, q_m\} \subset \mathbb{R}^3$: domain of g and f	Set of $3D$ points
f	Approximant $f: D \to \mathbb{R}^3$	Function

$\alpha_x, \alpha_y, \alpha_z$	Translation coefficients of the interpolant f	Scalars
$\beta_{xx}, \dots, \beta_{zz}$	Rotation coefficients of the interpolant f	Scalars
$\theta_{x_1}, \dots, \theta_{z_n}$	TPS warping coefficients of the interpolant f	Scalars
ϕ	$\phi(r) = r$: $3D$ TPS basis function	Function
$\lVert q_i - P_j \rVert$	Euclidean distance between P_j and q_i	Real number
U_{ij}	$U_{ij} = \phi(\lVert q_i - P_j \rVert)$	Function
M	$M = f(M_0)$: transformed $3D$ source model	$m \times 3$ matrix
$[1 \vert M_0]$	Augmented form of M_0	$m \times 4$ matrix
E	Matrix of the affine transformation coefficients	3×4 matrix
U	Basis matrix	$m \times n$ matrix
Q	Matrix of the TPS coefficients	$n \times 3$ matrix
T	Matrix of the target control points	$n \times 3$ matrix
Φ	TPS kernel matrix in $3D$	$n \times n$ matrix
P	Matrix of the source control points	$n \times 3$ matrix
A	Augmented form of P: $A = [1 \vert P]$	$n \times 4$ matrix
Ψ	$\Psi = \begin{bmatrix} \Phi & A \\ A^T & 0 \end{bmatrix}$	$(n+4) \times (n+4)$ matrix
Δ	Matrix of the affine and TPS coefficients	$(n+4) \times 3$ matrix
Υ	Augmented form of T: $\Upsilon = \begin{bmatrix} T \\ 0 \end{bmatrix}$	$(n+4) \times 3$ matrix

Symbols for Section 2.1.3

Symbol	**Definition**	**Type**
$I_2^3(f)$	Thin-plate functional of f for $d = 3, m = 2$	Real nonnegative value
m	Number of $3D$ points of the source model	Integer value
M_0	Undeformed $3D$ source model	$m \times 3$ matrix
M	Transformed $3D$ source model	$m \times 3$ matrix
n	Number of source control points	Integer value
E	Matrix of the affine transformation coefficients	3×4 matrix

U	Basis matrix	$m \times n$ matrix
Q	Matrix of the TPS coefficients	$n \times 3$ matrix
Φ	TPS kernel matrix in $3D$	$n \times n$ matrix
P	Matrix of the source control points	$n \times 3$ matrix
A	Augmented form of P: $A = [1\|P]$	$n \times 4$ matrix
$\mathcal{N}$	Affine subspace of the TPS warping space	$n \times (n-4)$ matrix
ψ	Non-affine subspace of the TPS warping space	$(n-4) \times 3$ matrix
$\boldsymbol{\mathcal{Q}}$	The matrix produced by $A = \boldsymbol{\mathcal{Q}\mathcal{R}}$	orthogonal $n \times n$ matrix
$\boldsymbol{\mathcal{Q}_1}$	The first four columns of $\boldsymbol{\mathcal{Q}}$	orthogonal $n \times 4$ matrix
$\boldsymbol{\mathcal{Q}_2}$	The last $(n-4)$ columns of $\boldsymbol{\mathcal{Q}}$	orthogonal $n \times (n-4)$ matrix
$\boldsymbol{\mathcal{R}}$	The matrix produced by $A = \boldsymbol{\mathcal{Q}\mathcal{R}}$	$n \times 4$ matrix
$\boldsymbol{\mathcal{R}_1}$	The matrix defined by $\boldsymbol{\mathcal{R}} = \begin{bmatrix} \boldsymbol{\mathcal{R}_1} \\ \mathbf{0} \end{bmatrix}$	4×4 matrix

$\boldsymbol{\mathcal{A}}$.2 Presenting the solution of the $I_m^d(f)$ functional

Let us first define the *nullspace* [80, 82] of the $I_m^d(f)$ functional of Equation (2.5) of Section 2.1.1.3. It is a space of M polynomials in d variables of total degree up to order $m-1$ where d, m have been defined in Section 2.1.1.3. The dimension of the nullspace is determined by

$$M = \binom{d+m-1}{d} = \frac{(d+m-1)!}{d!\,(m-1)!} \qquad (\mathcal{A}.1).$$

Suppose that $m = 2$. Let the $M = d+1$ polynomials that span the *nullspace* of $I_m^d(f)$ be depicted by $\{\delta_1, \dots, \delta_M\}$. If $d = m = 2$ then the following three monomials in two variables span the nullspace

$$\delta_1 = 1, \quad \delta_2 = x, \quad \delta_3 = y.$$

If $m = 2$ and $d = 3$ the following four monomials in three variables span the nullspace

$$\delta_1 = 1, \quad \delta_2 = x, \quad \delta_3 = y, \quad \delta_4 = z.$$

The solution of the $I_m^d(f)$ functional [80, 82] expressed in an analytical form is given by

$$f_s = \sum_{v=1}^{M} \alpha_v \delta_v + \sum_{i=1}^{n} \theta_i \phi(s, p_i) \qquad (\mathcal{A}.2)$$

where, for a d dimensional source image, p represents a source control point in d dimensions ($d = 1$, $d = 2$, $d = 3$ or $d = 4$ for time-varying $3D$ source images) and s corresponds to any other point of the d dimensional source image. The number n is the total number of source control points. The set $\{\alpha_1, \dots, \alpha_M\}$ is comprised of $1 \times d$ vectors which consist of the affine coefficients. The M polynomials $\delta_1, \dots, \delta_M$ span the nullspace of $I_m^d(f)$ [which is not measured by $I_m^d(f)$] as described previously. The term $\sum_{v=1}^{M} \alpha_v \delta_v$ represents the affine transformation component and the set of M polynomials is sufficient for an optimal affine transformation in the least-squares sense. The elements of the $\{\theta_1, \dots, \theta_n\}$ set are $1 \times d$ vectors which include the TPS coefficients. The TPS basis functions $\phi(s, p_i)$ depend only on m and d [80, 82]. It holds that $\phi(s, p) = \phi(\|s - p\|) = \phi(r)$ where

$$r = \|s - p\| = \sqrt{\sum_{k=1}^{d} (s_k - p_k)^2} \qquad (\mathcal{A}.3).$$

For all partial derivatives of f_s ($1 \times d$ vector)of total order $m = 2$ and in d image dimensions to be square integrable it must hold that

$$|f_s|^2 = \int_{\mathbb{R}^d} \sum_{k,l=1}^{d} \left(\frac{\partial^2 f}{\partial s_k \partial s_l} \right)^2 ds < \infty \qquad (\mathcal{A}.4).$$

By applying the requirement of $(\mathcal{A}.4)$ of square integrability for general m, d to $(\mathcal{A}.2)$ the following basis functions are produced

$$\phi(r) = \begin{cases} H_{m,d} r^{2m-d} \log r & if\ 2m - d\ an\ even\ integer \\ H_{m,d} r^{2m-d} & otherwise \end{cases}$$

where

$$H_{m,d} = \begin{cases} \dfrac{(-1)^{d/2+1+m}}{2^{2m-1} \pi^{d/2} (m-1)! \left(m - d/2\right)!} & if\ 2m - d\ an\ even\ integer \\ \dfrac{\Gamma\left(d/2 - m\right)}{2^{2m} \pi^{d/2} (m-1)!} & otherwise \end{cases}$$

where $\Gamma(x)$ is the Gamma function. It is defined by $\Gamma(x) = \int_0^\infty e^{-t} t^{x-1}\, dt$ for $x > 0$ and $\Gamma(x+1) = x\Gamma(x), \quad x \neq 0, -1, -2, \dots$

For $m = d = 2$ $\phi(r) = \frac{1}{8\pi} r^2 \log r$ and for $m = 2,\ d = 3$ $\phi(r) = -\frac{1}{8\pi} r$ using the aforementioned relationships. The empty entries of Table 2.1 of Section 2.1.1.3 are attributed to the fact that $2m - d > 0 \leftrightarrow m > {}^{d}/_{2}$.

Suppose that $m = 2,\ d = 3$. The α_v vectors of $(\mathcal{A}.2)$ can be summarized by

$$\alpha = (\alpha_1, \dots, \alpha_M)^T \qquad (\mathcal{A}.5).$$

Similarly the θ_i $1 \times d$ vectors of $(\mathcal{A}.2)$ can be summarized by

$$Q = (\theta_1, \dots, \theta_n)^T \qquad (\mathcal{A}.6).$$

To compute the affine and TPS coefficients that are respectively contained in these vectors the following system of linear equations must be solved

$$\begin{aligned} \Phi Q + A\alpha &= T \\ A^T Q \quad &= 0 \qquad (\mathcal{A}.7) \end{aligned}$$

where Φ, Q, A, $\alpha = E^T$, T were defined in Section 2.1.2. The system of equations $(\mathcal{A}.7)$ can also be written as

$$\begin{bmatrix} \Phi & A \\ A^T & 0 \end{bmatrix} \begin{bmatrix} Q \\ \alpha \end{bmatrix} = \begin{bmatrix} T \\ 0 \end{bmatrix} \qquad (\mathcal{A}.8)$$

which reflects the relationship (2.23) of Section 2.1.2, namely, $\Psi\Delta = \Upsilon$.

Appendix $\boldsymbol{\mathcal{B}}$

Mathematical derivations

$\boldsymbol{\mathcal{B}}$.1 Derivation of the maximum likelihood estimates of the $(\varphi_h, \mu_h, \Sigma_h)$ parameters

In the $\boldsymbol{\mathcal{M}} -$ step the following quantity is maximized *w.r.t.* $(\varphi_h, \mu_h, \Sigma_h)$

$$\sum_{i=1}^{m}\sum_{j=1}^{s} \mathscr{f}_{t^{(j)}}^{(i)} \log\left(\frac{P\left(v^{(i)} \middle| t^{(i)} = t^{(j)}; \mu, \Sigma\right) P\left(t^{(i)} = t^{(j)}; \varphi\right)}{\mathscr{f}_{t^{(j)}}^{(i)}}\right) =$$

$$= \sum_{i=1}^{m}\sum_{j=1}^{s} \mathscr{f}_{t^{(j)}}^{(i)} \log\left(\frac{\frac{1}{\sqrt{(2\pi)^3\left|\Sigma_j\right|}} exp\left[-\frac{1}{2}\left(v^{(i)} - \mu_j\right)^T \Sigma_j^{-1}\left(v^{(i)} - \mu_j\right)\right]\varphi_j}{\mathscr{f}_{t^{(j)}}^{(i)}}\right) \qquad (\mathcal{B}.1\,).$$

$\boldsymbol{\mathcal{B}}$.1.1 The derivation of $\mu_h \coloneqq \frac{\sum_{i=1}^{m} \mathscr{f}_{t^{(h)}}^{(i)} v^{(i)}}{\sum_{i=1}^{m} \mathscr{f}_{t^{(h)}}^{(i)}}$

$$\nabla_{\mu_h} \sum_{i=1}^{m}\sum_{j=1}^{s} \mathscr{f}_{t^{(j)}}^{(i)} \log\left(\frac{\frac{1}{\sqrt{(2\pi)^3\left|\Sigma_j\right|}} exp\left[-\frac{1}{2}\left(v^{(i)} - \mu_j\right)^T \Sigma_j^{-1}\left(v^{(i)} - \mu_j\right)\right]\varphi_j}{\mathscr{f}_{t^{(j)}}^{(i)}}\right) =$$

$$= \nabla_{\mu_h}\left(-\frac{1}{2}\sum_{i=1}^{m}\sum_{j=1}^{s} \mathscr{f}_{t^{(j)}}^{(i)} \left(v^{(i)} - \mu_j\right)^T \Sigma_j^{-1}\left(v^{(i)} - \mu_j\right)\right) \qquad (\mathcal{B}.2)$$

$$= \sum_{i=1}^{m} \mathscr{f}_{t^{(h)}}^{(i)} \Sigma_h^{-1}\left(v^{(i)} - \mu_h\right) = 0 \qquad (\mathcal{B}.3).$$

The relationship $(\mathcal{B}.3)$, which leads to the update rule, was derived from the differentiation of $(\mathcal{B}.2)$ *w.r.t.* each μ_h using

$$\frac{\partial}{\partial s}(x-s)^T W(x-s) = -2W(x-s)$$

where x and s are vectors and $W(=\Sigma_h^{-1})$ is a symmetric matrix (= positive semi-definite).

$\boldsymbol{\mathcal{B}}$.1.2 The derivation of $\Sigma_h \coloneqq \frac{\sum_{i=1}^{m} \mathscr{f}_{t(h)}^{(i)}(v^{(i)}-\mu_h)(v^{(i)}-\mu_h)^T}{\sum_{i=1}^{m} \mathscr{f}_{t(h)}^{(i)}}$

$$\nabla_{\Sigma_h} \sum_{i=1}^{m} \sum_{j=1}^{s} \mathscr{f}_{t(j)}^{(i)} \log \left(\frac{\frac{1}{\sqrt{(2\pi)^3 |\Sigma_j|}} exp\left[-\frac{1}{2}\left(v^{(i)}-\mu_j\right)^T \Sigma_j^{-1}\left(v^{(i)}-\mu_j\right)\right] \varphi_j}{\mathscr{f}_{t(j)}^{(i)}} \right) =$$

$$= \nabla_{\Sigma_h} \left(\sum_{i=1}^{m} \sum_{j=1}^{s} \mathscr{f}_{t(j)}^{(i)} \left[-\frac{1}{2} \log|\Sigma_j| + \left(-\frac{1}{2}\left(v^{(i)}-\mu_j\right)^T \Sigma_j^{-1}\left(v^{(i)}-\mu_j\right) \right) \right] \right) = \qquad (\mathcal{B}.4)$$

$$= -\frac{1}{2} \sum_{i=1}^{m} \mathscr{f}_{t(h)}^{(i)} \left[\Sigma_h^{-T} - \Sigma_h^{-T}\left(v^{(i)}-\mu_h\right)\left(v^{(i)}-\mu_h\right)^T \Sigma_h^{-T} \right] = 0 \qquad (\mathcal{B}.5)$$

which leads to the update rule. The Equation $(\mathcal{B}.5)$ was derived from the differentiation of $(\mathcal{B}.4)$ *w.r.t.* each Σ_h. The relationships that were used for the derivation of $(\mathcal{B}.5)$ are

$$\frac{\partial a^T X^{-1} b}{\partial X} = -X^{-T} a b^T X^{-T}$$

$$\frac{\partial \log det(X)}{\partial X} = X^{-T} = (X^{-1})^T = (X^T)^{-1}$$

where X is a matrix and a and b are vectors (see Ref. [85]).

$\boldsymbol{\mathcal{B}}$.1.3 The derivation of $\varphi_h \coloneqq \frac{1}{m}\sum_{i=1}^{m} \mathscr{f}_{t(h)}^{(i)}$

The maximization of $\mathcal{B}.1$ w.r.t. φ_h leads to the constrained optimization

$$max_{\varphi_j} \sum_{i=1}^{m} \sum_{j=1}^{s} \mathscr{w}_{t^{(j)}}^{(i)} \log \varphi_j$$

$$s.t. \quad g(\varphi_j) = \sum_{j=1}^{s} \varphi_j - 1 = 0$$

(See Section 2.2.2 for details about the constraints.).

Let’s define the Lagrangian

$$\mathcal{L}(\varphi_j, \beta) = f(\varphi_j) + \beta g(\varphi_j)$$

$$= \sum_{i=1}^{m} \sum_{j=1}^{s} \mathscr{w}_{t^{(j)}}^{(i)} \log \varphi_j + \beta \left(\sum_{j=1}^{s} \varphi_j - 1 \right)$$

where β is the Lagrange multiplier. Hence

$$\frac{\partial}{\partial \varphi_h} \mathcal{L} = \sum_{i=1}^{m} \frac{\mathscr{w}_{t^{(h)}}^{(i)}}{\varphi_h} + \beta = 0 \;\Rightarrow \varphi_h = -\frac{\sum_{i=1}^{m} \mathscr{w}_{t^{(h)}}^{(i)}}{\beta} \qquad (\mathcal{B}.6).$$

$$(\mathcal{B}.6) \Rightarrow \sum_{h=1}^{s} \varphi_h = -\frac{1}{\beta} \sum_{i=1}^{m} \left(\sum_{h=1}^{s} \mathscr{w}_{t^{(h)}}^{(i)} \right) = -\frac{m \cdot 1}{\beta} = 1 \;\Rightarrow -\beta = m \qquad (\mathcal{B}.7).$$

$$(\mathcal{B}.6) \overset{(\mathcal{B}.7)}{\Longrightarrow} \varphi_h = \frac{1}{m} \sum_{i=1}^{m} \mathscr{w}_{t^{(h)}}^{(i)} \qquad (\mathcal{B}.8).$$

$\boldsymbol{\mathcal{B}}$.2 The incremental maximization of the log likelihood function via the $\mathcal{EM}$ algorithm

Assume the parameters $\left(\varphi_h^{(t)}, \mu_h^{(t)}, \Sigma_h^{(t)}\right)$ and $\left(\varphi_h^{(t+1)}, \mu_h^{(t+1)}, \Sigma_h^{(t+1)}\right)$ which arise from two successive $\boldsymbol{\mathcal{EM}}$ iterations, *i.e.*, (t) and $(t+1)$, respectively. Hence, for the (t) iteration,

$$\left(\mathscr{w}_{t^{(h)}}^{(i)}\right)^{(t)} = P\left(t^{(i)} = t^{(h)} \middle| v^{(i)};\; \varphi_h^{(t)}, \mu_h^{(t)}, \Sigma_h^{(t)}\right)$$

$$l\left(\varphi_h^{(t)}, \mu_h^{(t)}, \Sigma_h^{(t)}\right) =$$

$$= \sum_{i=1}^{m}\sum_{h=1}^{s}\left(\mathscr{f}_{t^{(h)}}^{(i)}\right)^{(t)} \log\left(\frac{P\left(v^{(i)}\middle|t^{(i)} = t^{(h)}; \mu^{(t)}, \Sigma^{(t)}\right)P\left(t^{(i)} = t^{(h)}; \varphi^{(t)}\right)}{\left(\mathscr{f}_{t^{(h)}}^{(i)}\right)^{(t)}}\right)$$

Thus for the $(t+1)$ iteration

$$\left(\varphi_h^{(t+1)}, \mu_h^{(t+1)}, \Sigma_h^{(t+1)}\right) :=$$

$$:= \underset{\left(\varphi_h^{(t)}, \mu_h^{(t)}, \Sigma_h^{(t)}\right)}{\operatorname{argmax}} \sum_{i=1}^{m}\sum_{h=1}^{s}\left(\mathscr{f}_{t^{(h)}}^{(i)}\right)^{(t)} \log\left(\frac{P\left(v^{(i)}\middle|t^{(i)} = t^{(h)}; \mu^{(t)}, \Sigma^{(t)}\right)P\left(t^{(i)} = t^{(h)}; \varphi^{(t)}\right)}{\left(\mathscr{f}_{t^{(h)}}^{(i)}\right)^{(t)}}\right) \quad (\mathcal{B}.9)$$

$$l\left(\varphi_h^{(t+1)}, \mu_h^{(t+1)}, \Sigma_h^{(t+1)}\right) =$$

$$= \sum_{i=1}^{m}\sum_{h=1}^{s}\left(\mathscr{f}_{t^{(h)}}^{(i)}\right)^{(t+1)} \log\left(\frac{P\left(v^{(i)}\middle|t^{(i)} = t^{(h)}; \mu^{(t+1)}, \Sigma^{(t+1)}\right)P\left(t^{(i)} = t^{(h)}; \varphi^{(t+1)}\right)}{\left(\mathscr{f}_{t^{(h)}}^{(i)}\right)^{(t+1)}}\right) \quad (\mathcal{B}.10)$$

$$\geq \sum_{i=1}^{m}\sum_{h=1}^{s}\left(\mathscr{f}_{t^{(h)}}^{(i)}\right)^{(t)} \log\left(\frac{P\left(v^{(i)}\middle|t^{(i)} = t^{(h)}; \mu^{(t)}, \Sigma^{(t)}\right)P\left(t^{(i)} = t^{(h)}; \varphi^{(t)}\right)}{\left(\mathscr{f}_{t^{(h)}}^{(i)}\right)^{(t)}}\right) \quad (\mathcal{B}.11)$$

$$= l\left(\varphi_h^{(t)}, \mu_h^{(t)}, \Sigma_h^{(t)}\right) \quad (\mathcal{B}.12).$$

The log likelihood expression of $(\mathcal{B}.9)$ is maximized in the $\boldsymbol{\mathcal{M}} -$ step *w.r.t.* $(\varphi_h, \mu_h, \Sigma_h)$ and in the $\boldsymbol{\mathcal{E}} -$ step *w.r.t.* $\mathscr{f}_{t^{(h)}}^{(i)}$. Hence the transition from $(\mathcal{B}.10)$ to $(\mathcal{B}.11)$. Equations $(\mathcal{B}.9) - (\mathcal{B}.11)$ clearly show that the log likelihood $l(\varphi_h, \mu_h, \Sigma_h)$ increases monotonically with successive $\boldsymbol{\mathcal{EM}}$ iterations. It suffices to declare convergence of the $\boldsymbol{\mathcal{EM}}$ algorithm when (*i*) $\Delta l \leq j$ where j is a pre-set convergence parameter; and (*ii*) the increase of the log likelihood reaches a plateau.

$\boldsymbol{\mathcal{B}}$.3 The lower bound of the log likelihood function

The $\boldsymbol{\mathcal{EM}}$ algorithm maximizes the log likelihood $l(\varphi_h, \mu_h, \Sigma_h)$ of Equation (2.33) (of Section 2.2.2) incrementally (see Appendix $\mathcal{B}$.2 and Ref [93]). The lower bound of l can be estimated by

$$l(\varphi,\mu,\Sigma)=\sum_{i=1}^{m}\log\left(\sum_{t^{(h)}=t^{(1)}}^{t^{(s)}}P\big(v^{(i)}\big|t^{(h)};\mu,\Sigma\big)\ P\big(t^{(h)};\varphi\big)\right)$$

$$=\sum_{i=1}^{m}\log\left(\sum_{h=1}^{s}\mathscr{f}_{t^{(h)}}^{(i)}\left[\frac{P\big(v^{(i)}\big|t^{(i)}=t^{(h)};\mu,\Sigma\big)P\big(t^{(i)}=t^{(h)};\varphi\big)}{\mathscr{f}_{t^{(h)}}^{(i)}}\right]\right)$$

$$\geq\sum_{i=1}^{m}\sum_{h=1}^{s}\mathscr{f}_{t^{(h)}}^{(i)}\log\left(\frac{P\big(v^{(i)}\big|t^{(i)}=t^{(h)};\mu,\Sigma\big)P\big(t^{(i)}=t^{(h)};\varphi\big)}{\mathscr{f}_{t^{(h)}}^{(i)}}\right)\quad(\mathcal{B}.13).$$

The relationship of $(\mathcal{B}.13)$ is based on Jensen's inequality

$$h(E[X])\geq E[h(X)]\qquad(\mathcal{B}.14)$$

where $h(X)=\log X$ is a strictly concave function and $X\in\mathbb{R}^{+}$ is a random variable

$$X\equiv\left[\frac{P\big(v^{(i)}\big|t^{(i)}=t^{(h)};\mu,\Sigma\big)P\big(t^{(i)}=t^{(h)};\varphi\big)}{\mathscr{f}_{t^{(h)}}^{(i)}}\right]\qquad(\mathcal{B}.15).$$

However, the equality in $(\mathcal{B}.14)$ holds if and only if $E[X]=X$. Note that by definition [see Equation (2.82)]

$$\mathscr{f}_{t^{(h)}}^{(i)}=P\big(t^{(i)}=t^{(h)}\big|v^{(i)};\ \varphi,\mu,\Sigma\ \big)$$

$$=\frac{P\big(v^{(i)}\big|t^{(i)}=t^{(h)};\ \mu,\Sigma\ \big)P\big(t^{(i)}=t^{(h)};\ \varphi\big)}{P\big(v^{(i)};\varphi,\mu,\Sigma\big)}\qquad(\mathcal{B}.16).$$

$$\text{Eq. }(\mathcal{B}.15)\xrightarrow{\text{Eq. }(\mathcal{B}.16)}X=P\big(v^{(i)};\varphi,\mu,\Sigma\big)$$

$$=\sum_{j=1}^{s}\varphi_j\,P\big(v^{(i)}\big|t^{(i)}=t^{(j)};\mu_j,\Sigma_j\big)\quad(\mathcal{B}.17).$$

The variable X of Equation $(\mathcal{B}.17)$ is a 'constant-valued random variable' as it doesn't depend on $t^{(h)}$. It is hence due to the Equation (2.82) of the $\boldsymbol{\mathcal{E}}-$ step that

$$l(\varphi_h,\mu_h,\Sigma_h)=\sum_{i=1}^{m}\sum_{h=1}^{s}\mathscr{f}_{t^{(h)}}^{(i)}\log\left(\frac{P\big(v^{(i)}\big|t^{(i)}=t^{(h)};\mu,\Sigma\big)P\big(t^{(i)}=t^{(h)};\varphi\big)}{\mathscr{f}_{t^{(h)}}^{(i)}}\right)\quad(\mathcal{B}.18).$$

It is in the $\boldsymbol{\mathcal{M}}-$ step that $l(\varphi_h, \mu_h, \Sigma_h)$ of Equation $(\mathcal{B}.18)$ is maximized *w.r.t.* $(\varphi_h, \mu_h, \Sigma_h)$, *i.e.*,

$$(\varphi_h, \mu_h, \Sigma_h) \coloneqq \underset{(\varphi_h, \mu_h, \Sigma_h)}{\operatorname{argmax}} \sum_{i=1}^{m} \sum_{h=1}^{s} \not{f}_{t^{(h)}}^{(i)} \log\left(\frac{P\left(v^{(i)} \middle| t^{(i)}=t^{(h)}; \mu, \Sigma\right) P\left(t^{(i)}=t^{(h)}; \varphi\right)}{\not{f}_{t^{(h)}}^{(i)}}\right) \qquad (\mathcal{B}.19)$$

leading to Equations (2.83)-(2.85).

$\boldsymbol{\mathcal{B}}$.4 The maximization of the posterior probability distribution of θ

Consider the following series of relationships

$$\underset{\theta}{\operatorname{argmax}} P(\theta | \boldsymbol{\mathcal{M}}, \boldsymbol{\mathcal{S}}, \varphi, \mu, \Sigma) = \underset{\theta}{\operatorname{argmax}} \frac{P(\boldsymbol{\mathcal{M}} | \boldsymbol{\mathcal{S}}, \theta, \varphi, \mu, \Sigma) P(\theta)}{P(\boldsymbol{\mathcal{M}})} =$$

$$= \underset{\theta}{\operatorname{argmax}} P(\boldsymbol{\mathcal{M}} | \boldsymbol{\mathcal{S}}, \theta, \varphi, \mu, \Sigma) P(\theta) = \underset{\theta}{\operatorname{argmin}}(-\log P(\boldsymbol{\mathcal{M}} | \boldsymbol{\mathcal{S}}, \theta, \varphi, \mu, \Sigma) P(\theta))$$

$$\cong \underset{\theta}{\operatorname{argmin}} \left[-\sum_{i=1}^{m} \log\left(\sum_{h=1}^{s+1} \varphi_h \frac{1}{\sqrt{(2\pi)^3 |\Sigma_h|}} exp\left[-\frac{1}{2}\left(q^{(i)} - \mathcal{F}\left(t^{(h)}; \theta\right)\right)^T \Sigma_h^{-1} \left(q^{(i)} - \mathcal{F}\left(t^{(h)}; \theta\right)\right)\right]\right) + \lambda I(\theta)\right]$$

$$\cong \underset{\theta}{\operatorname{argmin}} \left[-\sum_{i=1}^{m} \sum_{h=1}^{s+1} \not{f}_{t^{(h)}}^{(i)} \log\left(\frac{\varphi_h \frac{1}{\sqrt{(2\pi)^3 |\Sigma_h|}} exp\left[-\frac{1}{2}\left(q^{(i)} - \mathcal{F}\left(t^{(h)}; \theta\right)\right)^T \Sigma_h^{-1} \left(q^{(i)} - \mathcal{F}\left(t^{(h)}; \theta\right)\right)\right]}{\not{f}_{t^{(h)}}^{(i)}}\right) + \lambda I(\theta)\right]$$

$$\cong \underset{\theta}{\operatorname{argmin}} \left[\sum_{i=1}^{m} \sum_{h=1}^{s+1} \not{f}_{t^{(h)}}^{(i)} \log \not{f}_{t^{(h)}}^{(i)} - \sum_{i=1}^{m} \sum_{h=1}^{s+1} \not{f}_{t^{(h)}}^{(i)} \log\left(\varphi_h \frac{1}{\sqrt{(2\pi)^3 |\Sigma_h|}} exp\left[-\frac{1}{2}\left(q^{(i)} - \mathcal{F}\left(t^{(h)}; \theta\right)\right)^T \Sigma_h^{-1} \left(q^{(i)} - \mathcal{F}\left(t^{(h)}; \theta\right)\right)\right]\right) + \lambda I(\theta)\right]$$

$$\cong \underset{\theta}{\operatorname{argmin}} \left[\sum_{i=1}^{m} \sum_{h=1}^{s+1} \mathscr{f}_{t^{(h)}}^{(i)} \frac{\left(q^{(i)} - \mathcal{F}\left(t^{(h)};\theta\right)\right)^{T} \Sigma_h^{-1} \left(q^{(i)} - \mathcal{F}\left(t^{(h)};\theta\right)\right)}{2} - \sum_{i=1}^{m} \sum_{h=1}^{s+1} \mathscr{f}_{t^{(h)}}^{(i)} \log \varphi_h \right.$$

$$+ \sum_{i=1}^{m} \sum_{h=1}^{s+1} \frac{3\mathscr{f}_{t^{(h)}}^{(i)}}{2} \log(2\pi) + \sum_{i=1}^{m} \sum_{h=1}^{s+1} \frac{\mathscr{f}_{t^{(h)}}^{(i)}}{2} \log|\Sigma_h| + \sum_{i=1}^{m} \sum_{h=1}^{s+1} \mathscr{f}_{t^{(h)}}^{(i)} \log \mathscr{f}_{t^{(h)}}^{(i)}$$

$$\left. + \lambda I(\theta) \right].$$

$\boldsymbol{\mathcal{B}}$.5 The derivation of the log-posterior cost function

$$Eq.(2.93) \xRightarrow{Eq.(2.95) \wedge Eq.(2.96)} \mathcal{E}_1(\mathcal{T},\theta) =$$

$$= \sum_{i=1}^{m+1} \sum_{h=1}^{s+1} \mathscr{f}_{t^{(h)}}^{(i)} \frac{\left\|q^{(i)} - \mathcal{F}\left(t^{(h)};\theta\right)\right\|^2}{2T} - \sum_{i=1}^{m+1} \sum_{h=1}^{s+1} \mathscr{f}_{t^{(h)}}^{(i)} \log \varphi_h + \sum_{i=1}^{m+1} \sum_{h=1}^{s+1} \frac{3}{2} \mathscr{f}_{t^{(h)}}^{(i)} \log(2\pi)$$

$$+ \sum_{i=1}^{m} \sum_{h=1}^{s} \frac{3}{2} \mathscr{f}_{t^{(h)}}^{(i)} \log T + \sum_{h=1}^{s} \frac{3}{2} \mathscr{f}_{t^{(h)}}^{(m+1)} \log T_0 + \sum_{i=1}^{m} \frac{3}{2} \mathscr{f}_{t^{(s+1)}}^{(i)} \log T_0 + \sum_{i=1}^{m+1} \sum_{h=1}^{s+1} \mathscr{f}_{t^{(h)}}^{(i)} \log \mathscr{f}_{t^{(h)}}^{(i)}$$

$$+ \lambda I(\theta)$$

$$\mathcal{E}_1(\mathcal{T},\theta) \approx \sum_{i=1}^{m+1} \sum_{h=1}^{s+1} \mathscr{f}_{t^{(h)}}^{(i)} \frac{\left\|q^{(i)} - \mathcal{F}\left(t^{(h)};\theta\right)\right\|^2}{2T} + \sum_{i=1}^{m} \sum_{h=1}^{s} \frac{3}{2} \mathscr{f}_{t^{(h)}}^{(i)} \log T + \sum_{h=1}^{s} \frac{3}{2} \mathscr{f}_{t^{(h)}}^{(m+1)} \log T_0$$

$$+ \sum_{i=1}^{m} \frac{3}{2} \mathscr{f}_{t^{(s+1)}}^{(i)} \log T_0 + \sum_{i=1}^{m+1} \sum_{h=1}^{s+1} \mathscr{f}_{t^{(h)}}^{(i)} \log \mathscr{f}_{t^{(h)}}^{(i)} + \lambda I(\theta)$$

$$\mathcal{E}_2(\mathcal{T},\theta) = T\mathcal{E}_1(\mathcal{T},\theta)$$

$$= \sum_{i=1}^{m} \sum_{h=1}^{s} \mathscr{f}_{t^{(h)}}^{(i)} \frac{\left\|q^{(i)} - \mathcal{F}\left(t^{(h)};\theta\right)\right\|^2}{2} + \sum_{h=1}^{s} \mathscr{f}_{t^{(h)}}^{(m+1)} \frac{\left\|q_{m+1} - \mathcal{F}\left(t^{(h)};\theta\right)\right\|^2}{2}$$

$$+ \sum_{i=1}^{m} \mathscr{f}_{t^{(s+1)}}^{(i)} \frac{\left\|q^{(i)} - \mu_{s+1}\right\|^2}{2} + T \sum_{i=1}^{m} \sum_{h=1}^{s} \frac{3}{2} \mathscr{f}_{t^{(h)}}^{(i)} \log T + T \sum_{h=1}^{s} \frac{3}{2} \mathscr{f}_{t^{(h)}}^{(m+1)} \log T_0$$

$$+ T \sum_{i=1}^{m} \frac{3}{2} \mathscr{f}_{t^{(s+1)}}^{(i)} \log T_0$$

$$+ T \left(\sum_{i=1}^{m} \sum_{h=1}^{s} \mathscr{f}_{t^{(h)}}^{(i)} \log \mathscr{f}_{t^{(h)}}^{(i)} + \sum_{h=1}^{s} \mathscr{f}_{t^{(h)}}^{(m+1)} \log \mathscr{f}_{t^{(h)}}^{(m+1)} + \sum_{i=1}^{m} \mathscr{f}_{t^{(s+1)}}^{(i)} \log \mathscr{f}_{t^{(s+1)}}^{(i)} \right)$$

$$+ \lambda T I(\theta)$$

$\boldsymbol{\mathcal{B}}.6$ Derivatives of the cost function *w.r.t.* ψ and E^T when $U \equiv \Phi$

Equation (2.103) can be rewritten in terms of the squared form of the Frobenius matrix norm of $\left(\mathrm{W} - \mathcal{F}(\boldsymbol{\mathcal{S}}_0)\right)^T \in \mathbb{R}^{3\times s}$

$$\left\|\left(\mathrm{W} - \mathcal{F}(\boldsymbol{\mathcal{S}}_0)\right)^T\right\|_F^2 = \|\mathrm{W} - \mathcal{F}(\boldsymbol{\mathcal{S}}_0)\|_F^2 = \sum_{h=1}^{s}\sum_{j=1}^{3}\left|w_{(j)}^{(h)} - \mathcal{F}\left(t_{(j)}^{(h)}\right)\right|^2$$

$$= \operatorname{trace}\left(\left(\mathrm{W} - \mathcal{F}(\boldsymbol{\mathcal{S}}_0)\right)^T\left(\mathrm{W} - \mathcal{F}(\boldsymbol{\mathcal{S}}_0)\right)\right)$$

$$= \operatorname{trace}\left(\left(\mathrm{W} - \mathcal{F}(\boldsymbol{\mathcal{S}}_0)\right)\left(\mathrm{W} - \mathcal{F}(\boldsymbol{\mathcal{S}}_0)\right)^T\right) \qquad (\mathcal{B}.20).$$

$$\text{Eq. } (2.103) \xRightarrow{\text{Eqs. } (2.105) \wedge (2.106) \wedge (\mathcal{B}.20)}$$

$$\mathcal{E}_4(E^T, \psi) = \frac{1}{2}\|\mathrm{W} - \mathcal{F}(\boldsymbol{\mathcal{S}}_0)\|_F^2 + \lambda \operatorname{trace}(\psi^T \mathcal{N}^T \Phi \mathcal{N} \psi)$$

$$= \frac{1}{2}\|\mathrm{F}\boldsymbol{\mathcal{M}_0} - [1|\boldsymbol{\mathcal{S}}_0]E^T - \Phi\mathcal{N}\psi\|_F^2 + \lambda \operatorname{trace}(\psi^T \mathcal{N}^T \Phi \mathcal{N} \psi) \qquad (\mathcal{B}.21).$$

$\boldsymbol{\mathcal{S}}_0$ is taken to be the set of control points. Consider the full rank $\boldsymbol{Q\mathcal{R}}$ decomposition of $[1|\boldsymbol{\mathcal{S}}_0]$ (see Equation (2.26) of Section 2.1.3 for details)

$$[1|\boldsymbol{\mathcal{S}}_0] = \boldsymbol{Q\mathcal{R}} = [\boldsymbol{Q_1}|\mathcal{N}]\begin{bmatrix}\boldsymbol{\mathcal{R}_1}\\ \boldsymbol{0}\end{bmatrix} = \boldsymbol{Q_1\mathcal{R}_1} \qquad (\mathcal{B}.22)$$

where $\boldsymbol{Q_1} \in \mathbb{R}^{s\times 4}$ and $\boldsymbol{Q}_1^T\boldsymbol{Q_1} = \boldsymbol{Q_1}\boldsymbol{Q}_1^T = I_4$, the left null space of $[1|\boldsymbol{\mathcal{S}}_0]$ $\mathcal{N} \in \mathbb{R}^{s\times(s-4)}$ and $\mathcal{N}^T\mathcal{N} = \mathcal{N}\mathcal{N}^T = I_{s-4}$, and $\boldsymbol{\mathcal{R}_1} \in \mathbb{R}^{4\times 4}$.

$$\text{Eq. } (\mathcal{B}.21) \xRightarrow{\text{Eq. } (\mathcal{B}.22)} \mathcal{E}_4(E^T, \psi) = \frac{1}{2}\|\mathrm{F}\boldsymbol{\mathcal{M}_0} - \boldsymbol{Q_1\mathcal{R}_1}E^T - \Phi\mathcal{N}\psi\|_F^2$$

$$+ \lambda \operatorname{trace}(\psi^T \mathcal{N}^T \Phi \mathcal{N} \psi) \qquad (\mathcal{B}.23)$$

Consider the following series of Equations

$$\|(\mathrm{F}\boldsymbol{\mathcal{M}_0} - \Phi\mathcal{N}\psi) - \boldsymbol{Q_1\mathcal{R}_1}E^T\|_F^2 = \|(\Phi\mathcal{N}\psi - \mathrm{F}\boldsymbol{\mathcal{M}_0}) + \boldsymbol{Q_1\mathcal{R}_1}E^T\|_F^2 =$$

$$= \operatorname{trace}([(\Phi\mathcal{N}\psi - \mathrm{F}\boldsymbol{\mathcal{M}_0}) + (\boldsymbol{Q_1\mathcal{R}_1}E^T)][(\Phi\mathcal{N}\psi - \mathrm{F}\boldsymbol{\mathcal{M}_0}) + (\boldsymbol{Q_1\mathcal{R}_1}E^T)]^T)$$

$$= \operatorname{trace}([\mathcal{A} + \mathcal{B}][\mathcal{A} + \mathcal{B}]^T)$$

$$= \text{trace}([\mathcal{A} + \mathcal{B}][\mathcal{A}^T + \mathcal{B}^T])$$

$$= \text{trace}(\mathcal{A}\mathcal{A}^T + \mathcal{A}\mathcal{B}^T + \mathcal{B}\mathcal{A}^T + \mathcal{B}\mathcal{B}^T)$$

$$= \text{trace}(\mathcal{A}\mathcal{A}^T) + \text{trace}(\mathcal{A}\mathcal{B}^T + (\mathcal{A}\mathcal{B}^T)^T) + \text{trace}(\mathcal{B}\mathcal{B}^T)$$

$$= \text{trace}(\mathcal{A}\mathcal{A}^T) + \text{trace}(\mathcal{B}\mathcal{B}^T) + \text{trace}(\mathcal{A}\mathcal{B}^T) + \text{trace}((\mathcal{A}\mathcal{B}^T)^T)$$

$$= \text{trace}(\mathcal{A}\mathcal{A}^T) + \text{trace}(\mathcal{B}\mathcal{B}^T) + 2\text{trace}(\mathcal{A}\mathcal{B}^T)$$

$$= \|\mathit{\Phi}\mathcal{N}\psi - \digamma\boldsymbol{\mathcal{M}_0}\|_F^2 + \|\boldsymbol{Q_1\mathcal{R}_1}E^T\|_F^2 + 2\text{trace}[(\mathit{\Phi}\mathcal{N}\psi - \digamma\boldsymbol{\mathcal{M}_0})(\boldsymbol{Q_1\mathcal{R}_1}E^T)^{\boldsymbol{T}}] \qquad (\mathcal{B}.24)$$

where $\mathcal{A} \equiv (\mathit{\Phi}\mathcal{N}\psi - \digamma\boldsymbol{\mathcal{M}_0})$ and $\mathcal{B} \equiv (\boldsymbol{Q_1\mathcal{R}_1}E^T)$.

$$\text{Eq. } (\mathcal{B}.23) \xRightarrow{\text{Eq. } (\mathcal{B}.24)} \mathcal{E}_5(E^T, \psi) = 2\mathcal{E}_4(E^T, \psi) =$$

$$= \|\digamma\boldsymbol{\mathcal{M}_0} - \boldsymbol{Q_1\mathcal{R}_1}E^T - \mathit{\Phi}\mathcal{N}\psi\|_F^2 + 2\lambda\text{trace}(\psi^T\mathcal{N}^T\mathit{\Phi}\mathcal{N}\psi)$$

$$= \|\mathit{\Phi}\mathcal{N}\psi - \digamma\boldsymbol{\mathcal{M}_0}\|_F^2 + \|\boldsymbol{Q_1\mathcal{R}_1}E^T\|_F^2 + 2\text{trace}[(\mathit{\Phi}\mathcal{N}\psi - \digamma\boldsymbol{\mathcal{M}_0})(\boldsymbol{Q_1\mathcal{R}_1}E^T)^{\boldsymbol{T}}]$$
$$+ 2\lambda\text{trace}(\psi^T\mathcal{N}^T\mathit{\Phi}\mathcal{N}\psi).$$

The derivative of $\mathcal{E}_5$ *w.r.t.* E^T is

$$\frac{\partial}{\partial E^T}\mathcal{E}_5(E^T, \psi) = \frac{\partial}{\partial E^T}\|\boldsymbol{Q_1\mathcal{R}_1}E^T\|_F^2 + 2\frac{\partial}{\partial E^T}\text{trace}[(\mathit{\Phi}\mathcal{N}\psi - \digamma\boldsymbol{\mathcal{M}_0})(\boldsymbol{Q_1\mathcal{R}_1}E^T)^{\boldsymbol{T}}]$$

$$= \frac{\partial}{\partial E^T}\text{trace}[(\boldsymbol{Q_1\mathcal{R}_1}E^T)(\boldsymbol{Q_1\mathcal{R}_1}E^T)^T] + 2\frac{\partial}{\partial E^T}\text{trace}[(\boldsymbol{Q_1\mathcal{R}_1})E^T(\mathit{\Phi}\mathcal{N}\psi - \digamma\boldsymbol{\mathcal{M}_0})^T]$$

$$= 2(\boldsymbol{Q_1\mathcal{R}_1})^{\boldsymbol{T}}(\boldsymbol{Q_1\mathcal{R}_1}E^T) + 2(\boldsymbol{Q_1\mathcal{R}_1})^{\boldsymbol{T}}(\mathit{\Phi}\mathcal{N}\psi - \digamma\boldsymbol{\mathcal{M}_0}) \qquad (\mathcal{B}.25)$$

where the first term of the right part of Equation $(\mathcal{B}.25)$ arises from

$$\frac{\partial}{\partial X}\text{trace}[(AXB + C)(AXB + C)^T] = 2A^T(AXB + C)B^T$$

and the second term from

$$\frac{\partial}{\partial X}\text{trace}(AXB) = A^TB^T.$$

Hence,

$$\min_{E^T} \mathcal{E}_5(E^T,\psi) \xrightarrow{\text{Eq. }(\mathcal{B}.25)} E^T = \boldsymbol{\mathcal{R}}_1^{-1}\boldsymbol{\mathcal{Q}}_1^T(\text{Ƒ}\boldsymbol{\mathcal{M}}_\mathbf{0} - \Phi\mathcal{N}\psi) \qquad (\mathcal{B}.26).$$

The derivative of $\mathcal{E}_5$ *w.r.t.* ψ is

$$\frac{\partial}{\partial\psi}\mathcal{E}_5(E^T,\psi) = \frac{\partial}{\partial\psi}\|\Phi\mathcal{N}\psi - \text{Ƒ}\boldsymbol{\mathcal{M}}_\mathbf{0}\|_F^2 + 2\frac{\partial}{\partial\psi}\text{trace}[(\Phi\mathcal{N}\psi - \text{Ƒ}\boldsymbol{\mathcal{M}}_\mathbf{0})(\boldsymbol{\mathcal{Q}}_\mathbf{1}\boldsymbol{\mathcal{R}}_\mathbf{1}E^T)^{\boldsymbol{T}}] \\ + 4\lambda\mathcal{N}^T\Phi\mathcal{N}\psi$$

$$= \frac{\partial}{\partial\psi}\text{trace}[(\Phi\mathcal{N}\psi - \text{Ƒ}\boldsymbol{\mathcal{M}}_\mathbf{0})(\Phi\mathcal{N}\psi - \text{Ƒ}\boldsymbol{\mathcal{M}}_\mathbf{0})^T] \\ - 2\frac{\partial}{\partial\psi}\text{trace}[(\text{Ƒ}\boldsymbol{\mathcal{M}}_\mathbf{0} - \Phi\mathcal{N}\psi)(\text{Ƒ}\boldsymbol{\mathcal{M}}_\mathbf{0} - \Phi\mathcal{N}\psi)^T] + 4\lambda\mathcal{N}^T\Phi\mathcal{N}\psi$$

$$= 2(\Phi\mathcal{N})^T(\Phi\mathcal{N}\psi - \text{Ƒ}\boldsymbol{\mathcal{M}}_\mathbf{0}) - 4(\Phi\mathcal{N})^T(\Phi\mathcal{N}\psi - \text{Ƒ}\boldsymbol{\mathcal{M}}_\mathbf{0}) + 4\lambda\mathcal{N}^T\Phi\mathcal{N}\psi$$

$$= -2(\Phi\mathcal{N})^T(\Phi\mathcal{N}\psi - \text{Ƒ}\boldsymbol{\mathcal{M}}_\mathbf{0}) + 4\lambda\mathcal{N}^T\Phi\mathcal{N}\psi.$$

Hence,

$$\min_{\psi} \mathcal{E}_5(E^T,\psi) \xrightarrow{\text{Eq. }(\mathcal{B}.26)} \psi = \mathcal{N}^T(\Phi - 2\lambda I)^{-1}\text{Ƒ}\boldsymbol{\mathcal{M}}_\mathbf{0}.$$

$\boldsymbol{\mathcal{B}}$.7 Derivatives of the cost function *w.r.t.* ψ' and E'^T for $U \neq \Phi'$

$$\text{Eq. }(2.103) \xrightarrow{\text{Eqs. }(2.104)\wedge(2.106)\wedge(\mathcal{B}.20)} \mathcal{E}_6(E'^T,\psi') = 2\mathcal{E}_4(E'^T,\psi') =$$

$$= \|\text{Ƒ}\boldsymbol{\mathcal{M}}_\mathbf{0} - [1|\boldsymbol{\mathcal{S}}_0]E'^T - U\mathcal{N}'\psi'\|_F^2 + 2\lambda\text{trace}(\psi'^T\mathcal{N}'^T\Phi'\mathcal{N}'\psi') \qquad (\mathcal{B}.27)$$

where $E'^T \in \mathbb{R}^{4\times3}$ represents the affine transformation, $U \in \mathbb{R}^{s\times n}$ is the basis matrix, $\Phi' \in \mathbb{R}^{n\times n}$ is the TPS kernel matrix, $\psi' \in \mathbb{R}^{(n-4)\times3}$ relates to the non-affine subspace of the TPS warping, $\mathcal{N}' \in \mathbb{R}^{n\times(n-4)}$ represents the left null space of $[1|\boldsymbol{\mathcal{P}}_0] \in \mathbb{R}^{n\times4}$ and $\boldsymbol{\mathcal{P}}_0 = \{P_1,\dots,P_n\}$ corresponds to the set of the original target control points.

Consider the full rank $\boldsymbol{\mathcal{QR}}$ decomposition of $[1|\boldsymbol{\mathcal{S}}_0]$ (see Equation (2.26) of Section 2.1.3 for details)

$$[1|\boldsymbol{\mathcal{S}}_0] = \boldsymbol{\mathcal{QR}} = [\boldsymbol{\mathcal{Q}}_\mathbf{1}|\boldsymbol{\mathcal{Q}}_\mathbf{2}]\begin{bmatrix}\boldsymbol{\mathcal{R}}_\mathbf{1}\\ \mathbf{0}\end{bmatrix} = \boldsymbol{\mathcal{Q}}_\mathbf{1}\boldsymbol{\mathcal{R}}_\mathbf{1} \qquad (\mathcal{B}.28)$$

where $\boldsymbol{\mathcal{Q}}_\mathbf{1} \in \mathbb{R}^{s\times4}$ and $\boldsymbol{\mathcal{Q}}_1^T\boldsymbol{\mathcal{Q}}_\mathbf{1} = \boldsymbol{\mathcal{Q}}_\mathbf{1}\boldsymbol{\mathcal{Q}}_1^T = I_4$, $\boldsymbol{\mathcal{Q}}_\mathbf{2} \in \mathbb{R}^{s\times(s-4)}$ and $\boldsymbol{\mathcal{Q}}_2^T\boldsymbol{\mathcal{Q}}_\mathbf{2} = \boldsymbol{\mathcal{Q}}_\mathbf{2}\boldsymbol{\mathcal{Q}}_2^T = I_{s-4}$ and $\boldsymbol{\mathcal{R}}_\mathbf{1} \in \mathbb{R}^{4\times4}$.

$$\text{Eq. }(\mathcal{B}.27) \xRightarrow{\text{Eq. }(\mathcal{B}.28)} \mathcal{E}_6(E'^T,\psi') = \|\text{Ғ}\boldsymbol{\mathcal{M}}_{\mathbf{0}} - \boldsymbol{\mathcal{Q}}_{\mathbf{1}}\boldsymbol{\mathcal{R}}_{\mathbf{1}}E'^T - U\mathcal{N}'\psi'\|_F^2 +$$
$$2\lambda\text{trace}(\psi'^T\mathcal{N}'^T\Phi'\mathcal{N}'\psi') \qquad (\mathcal{B}.29).$$

It can be proven that (see Appendix $\boldsymbol{\mathcal{B}}$.6)

$$\|(\text{Ғ}\boldsymbol{\mathcal{M}}_{\mathbf{0}} - U\mathcal{N}'\psi') - \boldsymbol{\mathcal{Q}}_{\mathbf{1}}\boldsymbol{\mathcal{R}}_{\mathbf{1}}E'^T\|_F^2 =$$

$$= \|U\mathcal{N}'\psi' - \text{Ғ}\boldsymbol{\mathcal{M}}_{\mathbf{0}}\|_F^2 + \|\boldsymbol{\mathcal{Q}}_{\mathbf{1}}\boldsymbol{\mathcal{R}}_{\mathbf{1}}E'^T\|_F^2 + 2\text{trace}[(U\mathcal{N}'\psi' - \text{Ғ}\boldsymbol{\mathcal{M}}_{\mathbf{0}})(\boldsymbol{\mathcal{Q}}_{\mathbf{1}}\boldsymbol{\mathcal{R}}_{\mathbf{1}}E'^T)^{\boldsymbol{T}}] \qquad (\mathcal{B}.30)$$

Hence

$$\text{Eq. }(\mathcal{B}.29) \xRightarrow{\text{Eq. }(\mathcal{B}.30)} \mathcal{E}_6(E'^T,\psi') =$$

$$= \|U\mathcal{N}'\psi' - \text{Ғ}\boldsymbol{\mathcal{M}}_{\mathbf{0}}\|_F^2 + \|\boldsymbol{\mathcal{Q}}_{\mathbf{1}}\boldsymbol{\mathcal{R}}_{\mathbf{1}}E'^T\|_F^2 + 2\text{trace}[(U\mathcal{N}'\psi' - \text{Ғ}\boldsymbol{\mathcal{M}}_{\mathbf{0}})(\boldsymbol{\mathcal{Q}}_{\mathbf{1}}\boldsymbol{\mathcal{R}}_{\mathbf{1}}E'^T)^{\boldsymbol{T}}]$$
$$+ 2\lambda\text{trace}(\psi'^T\mathcal{N}'^T\Phi'\mathcal{N}'\psi') \qquad (\mathcal{B}.31).$$

The derivative of $\mathcal{E}_6$ *w.r.t.* E'^T (see Appendix $\boldsymbol{\mathcal{B}}$.6) is

$$\frac{\partial}{\partial E'^T}\mathcal{E}_6(E'^T,\psi') = 2(\boldsymbol{\mathcal{Q}}_{\mathbf{1}}\boldsymbol{\mathcal{R}}_{\mathbf{1}})^T(\boldsymbol{\mathcal{Q}}_{\mathbf{1}}\boldsymbol{\mathcal{R}}_{\mathbf{1}}E'^T) + 2(\boldsymbol{\mathcal{Q}}_{\mathbf{1}}\boldsymbol{\mathcal{R}}_{\mathbf{1}})^T(U\mathcal{N}'\psi' - \text{Ғ}\boldsymbol{\mathcal{M}}_{\mathbf{0}}) \qquad (\mathcal{B}.32).$$

Hence,

$$\min_{E'^T}\mathcal{E}_6(E'^T,\psi') \xRightarrow{\text{Eq. }(\mathcal{B}.32)} E'^T = \boldsymbol{\mathcal{R}}_1^{-1}\boldsymbol{\mathcal{Q}}_1^T(\text{Ғ}\boldsymbol{\mathcal{M}}_{\mathbf{0}} - U\mathcal{N}'\psi') \qquad (\mathcal{B}.33).$$

To obtain $\mathcal{N}'$ the full rank $\boldsymbol{\mathcal{Q}}'\boldsymbol{\mathcal{R}}'$ decomposition of $[1|\boldsymbol{\mathcal{P}}_0]$ is performed

$$[1|\boldsymbol{\mathcal{P}}_0] = \boldsymbol{\mathcal{Q}}'\boldsymbol{\mathcal{R}}' = [\boldsymbol{\mathcal{Q}}'_{\mathbf{1}}|\mathcal{N}']\begin{bmatrix}\boldsymbol{\mathcal{R}}'_{\mathbf{1}}\\ \mathbf{0}\end{bmatrix} = \boldsymbol{\mathcal{Q}}'_{\mathbf{1}}\boldsymbol{\mathcal{R}}'_{\mathbf{1}} \qquad (\mathcal{B}.34)$$

where $\boldsymbol{\mathcal{Q}}'_{\mathbf{1}} \in \mathbb{R}^{n\times 4}$ and $\boldsymbol{\mathcal{Q}}'^{\boldsymbol{T}}_{\mathbf{1}}\boldsymbol{\mathcal{Q}}'_{\mathbf{1}} = \boldsymbol{\mathcal{Q}}'_{\mathbf{1}}\boldsymbol{\mathcal{Q}}'^{\boldsymbol{T}}_{\mathbf{1}} = I_4$, $\mathcal{N}'^T\mathcal{N}' = \mathcal{N}'\mathcal{N}'^T = I_{n-4}$ and $\boldsymbol{\mathcal{R}}'_{\mathbf{1}} \in \mathbb{R}^{4\times 4}$.

The derivative of $\mathcal{E}_6$ *w.r.t.* ψ' (see Appendix $\boldsymbol{\mathcal{B}}$.6) is

$$\frac{\partial}{\partial\psi'}\mathcal{E}_6(E'^T,\psi') = -2(U\mathcal{N}')^T(U\mathcal{N}'\psi' - \text{Ғ}\boldsymbol{\mathcal{M}}_{\mathbf{0}}) + 4\lambda{\mathcal{N}'}^T\Phi'\mathcal{N}'\psi' \qquad (\mathcal{B}.35).$$

Hence,

$$\min_{\psi'}\mathcal{E}_6(E'^T,\psi') \Rightarrow \psi' = \boldsymbol{\mathcal{U}}^{-\mathbf{1}}\mathcal{N}'^TU^T\text{Ғ}\boldsymbol{\mathcal{M}}_{\mathbf{0}} \qquad (\mathcal{B}.36)$$

where $\boldsymbol{\mathcal{U}} = [\mathcal{N}'^T U^T U \mathcal{N}' - 2\lambda \mathcal{N}'^T \Phi' \mathcal{N}']$ and $\boldsymbol{\mathcal{U}} \in \mathbb{R}^{(n-4)\times(n-4)}$.

Appendix $\boldsymbol{\mathcal{C}}$

Experimental results

	Exp A	***Exp B***	***Exp C***	***Exp D***	***Exp E***
$\mathcal{N}'_5$	**50**	**100**	**150**	**200**	**250**
σ_{max}	**0.015**	**0.015**	**0.18**	**0.345**	**0.345**
$TRE_{\sigma_{max}}^{(l=1)}$	**3.6422 ± 1.7970**	**2.4066 ± 1.4275**	**1.5480 ± 0.5692**	**1.6850 ± 0.5401**	**1.8732 ± 0.4236**
$TRE_{\sigma_{max}}^{(l=2)}$	**4.6446 ± 0.9847**	**2.8968 ± 0.6774**	**2.7120 ± 0.7497**	**1.9388 ± 0.5114**	**1.8633 ± 0.4968**
$TRE_{\sigma_{max}}^{(l=3)}$	**3.2314 ± 0.6518**	**3.1261 ± 1.3734**	**1.9171 ± 1.010**	**2.3598 ± 0.5268**	**2.0581 ± 0.4173**
$TRE_{\sigma_{max}}^{(l=4)}$	**3.1511 ± 0.9926**	**2.8123 ± 0.7179**	**3.0102 ± 0.5003**	**2.6383 ± 0.6090**	**1.8698 ± 0.4774**
$TRE_{\sigma_{max}}^{(l=5)}$	**4.0930 ± 1.2289**	**2.3728 ± 0.8802**	**2.5567 ± 0.7319**	**2.0028 ± 0.4461**	**2.3202 ± 0.3905**
$TRE_{\sigma_{max}}^{(l=6)}$	**3.8504 ± 1.5763**	**2.9552 ± 1.1289**	**1.9580 ± 0.5342**	**1.9517 ± 0.4865**	**1.8932 ± 0.6680**
$TRE_{\sigma_{max}}^{(l=7)}$	**3.7562 ± 2.0253**	**1.5832 ± 0.3503**	**2.3328 ± 0.8777**	**2.2140 ± 0.3436**	**2.3169 ± 0.4966**
$TRE_{\sigma_{max}}^{(l=8)}$	**3.1013 ± 1.0719**	**3.0074 ± 0.4945**	**2.2111 ± 0.4600**	**3.0866 ± 0.5969**	**1.8463 ± 0.352**
$TRE_{\sigma_{max}}^{(l=9)}$	**3.4642 ± 1.1048**	**3.3151 ± 1.1780**	**2.4895 ± 0.7998**	**2.1410 ± 0.3950**	**2.8627 ± 0.7466**
$TRE_{\sigma_{max}}^{(l=10)}$	**3.6942 ± 1.1969**	**2.7939 ± 0.6293**	**2.4464 ± 0.7089**	**2.0826 ± 0.3439**	**2.6657 ± 0.7034**
$TRE_{\sigma_{max}}^{(l=11)}$	**3.7499 ± 1.3900**	**2.5434 ± 0.5253**	**2.3831 ± 0.7184**	**2.4237 ± 0.7826**	**1.7895 ± 0.3490**
$TRE_{\sigma_{max}}^{(l=12)}$	**4.1391 ± 1.6332**	**3.2131 ± 0.8613**	**2.1472 ± 0.3954**	**2.6535 ± 0.4818**	**2.4246 ± 0.4828**
$TRE_{\sigma_{max}}^{(l=13)}$	**3.4453 ± 1.5370**	**3.2582 ± 0.9148**	**2.5853 ± 0.3725**	**2.3830 ± 0.4454**	**2.7195 ± 0.5094**
$TRE_{\sigma_{max}}^{(l=14)}$	**4.1730 ± 1.4540**	**3.7057 ± 1.2482**	**2.6378 ± 0.6026**	**2.3985 ± 0.5286**	**2.9216 ± 0.3718**
$TRE_{\sigma_{max}}^{(l=15)}$	**3.2668 ± 0.6315**	**2.9902 ± 1.0851**	**2.2420 ± 0.4180**	**2.9554 ± 0.7219**	**2.2330 ± 0.4630**
$TRE_{\sigma_{max}}^{(l=16)}$	**3.5031 ± 0.7215**	**3.1915 ± 1.0173**	**2.8171 ± 0.6761**	**2.5551 ± 0.4452**	**2.8929 ± 0.4859**
$TRE_{\sigma_{max}}^{(l=17)}$	**4.3445 ± 1.3186**	**3.2680 ± 0.7445**	**2.3769 ± 0.3831**	**2.6241 ± 0.5855**	**2.3697 ± 0.3516**
$TRE_{\sigma_{max}}^{(l=18)}$	**4.5456 ± 1.5632**	**3.1174 ± 0.9275**	**2.5373 ± 0.5080**	**2.8169 ± 0.4898**	**2.6418 ± 0.3901**
$TRE_{\sigma_{max}}^{(l=19)}$	**3.8078 ± 1.0234**	**3.3120 ± 0.6481**	**2.6522 ± 0.6930**	**2.7227 ± 0.4768**	**2.5459 ± 0.4590**
$TRE_{\sigma_{max}}^{(l=20)}$	**3.0654 ± 0.7355**	**3.0923 ± 1.0193**	**3.0338 ± 0.4356**	**2.7636 ± 0.4626**	**2.6878 ± 0.4158**

Table $\mathcal{C}.1$: Average $TREs$ for σ_{max} and $\forall\ l \in \{1, \dots, 20\}$ for the set of experiments $A - E$ of $Algorithm$ 9 using the $KC + TPS$ technique (Section 3.8.2.1).

	$Exp\ A$	$Exp\ B$	$Exp\ C$	$Exp\ D$	$Exp\ E$
$\mathcal{N}'_5$	**50**	**100**	**150**	**200**	**250**
σ_{max}	**0.015**	**0.015**	**0.18**	**0.345**	**0.345**
$TRE_{\sigma_{max}}^{(l=1)}$	**3.7824 ± 1.9496**	**2.2054 ± 1.2601**	**1.3844 ± 0.4705**	**1.7535 ± 0.7488**	**1.8634 ± 0.4972**
$TRE_{\sigma_{max}}^{(l=2)}$	**4.1332 ± 1.6552**	**2.8501 ± 0.6736**	**2.8006 ± 0.8077**	**1.8562 ± 0.4729**	**1.8204 ± 0.5214**
$TRE_{\sigma_{max}}^{(l=3)}$	**3.3777 ± 0.7285**	**2.9368 ± 1.2119**	**1.8630 ± 1.1882**	**2.2705 ± 0.5637**	**2.1715 ± 0.5071**
$TRE_{\sigma_{max}}^{(l=4)}$	**2.9926 ± 1.0366**	**2.7694 ± 0.8126**	**3.1117 ± 0.6314**	**2.5566 ± 0.6337**	**1.8298 ± 0.5588**
$TRE_{\sigma_{max}}^{(l=5)}$	**3.8111 ± 0.9537**	**2.4349 ± 0.8065**	**2.6184 ± 0.7903**	**2.0911 ± 0.8113**	**2.3913 ± 0.3924**
$TRE_{\sigma_{max}}^{(l=6)}$	**3.8154 ± 1.6264**	**2.7437 ± 0.8073**	**1.8465 ± 0.5360**	**2.0298 ± 0.5366**	**1.8629 ± 0.7374**
$TRE_{\sigma_{max}}^{(l=7)}$	**2.9474 ± 1.2840**	**1.6161 ± 0.3466**	**2.4485 ± 1.0308**	**2.1729 ± 0.3211**	**2.5485 ± 0.5668**
$TRE_{\sigma_{max}}^{(l=8)}$	**3.3764 ± 1.6932**	**2.9055 ± 0.4632**	**2.2275 ± 0.4372**	**3.0301 ± 0.5577**	**1.8194 ± 0.3621**
$TRE_{\sigma_{max}}^{(l=9)}$	**3.6361 ± 1.1988**	**3.2028 ± 1.0329**	**2.5671 ± 0.8535**	**2.2393 ± 0.3773**	**2.9610 ± 0.7533**
$TRE_{\sigma_{max}}^{(l=10)}$	**4.3498 ± 1.5669**	**2.8742 ± 0.7183**	**2.4205 ± 0.3655**	**2.0654 ± 0.3299**	**2.9204 ± 0.7069**
$TRE_{\sigma_{max}}^{(l=11)}$	**3.4363 ± 1.3928**	**2.4910 ± 0.6010**	**2.2027 ± 0.5155**	**2.6008 ± 0.8290**	**1.8263 ± 0.3600**
$TRE_{\sigma_{max}}^{(l=12)}$	**3.4358 ± 0.7472**	**3.3614 ± 0.7710**	**2.1409 ± 0.3358**	**2.5181 ± 0.4754**	**2.2107 ± 0.3843**
$TRE_{\sigma_{max}}^{(l=13)}$	**3.1631 ± 1.3328**	**3.2730 ± 0.9451**	**2.6759 ± 0.4259**	**2.2487 ± 0.3197**	**2.8468 ± 0.6309**
$TRE_{\sigma_{max}}^{(l=14)}$	**3.8837 ± 1.3107**	**3.7458 ± 1.1744**	**2.7432 ± 0.6717**	**2.3871 ± 0.5193**	**3.0613 ± 0.5796**
$TRE_{\sigma_{max}}^{(l=15)}$	**3.7050 ± 1.2106**	**3.1527 ± 1.1631**	**2.3537 ± 0.4612**	**3.0615 ± 0.6925**	**2.1514 ± 0.3616**
$TRE_{\sigma_{max}}^{(l=16)}$	**3.4212 ± 0.7815**	**3.2218 ± 0.7637**	**2.6789 ± 0.5221**	**2.5129 ± 0.3911**	**2.8813 ± 0.5646**
$TRE_{\sigma_{max}}^{(l=17)}$	**4.5615 ± 1.5656**	**3.2641 ± 0.6349**	**2.4267 ± 0.3875**	**2.6604 ± 0.5258**	**2.5711 ± 0.5701**
$TRE_{\sigma_{max}}^{(l=18)}$	**4.5448 ± 1.4955**	**3.0770 ± 0.7527**	**2.8891 ± 0.8985**	**2.9142 ± 0.5381**	**2.7258 ± 0.6372**
$TRE_{\sigma_{max}}^{(l=19)}$	**3.8692 ± 1.1602**	**3.3183 ± 0.7096**	**2.5086 ± 0.5337**	**2.9782 ± 0.6275**	**2.8403 ± 0.4190**
$TRE_{\sigma_{max}}^{(l=20)}$	**3.2793 ± 0.8629**	**3.1416 ± 1.0125**	**3.0552 ± 0.4313**	**2.7508 ± 0.4510**	**2.8783 ± 0.4985**

Table $C.2$: Average $TREs$ for σ_{max} and $\forall\ l \in \{1,\dots,20\}$ for the set of experiments $A-E$ of $Algorithm$ 9 using the $GMM+TPS$ technique (Section 3.8.2.2).

Appendix $\boldsymbol{\mathcal{D}}$

Additional registrations on selected clinical data

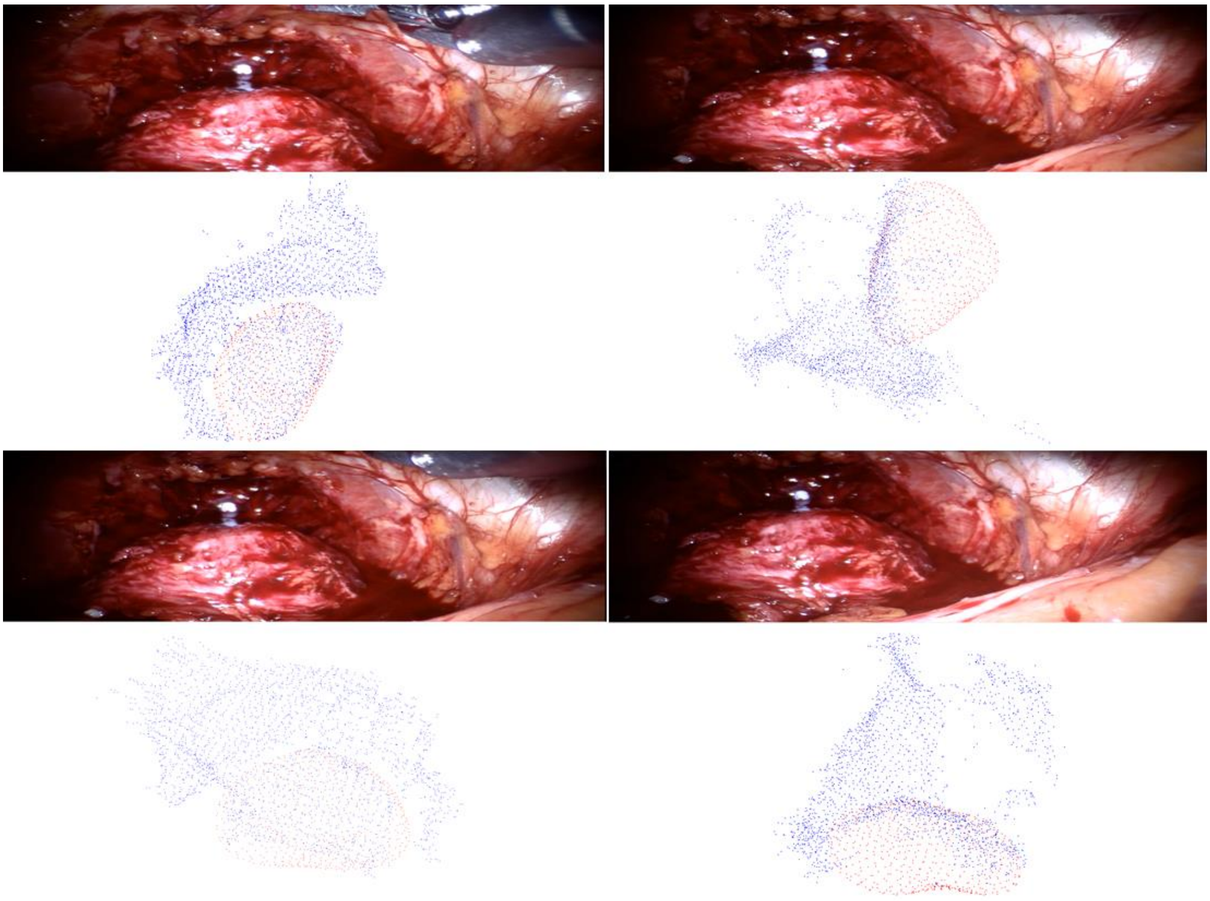

Figure $\mathcal{D}.1$: Selected video prostate images followed by the output of $KC + TPS$ non-rigid registration. The registered source is in red and the target prostate scene and its surrounding area are in blue. The registration output is not in scale to the video images.

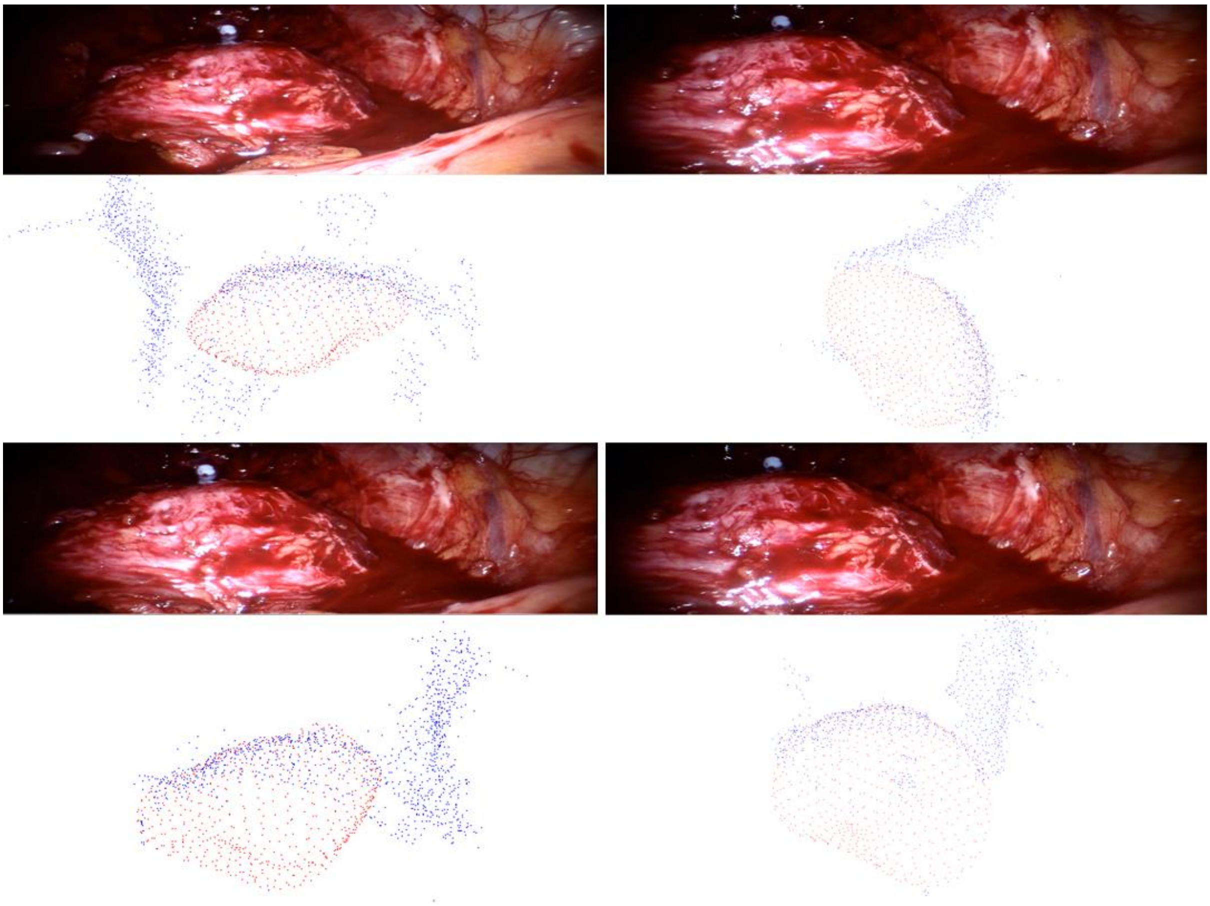

Figure $\mathcal{D}.2$: Selected video prostate images followed by the output of $GMM + TPS$ non-rigid registration. The registered source is in red and the target prostate scene and its surrounding area are in blue. The registration output is not in scale to the video images.

Bibliography

[1] COHEN, D., MAYER, E., CHEN, D., ANSTEE, A., VALE, J., YANG, G.-Z., DARZI, A., AND EDWARDS, P. Augmented reality image guidance in minimally invasive prostatectomy. *Lecture notes in computer science. International workshop on prostate cancer imaging (Springer Berlin), 6367 (2010), 101–110*, and references therein.

[2] http://emedicine.medscape.com/article/458677-overview (Retrieved on 12.11.2014).

[3] HOLMBERG, L., BILL-AXELSON, A., HELGESEN, F., SALO, J. O., FOLMERZ, P., HAGGMAN, M., ANDERSSON, S., SPANGBERG, A., BUSCH, C., NORDLING, S., PALMGREN, J., ADAMI, H., JOHANSSON, J., AND NORLEN, B. J. A randomized trial comparing radical prostatectomy with watchful waiting in early prostate cancer. *N. Engl. J. Med. 347* (2002), 781–789.

[4] http://www.ncbi.nlm.nih.gov/pmc/articles/PMC1477597/ (Retrieved on 12.11.2014)

[5] http://emedicine.medscape.com/article/458677-overview (Retrieved on 12.11.2014)

[6] FICARRA, V., NOVARA, G., ARTIBANI, W., CESTARI, A., GALFANO, A., GRAEFEN, M., GUAZZONI, G., GUILLONNEAU, B., MENON, M., MONTORSI, F., PATEL, V., RASSWEILER, J., AND VAN POPPEL, H. Retropubic, laparoscopic, and robot-assisted radical prostatectomy: a systematic review and cumulative analysis of comparative studies. *Eur. Urol. 55, 5* (2009), 1037–1063.

[7] GRAEFEN, M. Low quality of evidence for robot-assisted laparoscopic prostatectomy: a problem not only in the robotic literature. *Eur. Urol. 57* (2010), 938–940.

[8] http://www.intuitivesurgical.com/products/davinci_surgical_system/ (Retrieved on 14.11.2014)

[9] http://pubget.com/paper/21802281/Augmented_reality_in_laparoscopic_surgical_oncology (Retrieved on 12.11.2014)

[10] SOLER, L., NICOLAU, S., FASQUEL, J.-B., AGNUS, V., CHARNOZ, A., HOSTETTLER, A., MOREAU, J., FOREST, C., MUTTER, D., AND

MARESCAUX, J. Virtual reality and augmented reality applied to laparoscopic and notes procedures. *5th IEEE international symposium on biomedical imaging: from nano to macro (2008), 1399 – 1402.*

[11] SRIDHAR, A. N., HUGHES-HALLETT, A., MAYER, E. K., PRATT, P. J., EDWARDS, P. J., YANG, G.-Z., DARZI, A. W., AND VALE, J. A. Image-guided robotic interventions for prostate cancer. *Nat. Rev. Urol., Advance Online Publication* (2013), 1–11.

[12] YAKAR, D., DEBATS, O. A., BOMERS, J. G., SCHOUTEN, M. G., VOS, P. C., VAN LIN, E., FÜTTERER, J. J., AND BARENTSZ, J. O. Predictive value of MRI in the localization, staging, volume estimation, assessment of aggressiveness, and guidance of radiotherapy and biopsies in prostate cancer. *J. Magn. Reson. Imaging 35* (2012), 20–31.

[13] HASHIZUME, M. MRI-guided laparoscopic and robotic surgery for malignancies. *Int. J. Clin. Oncol. 12* (2007), 96–98.

[14] BHARATHA, A., HIROSE, M., HATA, N., WARFIELD, S. K., FERRANT, M., ZOU, K. H., SUAREZ-SANTANA, E., RUIZ-ALZOLA, J., D'AMICO, A., CORMACK, R. A., KIKINIS, R., JOLESZ, F. A., AND TEMPANY, C. M. Evaluation of three-dimensional finite element-based deformable registration of pre- and intraoperative prostate imaging. *Med. Phys. 28, 12* (2001), 2551–2560.

[15] CHENG, D., AND TEMPANY, C. MR imaging of the prostate and bladder. *Semin. Ultrasound CT MR 19* (1998), 67–89.

[16] SCHIEBLER, M. L., SCHNALL, M. D., POLLACK, H. M., LENKINSKI, R. E., TOMASZEWSKI, J. E., WEIN, A. J., WHITTINGTON, R., RAUSCHNING, W., AND KRESSEL, H. Y. Current role of MR imaging in the staging of adenocarcinoma of the prostate. *Radiology 189* (1993), 339–352.

[17] UKIMURA, O. Image-guided surgery in minimally invasive urology. *Curr. Opin. Urol. 20* (2010), 136–140.

[18] PETERS, T. M. Image-guidance for surgical procedures. *Phys. Med. Biol. 51, 14* (2006), R505–R540.

[19] MARKELJ, P., TOMAZEVIC, D., LIKAR, B., AND PERNUS, F. A review of 3D/2D registration methods for image-guided interventions. *Med. Image Anal. 16, 3* (2012), 642–661.

[20] MURPHY, M. J. Fiducial-based targeting accuracy for external-beam radiotherapy. *Med. Phys. 29, 3* (2002), 334–344.

[21] HILL, D. L. G., BATCHELOR, P. G., HOLDEN, M., AND HAWKES, D. J. Medical image registration. *Phys. Med. Biol. 46, 3* (2001), 1–45.

[22] MAINTZ, J. B. A., AND VIERGEVER, M. A. A survey of medical image registration. *Med. Image Anal. 2, 1* (1998), 1–36.

[23] ALTAMAR, H. O., ONG, R. E., GLISSON, C. L., VIPRAKASIT, D. P., MIGA, M. I., HERRELL, S. D., AND GALLOWAY, R. L. Kidney deformation and intraprocedural registration: a study of elements of image-guided kidney surgery. *J. Endourol. 25, 3* (2011), 511–517.

[24] http://cdn.intechopen.com/pdfs/13000/InTech-Image_fusion_for_biopsy_intervention_and_surgical_navigation_in_urology.pdf (Retrieved on 12.11.2014)

[25] EWERS, R., SCHICHO, K., UNDT, G., WANSCHITZ, F., TRUPPE, M., SEEMANN, R., AND WAGNER, A. Basic research and 12 years of clinical experience in computer-assisted navigation technology: a review. *Int. J. Oral Maxillofac. Surg. 34, 1* (2005), 1–8.

[26] ROBERTS, D. W., HARTOV, A., KENNEDY, F. E., MIGA, M. I., AND PAULSEN, K. D. Intraoperative brain shift and deformation: a quantitative analysis of cortical displacement in 28 cases. *Neurosurgery 43, 4* (1998), 749–758.

[27] CARTER, T. J., SERMESANT, M., CASH, D. M., BARRATT, D. C., TANNER, C., AND HAWKES, D. J. Application of soft tissue modelling to image-guided surgery. *Med. Eng. Phys. 27, 10* (2005), 893–909.

[28] BAUMHAUER, M., FEUERSTEIN, M., MEINZER, H. P., AND RASSWEILER, J. Navigation in endoscopic soft tissue surgery: perspectives and limitations. *J. Endourol. 22, 4* (2008), 751–766.

[29] SCHWEIKARD, A., GLOSSER, G., BODDULURI, M., MURPHY, M. J., AND

ADLER, J. R. Robotic motion compensation for respiratory movement during radiosurgery. *Comput. Aided Surg. 5, 4* (2000), 263–277.

[30] SCHNEIDER, C., NGUAN, C., LONGPRE, M., ROHLING, R., AND SALCUDEAN, S. Motion of the kidney between preoperative and intraoperative positioning. *IEEE Trans. Biomed. Eng. 60, 6* (2013), 1619–1627.

[31] MAURER, C. R., MACIUNAS, R. J., AND FITZPATRICK, J. M. Registration of head CT images to physical space using a weighted combination of points and surfaces. *IEEE Trans. Med. Imaging 17, 5* (1998), 753–761.

[32] KAGADIS, G. C., DELIBASIS, K. K., MATSOPOULOS, G. K., MOURAVLIANSKY, N. A., ASVESTAS, P. A., AND NIKIFORIDIS, G. C. A comparative study of surface- and volume-based techniques for the automatic registration between CT and SPECT brain images. *Med. Phys. 29, 2* (2002), 201–213.

[33] LEE, W.-C. C., TUBLIN, M. E., AND CHAPMAN, B. E. Registration of MR and CT images of the liver: comparison of voxel similarity and surface based registration algorithms. *Comput. Methods Programs Biomed. 78, 2* (2005), 101–114.

[34] HAN, Y., AND PARK, H. Automatic registration of brain magnetic resonance images based on Talairach reference system. *J. Magn. Reson. Imaging 20, 4* (2004), 572–580.

[35] ALVAREZ, N. A., AND SANCHIZ, J. M. Image registration from mutual information of edge correspondences. *Progress in pattern recognition, image analysis and applications. Lecture notes in computer science 3773 (2005), 528–539.*

[36] CRUM, W. R., HILL, D. L. G., AND HAWKES, D. J. Information theoretic similarity measures in non-rigid registration. *Inf. Process Med. Imaging 18* (2003), 378–387.

[37] PLUIM, J. P. W., MAINTZ, J. B. A., AND VIERGEVER, M. A. Mutual-information-based registration of medical images: a survey. *IEEE Trans. Med. Imaging 22, 8* (2003), 986–1004.

[38] SHEKHAR, R., AND ZAGRODSKY, V. Mutual information-based rigid and nonrigid registration of ultrasound volumes. *IEEE Trans. Med. Imaging 21, 1* (2002), 9–22.

[39] ROHLFING, T., MAURER, C. R., BLUEMKE, D. A., AND JACOBS, M. A. Volume-preserving nonrigid registration of MR breast images using free-form deformation with an incompressibility constraint. *IEEE Trans. Med. Imaging 22, 6* (2003), 730–741.

[40] CLATZ, O., DELINGETTE, H., TALOS, I. F., GOLBY, A. J., KIKINIS, R., JOLESZ, F. A., AYACHE, N., AND WARFIELD, S. K. Robust non-rigid registration to capture brain shift from intraoperative MRI. *IEEE Trans. Med. Imaging 24, 11* (2005), 1417–1427.

[41] GLADILIN, E., PEKAR, V., ROHR, K., AND STIEHL, H. A comparison between BEM and FEM for elastic registration of medical images. *Image Vision Comput. 24, 4* (2006), 375–379.

[42] SCHNABEL, J. A., TANNER, C., CASTELLANO-SMITH, A. D., DEGENHARD, A., LEACH, M. O., HOSE, D. R., HILL, D. L. G., AND HAWKES, D. J. Validation of nonrigid image registration using finite-element methods: application to breast MR images. *IEEE Trans. Med. Imaging 22, 2* (2003), 238–247.

[43] THOMPSON, S., PENNEY, G., BILLIA, M., CHALLACOMBE, B., HAWKES, D., AND DASGUPTA, P. Design and evaluation of an image-guidance system for robot-assisted radical prostatectomy. *BJU Int. 111, 7* (2013), 1081–1090, and references therein.

[44] http://www0.cs.ucl.ac.uk/staff/s.thompson/eau2008.pdf (Retrieved on 12.11.2013)

[45] PRATT, P., MAYER, E. K., VALE, J., COHEN, D., EDWARDS, E., DARZI, A., AND YANG, G. Z. An effective visualisation and registration system for image guided robotic partial nephrectomy. *J. Robot. Surg. 6* (2012), 23–31.

[46] FERRANT, M., WARFIELD, S. K., NABAVI, A., MACQ, B., AND KIKINIS, R. Registration of 3D intraoperative MR images of the brain using a finite element biomechanical model. *3rd international conference on medical robotics, imaging and computer-assisted surgery (MICCAI), Pittsburgh, PA, USA (A. M. DIGIOIA and S. DELP, eds., Springer-Verlag, Heidelberg, 2000), 19–28.*

[47] WARFIELD, S. K., FERRANT, M., GALLE, X., NABAVI, A., JOLESZ, F. A., AND KIKINIS, R. Real-time biomechanical simulation of volumetric brain

deformation for image guided neurosurgery. *High performance networking and computing conference, Dallas, USA (2000).*

[48] FERRANT, M., MACQ, B., NABAVI, A., AND WARFIELD, S. K. Deformable modeling for characterizing biomedical shape changes. *Discrete geometry for computer imagery. 9th International conference, DGCI 2000, Uppsala, Sweden (G. BORGEFORS, I. NYSTRÖM, and G. SANNITI DI BAJA, Springer, Heidelberg, 2000), 235–248.*

[49] CASH, D. M., MIGA, M. I., GLASGOW, S. C., DAWANT, B. M., CLEMENTS, L. W., CAO, Z., GALLOWAY, R. L., AND CHAPMAN, W. C. Concepts and preliminary data toward the realization of image-guided liver surgery. *J. Gastrointest. Surg. 11* (2007), 844–859.

[50] SIMPFENDÖRFER, T., BAUMHAUER, M., MÜLLER, M., GUTT, C. N., MEINZER, H.-P., RASSWEILER, J. J., GUVEN, S., AND TEBER, D. Augmented reality visualization during laparoscopic radical prostatectomy. *J. Endourol. 25, 12* (2011), 1841–1845.

[51] SU, L.-M., VAGVOLGYI, B. P., AGARWAL, R., REILEY, C. E., TAYLOR, R. H., AND HAGER, G. D. Augmented reality during robot-assisted laparoscopic partial nephrectomy: toward real-time 3D-CT to stereoscopic video registration. *J. Urol. 73, 4* (2009), 896–900.

[52] KARNIK, V. V., FENSTER, A., BAX, J., COOL, D. W., GARDI, L., GYACSKOV, I., ROMAGNOLI, C., AND WARD, A. D. Assessment of image registration accuracy in three-dimensional transrectal ultrasound guided prostate biopsy. *Med. Phys. 37, 2* (2010), 802–813.

[53] JIAN, B., AND VEMURI, B. C. Robust point set registration using Gaussian mixture models. *IEEE Trans. Pattern Anal. Mach. Intell. 33, 8* (2011), 1633–1645, and references therein.

[54] JIAN, B., AND VEMURI, B. C. A robust algorithm for point set registration using mixture of Gaussians. *Proceedings of the 10th IEEE international conference on computer vision (2005) 2, 1246–1251.*

[55] TSIN, Y., AND KANADE, T. A correlation-based approach to robust point set registration. *Proceedings of the European conference on computer vision (2004), 558–569,* and references therein.

[56] GLAUNES, J., TROUVÉ, A., AND YOUNES, L. Diffeomorphic matching of distributions: a new approach for unlabelled point-sets and sub-manifolds matching. *Proceedings of the IEEE computer society conference on computer vision and pattern recognition (2004), 712–718.*

[57] CHUI, H., AND RANGARAJAN, A. A new point matching algorithm for non-rigid registration. *Comput. Vis. Image Und. 89* (2003), 114–141.

[58] CHUI, H., AND RANGARAJAN, A. A feature registration framework using mixture models. *Proceedings of the IEEE workshop on mathematical methods in biomedical image analysis (2000), 190–197.*

[59] CHUI, H., AND RANGARAJAN, A. A new algorithm for non-rigid point matching. *Proceedings of the IEEE conference on computer vision and pattern recognition (2000), 44–51.*

[60] WELLS, W. Statistical approaches to feature-based object recognition. *Intl. J. Computer Vision 21, 1-2* (1997), 63–98.

[61] SCOTT, D. W. Parametric statistical modeling by minimum integrated square error. *Technometrics 43, 3* (2001), 274–285, and references therein.

[62] MA, J., ZHAO, J., TIAN, J., TU, Z., AND YUILLE, A. Robust estimation of nonrigid transformation for point set registration. *Proceedings of the IEEE conference on computer vision and pattern recognition (2013), 2147–2154.*

[63] SANDHU, R., DAMBREVILLE, S., AND TANNENBAUM, A. Point set registration via particle filtering and stochastic dynamics. *IEEE Trans. Pattern Anal. Mach. Intell. 32, 8* (2010), 1459–1473.

[64] JENSSEN, R., ERDOGMUS, D., PRINCIPE, J. C., AND ELTOFT, T. The laplacian PDF distance: a cost function for clustering in a kernel feature space. *Adv. Neural Inf. Process. Syst.* (2004), 625–632.

[65] SCOTT, D. W., AND SZEWCZYK, W. F. From kernels to mixtures. *Technometrics 43, 3* (2001), 323–335.

[66] AMBERG, B., ROMDHANI, S., AND VETTER, T. Optimal step nonrigid ICP algorithms for surface registration. *IEEE Conference on computer vision and pattern recognition (2007), 1–8.*

[67] ALLEN, B., CURLESS, B., AND POPOVIĆ, Z. The space of human body shapes: reconstruction and parameterization from range scans. *ACM Trans. Graph 22, 3* (2003), 587–594.

[68] C++ implementations of *state-of-the-art* algorithms that were used in the present work. These are publicly available at http://gmmreg.googlecode.com.

[69] MAURER, C. R., MCCRORY, J. J., AND FITZPATRICK, J. M. Estimation of accuracy in localizing externally attached markers in multimodal volume head images. *Proc. SPIE, Medical Imaging: Image Processing 1898* (1993), 43–54.

[70] FITZPATRICK, J. M., WEST, J. B., AND MAURER, C. R. Predicting error in rigid-body, point-based registration. *IEEE Trans. Med. Imaging 17, 5* (1998), 694–702, and references therein.

[71] SIBSON, R. Studies in the robustness of multidimensional scaling: perturbational analysis of classical scaling. *J. R. Statist. Soc. B 41* (1979), 217–229.

[72] CRUM, W. R., HARTKENS, T., AND HILL, D. L. G. Non-rigid image registration: theory and practice. *Br. J. Radiol. 77* (2004), S140–S153.

[73] HAJNAL, J. V., HILL, D. L. G., AND HAWKES, D. J. *Medical image registration. CRC Press (2001).*

[74] SCHESTOWITZ, R., TWINING, C., COOTES, T., PETROVIC, V., TAYLOR, C., AND CRUM, W. R. Assessing the accuracy of non-rigid registration with and without ground truth. *3rd IEEE Internal symposium on biomedical imaging: macro to nano (2006), 836–839.*

[75] GUO, Y., WERAHERA, P. N., NARAYANAN, R., LI, L., KUMAR, D., CRAWFORD, E. D., AND SURI, J. S. Image registration accuracy of a 3-

dimensional transrectal ultrasound-guided prostate biopsy system. *J. Ultrasound Med. 28, 11* (2009), 1561–1568.

[76] BUHMANN, M. D. Radial basis functions: theory and implementations. *Cambridge University Press, NY, USA (2003), ISBN:0521633389.*

[77] DUCHON, J. Splines minimizing rotation-invariant semi-norms in Sobolev spaces, Constructive theory of functions of several variables. *Proceedings of the conference held at the mathematical research institute, Oberwolfach, 1976. Lecture notes in mathematics (W. SCHEMPP and K. ZELLER, eds., Springer-Verlag, Berlin) 571 (1977), 85–100.*

[78] MEINGUET, J. Multivariate interpolation at arbitrary points made simple. *J. Appl. Math. Phys. (ZAMP) 30,* (1979), 292–304.

[79] MEINGUET, J. Surface spline interpolation: basic theory and computational aspects. *Approximation theory and spline functions (S. P. SINGH et al., eds., D. REIDEL Publishing Co., Dordrecht, Netherlands, 1984), 127–142.*

[80] WAHBA, G. Spline models for observational data. *SIAM (1990), ISBN 0–89871–244–0.*

[81] LAPEER, R. J., AND PRAGER, R. W. 3D shape recovery of a newborn skull using thin-plate splines. *Comput. Med. Imag. Graph. 24, 3* (2000), 193–204.

[82] ROHR, K. Landmark-based image analysis: using geometric and intensity models. *Kluwer Academic Publishers Norwell, MA, USA (2001), ISBN:0792367510.*

[83] BOOKSTEIN, F. L. Principal warps: thin-plate splines and the decomposition of deformations. *IEEE Trans. Pattern Anal. Mach. Intell. 11, 6* (1989), 567–585.

[84] COLEMAN, T. F., AND SORENSEN, D. C. A note on the computation of an orthonormal basis for the null space of a matrix. *Math. Program. 29* (1984), 234–242, and references therein.

[85] PETERSEN, K. B., AND PEDERSEN, M. S. The matrix cookbook. http://www.math.uwaterloo.ca/~hwolkowi/matrixcookbook.pdf, and references therein. (Retrieved on 12.11.2014).

[86] KANAZAWA, Y., AND KANATANI, K. Do we really have to consider covariance matrices for image features? *Proceedings of the 8th IEEE international conference on computer vision 2 (2001), 301–306.*

[87] PAULY, M., MITRA, N. J., GIESEN, J., GROSS, M. H., AND GUIBAS, L. J. Example-based 3D scan completion. *Symposium on Geometry Processing* (2005), 23–32.

[88] PARZEN, E. On estimation of a probability density function and mode. *Ann. Math. Statist. 33, 3* (1962), 1065–1076.

[89] HASTIE, T., TIBSHIRANI, R., AND FRIEDMAN, J. The elements of statistical learning, data mining, inference and prediction. *Springer, Berlin (2009), ISBN 978-0-387-84857-0.*

[90] CHUI, H., RAMBO, J., DUNCAN, J., SCHULTZ, R., AND RANGARAJAN, A. Registration of cortical anatomical structures via robust 3D point matching. *Information processing in medical imaging. Lecture notes in computer science (Springer, Berlin) 1613 (1999), 168–181, ISBN 978-3-540-66167-2.*

[91] GOLD, S., RANGARAJAN A., LU, C. P., PAPPU, S., AND MJOLSNESS, E. New algorithms for 2-D and 3-D point matching: pose estimation and correspondence. *Pattern Recognition 31, 8* (1998), 1019–1031.

[92] RANGARAJAN, A., CHUI, H., AND BOOKSTEIN, F. L. The softassign procrustes matching algorithm. *Information processing in medical imaging. Lecture notes in computer science (Springer, Berlin) 1230 (1997), 29–42, ISBN 978-3-540-63046-3.*

[93] HATHAWAY, R. Another interpretation of the EM algorithm for mixture distributions. *Statist. Probab. Lett. 4* (1986), 53–56, and references therein.

[94] YUILLE, A. L. Generalized deformable models, statistical physics, and matching problems. *Neural Comput. 2* (1990), 1–24.

[95] HOFMANN, T., AND BUHMANN, J. M. Pairwise data clustering by deterministic annealing. *IEEE Trans. Pattern Anal. Mach. Intell. 19, 1* (1997), 1–14.

[96] GEIGER, D., AND GIROSI, F. Parallel and deterministic algorithms from MRFs: surface reconstruction. *IEEE Trans. Pattern Anal. Mach. Intell. 13, 5* (1991), 401–412.

[97] http://www.vtk.org/ (Retrieved on 02.12.2014).

[98] http://hpc.cs.ucl.ac.uk/ (Retrieved on 02.12.2014).

[99] http://qt.digia.com/ (Retrieved on 05.01.2015).

[100] http://pointclouds.org/ (Retrieved on 05.01.2015).

[101] PAPAZOV, C., AND BURSCHKA, D. Deformable 3D shape registration based on local similarity transforms. *Comput. Graph. Forum 30, 5* (2011), 1493–1502.